CIRCULATION WEATHER TYPES AS A TOOL IN ATMOSPHERIC, CLIMATE AND ENVIRONMENTAL RESEARCH

EDITED BY: Alexandre M. Ramos, David Barriopedro and Emanuel Dutra

frontiers Research Topics

About Frontiers

Frontiers is more than just an open-access publisher of scholarly articles: it is a pioneering approach to the world of academia, radically improving the way scholarly research is managed. The grand vision of Frontiers is a world where all people have an equal opportunity to seek, share and generate knowledge. Frontiers provides immediate and permanent online open access to all its publications, but this alone is not enough to realize our grand goals.

Frontiers Journal Series

The Frontiers Journal Series is a multi-tier and interdisciplinary set of open-access, online journals, promising a paradigm shift from the current review, selection and dissemination processes in academic publishing. All Frontiers journals are driven by researchers for researchers; therefore, they constitute a service to the scholarly community. At the same time, the Frontiers Journal Series operates on a revolutionary invention, the tiered publishing system, initially addressing specific communities of scholars, and gradually climbing up to broader public understanding, thus serving the interests of the lay society, too.

Dedication to Quality

Each Frontiers article is a landmark of the highest quality, thanks to genuinely collaborative interactions between authors and review editors, who include some of the world's best academicians. Research must be certified by peers before entering a stream of knowledge that may eventually reach the public - and shape society; therefore, Frontiers only applies the most rigorous and unbiased reviews.

Frontiers revolutionizes research publishing by freely delivering the most outstanding research, evaluated with no bias from both the academic and social point of view.

By applying the most advanced information technologies, Frontiers is catapulting scholarly publishing into a new generation.

What are Frontiers Research Topics?

Frontiers Research Topics are very popular trademarks of the Frontiers Journals Series: they are collections of at least ten articles, all centered on a particular subject. With their unique mix of varied contributions from Original Research to Review Articles, Frontiers Research Topics unify the most influential researchers, the latest key findings and historical advances in a hot research area! Find out more on how to host your own Frontiers Research Topic or contribute to one as an author by contacting the Frontiers Editorial Office: **researchtopics@frontiersin.org**

CIRCULATION WEATHER TYPES AS A TOOL IN ATMOSPHERIC, CLIMATE AND ENVIRONMENTAL RESEARCH

Topic Editors:
Alexandre M. Ramos, Instituto Dom Luiz, Faculdade de Ciências, Universidade de Lisboa, Portugal
David Barriopedro, Universidad Complutense de Madrid, Spain and Instituto de Geociencias (CSIC, UCM), Spain
Emanuel Dutra, European Centre for Medium-Range Weather Forecasts, United Kingdom

The aftermath of Gong wind storm in Praia Grande, Sintra, Portugal.
Image by Alexandre M. Ramos

Classifications of circulation weather systems have a long history in meteorology and climatology. Starting with manual classifications over specific regions of the globe, these tools (generally called "catalogs of synoptic types") were restricted mainly to weather forecasting and historical climate variability studies. In the last decades, the advance of computing resources and the availability of datasets have fostered the development of fast and objective methods that process large amount of data.

In recent years numerous methods of circulation type classification have been designed, showing their usefulness on a wide range of applications in scientific domains related to weather, climate, and environment.

This Research Topic highlights methodological advances in circulation weather types and also their applications to different research areas. The articles included in this research topic show that circulation weather types can be used not only in Europe, where they have been always more frequent, but also applied to other regions of the world.

Table of Contents

Circulation weather types as a tool in atmospheric, climate, and environmental research

Alexandre M. Ramos[1]*, David Barriopedro[2, 3] and Emanuel Dutra[4]

[1] Instituto Dom Luiz, Faculdade de Ciências, Universidade de Lisboa, Lisbon, Portugal, [2] Departamento de Física de la Tierra II, Universidad Complutense de Madrid, Madrid, Spain, [3] Instituto de Geociencias, Consejo Superior de Investigaciones Científicas-Universidad Complutense Madrid, Madrid, Spain, [4] European Centre for Medium-Range Weather Forecasts, Reading, UK

Classifications of circulation weather systems have a long history in meteorology and climatology. Starting with manual classifications (Hess and Brezowsky, 1952; Lamb, 1972) over specific regions of the globe, these tools (generally called "catalogs of synoptic types") were restricted mainly to weather forecasting and historical climate studies.

In the last decades, the advance of computing resources and the availability of datasets have fostered the development of fast and objective methods that process large amounts of data. Many climatological studies and applications require these data to be as simplified as possible; this is often achieved by analyzing gridded datasets (usually sea level pressure or geopotential height at different levels), and grouping the data into a relatively small number of distinct categories. Since these types are based on meteorological fields observed at a specific instant, they are also called Eulerian classifications.

Several classification methods of circulation weather types have been developed, and are currently used in a wide range of applications (Huth et al., 2008, 2010; Philipp et al., 2010). In addition, in 2002, Sheridan stated that the "Synoptic weather-typing, or the classification of weather conditions or patterns into categories, continues to be popular, and numerous methods have been developed over the past century" (Sheridan, 2002). The increasing interdisciplinary use of circulation weather types in Europe became clear when the European project "Harmonization and Applications of Weather Types Classifications for European Regions—COST733," where a wide range of classification schemes for different spatial domains were developed and compared within the scope of distinct applications. (Huth et al., 2008, 2010; Philipp et al., 2010).

In recent years, the usefulness of circulation weather type classifications has been demonstrated in a large number of scientific domains from climate (Kysely and Domonkos, 2006; Lorenzo et al., 2011), to environmental areas such as air quality (Demuzere et al., 2009) and forest fires (Kassomenos, 2010) or upwelling activity (Ramos et al., 2013). The relationship between circulation weather type classifications and high-impact weather events was also shown in extreme temperature episodes (Kysely, 2008, floods Prudhomme and Genevier, 2011), droughts (Russo et al., 2015), or even lightning activity (Ramos et al., 2011).

Automatic circulation weather type classification algorithms have also allowed exploring the variability of the atmospheric circulation over Europe during the last centuries. This has been possible by using either historical monthly mean grids going back to the eighteenth century (Beck et al., 2007) or daily fields that extend to 1871 in reanalysis products (e.g., Jones et al., 2013), to 1850 in historical data (Philipp et al., 2007) and to 1685 for some weather types (Barriopedro et al., 2014). These studies stress that changes in weather type frequencies can explain an important amount of temperature and precipitation variability. However, one must acknowledge that there are caveats such as non-stationarities in the connection between atmospheric circulation and surface

climate. In fact, about half of the European surface climate variability (even more on long-term temporal scales) has been related to varying internal properties of some circulation weather types (the so-called within-type variations, e.g., Beck et al., 2007; Jones and Lister, 2009). Recent global warming is also manifesting in additional difficulties, as some studies have noticed a "decoupling" between atmospheric circulation patterns and the surface climate responses since the 1990s (Vautard and Yiou, 2009).

This research topic, "Circulation Weather types as a tool in atmospheric, climate, and environmental research," intends to highlight methodological advances in circulation weather types and also their applications to different research areas. The articles included in this research topic show that circulation weather types can be used not only in Europe, where they have been always more frequent, but also applied to other regions of the world. Therefore, six out of the 10 articles focus on areas outside of Europe, including central and northern America as well as southern Africa. Regarding new methodologies, a circulation type classification based upon Lagrangian air trajectories is proposed by Ramos et al. (2014a). Two different studies highlight the importance of the Lamb circulation weather types (Jenkinson and Collison, 1977) in explaining the precipitation (Ramos et al., 2014b) and drought variability (Russo et al., 2015) over the Iberian Peninsula. An automated version of the Lamb weather type classification and its relationship with precipitation is also applied with success to Saudi Arabia (El Kenawy et al., 2014). Furthermore, Hidalgo et al. (2014) shows that circulation weather types can be used to generate long term near surface climatic time series at high temporal frequencies suitable to force Soil-Vegetation-Atmosphere transfer models. Regarding tropical regions, cold surge activity over the Gulf of Mexico (Pérez et al., 2014) and low level wind regimes over Central America (Sáenz and Durán-Quesada, 2015) are addressed with

a circulation weather types approach. Finally, three papers focus on the Southern Hemisphere. Bardossy et al. (2015) explores Fuzzy Rule Based Circulation Patterns to identify different spatial rainfall and ocean wave fields in Southern Africa. Moron et al. (2015) uses a cluster analysis to characterize the variability of circulation weather types across the Maritime Continent. Finally, a synoptic climatology of heavy rain events in the Lake Eyre and Lake Frome catchments is presented by Pook et al. (2014).

During the last few decades, circulation weather type' classifications have been extremely useful to gain insight of the atmospheric processes at the synoptic scale, but also studying the relationship between atmospheric circulation and surface climate variability. As proven in this research topic, the use of circulation weather types' classifications is also becoming frequent to explore climate variability in regions outside Europe. Regarding methodologies, the use of nonlinear methods such as the self-organizing maps (Sheridan and Lee, 2011) is becoming popular, and the introduction of new methodologies, such as the merging weather types and Lagrangian transport presented in the research topic (e.g., Ramos et al., 2014a) is also expected.

Circulation weather types' classifications and their applications will continue to play a fundamental role in characterizing and understanding current and future changes of large-scale circulation and their local impacts in different areas of environmental sciences.

Acknowledgments

References

Bardossy, A., Pegram, G., Sinclair, S., Pringle, J., and Stretch, D. (2015). Circulation Patterns identified by spatial rainfall and ocean wave fields in Southern Africa. *Front. Environ. Sci.* 3:31. doi: 10.3389/fenvs.2015.00031

Barriopedro, D., Gallego, D., Álvarez-Castro, M. C., García-Herrera, R., Wheeler, D., Peña-Ortiz, C., et al. (2014). Witnessing North Atlantic westerlies variability from ships' logbooks (1685–2008). *Clim. Dyn.* 43, 939–955. doi: 10.1007/s00382-013-1957-8

Beck, C., Jacobeit, J., and Jones, P. D. (2007). Frequency and within-type variations of large-scale circulation types and their effects on low-frequency climate variability in Central Europe since 1780. *Int. J. Climatol.* 27, 473–491. doi: 10.1002/joc.1410

Demuzere, M., Trigo, R. M., Vila-Guerau de Arellano, J., and van Lipzig, N. P. M. (2009). The impact of weather and atmospheric circulation on O3 and PM10 levels at a rural mid-latitude site. *Atmos. Chem. Phys.* 9, 2695–2714. doi: 10.5194/acp-9-2695-2009

El Kenawy, A. M., McCabe, M. F., Stenchikov, G. L., and Raj, J. (2014). Multi-decadal classification of synoptic weather types, observed trends and links to rainfall characteristics over Saudi Arabia. *Front. Environ. Sci.* 2:37. doi: 10.3389/fenvs.2014.00037

Hess, P., and Brezowsky, H. (1952). Katalog der Großwetterlagen Europas (catalog of the European large scale weather types). *Ber. Dt. Wetterd. US-Zone* 33, 39.

Hidalgo, J., Masson, V., and Baehr, C. (2014). From daily climatic scenarios to hourly atmospheric forcing fields to force Soil-Vegetation-Atmosphere transfer models. *Front. Environ. Sci.* 2:40. doi: 10.3389/fenvs.2014.00040

Huth, R., Beck, C., Phillipp, A., Demuzere, M., Ustrnul, Z., Cahynová, M., et al. (2008). Classifications of atmospheric circulation patterns: recent advances and applications. *Trends Dir. Clim. Res. Ann. N.Y. Acad. Sci.* 1146, 105–152. doi: 10.1196/annals.1446.019

Huth, R., Beck, H., and Tveito, O. E. (2010). Preface of classifications of atmospheric circulation patterns—theory and applications. *Phys. Chem. Earth.* 35, 307–308. doi: 10.1016/j.pce.2010.06.005

Jenkinson, A. F., and Collison, F. P. (1977). *An Initial Climatology of Gales Over the North Sea, Synoptic Climatol. Branch Memo.* 62. Bracknell: Meteorol. Off.

Jones, P. D., Harpham, C., and Briffa, K. R. (2013). Lamb weather types derived from Reanalysis products. *Int. J. Climatol.* 33, 1129–1139. doi: 10.1002/joc.3498

Jones, P. D., and Lister, D. H. (2009). The influence of the circulation on surface temperature and precipitation patterns over Europe. *Clim. Past* 5, 259–267. doi: 10.5194/cp-5-259-2009

Kassomenos, P. (2010). Synoptic circulation control on wild fire occurrence. *Phys. Chem. Earth.* 35, 544–552. doi: 10.1016/j.pce.2009.11.008

Kysely, J. (2008). Influence of the persistence of circulation patterns on warm and cold temperature anomalies in Europe: analysis over the 20th century. *Glob. Planet. Change* 62, 147–163. doi: 10.1016/j.gloplacha.2008.01.003

Kysely, J., and Domonkos, P. (2006). Recent increase in persistence of atmospheric circulation over Europe: comparison with long-term variations since 1881. *Int. J. Climatol.* 26, 461–483. doi: 10.1002/joc.1265

Lamb, H. H. (1972). British Isles weather types and a register of daily sequence of circulation patterns, 1861–1971. *Geophys. Memoir.* 116, 85L.

Lorenzo, M. N., Ramos, A. M., Taboada, J. J., and Gimeno, L. (2011). Changes in present and future circulation types frequency in Northwest Iberian Peninsula. *PLoS ONE* 6:e16201. doi: 10.1371/journal.pone.0016201

Moron, V., Robertson, A. W., Qian, J.-H., and Ghil, M. (2015). Weather types across the Maritime Continent: from the diurnal cycle to interannual variations. *Front. Environ. Sci.* 2:65. doi: 10.3389/fenvs.2014.00065

Pérez, E. P., Magaña, V., Caetano, E., and Kusunoki, S. (2014). Cold surge activity over the Gulf of Mexico in a warmer climate. *Front. Earth Sci.* 2:19. doi: 10.3389/feart.2014.00019

Philipp, A., Bartholy, J., Beck, C., Erpicum, M., Esteban, P., Fettweis, R., et al. (2010). Cost733cat—a database of weather and circulation type classifications. *Phys. Chem. Earth* 35, 360–373. doi: 10.1016/j.pce.2009.12.010

Philipp, A., Della-Marta, P. M., Jacobeit, J., Fereday, D. R., Jones, P. D., Moberg, A., et al. (2007). Long-term variability of daily North Atlantic–european pressure patterns since 1850 classified by simulated annealing clustering. *J. Climate* 20, 4065–4095. doi: 10.1175/JCLI4175.1

Pook, M. J., Risbey, J. S., Ummenhofer, C. C., Briggs, P. R., and Cohen, T. J. (2014). A synoptic climatology of heavy rain events in the Lake Eyre and Lake Frome catchments. *Front. Environ. Sci.* 2:54. doi: 10.3389/fenvs.2014.00054

Prudhomme, C., and Genevier, M. (2011). Can atmospheric circulation be linked to flooding in Europe? *Hydrol. Process.* 25, 1180–1190. doi: 10.1002/hyp.7879

Ramos, A. M., Cordeiro Pires, A., Sousa, P. M., and Trigo, R. M. (2013). The use of circulation weather types to predict upwelling activity along the Western Iberian Peninsula coast. *Cont. Shelf. Res.* 69, 38–51. doi: 10.1016/j.csr.2013.08.019

Ramos, A. M., Cortesi, N., and Trigo, R. M. (2014b). Circulation weather types and spatial variability of daily precipitation in the Iberian Peninsula. *Front. Earth Sci.* 2:25. doi: 10.3389/feart.2014.00025

Ramos, A. M., Ramos, R., Sousa, P., Trigo, R. M., Janeira, M., and Prior, V. (2011). Cloud to ground lightning activity over Portugal and its association with circulation weather types. *Atmos. Res.* 101, 84–101. doi: 10.1016/j.atmosres.2011.01.014

Ramos, A. M., Sprenger, M., Wernli, H., Durán-Quesada, A. M., Lorenzo, M. N., and Gimeno, L. (2014a). A new circulation type classification based upon Lagrangian air trajectories. *Front. Earth Sci.* 2:29. doi: 10.3389/feart.2014.00029

Russo, A. C., Gouveia, C. M., Trigo, R. M., Liberato, M. L. R., and DaCamara, C. C. (2015). The influence of circulation weather patterns at different spatial scales on drought variability in the Iberian Peninsula. *Front. Environ. Sci.* 3:1. doi: 10.3389/fenvs.2015.00001

Sáenz, F., and Durán-Quesada, A. (2015). A climatology of low level wind regimes over Central America using a weather type classification approach. *Front. Earth Sci.* 3:15. doi: 10.3389/feart.2015.00015

Sheridan, S. C. (2002). The redevelopment of a weather-type classification scheme for North America. *Int. J. Climatol.* 22, 51–68. doi: 10.1002/joc.709

Sheridan, S. C., and Lee, C. C. (2011). The self-organizing map in synoptic climatological research. *Prog. Phys. Geogr.* 35, 109–119. doi: 10.1177/0309133310397582

Vautard, R., and Yiou, P. (2009). Control of recent European surface climate change by atmospheric flow. *Geophys. Res. Lett.* 36, L22702, doi: 10.1029/2009GL040480

Conflict of Interest Statement: The authors declare that the research was conducted in the absence of any commercial or financial relationships that could be construed as a potential conflict of interest.

A new circulation type classification based upon Lagrangian air trajectories

Alexandre M. Ramos[1]*, Michael Sprenger[2], Heini Wernli[2], Ana M. Durán-Quesada[3], Maria N. Lorenzo[4] and Luis Gimeno[4]

[1] Instituto Dom Luiz, Faculdade de Ciências, Universidade de Lisboa, Lisboa, Portugal
[2] Institute for Atmospheric and Climate Science, ETH Zurich, Zurich, Switzerland
[3] School of Physics and Center for Geophysical Research, University of Costa Rica, San Jose, Costa Rica
[4] Environmental Physics Laboratory, Universidad de Vigo, Ourense, Spain

*Correspondence:
Alexandre M. Ramos, Instituto Dom
Luiz, Faculdade de Ciências,
Universidade de Lisboa, Campo
Grande, Edf. C8, Piso 3, Sala 8.3.1,
1749-016 Lisboa, Portugal
e-mail: amramos@fc.ul.pt

A new classification method of the large-scale circulation characteristic for a specific target area (NW Iberian Peninsula) is presented, based on the analysis of 90-h backward trajectories arriving in this area calculated with the 3-D Lagrangian particle dispersion model FLEXPART. A cluster analysis is applied to separate the backward trajectories in up to five representative air streams for each day. Specific measures are then used to characterize the distinct air streams (e.g., curvature of the trajectories, cyclonic or anticyclonic flow, moisture evolution, origin and length of the trajectories). The robustness of the presented method is demonstrated in comparison with the Eulerian Lamb weather type classification. A case study of the 2003 heatwave is discussed in terms of the new Lagrangian circulation and the Lamb weather type classifications. It is shown that the new classification method adds valuable information about the pertinent meteorological conditions, which are missing in an Eulerian approach. The new method is climatologically evaluated for the 5-year time period from December 1999 to November 2004. The ability of the method to capture the inter-seasonal circulation variability in the target region is shown. Furthermore, the multi-dimensional character of the classification is shortly discussed, in particular with respect to inter-seasonal differences. Finally, the relationship between the new Lagrangian classification and the precipitation in the target area is studied.

Keywords: circulation types, backward trajectories, cluster analysis, Northwest Iberian Peninsula, precipitation

INTRODUCTION

The interest in the relationship between circulation types and surface climate increased in the last decades. Circulation type classifications were recently applied in climate studies (Huth et al., 2008; Jacobeit, 2010) and to investigate how the frequency of circulation types is associated with changes in surface weather parameters like precipitation (e.g., Goodess and Palutikof, 1998; Fowler and Kilsby, 2002; Kyselý, 2008; Jones and Lister, 2009). In a certain region and at a given time, the atmospheric circulation can be described in different ways, which is reflected in the large number of different circulation-based classifications (Huth et al., 2008; Philipp et al., 2010). Traditionally, circulation types are specific to a certain region and result from the examination of gridded synoptic weather data, typically based on sea level pressure (SLP) or geopotential height at 500 hPa (H500). These types are often defined for each day or a group of consecutive days and tend to reflect the circulation in a certain region (e.g., Hess and Brezowsky, 1952; Kruizinga, 1979; Jones et al., 1993; Philipp et al., 2007). Since these types are based on fields of SLP or H500 at one time instant, they are called Eulerian classifications.

The analysis of trajectories approaching a target region provides an alternative possibility of studying circulation types (e.g.,

Stohl and Scheifinger, 1994; Jorba et al., 2004; Nyanganyura et al., 2008). For such applications, Lagrangian models, which divide the atmosphere into a finite number of air parcels moving according to the three-dimensional winds (Stohl, 1998; Stohl et al., 2001), are very useful. The path followed by the air parcels, i.e., the trajectory, accurately characterizes the history of the air streams arriving at a specific site. Trajectory analyses are commonly used in air quality studies and cluster analysis is often used to handle large sets of trajectories (e.g., Dorling et al., 1992; Riccio et al., 2007). These studies mainly rely on the position (latitude, longitude, and height) of the air parcels. If specific humidity along the trajectories is also considered, they can be used to study atmospheric moisture transport by tracking air parcels moving to a given area (James et al., 2004; Dirmeyer and Brubaker, 2006) or to identify moisture sources of precipitation events (Sodemann et al., 2008). Trajectory analysis has also been used to examine meteorological phenomena like warm conveyor belts and tropical moisture export (e.g., Wernli and Davies, 1997; Stohl, 2001; Eckhardt et al., 2004; Knippertz and Wernli, 2010).

In this work, a new classification method of the synoptic-scale circulation is presented. It is based on the analysis of backward trajectories and determines the representative airflow to the target

region (Northwest Iberian Peninsula) for each day at 12 UTC. The new method is compared to an automated version of the Eulerian Lamb weather type classification (LWT, Lamb, 1972; Jones et al., 1993). Additionally, the relationship between each circulation type and precipitation is analyzed in order to investigate whether the new method is able to distinguish different precipitation characteristics. Section Target Region and Data Sets provides a brief description of the target region and the data sets used. In Section A New Classification Based on Lagrangian Backward Trajectories, the new circulation type classification is described in detail and applied to a case study. Section Inter-Seasonal Variability of Individual Characteristics presents an analysis of the seasonality of the distinct classes and flow characteristics, followed by the link between the Lagrangian classification and precipitation in the target region in Section Precipitation Associated with Trajectory Types. The co-occurrence of the Lagrangian characteristics is studied (Section Combined Characteristics) and the Lagrangian classification is compared with the LWT (Section Comparison of Lamb Weather Types and Lagrangian Circulation Types). Finally, Section Summary and Conclusions summarizes the main results.

TARGET REGION AND DATA SETS

REGION AND PRECIPITATION DATA

The northwestern Iberian Peninsula (NW IP) (41°N–44.5°N and 10°W–6°W), surrounded by the Atlantic Ocean and the Cantabrian Sea, is often affected by the passage of cold fronts associated with the storm track in the North Atlantic (Trigo, 2005). Gómez-Gesteira et al. (2011) comprehensively studied the climate of the NW IP during the last 40 years. In general, the coastal and adjacent areas are characterized by a maritime climate with mild summers and rainy winters. The interior regions are characterized by a continental climate with dry summers and cold winters. The atmospheric circulation of the area, under the influence of the mid-latitude weather systems of the North Atlantic, is determined by two main centers of activity: an anticyclone south of 40°N centered near the Azores (Azores High) and a low pressure area centered around 60°N near Iceland (Iceland Low). A thermal low develops over the IP from April to September, giving rise, in combination with the Azores High, to equatorward coastal winds in the NW IP (Hoinka and de Castro, 2003). Previous studies have shown that the precipitation variability in the region is linked to the main North Atlantic modes of low frequency variability: the North Atlantic Oscillation (NAO), the Scandinavia pattern (SCA) and the East Atlantic/West Russia Pattern (EA/WR) (Lorenzo and Taboada, 2005; deCastro et al., 2006; Ramos et al., 2010). Different circulation type methodologies were applied successfully in the IP (e.g., Romero et al., 1999; Trigo and DaCamara, 2000; Esteban et al., 2005; Lorenzo et al., 2008).

The correlation between the variability in precipitation at the Lourizán weather station (42.42°N, 8.67°W) and the variability in precipitation in the North-Atlantic European sector (data from the Global Precipitation Climatology Project) was reviewed by Lorenzo et al. (2008). It was found that the precipitation data from Lourizán station is representative of the precipitation in the entire NW IP area.

TRAJECTORY DATASET

Backward trajectories were generated using the Lagrangian dispersion model FLEXPART (Stohl et al., 2005). This model has been applied in a variety of studies on, e.g., atmospheric transport (James et al., 2008; Stohl and Sodemann, 2010), convection and pollution (Palau et al., 2009), biomass burning (Cammas et al., 2009), and source-receptor relationships (Paris et al., 2010). In this study, 6-h ECMWF meteorological analysis data was used as input for the FLEXPART model for the period from 1/11/1999 to 30/11/2004. Positions of each particle (latitude, longitude and height) as well as its physical properties (specific humidity, density, and temperature) were recorded at each time step. The atmosphere was divided into a total of 1,398,800 homogeneous air parcels (referred to as particles) homogeneously distributed over the entire globe. Three-dimensional winds and other fields from ECMWF ERA-40 Reanalysis data were used to set the meteorological conditions for the particles. A set of parameterizations describes the subgrid-scale physical processes within the FLEXPART model, for details see the FLEXPART technical note (Stohl et al., 2005). At any given time, the particles in the target region (NW IP) and the vertical layer from the surface to 14 km were selected for studying their backward trajectories in more detail (see Section A New Classification Based on Lagrangian Backward Trajectories).

DEFINITION OF THE LAMB WEATHER TYPES

The daily SLP fields were retrieved from the NCEP/NCAR reanalysis (Kalnay et al., 1996) on a 2.5° grid. Eulerian circulation types computed for Galicia by Lorenzo et al. (2008) are used in this study, based on the daily SLP fields. This classification is an automated version of the LWT procedure (Jones et al., 1993). In recent years, this method has been successfully applied to other European regions (Goodess and Palutikof, 1998; Trigo and DaCamara, 2000). The circulation conditions are determined using physical or geometrical parameters, such as the direction and strength of the airflow, and the degree of cyclonicity based on 16 grid points. This method distinguishes between 26 different circulation types (including hybrid ones). In this study, 12 circulation types are analyzed, eight determined by the direction of the flow (NE, E, SE, S, SW, W, NW, N), two by the shear vorticity [cyclonic (C) or anticyclonic (A)], and two hybrid ones [hybrid cyclonic (HC) and hybrid anticyclonic (HA)].

For the sake of brevity, we do not describe in detail the LWT methodology. Additional information regarding the LWT can be found in previous publications by the authors (e.g., Lorenzo et al., 2008; Ramos et al., 2011). The frequency of each LWT is shown in **Table 1**. Circulation type A is the most frequent one with almost 25% of the days followed by the SW and W type. Since the HC and HA circulation types are a mixture of all the hybrid directional types, the following discussion is only focused on the pure types.

A NEW CLASSIFICATION BASED ON LAGRANGIAN BACKWARD TRAJECTORIES

From the global dataset, the particles that arrive to the NW IP on a particular day are selected and the classification is based on the properties of these air particles. In our case, the number of daily trajectories ranges approximately between 50 and 400. The

Table 1 | Frequency (%) of occurrence of Lamb circulation weather types during the 1/12/1999 to 30/11/2004 period.

LWT	Number of days (%)
NE	4.3
E	2.5
SE	1.8
S	2.4
SW	10.2
W	10.5
NW	5.7
N	2.6
C	7.2
A	25.9
HC	7.6
HA	19.4

number of air particles has a seasonal cycle with higher values in winter and lower values in summer. The main idea is to find the representative airflows that arrive in the NW IP. The applied procedure is as follows: (i) a two-step clustering is applied (Section Clustering of Trajectories) to find a maximum of five distinct air streams representing the flow on a particular day, each of them characterized by the temporal evolution of latitude, longitude, height, specify humidity and distance to the target region; (ii) the representative backward trajectories are further analyzed and characterized by four distinct Lagrangian flow properties (Section New Characteristics and Dynamical Classification). This classification enables to attribute an "index" for each of the four flow properties to each air stream.

In Section Clustering of Trajectories and New Characteristics and Dynamical Classification a detailed description of the new classification procedure is given, while a diagram summarizing the method is shown in **Figure 1**. The resulting classification catalog for the 5 years and a specific case study are presented in Section Final Catalog and Case Study Example.

CLUSTERING OF TRAJECTORIES
Trajectories of air parcels that are in the target domain at the chosen time step were selected and the respective 90-h backward trajectories were retrieved from the global dataset. The circulation types, for each day at 12 UTC, were assumed to be characterized by at most five distinct air streams (trajectory clusters). A two-step clustering is used in order to obtain at most five distinct air streams. This choice of a maximum of five air streams is not arbitrary. A preliminary analysis (not shown) showed that the most frequent number of clusters per day is 5, therefore this is considered to be the optimal number of distinct air streams per day.

First clustering step
The squared Euclidean distance is used as a similarity measure between the members of a predefined set of trajectories. The aim is to horizontally separate different air streams. The approach is based on the first part of the method proposed by Dorling et al. (1992), see their sections 2a to 2c for details. The method

uses the latitude-longitude coordinates to separate the different air streams. An example for a particular day (11/11/1999) is provided in **Figure 2** with the color lines showing the trajectories of different clusters and the thick black lines representing the centroid trajectory of each cluster, which is defined at each time as the average of the latitude-longitude coordinates and the meteorological variables (see Section Trajectory Dataset) of the trajectories in that cluster. In the Dorling method there is no need to set an a priori number of clusters. The method is able to autonomously determine the number of clusters (based only, as mentioned before, on the latitude and longitude information) for a given day. Clusters with less than 10 trajectories are not included in the next clustering step. This is done to keep only the most representative air streams for a given day. If less than five centroid trajectories are found, the assumption is made that they are meteorologically different and no additional action is required. On the other hand, if the number of clusters from the first (horizontal) clustering exceeds five, a second (hierarchical) clustering is performed based on the centroid trajectories of the previous clustering step.

Second clustering step
Information of the height of the centroid trajectory (H), the distance to the target area (D), specific humidity (Q) and latitude (LAT) are used as main characteristics of the trajectories at each time step. Hierarchical clustering constructs a hierarchy of sets of groups, each of which is formed by merging one pair from the collection of previously defined groups. A linkage criterion, which specifies the dissimilarity of the trajectories as a function of the pairwise distances of observations, is also used (Wilks, 2006). Here, the dissimilarity of the trajectories is the weighted average distance (Hastie et al., 2009). This process is iterated until the maximum number of clusters in the hierarchical clustering converges to five. It is important to point out that the centroids of the hierarchical clustering are computed initially based on the centroid trajectories taken from the non-hierarchical clustering.

Finally, a maximum of five distinct air streams represent the flow on a particular day, each being characterized by their temporal evolution of latitude, longitude, height, specify humidity and distance to the target region. As an example, the hierarchical clustering for the day shown in **Figure 2** is provided in **Figure 3**, where the time evolution of the back trajectory properties for each variable used in the clustering is also shown.

NEW CHARACTERISTICS AND DYNAMICAL CLASSIFICATION
Once the trajectories were reduced to a maximum of five clusters, a dynamical classification was done based on four distinct Lagrangian flow properties. This classification enables the attribution of an "index" for each of the four studied parameters to each air stream. Therefore, the representative flows were classified using their temporal evolution of latitude, longitude, height, specify humidity and distance to the target region. A description of the respective characteristics and criteria is given below with a summary in **Table 2**. The flow properties chosen were: (a) the moisture uptake during the path of the air mass; (b) zonality of the flow; (c) cyclonicity of the flow,
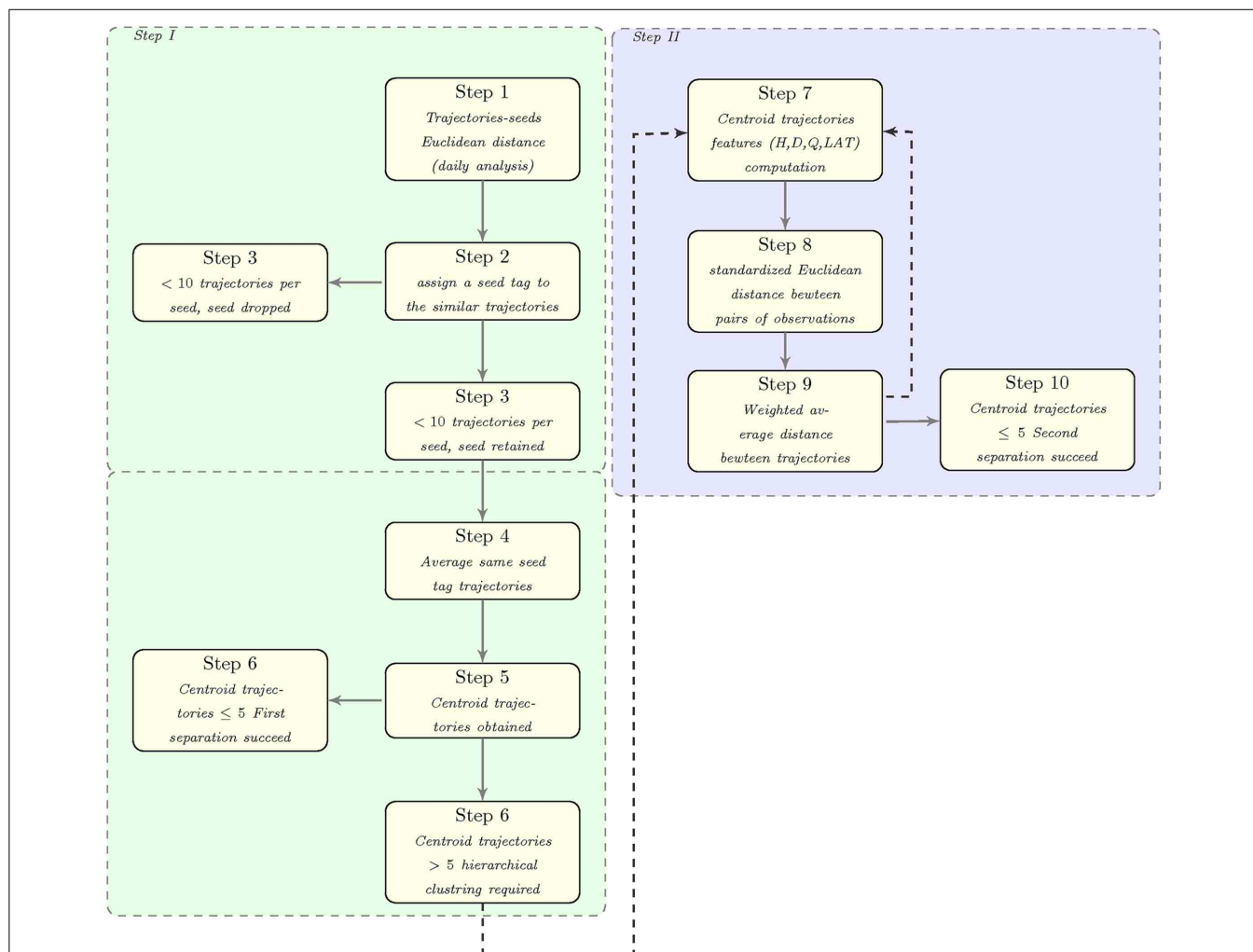
FIGURE 1 | Diagram summarizing the synoptic-scale circulation classification method based on Lagrangian Backward Trajectories.

and (d) the traveled distance and origin of the air mass. We considered that this set of 4 characteristics allow a detailed classification of the main air masses that arrive in the NW IP. For each characteristic, a reasonable number of classes are defined.

Moisture uptake (MU)

MU describes the moisture uptake of the air stream. It represents the change in specific humidity (ΔQ) of an individual air stream from the initial point (i) to the arrival in the target region (f), computed as:

$$\Delta Q = Q_f - Q_i, \tag{1}$$

The histogram of ΔQ (**Figure 4A**) for all air streams resembles a normal distribution and the division is made into three classes: (Q−) ΔQ in the lower tercile of the distribution; it corresponds to a decrease in humidity along the path; (Q+) ΔQ in the upper tercile of the distribution; it corresponds to an increase in humidity along the path; and (Q0) if ΔQ falls between the two classes

mentioned above; it corresponds to small changes (positive or negative) of the humidity along path.

Distance and origin (DO)

This feature classifies each air stream both in terms of integrated distance D along the air stream (short, medium and long range transport) and its initial position. A four-point compass is centered in the domain allowing 90° per sector (see **Figure 5** for details) and the variable O (origin quadrant) therefore can take on four discrete values (NE, SE, SW, and NW). O is determined by the position of the initial point of the air stream. The histogram of D is shown in **Figure 4B** for all air streams, and it is divided into three classes: (S) D in the lower tercile of the distribution (less than 3076 km), corresponding to short range transport; (M) D in the middle tercile of the distribution (greater than 3076 km and less than 5391 km), corresponding to medium range transport; and (L) D in the upper tercile of the distribution (greater than 5391 km), corresponding to long-range transport. As an example, if an air stream is classified as L-SW in terms of DO it means that it
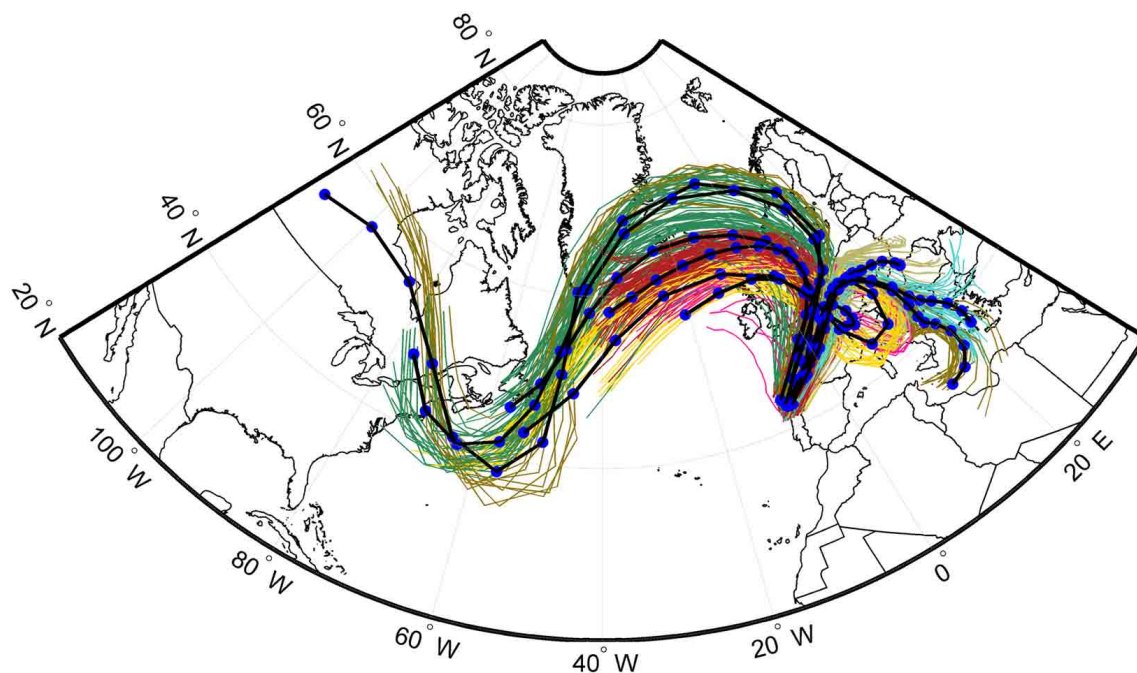
FIGURE 2 | Backward trajectories (90 h) arriving to the northwest Iberia Peninsula (41°N–44.5°N and 10°W–6°W) on a particular day (11/11/1999—12 UTC) in color lines and the respective clusters position (blue dots) computed by the Dorling method (dark lines).

experienced long-range transport and its initial point was in the 3rd quadrant (SW).

Cyclonicity index (CI)

This index determines whether the flow is cyclonic or anticyclonic, and to which extent this applies. It is based on the radius of curvature (R) of the air stream and combines three flow features:

(a) R_C, the percentage of the air stream with a small cyclonic radius of curvature between 0 and 1000 km; as an example, if R_C is 25%, 25% of the air stream has a small cyclonic radius of curvature.

(b) R_A, the corresponding percentage with a small anticyclonic radius of curvature between 0 and 1000 km.

(c) R_{net}, the net curvature of the flow (negative for anticyclonic and positive for cyclonic) computed by integrating the value of the curvature along the air stream (the histogram for R_{net} is presented in **Figure 4C**):

$$R_{net} = \sum_{t=i}^{t=f} (R_t) \qquad (2)$$

Based on these three flow features the following five classes of the Cyclonicity Index CI are defined: (C_s) $R_C > 25\%$ and $R_A < 25\%$, the air stream has small cyclonic curvatures during at least 25% of the path; it is strongly affected by meso- and synoptic-scale cyclonic systems (e.g., extra-tropical cyclones); (A_s) $R_A > 25\%$ and $R_C < 25\%$, the air stream has small anticyclonic curvatures during at least 25% of the path; (C_sA_s) $R_C > 25\%$, and $R_A > 25\%$,

during the path the air stream has both small cyclonic and anticyclonic curvatures; if the three classes above do not apply then R_{net}, is used: (C_{net}) if $R_{net} > 0$, i.e., on average cyclonic path; and (A_{net}) for an average anticyclonic path, i.e., $R_{net} < 0$.

Zonality index (ZI)

ZI describes the curvature of the path of the air streams (curved or straight). It is computed by integrating the absolute value of the radius of curvature (R) for each sub-section of the air stream:

$$ZI = \sum_{t=i}^{t=f} (|R_t|) \qquad (3)$$

It can be seen as a Lagrangian based zonality index—the term "zonality" is used in a generalized way and serves here to distinguish between weakly curved and strongly undulating flows. The histogram of ZI (**Figure 4D**) shows a positively skewed distribution. It is divided into two classes: (Z−) ZI below the median, corresponding to a weakly curved air stream; and (Z+) ZI above the median, corresponding to a strongly curved air stream.

FINAL CATALOG AND CASE STUDY EXAMPLE

The purpose of Section Clustering of Trajectories and New Characteristics and Dynamical Classification is to have a final catalog of the properties of the air streams that arrive each day which are expressed by the four parameters (MU, ZI, CI, and DO) described above and listed in **Table 2**. A sample of the catalog from 01/12/1999 to 18/02/2000 is provided in **Figure 6**. Additionally, 1 day or multiple days can be characterized by a
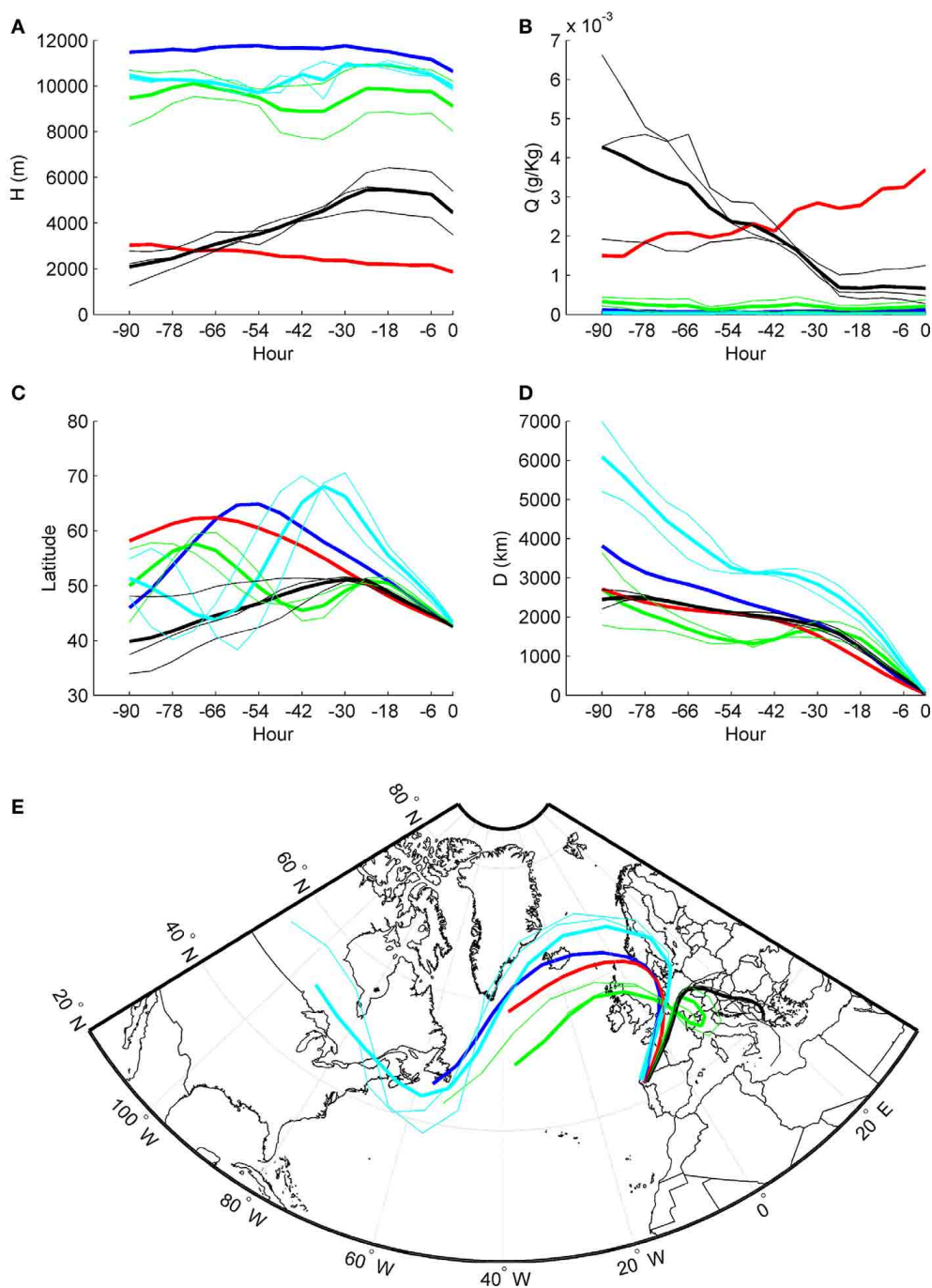
FIGURE 3 | Time evolution of the back-trajectory properties for (A) height of trajectory (H), (B) specific humidity (Q), (C) latitude and (D) distance to the center (D) shown in Figure 1. The colored thin line corresponds to the centroid trajectories (previous computed with the Dorling method) while the colored thick lines correspond to the final five air streams characterizing the day (see text for details). In **(E)** the final air streams are shown. The color code is the same as in **(A–D)**

single string of labels indicating the most frequent classes encountered for each characteristic. For example, the classification [Q−, Z+, A$_{net}$, L-SW], corresponds to the first air stream of the first day (01/12/1999) and is shown in **Figure 6**. In such a situation the majority of the air streams had respectively: a decrease in humidity during the path, a significantly curved trajectory, a

mean anticyclonic path, and a long-distance pathway from the SW quadrant.

As a more specific example, we consider the heatwave event of 2003 (01/08/2003 to 15/08/2003), which stroke not only Central Europe (Garcia-Herrera et al., 2010) but also the NW IP (Trigo et al., 2009; deCastro et al., 2011). The northward displacement of

Table 2 | Characteristics and respective classes used to classify the representative air masses.

Characteristic	Class	Description
Moisture uptake	Q−	Decrease in humidity along the path
	Q+	Increase in humidity along the path
	Q0	Small changes of the humidity along path
Zonality index	Z-	Weakly-curved air stream along the path
	Z+	Strongly curved air stream along the path
Cyclonicity index	Cs	Air stream with small cyclonic curvatures during at least 25% of the path
	As	Air stream with small anticyclonic curvatures during at least 25% of the path
	CsAs	Air stream with both small cyclonic and anticyclonic curvatures during the path
	Cnet	If the three classes above do not apply then if air stream with average cyclonic during path
	Anet	Same as Cnet but for if air stream with average anticyclonic path
Combination between distance and origin	S	Short range transport
	D	Medium range transport
	L	Long range transport
	NE	Flow from the NE quadrant
	SE	Flow from the SE quadrant
	SW	Flow from the SW quadrant
	NW	Flow from the NW quadrant

the North Atlantic Subtropical High is recognized to be the most probable mechanism responsible for the August 2003 heatwave (e.g., Black et al., 2004; deCastro et al., 2011). The correspondent daily LWT for this period is shown in **Table 3**. Most of the days are A-related types followed by type C, which occurs probably due to the thermal low that frequently develops over the IP in summer (Hoinka and de Castro, 2003). Additional information can be retrieved from the statistics of the Lagrangian types during this event (**Figure 7**). Short-range transport dominates (almost 2/3 of the air streams). In addition, there is advection of African air to the IP. Concerning MU, Q+ (increase in specific humidity) is the most frequent class. Regarding CI, the most frequent classes are A_s (small anticyclonic curvatures) and C_{net} (air streams with averaged cyclonic path). This is very interesting because the Lagrangian method is not only able to capture the thermal low, responsible for the re-circulations in the IP with short range transport, but also the anticyclonic circulation associated with

medium and long-range transport. This heatwave event, according to the Lagrangian classification, is categorized as $[Q+, Z+, A_s, S\text{-}SW]$.

Further case studies can be found in the Supplementary Material S1, where additional typical weather situations in the target region are discussed: a cold frontal passage, a cut-off low and a blocking high.

CLIMATOLOGICAL ASSESSMENT
INTER-SEASONAL VARIABILITY OF INDIVIDUAL CHARACTERISTICS
In this section we analyze if the new method presented in Section A New Classification Based on Lagrangian Backward Trajectories is able to distinguish the inter-seasonal circulation variability in the region (Lorenzo et al., 2008; Gómez-Gesteira et al., 2011), and to this end the mean frequency of the different characteristics of air streams is examined for all seasons: winter (DJF), spring (MAM), summer (JJA), and autumn (SON). In addition, the respective seasonal standard deviation is used to have an insight of the inter-annual variability.

The analysis first focuses on the DO characteristic (Distance and Origin) (**Table 4**). Results show that the western quadrants (S-SW, S-NW, M-SW, M-NW, L-SW, L-NW) are found more frequently than the eastern ones (S-SE, S-NE, M-SE, M-NE, L-SE, L-NE) in all seasons, which reflects the fact that most of the time the domain is under the influence of the westerlies, in good agreement with previous weather type analyses such as Spellman (2000). A remarkable difference between winter and summer occurs for the transport distance. Short transport classes are more frequent in summer (almost 43%) while the frequency of long-range transport is larger in winter (nearly 45%). This is in line with the intensification of the Northern Hemisphere jet stream in winter compared to summer. In addition, the poleward shift by about 10° latitude of the belt of westerlies in summer (Peixoto and Oort, 1992) is captured by the method. The atmospheric circulation in summer in the IP is, most of the time, under the influence of a thermal low (Hoinka and de Castro, 2003). This thermal low is responsible for short-range transport and re-circulations in the region. Finally, differences between spring and autumn are small. The highest standard deviation is in general found in the transitions season's spring and autumn.

For the MU parameter (Moisture Uptake), **Figure 8A** shows that Q0 dominates in winter and spring, i.e., only small changes (positive or negative) of humidity are found along the air streams. In contrast, Q+ is the most frequent class in summer corresponding to an increase of humidity along the path. This fact can be associated with high values of sea surface temperature (SST) of the Atlantic Ocean and Mediterranean Sea, favoring evaporation in summer. In autumn, Q− is the most frequent class, associated with a loss of humidity due to precipitation along the air stream. The seasonal variability (standard deviation) is relatively small for the MU parameter.

With respect to ZI (Zonality Index) (**Figure 8B**), Z+, i.e., strongly curved air streams, are more frequent during the transition seasons. The frequencies of the classes differ clearly in winter and summer. In summer, Z− is more frequent than Z+, while
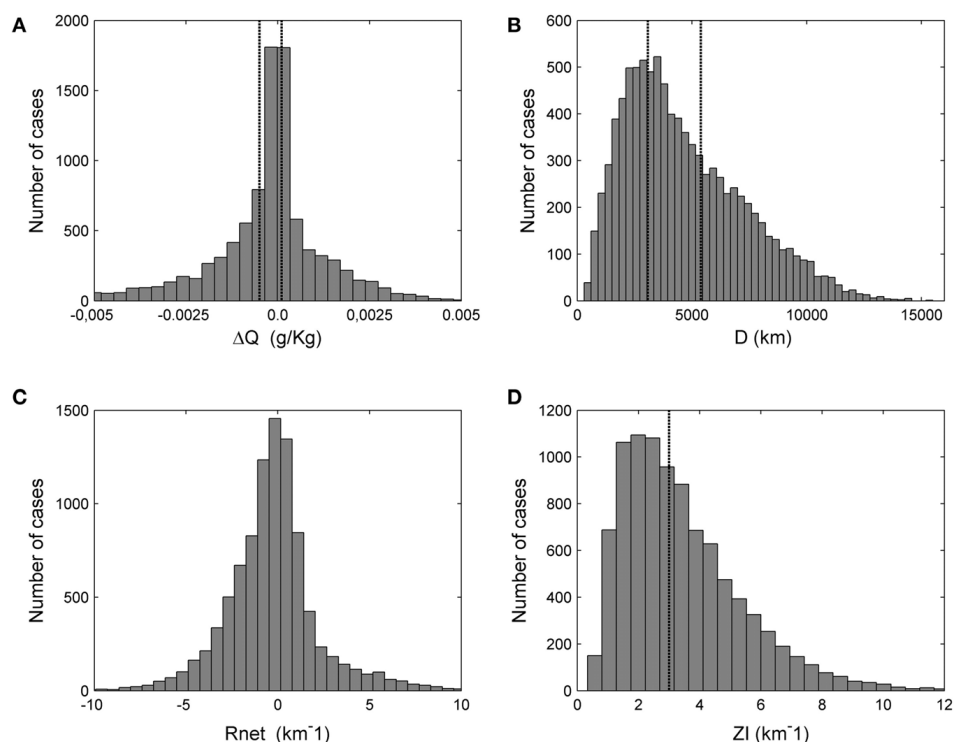
FIGURE 4 | Histograms distribution for: (A) integrated changes in specific humidity (Q), (B) distance "traveled" by the particle (D); (C) integrated value of the curvature (R$_{net}$) and (D) integrated absolute value of the curvature (ZI). For Q and D the tercile values are indicated with a dotted black line and for ZI the 50% percentile.
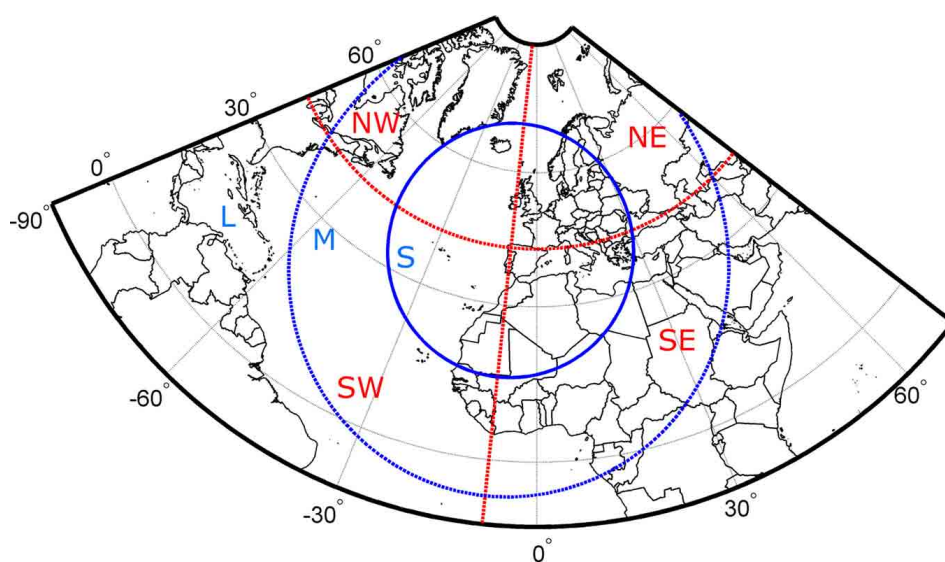
FIGURE 5 | Definition for the Distance and Origin (DO) characteristic for the air streams. The circles separate the different distance (D) classes: short range (S), medium range (M), and long range (L).The origin of the air streams is split into the four regions SW, NW, SE, and NE. In total, 12 classes result for DO.

in winter both classes have similar frequencies. Again, the highest standard deviations are found for spring and autumn.

The frequency distribution for CI (Cyclonicity Index) (**Figure 8C**) is again similar for the different classes during spring

and autumn, with A$_{net}$ being the most frequent class. In winter the most frequent class is A$_{net}$ with 45% of the cases followed by the averaged cyclonic class (C$_{net}$) with a frequency near 25%. For summer the averaged anticyclonic and cyclonic classes (A$_{net}$ and
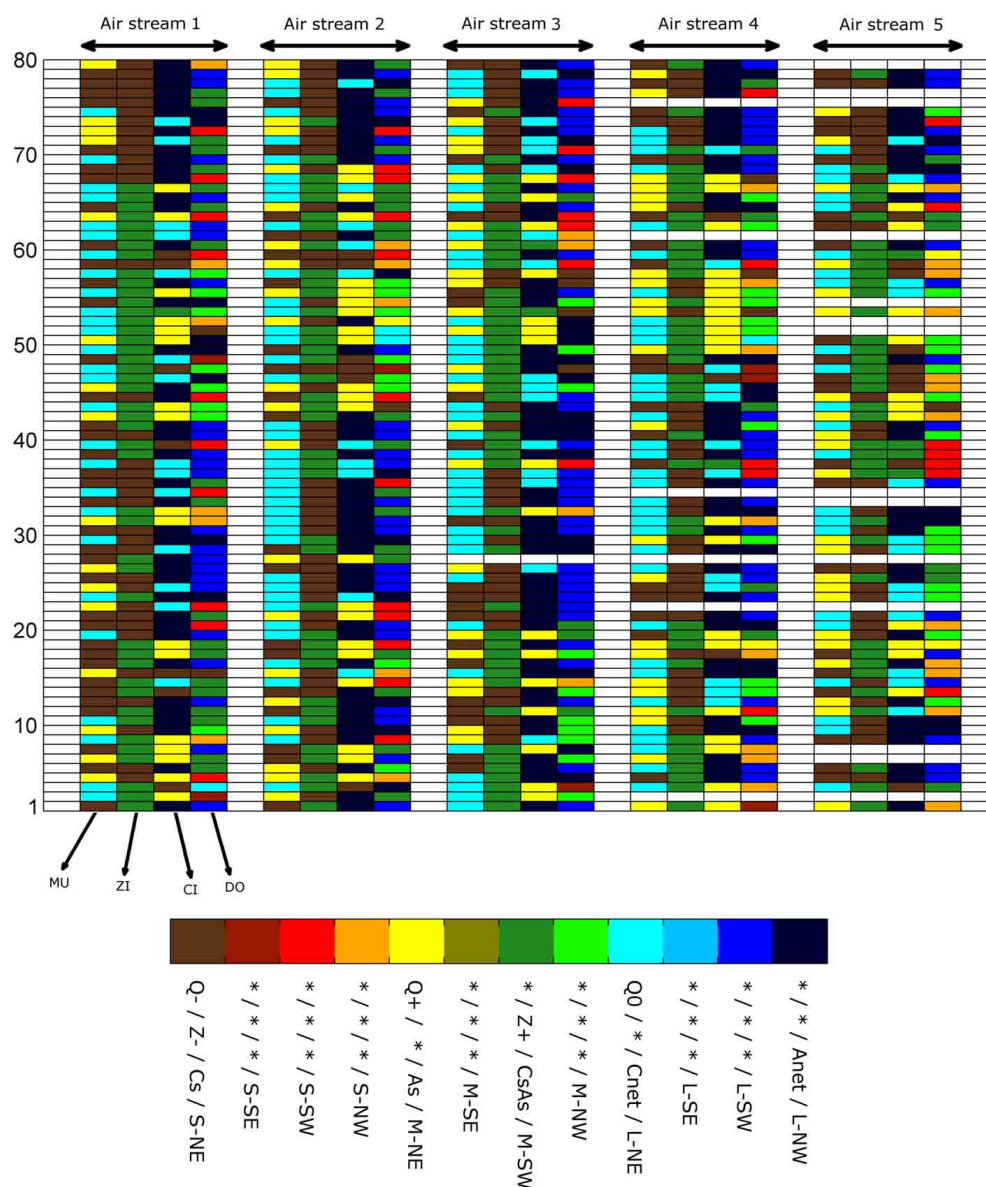
FIGURE 6 | Representation of the final catalog for 80 first days (from 01/12/1999 to 18/02/2000). Each day is characterized by at most five air streams and each air stream can be described by four flow properties (MU, ZI, CI, and DO), as discussed in Section A New Classification Based on Lagrangian Backward Trajectories. The legend should be interpreted like this: for different categories the colors indicates a different class. For example, the first air stream of the first day (01/12/1999) is classified has [Q−, Z+, Anet, L-SW]. The * in the legend indicates that there is no correspondent class.

C_{net}) have similar frequencies (near 32%) and also the classes with small anticyclonic (A_s) and cyclonic curvature (C_s) exhibit similar frequencies (near 14%). In winter, as discussed above, most of the transport is long-range and from the western quadrants. In the selected domain, these quadrants correspond to the North Atlantic domain frequently associated with an anticyclonic CI. As mentioned before, in summer, it is interesting to note that most of the time the IP is under the influence of a thermal low (Hoinka and de Castro, 2003) and the method is able to identify this cyclonic feature in the region by an increase of the frequency of the cyclonic CI class. For CI the standard deviations are relativity high compared to the other characteristics (MU, ZI, and DO).

PRECIPITATION ASSOCIATED WITH TRAJECTORY TYPES

Circulation types are often reflected in several surface climate variables (Goodess and Jones, 2002; Hope et al., 2006; Lorenzo et al., 2008). In the IP, the relationship is particularly strong with precipitation, therefore many studies have investigated the impact of circulation types on precipitation (Trigo and DaCamara, 2000; Lorenzo et al., 2008; Gómez-Gesteira et al., 2011). The most prominent differences occur between summer and winter (see Section Inter-Seasonal Variability of Individual Characteristics), and therefore results are only shown for these two seasons. For each season, the average rainfall associated with each class and its inter-annual variability has been computed. To do so, only the

Table 3 | Lamb weather types for each day of the (a) heatwave case study (1/8/2003 to 15/8/2003).

Date	LWT
1/8/2003	A
2/8/2003	A
3/8/2003	S
4/8/2003	C
5/8/2003	N
6/8/2003	A
7/8/2003	A
8/8/2003	A
9/8/2003	AN
10/8/2003	N
11/8/2003	A
12/8/2003	A
13/8/2003	A
14/8/2003	C
15/8/2003	C

days with at least two air streams with the same class were chosen. This is done in order to choose only the days where a dominant class occurs. For instance, when computing the average rainfall related to the class Q− of the characteristic MU, only days with at least two air streams classified as Q− were chosen.

First of all, as expected, the average rainfall is higher in winter than in summer (**Figure 9A**). For MU, there is no difference in the average rainfall for the different classes during summer, while in winter a considerably higher average rainfall is found for Q+ than for the other classes. There is long-range transport mainly from the western quadrants for this season, conversely the lowest average rainfall is found for Q0 (small changes in humidity). For the ZI characteristic, there is no particular difference in precipitation during summer, while during winter higher values of average rainfall are found for the less curved trajectories (Z−). In the NW IP, most of the precipitation in winter is associated with extratropical cyclones within the storm track (Trigo, 2005), mainly via frontal systems passing over the region (Lorenzo et al., 2008). These frontal systems are typically characterized by rather straight air streams. The CI characteristic is particularly interesting in terms of the associated average rainfall. The cyclonic classes (C_s and C_{net}) present the highest values of average rainfall and the anticyclonic classes (A_s and A_{net}) the lowest values. This result confirms the findings by Lorenzo et al. (2008), who showed that the cyclonic circulation types are most prominent in situations with rainfall in the NW IP. Finally the DO characteristic presents high variability of average rainfall for each class. In winter, it is found that the air streams that come mainly from the western quadrant (S-SW, S-NW, M-SW, M-NW, L-SW, L-NW) are associated with the highest values of average rainfall. For these air streams, the highest precipitation values occur for medium and long-range transport, in agreement with the results by Gimeno et al. (2010).

As a final investigation, five classes of rainfall magnitude are defined: no rain, light rain, moderate, intense and very intense following the method adopted in previous studies (Osborn

et al., 2000; Lorenzo et al., 2008). The definition of the rainfall magnitude classes for summer and winter can be found in Supplementary Material S2 and results are shown in **Figure 9B**. In general, the highest values of average rainfall (**Figure 9A**) correspond to the highest values of days with intense and very intense rainfall (**Figure 9B**). The most interesting case is perhaps related to CI where the cyclonic class (C_{net}) has almost 50% of the cases considered as intense or very intense precipitation days. Conversely, for the anticyclonic class (A_s and A_{net}) most of the days (almost 80 and 70%, respectively) correspond to the no precipitation or light precipitation class.

COMBINED CHARACTERISTICS

In this section, the combination of the different characteristics is considered, separately for summer and winter. The characteristics MU, ZI, CI, and DO span a 4-dimensional phase space, with in total $3 \times 2 \times 5 \times 12$ discrete "boxes" according to the number of classes for each characteristic—3 for MU; 2 for ZI; 3 for CI and 12 for DO (which in this section is divided into 3 (D) × 4(O) characteristics. But due to physical constraints some combinations are evidently rather unlikely. For instance, air streams that are classified as long-range transport for the east quadrants are very rare due to the typical westerlies in the target region.

In order to look to this phase space a multi panel plot is shown in **Figure 10** with a total of 5×5 panels for each characteristic for both summer (a) and winter (b). Each panel consists of a small matrix with the frequency of occurrence between the corresponding characteristics, e.g., the panel in row 1 and column 2 (MU vs. ZI) is a 2×3 matrix according to the classes Z− and Z+ and Q−, Q+, and Q0. In each panel the circles of different sizes indicate the frequency with which a specific combination is found, i.e., the radius of the circles is proportional to this frequency. In addition, for each panel, the combination with the highest frequency is marked with a red dot. With this multi panel plot it is possible to see the combinations shift from summer to winter, especially for the CI, D, and O characteristics. For summer the most frequent air stream is [Q−, Z−, A_{net}, M-SW], while for winter it is [Q−, Z−, A_{net}, L-SW]. It is interesting to note that the most frequent air streams for summer and winter are almost the same; the only change is found for the DO characteristic (M-SW vs. L-SW). These air streams correspond to a decrease in humidity along the path within a mainly zonal and anticyclonically curved flow. This means that some of the humidity that is advected, e.g., from the Gulf of Mexico, across the North Atlantic is lost during transport.

Since an exhaustive description of **Figure 10** is neither practical nor simple, the most common combinations are marked by red dots and will be further discussed for summer and winter. For the MU class Q-, the most frequent classes of the other characteristics are: Z−, A_{net}, and M-SW in summer and L-SW in winter, respectively. The latter is the most frequent combination in the entire catalog as mentioned before. For Q+ the most frequent combination is Z−, C_{net}, and S-NW in summer and L-NW in winter, respectively.

Regarding the Z− category, the most frequent combination is Q−, C_{net} and M-SW in summer, and Q+, A_{net}, and L-SW in winter. For Z+, the preferred combination is Q+, C_s, and S-SW in summer and Q0, A_{net}, and L-SW in winter. In
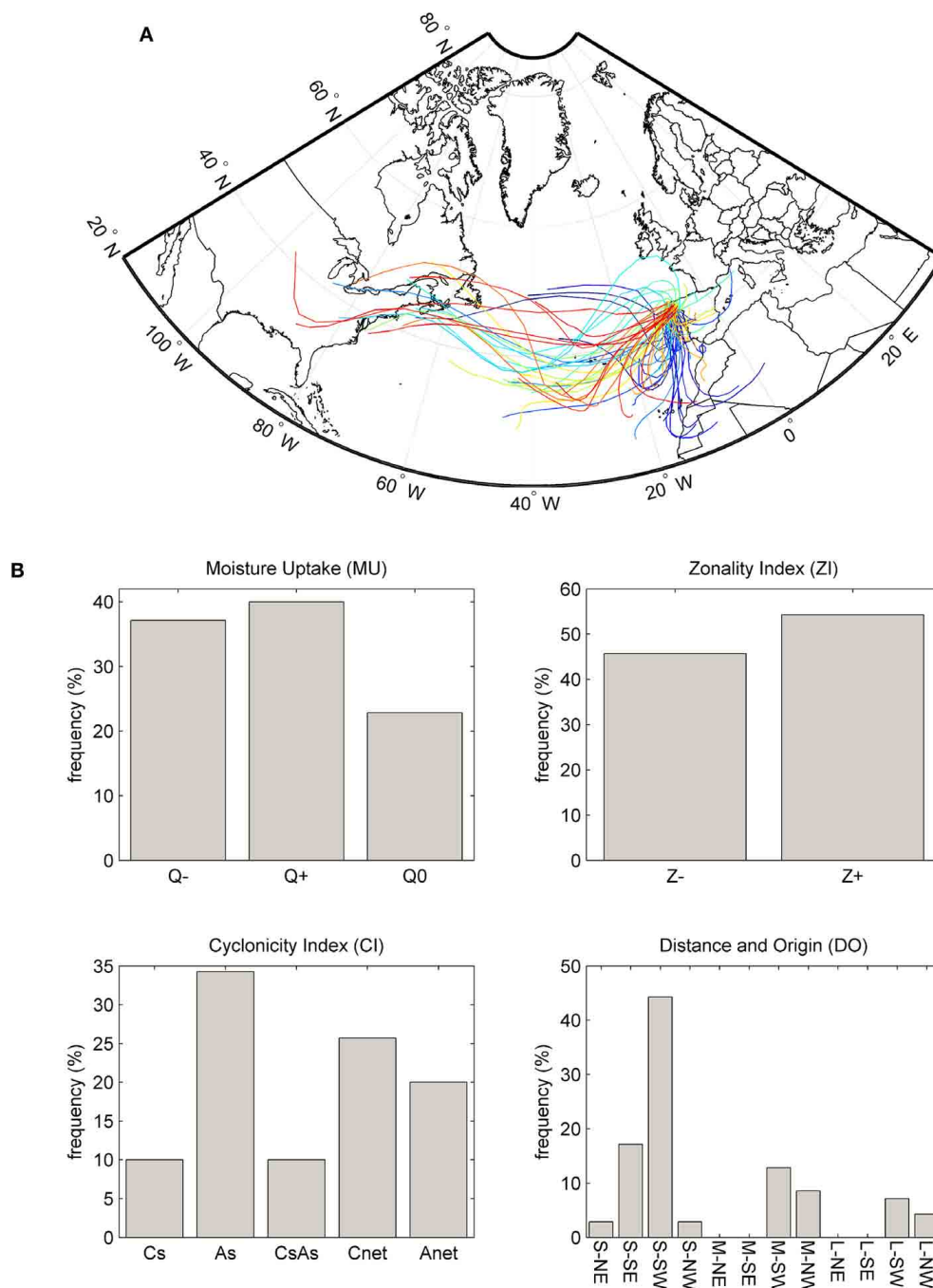
FIGURE 7 | (A) Air streams (each color represent a different day) and **(B)** characteristics of the trajectory types classification for the heatwave case study (01/08/2003 to 15/08/2003).

summer this most frequent combination is associated with air streams that come from the SW, experience short-range transport and an increase in humidity along their path. In winter, the more meridional circulation (Z+) is often related with mean anticyclonic circulation that can be associated to blocking events.

The last characteristic discussed here is CI. There are no particular differences in the three classes that correspond to

small-radius circulations (C_s, A_s, and C_sA_s), and we therefore focus on the C_{net} and A_{net} classes. The most probable combination with C_{net} in summer is Q0, Z−, and M-NW and in winter Q+, Z−, and L-SW, respectively. It is interesting to note that for summer C_{net} is associated with Q0 while in winter it is more frequently associated with Q+. Regarding A_{net}, results for ZI, D, and O are very similar to the ones found for C_{net}. The main difference

Table 4 | Mean frequencies (%) of occurrence of the different classes for category Distance and Origin (DO) and the respective standard deviation (%) in brackets.

(A)					
Short (S)	**NE**	**SE**	**SW**	**NW**	**Total**
Winter	4.0 (1.4)	2.1 (1.6)	10.4 (3.3)	7.6 (1.7)	24.1
Spring	7.0 (3.5)	2.9 (0.9)	12.2 (4.6)	11.2 (1.0)	33.4
Summer	3.6 (1.8)	2.3 (1.8)	19.1 (2.0)	17.9 (1.7)	42.9
Autumn	3.6 (2.4)	2.5 (1.3)	14.1 (3.4)	12.8 (2.4)	33.1
(B)					
Medium (M)	**NE**	**SE**	**SW**	**NW**	**Total**
Winter	1.7 (0.9)	0.2 (0.2)	15.5 (1.7)	13.2 (2.8)	30.6
Spring	1.2 (0.6)	0.3 (0.2)	14.7 (3.5)	17.3 (2.0)	33.4
Summer	0.5 (0.3)	0.0 (0.0)	16.8 (2.1)	17.3 (1.1)	34.7
Autumn	1.4 (0.8)	0.1 (0.2)	13.4 (1.9)	18.0 (1.5)	32.9
(C)					
Long (L)	**NE**	**SE**	**SW**	**NW**	**Total**
Winter	0.4 (0.3)	0.0 (0.0)	30.9 (4.3)	14.0 (1.7)	45.3
Spring	0.2 (0.2)	0.0 (0.1)	20.7 (5.1)	12.2 (2.0)	33.2
Summer	0.0 (0.1)	0.0 (0.0)	8.9 (1.3)	13.4 (1.7)	22.4
Autumn	0.0 (0.1)	0.0 (0.1)	18.1 (2.9)	15.8 (1.6)	34.0

They are shown during winter (DJF), spring (MAM), summer (JJA), and autumn (SON) seasons in the 1/12/1999 to 30/11/2004 period and disaggregated by (A) short, (B) medium, and (C) long range transport.

occurs for MU with the most frequent class being Q− in summer and Q0 in winter.

COMPARISON OF LAMB WEATHER TYPES AND LAGRANGIAN CIRCULATION TYPES

For each day with a certain LWT, the frequency of the Lagrangian classes is analyzed. For MU (**Figure 11A**), there is a clear difference when comparing the easterly with the westerly types. In general, easterly types are characterized by small changes in humidity along the path, while the westerlies are characterized by a decrease in the humidity. The difference between the C and A type is also prominent; higher frequencies are found for Q+ in the case of C type and Q0 in the case of the A type. For the zonal index (ZI) (**Figure 11B**), a marked difference between easterly and westerly types is observed. The easterlies are characterized by more frequently curved trajectories (Z+) while the opposite occurs for the westerlies (less curved trajectories). The difference between the C type and the A types is also noticeable with the trajectories being frequently more curved in the C type than in the A type. Results for the cyclonicity index (CI) (**Figure 11C**) show a good differentiation between the frequencies of the five classes when comparing different circulation types. For example, in the C types the frequency of the air streams which have C_s (small cyclonic curvatures) and C_{net} (averaged cyclonic trajectory) is very high, 40 and 37.5%, respectively. On the contrary, the A type presents higher frequencies for class A_s (small anticyclonic curvatures) and A_{net} (averaged anticyclonic curvatures). For the NW and W types also the A_{net} class is more frequent while for the SW types the

C_{net} class is more frequent. Regarding the distance characteristic (D) (**Figure 11D**), the frequencies of the different classes are expected to differ between the LWT. For the NE, E, SE, and S types nearly 45% of the air streams show short-range transport, while the SW, W, and NW types are typically characterized by medium and long-range transport.

To conclude this section, the origin characteristic (O) (**Figure 11E**) are analyzed. As expected, when an S/SW/W/NW circulation type occurs, the air streams for these days have their origin points mainly in the SW/NW quadrants. Concerning the NE/E/SE circulation type days, results show that despite an increase in the air streams coming from the NE and SE quadrants (regarding the O characteristic) the majority of the air streams are classified as coming from the SW and NW. This can be explained because the LWT are based on the surface level, while the trajectory types are taking into account the 3-D structure of the atmospheric motion. For this reason the signature of the jet stream (air streams where its initial point is in the NW and SW quadrant) is present in the majority of the analyzed days.

SUMMARY AND CONCLUSIONS

A new classification method of circulation types, based on the analysis of backward trajectories, is presented in this work. A representative air stream was determined for each day (at 12 UTC) for the target region in the NW IP. Air parcels that are in the NW IP at the chosen time steps were selected and the corresponding 90-h backward trajectories were then retrieved. The inherent time scale of 90 h was chosen in order to focus the study not only on the local circulation but also to include the main synoptic-scale features that often affect the target area. In a first step, a clustering algorithm was applied allowing a horizontally separation of the different air streams. Secondly, if the number of clusters from the first (horizontal) clustering exceeded five, a further reduction was accomplished with a secondary clustering based on the height of the trajectory (H), the distance to the target area (D), specific humidity (Q), and latitude (LAT). When the main representative air streams are finally found, each air stream is characterized by four distinct flow properties: (1) Moisture Uptake (MU) represents the integrated change in specific humidity; (2) Zonality Index (ZI) represents the curvature of the path; (3) Cyclonicity Index (CI) represents the cyclonicity of the flow; and (4) Distance and Origin (DO) classifies the air stream in terms of distance and initial position. The final catalog has for each time step a maximum of five air streams, each being characterized by the four characteristics described above. This method is able to reduce a large amount of information from a comprehensive trajectory data set into a small number of distinct air streams, which capture the essential characteristics of the mesoscale and synoptic-scale flow situation. Note that the method describes the three-dimensional complexity of the atmospheric circulation. Moreover it provides time-integrated physical information on the development of the systems (Lagrangian perspective), which goes beyond the traditional description of the instantaneous synoptic situation (Eulerian perspective). For example, the Lagrangian classification allows capturing changes in moisture along the flow due to evaporation and precipitation.

FIGURE 8 | Frequencies (%) of occurrence of the different characteristics for (A) Moisture Uptake (MU), (B) Zonal Index (ZI), and (C) Cyclonicity Index (CI), during winter (DJF), spring (MAM), **summer (JJA), and autumn (SON) seasons in the 1/12/1999 to 30/11/2004 period.** The respective seasonal standard deviation is also shown (red lines).
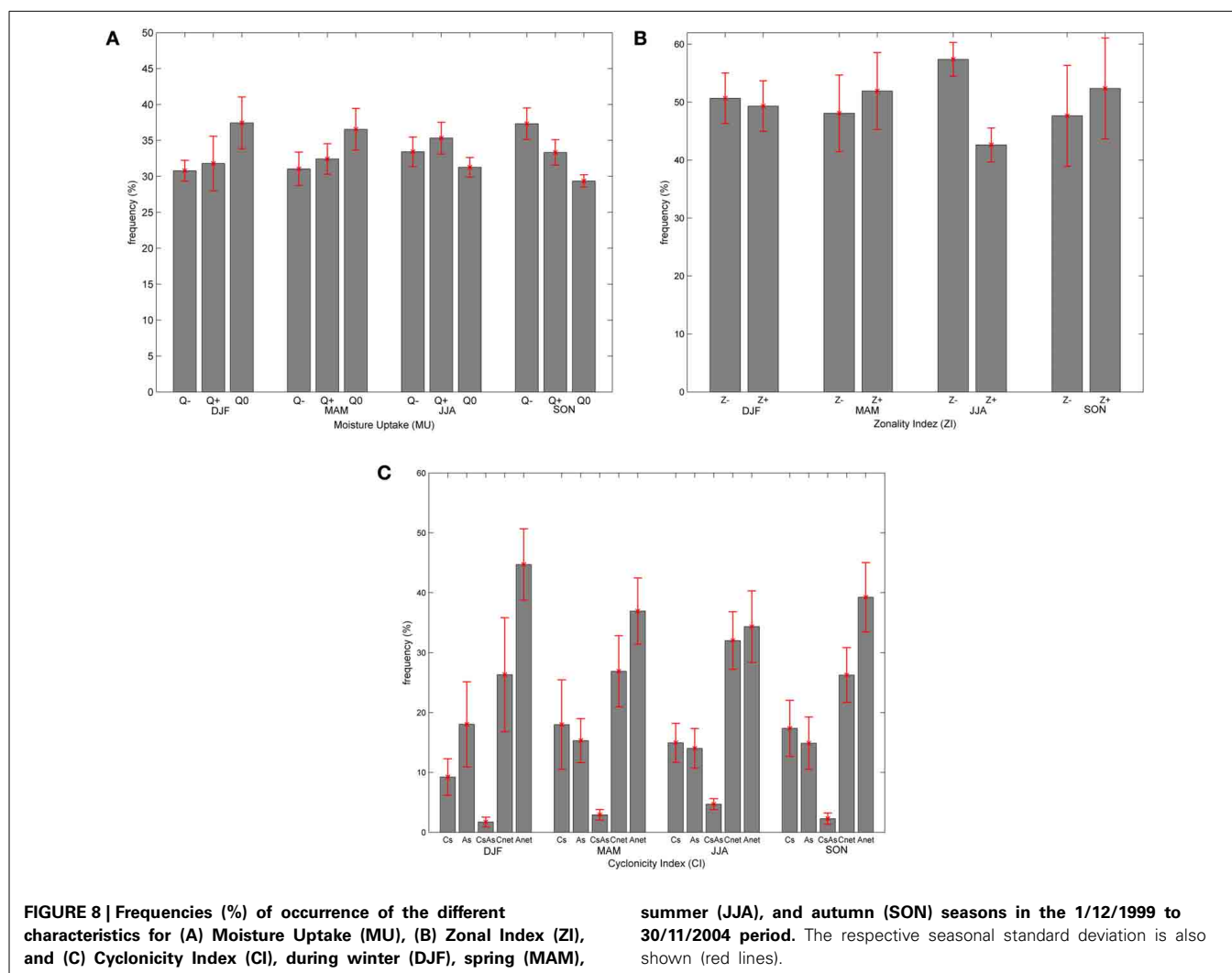
The climatological assessment of this new classification shows that the method is able to capture with good accuracy the main features of the seasonality of regional climate. It allows a proper distinction of processes between seasons and helps determining aspects of the inter-seasonal variability. For example, the short-range transport classes are most frequent in summer (43%) while the frequency of long-range transport is largest in winter (45%).

Besides characterizing aspects of the annual cycle, the method is able to identify distinct dynamical structures. Case studies illustrate the Lagrangian categorization of intense precipitation events, heatwaves, cold fronts, blocking systems, cut off lows and extra-tropical cyclones. For example, for the 2003 heatwave in the IP, the method captures the short-range transport associated with the thermal low, advection of African air streams, and the medium and long-range transport associated with the anticyclonic circulation. As a further example, the cut-off low systems with its high-altitude depression is picked up by the new method, whereas the Eulerian LWT is only able to pick up surface characteristics of the flow (see Supplementary Material S1). In this sense, the method goes a step further in adding valuable information to the classification of a particular atmospheric

flow situation. Indeed, a comparison between this method and an automated version of the LWT for the IP is shown in Section Comparison of Lamb Weather Types and Lagrangian Circulation Types and illustrates the general agreement while providing important additional information.

In summary, the key advantages of the new method are:

(1) It is able to summarize the complexity of the atmospheric circulation by a string of five labels denoting, for each of the considered flow characteristics, the class populated by the largest number of air streams.
(2) In contrast to the Eulerian circulation type classification it takes into account the origin and the proprieties of the flow reaching a certain area. It captures both local and large-scale characteristics of the meteorological situation and incorporates important information about the dynamic and thermodynamic processes associated with the flow state.
(3) It captures aspects of the three-dimensional structure of the atmosphere since the backward trajectories entering the flow classification scheme are calculated on several tropospheric levels.
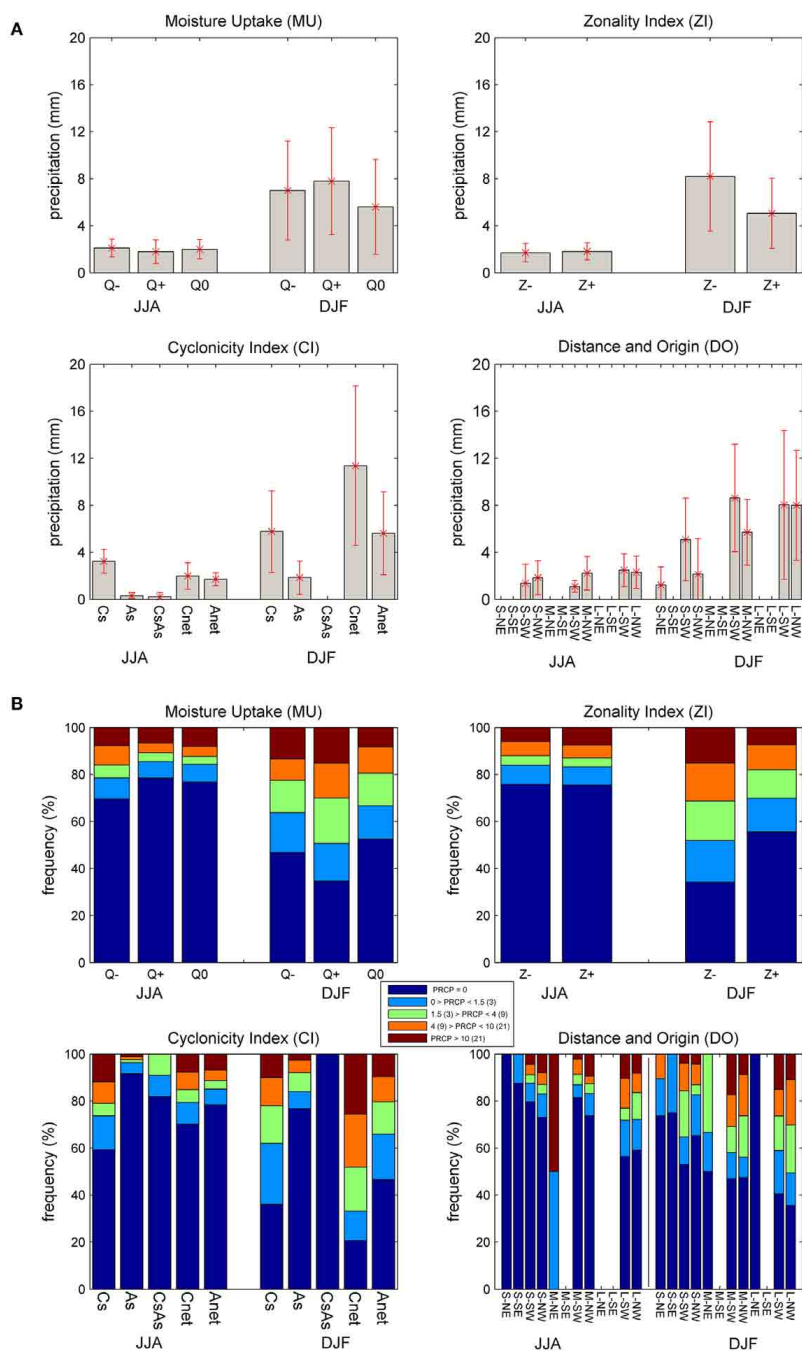
FIGURE 9 | (A) Seasonal average precipitation (mm) and the corresponding inter-annual variability (red lines) attributed to the Lagrangian classes; **(B)** Contribution of each Lagrangian type (in %) to five different categories of precipitation. The definitions of each category of precipitation are shown for summer (winter) in the legend and are summarized in Supplementary Material S2.

(4) It is able to pinpoint synoptic situations, like cut-off low pressure systems, that may not have a clear signature at lower atmospheric levels and would be missed by classifications based upon the SLP field only.

Some disadvantages of using the new trajectory-based method can also be found. First, the novel classification method is

computationally more demanding than traditional Eulerian ones. In addition, if the target domain is increased, the number of trajectories also increases and therefore the computations take longer. Furthermore, the novel method characterizes the complexity of the atmospheric circulation by a set of five parameters. Clearly, this multi-dimensional approach results in a more challenging daily catalog compared to the classical circulation type

FIGURE 10 | Multi-dimensional catalog frequencies for (A) summer and (B) winter. Each panel correspond the frequency of one characteristics compared with other. For example in the MU vs. ZI panel for summer and winter, it is shown that the most common combination for the Q− class is the Z− class. For each panel the combination with highest frequency is marked with a red dot.
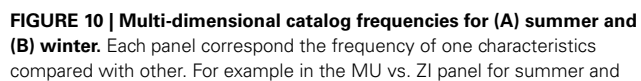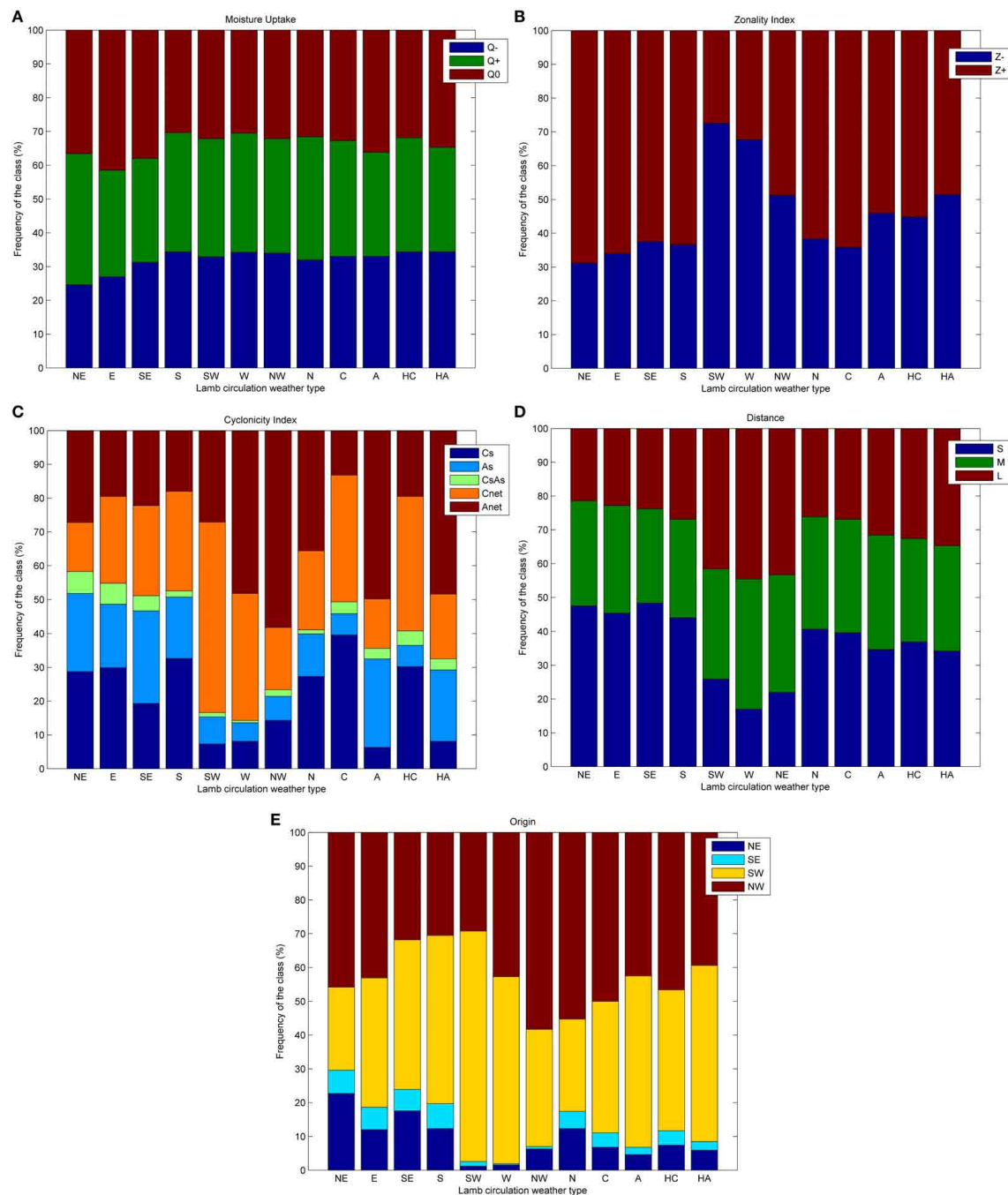
FIGURE 11 | Relationship between Lamb circulation weather type and the Lagrangian flow properties (A) MU, (B) ZI, (C) CI, (D) D, and (E) O. Each column correspond to the frequency (%) of each class when a certain Lamb circulation weather type occur.

classifications. The novel approach, developed here for the region of the Iberian Peninsula, should be general enough to be suitable for the classification of air streams over other regions on the globe.

SUPPLEMENTARY MATERIAL

The Supplementary Material for this article can be found online at: http://www.frontiersin.org/journal/10.3389/feart.2014.00029/abstract

REFERENCES

Black, E., Blackburn, M., Harrison, G., Hoskins, B., and Methven, J. (2004). Factors contributing to the summer 2003 European heat wave. *Weather* 59, 217–223. doi: 10.1256/wea.74.04

Cammas, J. P., Brioude, J., Chaboureau, J. P., Duron, J., Mari, C., Mascart, P., et al. (2009). Injection in the lower stratosphere of biomass fire emissions followed by long-range transport: a MOZAIC case study. *Atmos. Chem. Phys.* 9, 5829–5846. doi: 10.5194/acp-9-5829-2009

deCastro, M., Gomez-Gesteira, M., Ramos, A. M., Álvarez, I., and deCastro, P. (2011). Identification of heat waves in Galicia over the period 1987-2006: effects on mortality. *Clim. Res.* 48, 333–341. doi: 10.3354/cr00988

deCastro, M., Lorenzo, M. N., Taboada, J. J., Sarmiento, M., Álvarez, I., and Gomez-Gesteira, M. (2006). Teleconnection patterns influence on precipitation variability and on river flow regimes in the Miño River basin (NW Iberian Peninsula). *Clim. Res.* 32, 63–73. doi: 10.3354/cr032063

Dirmeyer, P. A., and Brubaker, L. (2006). Evidence for trends in the Northern Hemisphere water cycle. *Geophys. Res. Lett.* 33:L14712. doi: 10.1029/2006GL026359

Dorling, S. R., Davies, T. D., and Pierce, C. E. (1992). Cluster analysis: a technique for estimating the synoptic meteorological controls on air and precipitation chemistry method and applications. *Atmos. Environ.* 26A, 2575–2581. doi: 10.1016/0960-1686(92)90110-7

Eckhardt, S., Stohl, A., Wernli, H., James, P., Forster, C., and Spichtinger, N. (2004). A 15-year climatology of warm conveyor belts. *J. Clim.* 17, 218–237. doi: 10.1175/1520-0442(2004)017<0218:AYCOWC>2.0.CO;2

Esteban, P., Jones, P. D., Martín-Vide, J., and Mases, M. (2005). Atmospheric circulation patterns related to heavy snowfall days in Andorra, Pyrenees. *Int. J. Climatol.* 25, 319–329. doi: 10.1002/joc.1103

Fowler, H. J., and Kilsby, C. G. (2002). A weather-type approach to analyzing water resource drought in the Yorkshire region from 1881 to 1998. *J. Hydrol.* 262, 177–192. doi: 10.1016/S0022-1694(02)00034-3

Garcia-Herrera, R., Diaz, J., Trigo, R. M., Luterbacher, J., and Fischer, E. M. (2010). A review of the European Summer Heat Wave of 2003. *Crit. Rev. Environ. Sci. Technol.* 40, 267–306. doi: 10.1080/10643380802238137

Gimeno, L., Nieto, R., Trigo, R., Vicente, S., and Lopez-Moreno, J. I. (2010). Where does the Iberian Peninsula moisture come from? An answer based on a Largrangian approach. *J. Hydrometeorol.* 11, 421–436. doi: 10.1175/2009JHM1182.1

Gómez-Gesteira, M., Gimeno, L., deCastro, M., Lorenzo, M. N., Alvarez, I., Nieto, N., et al. (2011). The state of climate in NW Iberia. *Clim. Res.* 48, 109–144. doi: 10.3354/cr00967

Goodess, C. M., and Jones, P. D. (2002). Links between circulation and changes in the characteristics of Iberian rainfall. *Int. J. Climatol.* 22, 1593–1615. doi: 10.1002/joc.810

Goodess, C. M., and Palutikof, J. P. (1998). Development of daily rainfall scenarios for southeast Spain using a circulation-type approach to downscaling. *Int. J. Climatol.* 18, 1051–1083.

Hastie, T., Tibshirani, R., and Friedman, J. (2009). *The Elements of Statistical Learning: Data Mining, Inference, and Prediction, 2nd Edn*. New York, NY: Springer Series in Statistics, 763. doi: 10.1007/978-0-387-84858-7

Hess, P., and Brezowsky, H. (1952). "Katalog der Großwetterlagen Europas (Catalog of the European Large Scale Weather Types)," in *Berichte des Deutschen Wetterdienstes in der US-Zone 33* (Bad Kissingen: Meteorological Office in Germany).

Hoinka, K. P., and de Castro, M. (2003). The Iberian Peninsula thermal low. *Q. J. R. Meteorol. Soc.* 129, 1491–1511. doi: 10.1256/qj.01.189

Hope, P. K., Drosdowsky, W., and Nicholls, N. (2006). Shifts in the synoptic systems influencing southwest Western Australia. *Clim. Dyn.* 26, 751–764. doi: 10.1007/s00382-006-0115-y

Huth, R., Beck, C., Philipp, A., Demuzere, M., Ustrnul, Z., Cahynova, M., et al. (2008). Classifications of atmospheric circulation patterns: recent advances and applications. Trends and directions in climate research. *Ann. N.Y. Acad. Sci.* 1146, 105–152. doi: 10.1196/annals.1446.019

Jacobeit, J. (2010). Classifications in climate research. *Phys. Chem. Earth* 35, 411–421. doi: 10.1016/j.pce.2009.11.010

James, P., Stohl, A., Spichtinger, N., Eckhardt, S., and Forster, C. (2004). Climatological aspects of the extreme European rainfall of August 2002 and a trajectory method for estimating the associated evaporative source regions. *Nat. Hazards Earth Syst. Sci.* 4, 733–746. doi: 10.5194/nhess-4-733-2004

James, R., Bonazzola, M., Legras, B., Surbled, K., and Fueglistaler, S. (2008). Water vapor transport and dehydration above convective outflow during Asian monsoon. *Geophys. Res. Lett.* 35:L20810. doi: 10.1029/2008GL035441

Jones, P. D., Hulme, M., and Briffa, K. R. (1993). A comparison of Lamb circulation types with an objective classification scheme. *Int. J. Climatol.* 13, 655–663. doi: 10.1002/joc.3370130606

Jones, P. D., and Lister, D. H. (2009). The influence of the circulation on surface temperature and precipitation patterns over Europe. *Clim. Past* 5, 259–267. doi: 10.5194/cp-5-259-2009

Jorba, O., Pérez, C., Rocadenbosch, F., and Baldasano, J. M. (2004). Cluster analysis of 4-day back trajectories arriving in the Barcelona area, Spain, from 1997 to 2002. *J. Appl. Meteorol.* 43, 887–901. doi: 10.1175/1520-0450(2004)043<0887:CAODBT>2.0.CO;2

Kalnay, E., Kanamitsu, M., Collins, W., Deaven, D., Gandin, L., Iredell, M., et al. (1996). The NCEP/NCAR 40-year reanalysis project. *Bull. Am. Meteorol. Soc.* 77, 437–470.

Knippertz, P., and Wernli, H. (2010). A Lagrangian climatology of tropical moisture exports to the Northern Hemispheric extratropics. *J. Clim.* 23, 987–1003. doi: 10.1175/2009JCLI3333.1

Kruizinga, S. (1979). "Objective classification of daily 500 mbar patterns," in *Preprints Sixth Conference on Probability and Statistics in Atmospheric Sciences, Banff, Alberta* (Boston, MA: American Meteorological Society), 126–129.

Kyselý, J. (2008). Influence of the persistence of circulation patterns on warm and cold temperature anomalies in Europe: analysis over the 20th century. *Glob. Planet. Change* 62, 147–163. doi: 10.1016/j.gloplacha.2008.01.003

Lamb, H. H. (1972). "British Isles weather types and a register of daily sequence of circulation patterns, 1861–1971," in *Geophysical Memoir 116* (London: HMSO).

Lorenzo, M. N., and Taboada, J. J. (2005). Influences of atmospheric variability on freshwater input in Galician Rías in winter. *J. Atmos. Ocean. Sci.* 10, 377–387. doi: 10.1080/17417530601127472

Lorenzo, M. N., Taboada, J. J., and Gimeno, L. (2008). Links between circulation weather types and teleconnection patterns and their influence on precipitation patterns in Galicia (NW Spain). *Int. J. Climatol.* 28, 1493–1505. doi: 10.1002/joc.1646

Nyanganyura, D., Makarau, A., Mathuthu, M., and Meixner, F. X. (2008). A five-day back trajectory climatology for Rukomechi research station (northern Zimbabwe) and the impact of large-scale atmospheric flows on concentrations of airborne coarse and fine particulate mass. *S. Afr. J. Sci.* 104, 43–52.

Osborn, T. J., Hulme, M., Jones, P. D., and Basnett, T. A. (2000). Observed trends in the daily intensity of United Kingdom precipitation. *Int. J. Climatol.* 20, 34–364. doi: 10.1002/(SICI)1097-0088(20000330)20:4<347::AID-JOC475>3.0.CO;2-C

Palau, J. L., Pérez-Landa, G., and Millán, M. M. (2009). Transitional dispersive scenarios driven by mesoscale flows on complex terrain under strong dry convective conditions. *Atmos. Chem. Phys.* 9, 119–130. doi: 10.5194/acp-9-119-2009

Paris, J. D., Stohl, A., Ciais, P., Nédélec, P., Belan, B. D., Arshinov, M. Y., et al. (2010). Source-receptor relationships for airborne measurements of CO_2, CO and O_3 above Siberia: a cluster-based approach. *Atmos. Chem. Phys.* 10, 1671–1687. doi: 10.5194/acp-10-1671-2010

Peixoto, J. P., and Oort, A. (1992). *Physics of Climate*. New York, NY: American Institute of Physics, 520.

Philipp, A., Bartholy, J., Beck, C., Erpicum, M., Esteban, P., Fettweis, X., et al. (2010). COST733CAT—a database of weather and circulation type classifications. *Phys. Chem. Earth* 35, 360–373. doi: 10.1016/j.pce.2009.12.010

Philipp, A., Della-Marta, P. M., Jacobeit, J., Fereday, D. R., Jones, P. D., Moberg, A., et al. (2007). Long term variability of daily North Atlantic–European pressure patterns since 1850 classified by simulated annealing clustering. *J. Clim.* 20, 4065–4095. doi: 10.1175/JCLI4175.1

Ramos, A. M., Lorenzo, M. N., and Gimeno, L. (2010). Compatibility between modes of low frequency variability and Circulation Types: a case study of the North West Iberian Peninsula. *J. Geophys. Res.* 115:D02113. doi: 10.1029/2009JD012194

Ramos, A. M., Ramos, R., Sousa, P., Trigo, R. M., Janeira, M., and Prior, V. (2011). Cloud to ground lightning activity over Portugal and its association with Circulation Weather Types. *Atmos. Res.* 101, 84–101. doi: 10.1016/j.atmosres.2011.01.014

Riccio, A., Giunta, G., and Chianese, E. (2007). The application of a trajectory classification procedure to interpret air pollution measurements in the urban area of Naples (Southern Italy). *Sci. Total Environ.* 376, 198–214. doi: 10.1016/j.scitotenv.2007.01.068

Romero, R., Sumner, G., Ramis, C., and Genovés, A. (1999). A classification of the atmospheric circulation patterns producing significant daily rainfall in the Spanish Mediterranean area. *Int. J. Climatol.* 19, 765–785.

Sodemann, H., Schwierz, C., and Wernli, H. (2008). Inter-annual variability of Greenland winter precipitation sources. Lagrangian moisture diagnostic and North Atlantic Oscillation influence. *J. Geophys. Res.* 113:D03107. doi: 10.1029/2007JD008503

Spellman, G. (2000). The application of an objective weather-typing system to the Iberian peninsula. *Weather* 55, 375–385. doi: 10.1002/j.1477-8696.2000.tb04023.x

Stohl, A. (1998). Computation, accuracy and applications of trajectories a review and bibliography. *Atmos. Environ.* 32, 947–966. doi: 10.1016/S1352-2310(97)00457-3

Stohl, A. (2001). A one-year Lagrangian "climatology" of airstreams in the Northern Hemisphere troposphere and lowermost stratosphere. *J. Geophys. Res.* 106, 7263–7279. doi: 10.1029/2000JD900570

Stohl, A., Forster, C., Frank, A., Seibert, P., and Wotawa, G. (2005). Technical note: the Lagrangian particle dispersion model FLEXPART version 6.2. *Atmos. Chem. Phys.* 5, 2461–2474. doi: 10.5194/acp-5-2461-2005

Stohl, A., Haimberger, L., Scheele, M. P., and Wernli, H. (2001). An inter-comparison of three trajectory models. *Meteorol. Appl.* 8, 127–135. doi: 10.1017/S1350482701002018

Stohl, A., and Scheifinger, H. (1994). A weather pattern classification by trajectory clustering. *Meteorol. Z.* 6, 333–336.

Stohl, A., and Sodemann, H. (2010). Characteristics of atmospheric transport into the Antarctic troposphere, *J. Geophys. Res.* 115:D02305. doi: 10.1029/2009JD012536

Trigo, I. F. (2005). Climatology and interannual variability of storm-tracks in the Euro-Atlantic sector: a comparison between ERA-40 and NCEP/NCAR reanalyses. *Clim. Dyn.* 26, 127–143. doi: 10.1007/s00382-005-0065-9

Trigo, R. M., and DaCamara, C. C. (2000). Circulation weather types and their influence on the precipitation regime in Portugal. *Int. J. Climatol.* 20, 1559–1581. doi: 10.1002/1097-0088(20001115)20:13<1559::AID-JOC555>3.0.CO;2-5

Trigo, R. M., Ramos, A. M., Nogueira, P., Santos, F. D., Garcia-Herrera, R., Gouveia, C., et al. (2009). Evaluating the impact of extreme temperature based indices in the 2003 heatwave excessive mortality in Portugal. *Environ. Sci. Policy* 12, 844–854. doi: 10.1016/j.envsci.2009.07.007

Wernli, H., and Davies, H. C. (1997). A Lagrangian-based analysis of extratropical cyclones. I: the method and some applications. *Q. J. R. Meteorol. Soc.* 123, 467–489. doi: 10.1002/qj.49712353811

Wilks, D. S. (2006). *Statistical Methods in the Atmospheric Sciences, International Geophysics Series,* Vol. 91, *2nd Edn.* (London: Academic Press), 627.

Conflict of Interest Statement: The authors declare that the research was conducted in the absence of any commercial or financial relationships that could be construed as a potential conflict of interest.

Circulation weather types and spatial variability of daily precipitation in the Iberian Peninsula

Alexandre M. Ramos[1]*, Nicola Cortesi[2] and Ricardo M. Trigo[1]

[1] Instituto Dom Luiz, Faculdade de Ciências, Universidade de Lisboa, Lisboa, Portugal
[2] Centre Européen de Recherche et de Formation Avancée en Calcul Scientifique, Meteo France, Toulouse, France

*Correspondence:
Alexandre M. Ramos, Faculdade de Ciências, Instituto Dom Luiz, Universidade de Lisboa, Campo Grande, Edf. C8, Piso 3, Sala 8.3.1, 1749-016 Lisboa, Portugal
e-mail: amramos@fc.ul.pt

The relationships between atmospheric circulation patterns and daily Iberian rainfall are here explored at high spatial resolution (0.2°) using the Jenkinson and Collison automated classification scheme with 26 Weather Types (WTs). The WTs were computed by means of the daily EMULATE Mean Sea Level Pressure dataset (EMSLP) while the high resolution precipitation database corresponds to the recent Iberia02 daily gridded precipitation dataset over the 1950–2003 period. Six monthly indexes relating the WTs and precipitation were analyzed: their Frequency, the Mean Precipitation, the Percentage Contribution, the Area of Influence, the Precipitation Intensity, and Efficiency. Except for the Frequency of the WTs, all other indexes were evaluated studying their spatial distribution over the Iberian Peninsula, focusing on a WT and a month at time. A small number of WTs (7) was found to capture a high percentage (~70%) of monthly Iberian precipitation. The Westerly WT is the most influent one, followed by the Cyclonic, the Northwesterly and the Southwesterly WTs. Westerly flows, however, do not affect the Mediterranean fringe or the Cantabrian coast, which are dominated by the Easterly and Northerly WTs, respectively. Rainfall along the Mediterranean coastline and the Ebro basin depends on a variety of WTs, but their effects are confined to narrow areas and short temporal intervals, suggesting that local factors such as convective processes, orography and the proximity to a warm water body could play a major role in precipitation processes. We show that the use of daily gridded precipitation dataset holds the advantage of measuring the daily rainfall amount due to each WT directly instead to relying on the predicted values of the regression model as done in previous works.

Keywords: circulation weather types, daily gridded precipitation, Iberian Peninsula, spatial variability, seasonal variability

INTRODUCTION

Rainfall variability is a well know characteristic of Mediterranean climate, and it has been particularly well studied around Mediterranean Basin particularly at the monthly and seasonal scales (Corte-Real et al., 1995; Kutiel et al., 1996; Xoplaki et al., 2004; Paredes et al., 2006). A comprehensive analysis for the entire Mediterranean is presented in Dünkeloh and Jacobeit (2003), which the authors show that their main modes of variability capture 75% of precipitation variability, with up to five significant atmospheric patterns responsible for Mediterranean seasonal precipitation.

In the context of Mediterranean basin, the Iberian Peninsula (IP) has been recognized as one of the most challenging places for analyzing spatial and temporal climate variability due to a number of reasons (Lionello et al., 2012), namely: (1) the singular location of the IP in the transition between tropical to mild climate in western area of Mediterranean basin; (2) its confinement between two contrasted water masses (the Atlantic Ocean and the Mediterranean sea); (3) its compact configuration with the vast majority of the Peninsular area (circa 500,000 km^2) being enclosed by mountain chains. Additionally, the east-west alignment of the major mountain chains contributes to shape the high spatial variability of the region (Martin-Vide, 2004; Morata et al., 2006; Valero et al., 2009; Casado et al., 2010). In particular the IP orography has a strong influence on how low pressure systems affect the climate at a more local scale, as mountain ranges can shield eastern regions from the predominant Atlantic moisture advection (Gimeno et al., 2010). Some of these constraining factors can produce a relative disconnection from general circulation in some areas of IP, particularly in what concerns the Mediterranean fringe and Ebro basin to the east, where local factors can give marked regional variations as well as a high regional variability of precipitation (Muñoz-Diaz and Rodrigo, 2004; Martin-Vide and Lopez-Bustins, 2006).

As an example of rainfall variability in the IP, **Table 1** shows a brief list of previous studies focusing on the regionalization of precipitation. Differences in the number of regions retained can result from different choices in what concerns: length of periods considered, different spatial station density, but also distinct statistical methods used. Nevertheless, it is possible to state that three main areas are often defined: northern and eastern fringes, (i.e., Cantabrian and Mediterranean coastland), and central-south, being the mountain chains the frontiers (see **Figure 1A**), although they do not exactly match between authors.

Table 1 | Examples of regionalization of precipitation in the IP.

Authors	Time resolution	Number of series	Grid resolution	Period	Number of years	Number of regions
Fernandez-Mills, 1995	Daily	68	–	1961–1990	30	10
Rodriguez-Puebla et al., 1998	Annual	51	–	1949–1995	47	4
Esteban-Parra et al., 1998	Seasonal	40	–	1880–1992	112	3
Martin-Vide and Gomez, 1999	Daily	35	–	1951–1990	40	3
Serrano et al., 1999	Monthly	40	–	1919–1992	74	7
Garcia et al., 2002	Monthly	40	–	1919–1992	74	6
Muñoz-Diaz and Rodrigo, 2004	Seasonal	32	–	1912–2000	89	3–4*
Morata et al., 2006	Daily	960	$25\,km^2$	1961–2003	43	7-5-3**
Queralt et al., 2009	Daily	102	–	1997–2006	10	8
Casado et al., 2010	Daily	n.a.	$50\,km^2$	1961–1990	30	3
Cortesi et al., 2013a,b	Monthly	3030	$10\,km^2$	1948–2003	56	1

*Depending on season.

**Different lags.

The aforementioned variability introduces difficulties when modeling IP precipitation regimes particularly within the scope of generation of climate change scenarios. Thus, downscaling of precipitation over a limited region is often attempted through the identification of the dynamical-statistical links between local precipitation features and large scale atmospheric circulation patterns (e.g., Quadrelli et al., 2001; Trigo and Palutikof, 2001; Ramos et al., 2010).

There are several previous examples of atmospheric circulation approach and precipitation analyses around the Mediterranean basin. Kostopoulou and Jones (2007a,b) developed a classification of circulation types for the Eastern Mediterranean and established links with temperature and precipitation. In Greece, Michailidou et al. (2009) presented a method for grouping weather types (WTs) restricted to the cold and wet sub-period of the year. In Israel, Saaroni et al. (2010) analyzed the relationship between the low of Cyprus and precipitation during wet period (November March). In Italy, Tartaglione et al. (2009) analyzed intense precipitation events covering the period from 1951 to 2000, comparing the resemblance between two states of the atmosphere leading to the same outcome. In the boundary region of the Swiss Alps, Hanggi et al. (2011) analyzed how changes in WTs were related to precipitation trends.

Likewise, there have also been developed downscaling approaches linking the large scale atmospheric circulation and the precipitation over the IP. The first objective classifications of the atmospheric circulation were developed in the 1990s (e.g., Zorita et al., 1992; Zhang et al., 1997; Romero et al., 1999; Santos et al., 2005). At the same time a number of researchers was also interested in adopting a different approach, using slightly different versions of the automated version of the Lamb WTs (e.g., Goodess and Palutikof, 1998; Spellman, 2000; Trigo and DaCamara, 2000; Goodess and Jones, 2002).

Queralt et al. (2009) presents an analysis of winter intensity and frequency of precipitation based on 102 daily precipitation stations over Spain which have been merged in eight different regions. It was shown the complex regional relationship between the most important large-scale atmospheric pattern, the North Atlantic Oscillation (NAO) and precipitation which was also revealed through the modulation of the NAO in the preferred WTs associated to precipitation in each region. Casado et al. (2010) using a grid of 203 points, described the variability of winter precipitation over different climatic regions of Spain for the period 1961–1990 using different WTs classification. In the Ebro basin (northeast inland of IP), Vicente-Serrano and Lopez-Moreno (2006) analyzed WTs and drought in winter period during 1952–1999; they found a high spatial variability, and identified different sectors and WTs related to intensification of droughts. All of the above mentioned works deal with datasets characterized in general by a low station density for the vast area (circa $500{,}000\,km^2$) of IP, but also the use of different periods, and the tendency to restrict the analysis to wet winter season. In this regard, the accuracy of spatial detail is quite low and information for not-winter months is scarce. As a consequence, the spatial and temporal variability of precipitation in the IP is not entirely captured and transitional areas, relief barrier effects, altitudinal effect and subregional details, between other research targets, are not well known. Last but not least, an extended area of IP registers its maximum precipitation in transitional seasons, i.e., in spring or autumn (de Luis et al., 2010) being information about such periods virtually absent in many cases.

This limitation prompted the authors to use a much denser dataset with ~3000 stations for all Iberia (Cortesi et al., 2013a,b) to model the monthly relationship between WTs and precipitation following the approach of Trigo and DaCamara (2000). In that work a large number of regression models were developed at the monthly scale (one per station, about 3000 stations). Such a vast amount of long-term (1948–2003) time series was obtained after merging the dense network of monthly precipitation series from MOPREDAS database (MOnthly PREcipitation DAtabase of Spain) for Spanish land (Gonzalez-Hidalgo et al., 2011) and a Portuguese database from INAG—Instituto da Água (Servicio Nacional de Informaçao de Recurcos Hídricos) (Lorenzo-Lacruz et al., 2011). According to this high density analysis it was found that precipitation depends on higher number of WTs to the west than to the East and in general better prediction is expected to the west.

However, despite the massive number of stations employed in Cortesi et al. (2013a,b) it became apparent that modeling monthly precipitation based on monthly frequency of WTs
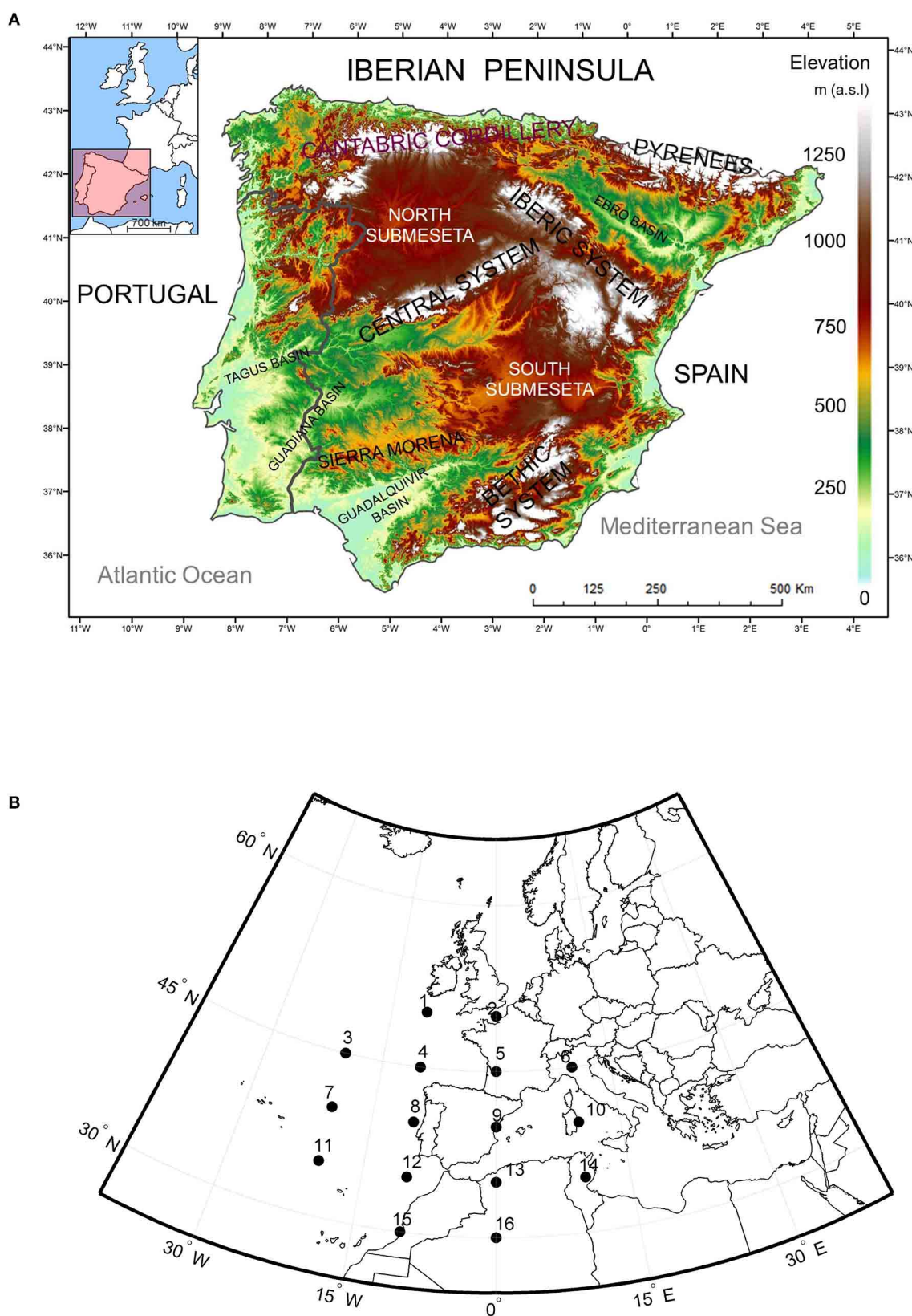
FIGURE 1 | (A) Main Mountain Ranges and Depressions of the Iberian Peninsula and (B) 16 SLP grid points used in the WTs computation.

implied major disadvantages. The main caveat is related with the unavoidable large estimation errors due to the limited number of predictors, but also as a consequence of multicollinearity and heteroscedasticity that hamper the overall quality of attained models (Wilks, 2006). Another serious limitation found was a positive (negative) bias for the wet (dry) WTs, overestimating the contribution for the WTs selected as predictors and underestimating it for the WTs not selected by the regression model. Therefore, the use of a daily dataset, even with a smaller total number of stations, could represent an advantage to the analysis. This goal has become feasible only recently due to the merging of Spanish (Herrera et al., 2012) and Portuguese (Belo-Pereira et al., 2011), into the high density daily gridded precipitation data set "Iberia02."

To a certain extent, this work provides the extension of the previous studies by the authors Cortesi et al. (2013a,b), with several major changes; on the one hand, unlike the monthly regression model widely used in Cortesi et al. (2013a), the analysis in this work was performed using the daily gridded "Iberia02" precipitation dataset. The use of a daily dataset holds the obvious advantage of measuring the daily rainfall amount due to each WT directly instead to relying on the predicted values of the regression model as done by the authors in their previous works. On the other hand, the use of daily data allows the study of several precipitation intensity related indices that are highly informative and impossible to measure directly with monthly data, including the mean precipitation of each WT and its relative Precipitation Contribution, Precipitation Intensity, and Efficiency. Thus, the broad objective of this work is to analyze at the higher possible spatial and temporal detail the role played by each individual WT at the daily scale and how they determine the Iberian precipitation regime. To the best of our knowledge no previous work has defined these daily WTs characteristics with so many stations covering the entire IP.

DATABASE AND METHODS
PRECIPITATION DATABASE
As previously mentioned, the current work relies on the use of the new daily gridded precipitation database "Iberia02," which spans the period 1950–2003 with a resolution of 0.2° ($\sim$16 $\times$ 22 km at latitude 40°), for a total of 1673 pixels. It is based on a dense network of rain gauges, combining two national data sets, "Spain02" for peninsular Spain and Balearic islands (Herrera et al., 2012), and "PT02" for mainland Portugal (Belo-Pereira et al., 2011), with a total of more than 2000 station over Spain and four hundred stations over Portugal, all quality-controlled and homogenized. Although the actual number of stations in any given year varies substantially due to variable availability of stations. Specifically, Spain02 is based on 2756 stations with at least 20 years of data and was interpolated by an indicator Kriging (to select pixel with rainfall) followed by an ordinary Kriging. The Portuguese dataset is based on a total of 806 station, most of which (726) have at least 10 years of data. Although several interpolation methods were tested to build the Portuguese gridded dataset (Belo-Pereira et al., 2011), the final choice was the same ordinary Kriging employed for the Spanish data (Herrera et al., 2012).

Although Iberia02 results from a combination of two different data sets, albeit with a common grid, there is no evidence of artificial features at the border between Spain and Portugal, neither at the monthly scale nor at daily scale (Belo-Pereira et al., 2011). The most important difference between Spain02 and PT02 is in the start of the daily accumulation period: daily precipitation records obtained in Portugal for any given day n correspond to the precipitation registered between 0900 UTC of day $n - 1$ and 0900 UTC of day n. On the other hand, Spanish rainfall records for the same day n correspond to the precipitation registered between 0700 UTC of day n and 0700 UTC of day $n + 1$ (notice the difference in both the hours and the days). Thus, in order to derive the most consistent common data set, the Portuguese daily precipitation database was shifted by 1 day, reducing the temporal difference between the two database from 22 h to only 2 h. The Spain02 has been recently used by the authors to rank precipitation events in the IP and several major river basins (Ramos et al., 2014).

WEATHER TYPES CLASSIFICATION
In this study we applied the WT classification methodology adopted by Trigo and DaCamara (2000) for Portugal and that takes into account physical and geometrical considerations, i.e., the direction and strength of airflow, the direction and vorticity of geostrophic flow, and the signal and intensity of cyclonicity. This approach is based on the corresponding objective classification defined for the British Isles (Jenkinson and Collison, 1977; Jones et al., 1993).

To determine the daily WTs for period 1950–2003, a set of 16 points (**Figure 1B**—p1 to p16) centered in IP was used to extract daily SLP series from EMULATE Mean Sea Level Pressure dataset (EMSLP), compiled by Ansell et al. (2006) with a resolution of 5° latitude by 5° longitude. Compared with Trigo and DaCamara (2000), these points were shifted 5° eastwards in order to center the entire grid in the middle of the IP. The indices used to compute the WTs by means of the 16 daily SLP points were the following: southerly flow (SF), westerly flow (WF), total flow (F), southerly shear vorticity (ZS), westerly shear vorticity (ZW), and total shear vorticity (Z):

$$\text{SF} = 1.305[0.25(\text{p5} + 2\text{p9} + \text{p13}) - 0.25(\text{p4} + 2\text{p8} + \text{p12})]$$

$$\text{WF} = [0.5(\text{p12} + \text{p13}) - 0.5(\text{p4} + \text{p5})]$$

$$\text{ZS} = 0.85[0.25(\text{p6} + 2\text{p10} + \text{p14}) - 0.25(\text{p5} + 2\text{p9} + \text{p13})$$
$$- 0.25(\text{p4} + 2\text{p8} + \text{p12}) + 0.25(\text{p3} + 2\text{p7} + \text{p11})]$$

$$\text{ZW} = 1.12[0.5(\text{p15} + \text{p16}) - 0.5(\text{p8} + \text{p9})]$$
$$- 0.91[0.5(\text{p8} + \text{p9}) - 0.5(\text{p1} + \text{p2})]$$

$$\text{F} = (\text{SF2} + \text{WF2})^{1/2}$$

$$\text{Z} = \text{ZS} + \text{ZW}$$

The conditions established to define different types of circulation are the same as in Trigo and DaCamara (2000), and thus the same set of rules were adopted:

(a) Direction of flow was given by $\tan^{-1}(\text{WF/SF})$, 180° being added if WF was positive. The appropriate direction was computed using an eight-point compass, allowing 45° per sector.

(b) If $|Z| < F$, the flow is essentially straight and was considered to be of a pure directional type (eight different cases, according to the directions of the compass).

(c) If $|Z| > 2F$, the pattern was considered to be of a pure cyclonic type if $Z > 0$, or of a pure anticyclonic type if $Z < 0$.

(d) If $F < |Z| < 2F$, the flow was considered to be of a hybrid type and was therefore characterized by both direction and circulation (8×2 different types).

Taking into account this set of rules, a total of 26 WTs were defined, 10 pure types (**Figure 2**: NE, E, SE, S, SW, W, NW, N, C, and A), and 16 hybrid types (8 for each C or A hybrid). The 8 pure types associated to a specific wind direction are called Directional types. We disseminated the fairly few cases (<1%) with possibly unclassified situations among the 26 classes.

PRECIPITATION INDICES

To study the relationship between daily precipitation and WTs, six mean monthly indices were analyzed: the WTs Frequency, Mean Precipitation, Percentage Contribution, Intensity, Efficiency, and Area of Influence. All these indexes (except the WTs Frequency) are first calculated for each individual pixel of the precipitation grid, and then are averaged over the 1673 Iberian pixel (including Balearic Islands).

The shift from monthly to daily precipitation allows to compute new rainfall indexes such as the Mean Precipitation of each WT, the Precipitation Intensity and Efficiency that were not studied in the previous work (Cortesi et al., 2013b). In that work a large number of regression models were developed at the monthly scale for each station; however, such approach presents serious limitations, for example the systematical overestimation of precipitation assigned to the WTs that were selected as predictors by the stepwise regression model and vice versa, the wrong attribution of no rainfall amount to the WTs that were not selected as predictors. In order to avoid any misleading interpretation of the results obtained we would like to provide a brief description of all the precipitation indices used:

- The Mean Precipitation of each WT is the simple sum of the rainfall amount during the days affected by that specific WT throughout all the years of the study period (1950–2003) at monthly level, divided by the total number of years (i.e., the monthly climatology of the WT in mm):

$$\overline{P}_{wt} = \frac{\sum_{j=1950}^{2003} \sum_{i=1}^{365} P_{wt}(i,j)}{N}$$

- The Percentage Contribution of each WT is equal to the Mean Precipitation of that WT divided by the mean monthly total precipitation during the same period:

$$\overline{C}_{wt} = \frac{\overline{P}_{wt}}{\overline{P}_{tot}}$$

- The Precipitation Intensity for a given WT is defined as the sum of the daily precipitation due to the WT during the period 1950–2003 at monthly level, divided by the total number of days that belong to the same WT and period (including dry days):

$$I_{wt} = \frac{\sum_{j=1950}^{2003} \sum_{i=1}^{365} P_{wt}(i,j)}{\sum_{y=1950}^{2003} n_{wt}(y)}$$

- WT monthly Precipitation Efficiency is a percentage defined as the ratio between the number of wet days (≥ 1 mm.) affected by the WT for all the same months during the whole period 1950–2003 and the total number of days affected by the WT in all months of the same period. Thus, it measures the daily rainfall probability (%) of the WT:

$$E_{wt} = \frac{\sum_{y=1950}^{2003} n_{wt}^{wet}(y)}{\sum_{y=1950}^{2003} n_{wt}(y)}$$

- The Area of Influence of each WT is the ratio between the number of grid pixel with Mean Precipitation of 1 mm. or greater and the total number of IP pixel. As such, it measures the % of the IP land surface where a WT has at least a small influence (1 mm) on precipitation:

$$A_{wt} = \frac{N_{pixel}(\overline{P}_{wt} \geq 1\,\text{mm})}{N_{pixel}^{tot}}$$

The Mean Precipitation, Percentage Contribution, and the Precipitation Intensity were first introduced by Trigo and DaCamara (2000) and where also measured by Fernández-González et al. (2012), who in the same paper presented the Precipitation Efficiency index for the key series of Leon (NW Spain). In particular the Area of Influence index, to the best of our knowledge, was never presented before in literature.

WT FREQUENCY AND OVERALL CONTRIBUTION TO PRECIPITATION

WT FREQUENCY

A crucial characteristic to determine the role played by the WTs on the monthly precipitation regime is provided by how often they occur, i.e. by their frequency. The monthly frequency of WTs, expressed in % of days per month, is shown in **Table 2**. It is immediately noticeable that no WT occurs more than 30% of days for a given month.

The pure A type is the most frequent WT from September to May (maximum of 27.2% in January); in June it is replaced by the NE as the most frequent WT during the three summer months (maximum of 28.6% in July). If we are interested in the top three WTs throughout the year than A, W, and SW are more frequent during winter, while NE, N, and E during summer. On the other hand C, SE, and NW present higher frequencies during spring and S during autumn. Hybrid Anticyclonic WTs globally dominate in winter, with a global overall maximum of 49.5% in January and a minimum of 28.4% in July. Hybrid Cyclonic WTs are the less frequent, with a combined maximum of 19.5% in
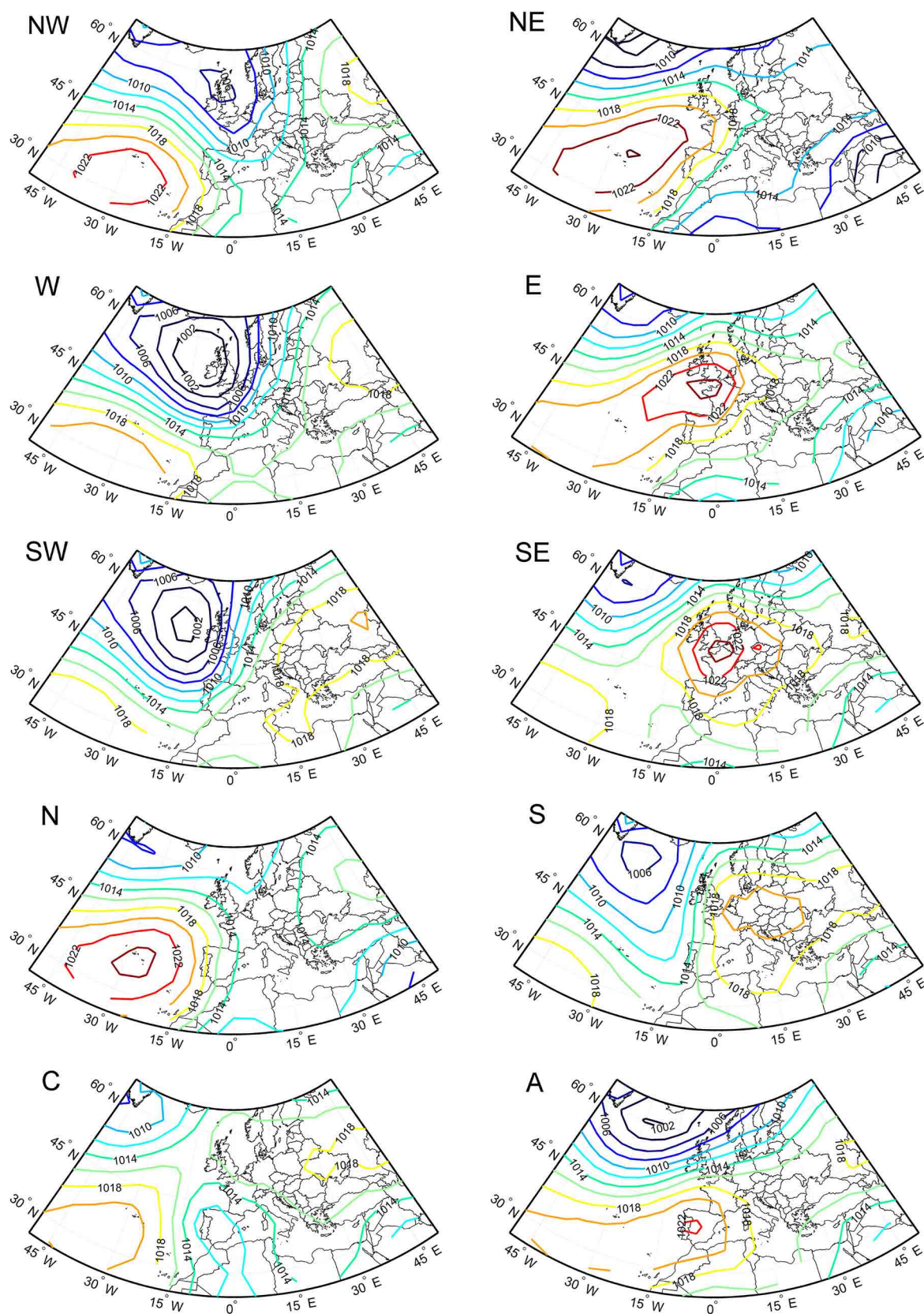
FIGURE 2 | Mean SLP field configuration of the 10 pure WTs for period 1950–2003. The contour interval is 2 hPa.

Table 2 | WTs mean monthly frequency (in %) from 1950 to 2003, starting from December.

	Weather Types (WTs)	Short form	Winter			Spring			Summer			Autumn			Mont. Mean
			Dec	Jan	Feb	Mar	Apr	May	Jun	Jul	Aug	Sep	Oct	Nov	
Directional WTs	Northeasterly	NE	4.4	5.0	5.5	5.3	12.0	14.5	21.8	28.6	26.3	10.9	7.3	6.1	12.3
	Easterly	E	4.4	4.4	7.6	9.4	8.4	8.9	13.1	15.9	13.6	13.1	9.4	6.0	9.5
	Southeasterly	SE	4.2	3.6	3.5	5.1	3.3	2.3	1.0	0.6	1.0	2.8	4.2	3.2	2.9
	Southerly	S	1.9	2.7	2.6	2.0	0.8	0.9	0.1	0.0	0.1	0.7	2.8	2.2	1.4
	Southwesterly	SW	6.2	5.7	6.6	4.9	2.7	2.3	0.4	0.1	0.1	1.7	5.3	5.2	3.4
	Westerly	W	8.7	10.0	9.2	7.7	7.0	5.9	1.6	0.3	1.0	4.6	7.9	9.0	6.1
	Northwesterly	NW	6.9	6.8	6.9	6.0	7.4	8.7	6.3	3.7	4.7	6.0	5.1	7.3	6.3
	Northerly	N	5.3	3.6	4.1	6.0	9.1	9.8	11.9	14.8	14.8	7.4	4.8	5.2	8.1
Cyclonic WTs	Pure cyclonic	C	5.4	4.7	4.3	5.3	9.0	5.4	2.7	1.6	1.6	2.4	3.9	5.1	4.3
	Cyclonic Northeasterly	CNE	1.0	0.2	0.7	1.2	2.5	2.0	2.4	3.0	1.3	1.4	0.8	0.8	1.4
	Cyclonic Easterly	CE	1.0	0.8	0.7	1.2	3.1	2.3	2.2	1.4	1.3	2.2	2.0	1.0	1.6
	Cyclonic Southeasterly	CSE	1.0	0.5	0.5	0.8	0.9	0.7	0.2	0.2	0.2	0.6	0.7	0.9	0.6
	Cyclonic Southerly	CS	0.9	0.4	0.6	0.7	0.4	0.4	0.1	0.0	0.1	0.3	0.5	1.6	0.5
	Cyclonic Southwesterly	CSW	0.7	0.5	0.6	0.7	0.9	0.5	0.1	0.0	0.0	0.3	0.7	1.0	0.5
	Cyclonic Westerly	CW	0.8	0.9	1.2	0.4	0.6	0.9	0.2	0.1	0.2	0.3	0.9	0.4	0.6
	Cyclonic Northwesterly	CNW	0.7	0.5	0.7	0.4	0.9	0.5	0.6	0.2	0.1	0.4	0.5	0.7	0.5
	Cyclonic Northerly	CN	0.4	0.2	0.7	0.5	1.2	1.0	1.2	1.1	1.0	0.4	0.2	0.7	0.7
Anticyclonic WTs	Pure anticyclonic	A	23.8	27.2	23.1	20.7	13.3	17.6	14.3	9.6	14.2	23.0	22.3	23.6	19.4
	Anticyclonic Northeasterly	ANE	2.4	1.6	2.0	2.3	2.8	3.0	6.5	7.5	6.8	4.3	2.6	2.0	3.7
	Anticyclonic Easterly	AE	2.0	1.9	1.8	2.5	1.0	1.9	2.2	2.0	1.4	2.8	3.1	2.3	2.1
	Anticyclonic Southeasterly	ASE	1.6	1.4	1.6	1.6	0.6	0.5	0.4	0.1	0.1	1.2	1.5	1.4	1.0
	Anticyclonic Southerly	AS	0.8	1.0	1.0	0.8	0.4	0.1	0.2	0.1	0.1	0.6	1.5	0.7	0.6
	Anticyclonic Southwesterly	ASW	2.0	2.0	2.0	2.0	0.7	0.6	0.2	0.0	0.0	0.5	1.9	1.5	1.1
	Anticyclonic Westerly	AW	5.2	6.8	5.3	4.5	2.5	2.2	0.5	0.1	0.6	2.4	3.3	4.3	3.1
	Anticyclonic Northwesterly	ANW	5.1	5.1	4.7	4.7	4.0	3.8	4.4	2.7	3.5	5.1	3.6	4.6	4.3
	Anticyclonic Northerly	AN	3.2	2.5	2.6	3.4	4.6	3.5	5.4	6.3	6.0	4.5	2.9	3.1	4.0
	Sum of directional WTs		42.0	41.8	46.0	46.4	50.7	53.3	56.2	64.0	61.6	47.2	46.8	44.2	50.0
	Sum of cyclonic WTs		11.9	8.7	10.0	11.2	19.5	13.7	9.7	7.6	5.8	8.3	10.2	12.2	10.7
	Sum of anticyclonic WTs		46.1	49.5	44.1	42.5	29.9	33.2	34.1	28.4	32.7	44.4	42.7	43.5	39.3

0   28.6

Last column shows the mean of the 12 monthly values for each WT. Color scale helps visualize inter monthly variability. Scale number at right (28.6) refers to the highest frequency of all 26 WTs, while scale midpoint (white color) is equal to the first quartile (0.7). A similar red/blue scale is applied to the last three rows, but with different quartile and maximum values (not showed).

April and a minimum of 5.8% in August, but individually are often below 0.5%, suggesting that these classes represent much less common atmospheric configurations. Some of these WTs classes show a maximum of occurrence in spring, or a bimodal annual cycle with maximum in spring and autumn. Overall, it is interesting to note from **Table 2** that the mean annual frequencies of the Directional, Cyclonic, and Anticyclonic WTs are roughly 50, 10, and 40%, respectively. These results are similar with those described in Cortesi et al. (2013b), in which the same reanalysis dataset EMSLP was employed, but during a slightly different period (1948–2003 instead of 1950–2003). In addition, new information regarding the monthly means and the WTs sub-totals are grouped into seasons.

PERCENTAGE CONTRIBUTION

Previous works with just a few stations have shown that a relatively small number of WTs are responsible for the bulk of the precipitation over western Iberia (Trigo and DaCamara, 2000) or southern Spain (Goodess and Palutikof, 1998) of northwestern Galicia (Lorenzo et al., 2008). Here we intend to evaluate this

dependence using a much larger precipitation dataset and using the spatial averaged values over the entire IP. Thus, the monthly sequence of the seven "wettest" WTs for each month is presented in **Figure 3** and **Table 3**. A simple glance to this figure shows that roughly 20% of total monthly Iberian precipitation depends from a single WT in autumn and winter months (W), and around 50% only from three WTs (W+C+SW). However, these three WTs have a combined frequency of occurrence of about 15%, i.e., confirming that a small number of WTs indeed captures a high percentage of monthly precipitation variability. If one considers all the months of the year then seven non-hybrid WTs generate almost 70% of total monthly Iberian precipitation: W (14.7%), C (12.4%), NE (11.4%), SW (8.8%), NW (8.4%), N (7.7%), and E (6.2%).

The type and order of the seven wettest WTs varies substantially throughout the year. The W type is the highest contributor, from September to March generating about 20% (maximum of 23.3% in January) of monthly rainfall amount, and at the same time during these months its contribution is the highest between all the 26 WTs. During the transitional months of April and May

FIGURE 3 | Percentage Contribution of the seven "wettest" WTs to total monthly Iberian precipitation (1950–2003). Highest WT contributors are placed at bottom and the lowest at the top. At monthly level, the type and the order of the seven wettest WTs varies, but considering also repeated WTs, the total number of WTs is 13. Red line shows the Mean Precipitation in mm.
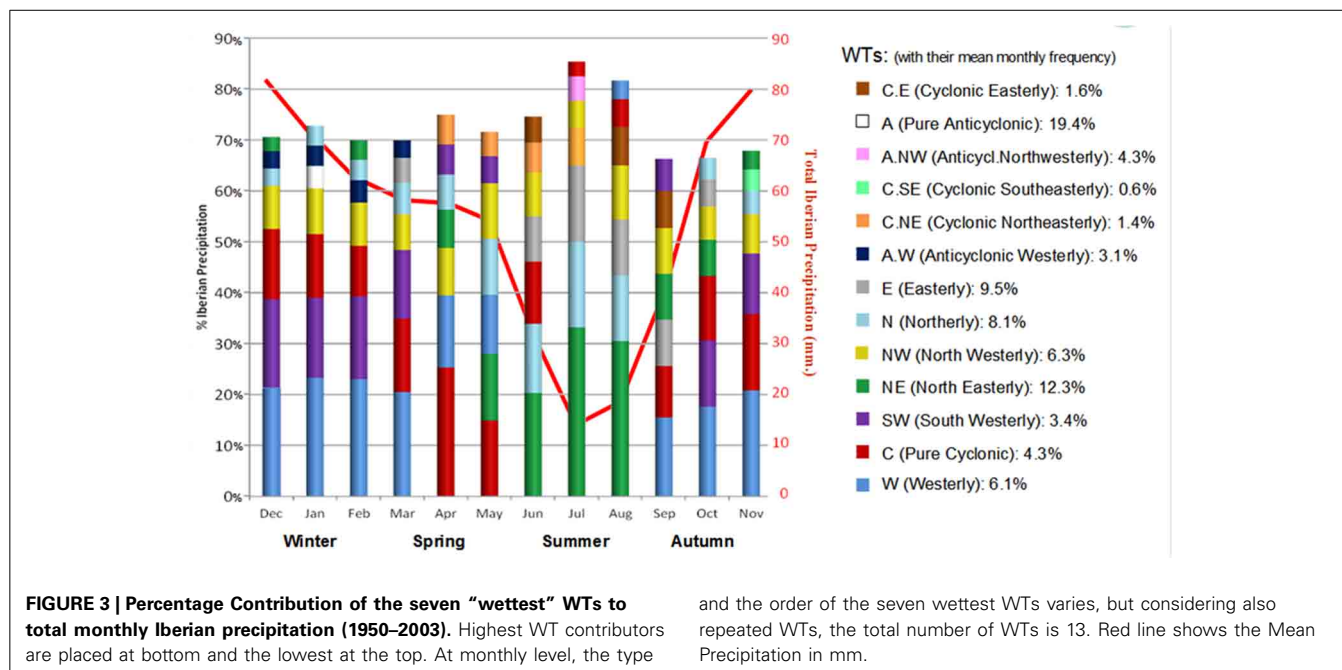
the C type replaces the W type as main contributor (especially in April, when the % difference between C and W is of 11%) and also affects considerably all not-summer months (contribution >10% during September–June), always positioning in the top three contributors position with the exception between July and August. During the three summer months, W and SW lose importance in favor of NE and N types; however, it must be stressed that despite their high percentage it accounts for only a few mm of precipitation due to the small total Iberian Precipitation in summer (red line in **Figure 3**). September is another transitional month during which the W type returns as the main WT contributor through the subsequent autumn and winter months up to March (included). The fourth WT with the largest contribution is the SW type; its contribution is particularly large during the extended winter half of the year, i.e., from October to March, being responsible of more than >13% of monthly precipitation, with a peak of 17.4% in December. Despite never reaching the rank of most important WT contributor, it plays a major role as along with W and C, with the "C-W-SW wet triplet" being responsible for about 50% of total rainfall from October to March. The overall contribution of NW type is quite constant in time, as it always appears in the fourth or fifth rank (third in April), followed by the N type, which has a temporal pattern similar to the NE type, both with a summer maximum. The only Anticyclonic WT observed is the pure A type in fifth position in February. Its frequency is the highest between all WTs (almost 1 day of 5), but its mean monthly Percentage Contribution is quite small compared to its frequency: only 3.1%. It is worth to notice that the S and SE Directional WTs never appear in the sequence of the seven wettest WTs. Thus, from the eight original Directional WTs, only six of them contribute significantly to Iberian precipitation.

The Percentage Contribution index attributes equal weight to each month, including summer months which have only a fraction of the winter precipitation; if we consider instead the seven wettest WTs for the Mean Precipitation index (not shown), than the importance of NE diminishes, shifting from third to fifth position in the wettest WTs sequence, and there are other minor changes in the order of the sequence.

We acknowledge that some of the results presented in this section do not differ substantially from those obtained previously for IP using precipitation at the monthly scale (e.g., Paredes et al., 2006; Cortesi et al., 2013a,b). Nevertheless, the use of a daily dataset ensures considerably more reliable values of individual WTs Percentage Contribution. This better assessment results from the strong caveats associated with the monthly model precipitation methodology, based on monthly frequency of WTs. In fact, the modeling approach presents misleading results for the less frequent WTs, implying positive (negative) bias for the wet (dry) WTs. These biases are responsible that the apparent negligible contribution from the drier WTs and exaggerated contribution associated to wetter WTs (compare Table 2 from Cortesi et al., 2013b with present work **Table 3**).

Additional analysis on the role of different WTs can be obtained clustering them according to their primary characteristic (**Figure 4**), i.e., dominated by the geostrophic flow (Directional types) or dominated by the geostrophic vorticity (Cyclonic and Anticyclonic broad classes). If one considers again the entire IP then the total annual precipitation depends more than 60% from Directional types, almost 30% from Cyclonic WTs and a little more than 10% from Anticyclonic WTs. This is particularly interesting if compared with the average monthly WTs frequencies from **Table 2**, which are about 50, 10, and 40%, respectively. Thus, Cyclonic WTs have a small occurrence (10.7%), but are responsible of almost 30% of overall precipitation, three times their frequency, while Anticyclonic WTs are frequent (39.3%), but contribute only to 11.3% of monthly rainfall, almost four times less than their frequency. This imbalance between WT frequency and Percentage Contribution is expressed

Table 3 | Percentage Contribution of each WT to total monthly Iberian precipitation.

	Weather Types (WTs)	Short form	Winter			Spring			Summer			Autumn			Mont. Mean
			Dec	Jan	Feb	Mar	Apr	May	Jun	Jul	Aug	Sep	Oct	Nov	
Directional WTs	Northeasterly	NE	2.8	2.6	3.8	3.2	7.5	13.1	20.3	33.2	30.5	9.0	7.1	3.7	11.4
	Easterly	E	2.3	3.5	3.4	4.9	2.8	4.4	8.9	15.0	11.0	9.1	5.3	3.2	6.2
	Southeasterly	SE	2.4	1.5	2.7	2.1	1.4	0.5	0.4	0.1	0.4	0.8	2.9	1.8	1.4
	Southerly	S	1.9	3.8	4.0	2.1	0.6	1.1	0.0	0.0	0.2	1.0	3.2	3.0	1.7
	Southwesterly	SW	17.4	15.7	16.3	13.5	5.9	5.3	0.4	0.2	0.2	6.3	13.0	11.9	8.8
	Westerly	W	21.3	23.3	23.0	20.5	14.2	11.6	4.0	0.9	3.7	15.5	17.6	20.8	14.7
	Northwesterly	NW	8.5	9.0	8.5	7.0	9.3	10.9	8.6	5.2	10.6	9.0	6.5	7.7	8.4
	Northerly	N	3.4	3.9	3.1	6.2	6.9	11.0	13.6	16.8	12.9	6.1	4.3	4.6	7.7
Cyclonic WTs	Pure cyclonic	C	13.8	12.5	9.9	14.4	25.3	14.9	12.2	2.9	5.4	10.1	12.7	15.0	12.4
	Cyclonic Northeasterly	CNE	1.4	0.7	1.7	2.2	5.9	4.8	5.9	7.5	3.2	3.4	1.3	1.0	3.3
	Cyclonic Easterly	CE	2.2	1.6	1.9	2.9	4.4	4.1	5.1	2.5	7.6	7.3	4.3	2.7	3.9
	Cyclonic Southeasterly	CSE	2.0	1.0	1.0	0.7	1.1	1.1	0.6	0.0	1.1	1.4	2.4	2.0	1.2
	Cyclonic Southerly	CS	2.0	1.5	1.3	2.0	0.5	1.1	0.1	0.0	0.0	2.0	1.2	4.2	1.3
	Cyclonic Southwesterly	CSW	2.1	2.0	1.9	3.2	2.6	1.2	0.3	0.0	0.0	1.1	2.5	3.6	1.7
	Cyclonic Westerly	CW	2.2	2.2	3.3	1.4	1.7	3.0	0.7	0.3	1.3	0.7	3.0	1.1	1.7
	Cyclonic Northwesterly	CNW	1.6	1.1	0.9	1.1	2.0	1.5	2.2	0.4	0.1	1.0	1.1	1.7	1.2
	Cyclonic Northerly	CN	0.6	0.3	0.9	1.2	1.9	2.2	4.6	2.7	1.4	1.0	0.4	0.9	1.5
Anticyclonic WTs	Pure anticyclonic	A	2.4	4.4	2.6	2.8	1.8	2.9	3.8	2.3	3.0	5.6	3.2	2.8	3.1
	Anticyclonic Northeasterly	ANE	0.5	0.3	0.5	0.4	0.2	0.7	1.7	2.1	1.5	1.2	0.6	0.4	0.8
	Anticyclonic Easterly	AE	0.2	0.6	0.1	0.2	0.1	0.1	0.1	0.2	0.1	0.5	0.5	0.2	0.2
	Anticyclonic Southeasterly	ASE	0.2	0.1	0.5	0.0	0.0	0.1	0.1	0.0	0.0	0.1	0.2	0.5	0.2
	Anticyclonic Southerly	AS	0.3	0.2	0.4	0.3	0.1	0.0	0.2	0.0	0.0	0.2	0.7	0.1	0.2
	Anticyclonic Southwesterly	ASW	1.1	0.9	1.2	1.2	0.2	0.2	0.2	0.0	0.0	0.7	0.7	0.8	0.6
	Anticyclonic Westerly	AW	3.4	4.0	4.4	3.4	1.1	1.4	1.5	0.0	1.2	2.3	2.5	3.3	2.4
	Anticyclonic Northwesterly	ANW	2.6	2.5	1.9	2.0	1.4	1.4	2.1	4.8	2.2	2.9	1.7	1.9	2.3
	Anticyclonic Northerly	AN	1.1	0.8	0.8	1.1	1.0	1.4	2.3	2.8	2.5	1.6	1.0	0.9	1.4
	Sum of directional WTs		60.0	63.3	64.8	59.5	48.6	57.9	56.2	71.4	69.5	56.8	59.9	56.7	60.4
	Sum of cyclonic WTs		27.9	22.9	22.8	29.1	45.4	33.9	31.7	16.3	20.1	28.0	28.9	32.2	28.3
	Sum of anticyclonic WTs		11.8	13.8	12.4	11.4	5.9	8.2	12.0	12.2	10.5	15.1	11.1	10.9	11.3

0 ▬▬▬▬▬▬▬▬ 33.2

Last column shows the mean of the 12 monthly values for each WT. Color scale helps visualize inter monthly variability. Scale number at right (33.2%) refers to the highest contribute of all 26 WTs, while scale midpoint (white color) is equal to the first quartile (0.8%).

Directional WTs
Frequency: 50.6%
% Contribution: 60.4%
Efficiency: 24.2%

Cyclonic WTs
Frequency: 10.7%
% Contribution: 28.3%
Efficiency: 40.6%

Anticyclonic WTs
Frequency: 39.3%
% Contribution: 11.3%
Efficiency: 9.9%

FIGURE 4 | Monthly mean of WT Frequency, Percentage Contribution, and Precipitation Efficiency for the three main WT classes: Directional (N, NE, E, SE, S, SW, W, NW), Cyclonic (C, CN, CNE, CE, CSE, CS, CSW, CW, CNW), and Anticyclonic (A, AN, ANE, AE, ASE, AS, ASW, AW and ANW).

by the Precipitation Efficiency that is considerably higher for the Cyclonic types (40.6%) and low for Anticyclonic ones (9.9%) as shown in **Figure 4**.

SPATIAL ANALYSIS

The effects of each WT on the precipitation regime of the IP are related to all the indices mentioned in the Methods Section, i.e., its temporal Frequency (**Table 2**), Mean Precipitation (**Table 3**), Percentage Contribution (Table S1), total Area affected (Table S2), Precipitation Intensity (Table S3), and Efficiency (Table S4). This preliminary analysis conducted in the previous section and also in the above mentioned Tables is based only on precipitation averaged over the entire IP. Naturally, results will vary considerably if one looks into the individual behavior of each single grid cell or pixel. Therefore, it is of paramount importance to analyze the spatial distribution of each index, focusing on one WT at a time.
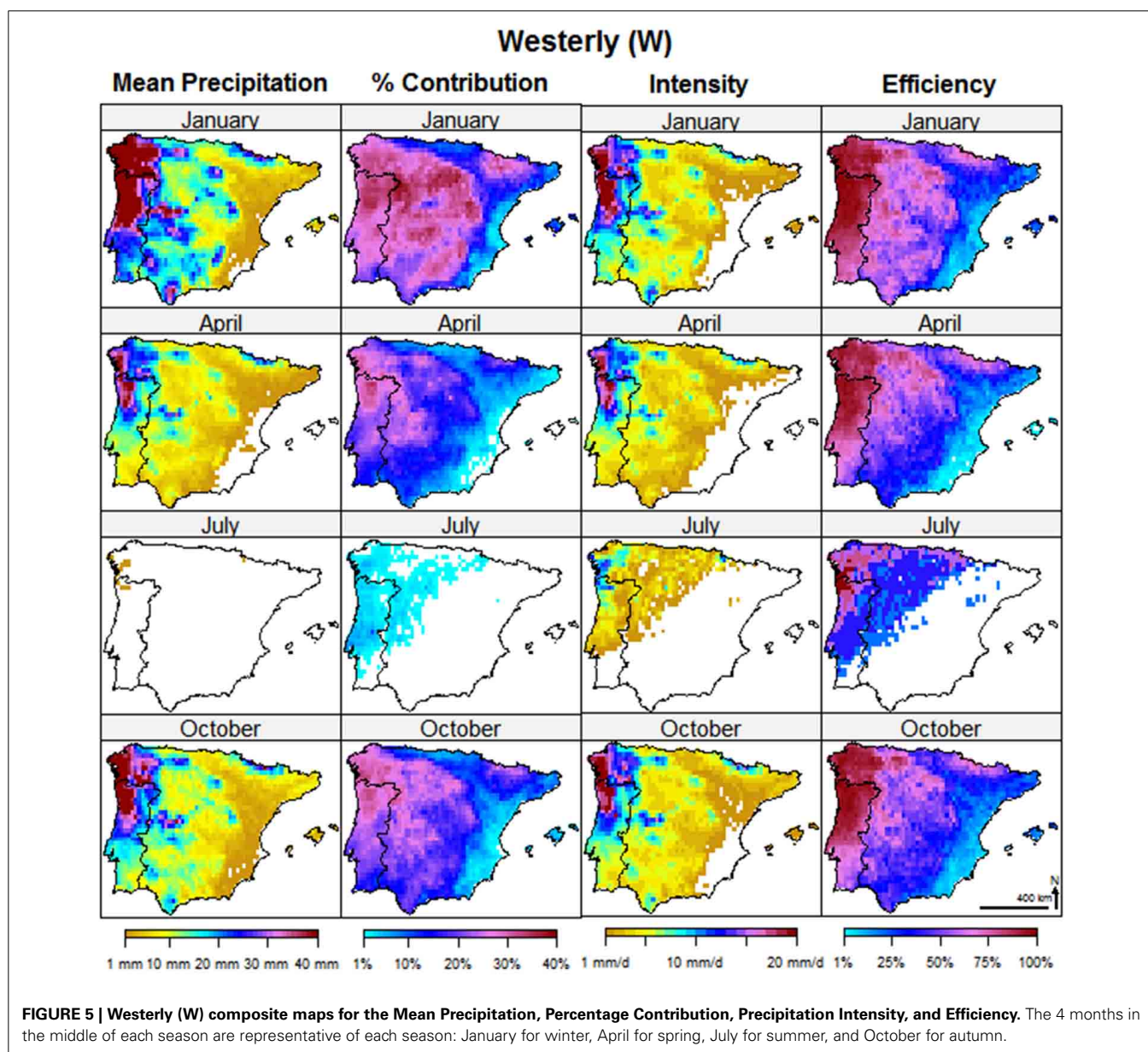
The analysis of WTs that follows illustrates the spatial distribution of the effects on monthly precipitation relative to three

of the seven most prominent (i.e., wettest) WTs, namely; the W, C, and NE (**Figures 4–6**) with the remaining WTs being showed in the Supplementary Material. Taking into account the strong seasonal cycle but also the impossibility of showing the results for all the months we have limited this analysis to the four representative months in the middle of each season: January for winter, April for spring, July for summer, and October for autumn. Each figure includes 16 different sub-plots of the area affected by the specific WT at the monthly scale relative to four indices; (1) Mean Precipitation, (2) Percentage Contribution, (3) Precipitation Intensity, and (4) Precipitation Efficiency. Note that the spatial distribution of the Mean Precipitation is always proportional to the Precipitation Intensity, only the magnitude is different (recall definitions in Section Precipitation Indices).

WESTERLY (W) WEATHER TYPE

The most prominent WT affecting IP precipitation at monthly level is W and the overall characterization is shown in **Figure 5**. The corresponding atmospheric circulation pattern consists of high pressure centered west of the Canary Islands and a low pressure system placed on average just west of Ireland (**Figure 2**). As a consequence, Atlantic westerly flows enter in the IP reaching the mountain arch and affecting the entire IP but particularly the north-western sector. This pattern affects substantially from September to March. Highest effects are noticed to the northwestern areas where more than 30% of January, February and March precipitation depends on this WT, even if its influence spreads even along the western part of the Pyrenees (**Figure 1**). There are two areas in which the effects of W type do not contribute notoriously to explain monthly precipitation: the Cantabric coastland

FIGURE 5 | Westerly (W) composite maps for the Mean Precipitation, Percentage Contribution, Precipitation Intensity, and Efficiency. The 4 months in the middle of each season are representative of each season: January for winter, April for spring, July for summer, and October for autumn.
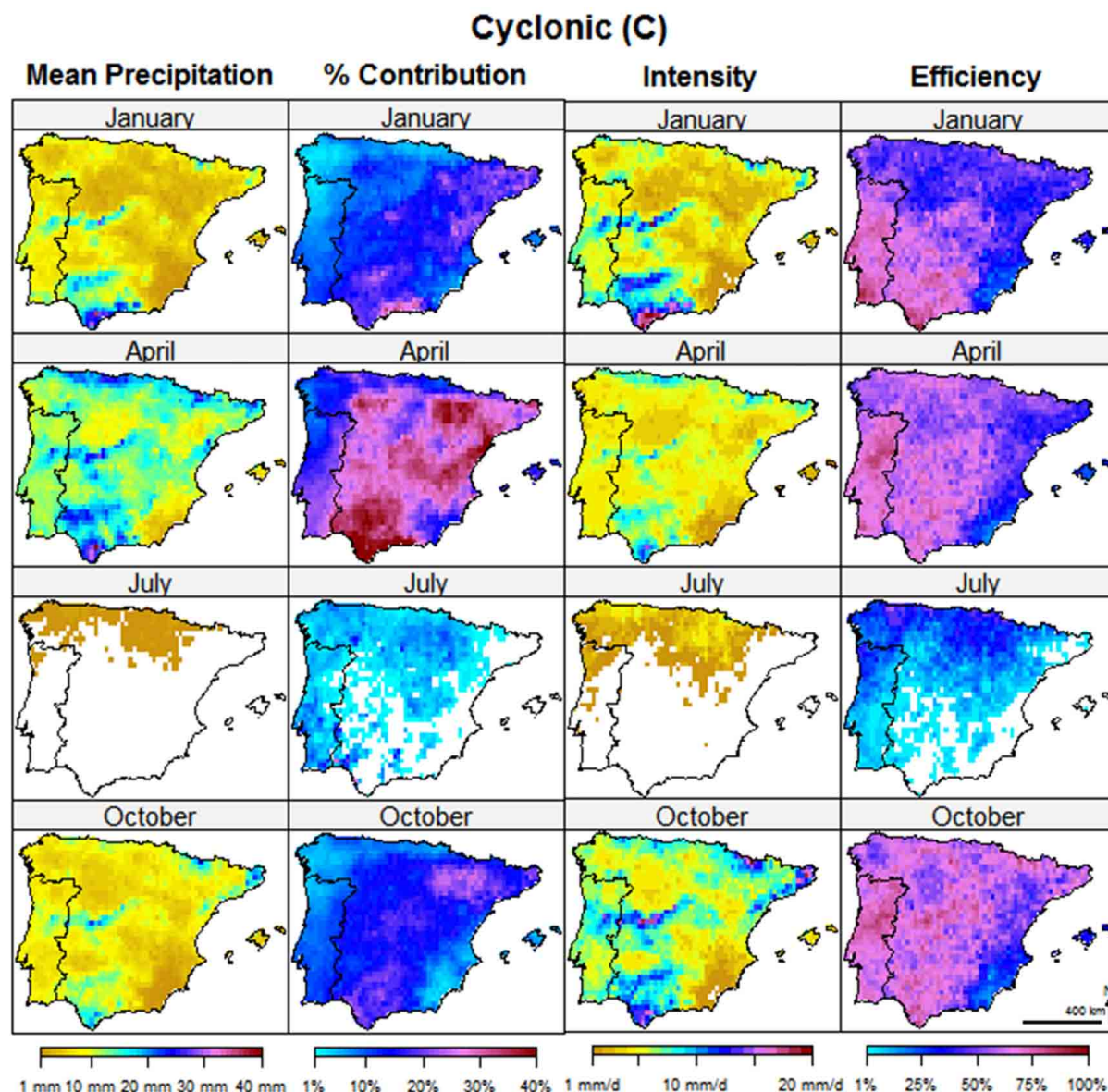
FIGURE 6 | As Figure 5 but relative to the Cyclonic (C) class.

to the north, and the Mediterranean fringe to the east, including the north-inland Ebro basin. Precipitation Intensity is highest in the northwestern areas (including most of Portugal) because of local orography. The same is true for Precipitation Efficiency, which reaches a maximum of almost 100% in the same areas and then decreases to almost 0% in a clear diagonal gradient from north-west to south-east.

PURE CYCLONIC (C) WEATHER TYPE

The spatial distribution and contribution to precipitation associated to the C type is shown in **Figure 6**. The corresponding composite SLP pattern (**Figure 2**) is dominated by a low pressure center over the IP. The spatial impact of this WT type is different from the W type described previously. Its maximum effects,

in terms of contribution to monthly precipitation are clearly observed in spring season, but are also relevant during autumn and winter. The shape of the affected area of its Percentage Contribution has a diagonal orientation from north-east to south-west, i.e., relative precipitation in the northwest and southeast sectors of IP does not depend much on this WT, while the shape of the affected area of its Mean Precipitation gives more weight to the orography, particularly to the Central System and the Bethic System. Differently from the Percentage Contribution, the Precipitation Intensity is highest in autumn and winter, not in spring, because C frequency is smaller in the former season, while the Precipitation Efficiency is almost the same for both seasons, generally between 25 and 75%, and increasing from west to east, with a spatial variation inferior than the Westerly

WT, which in the same month could range from 1 to 100% of Efficiency.

NORTHEASTERLY (NE) WEATHER TYPE

The NE type pattern consists of a high SLP center located to the north of Azores but extending further north and east than the average patterns for the N type (**Figure 2**). Its effects on IP precipitation are less extended than those described previously for the W and C types and with a different peak season (**Figure 7**). Thus, the Mean Precipitation and Area of Influence are lower throughout the year (Tables S1 and S2), and limited to some coastal areas to the east and north of IP. Only its Percentage Contribution is very high in summer, particularly in July and August, because in these months there are few WTs contributing to monthly rainfall. Thus, its Percentage Contribution can reach very high values (>40%), even if the Mean Precipitation is small or very small (<1–2 mm.). This is also due to the very high summer NE frequencies, that distributes the small NE rainfall amount in a large number of

days, determining a very small summer Precipitation Intensity (<1 mm/day) and Efficiency (<25% for the majority of IP).

COMBINED ANALYSIS OF PRECIPITATION INDICES

In this section we perform a combined analysis of the three most innovative precipitation indices (Precipitation Intensity, Precipitation Efficiency, and Area of Influence). In this way, we can identify visually in appropriate scatter-plots the nature of these relationships (e.g., linear vs. non-linear, level of dispersion, etc.) and also how such links vary with WTs. In these representations (**Figures 8–10**) each point represents a single WT during a specific month, therefore there is a total of 312 values (26 × 12 = 312 points).
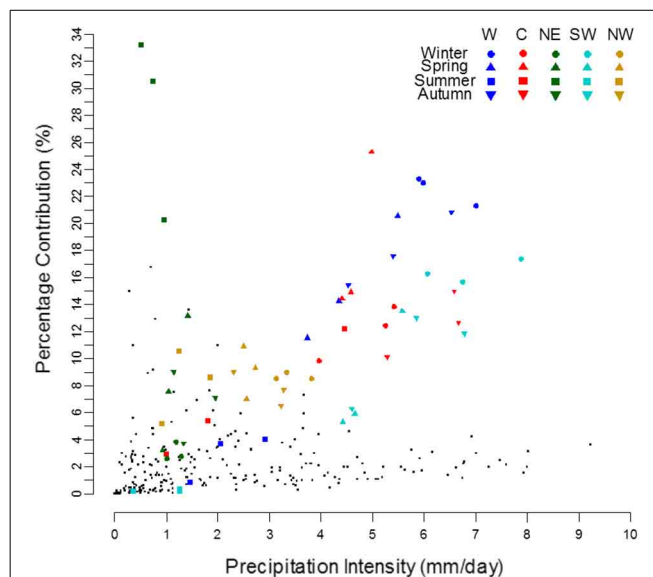
PRECIPITATION INTENSITY vs. PRECIPITATION EFFICIENCY

Due to the similar definition of Precipitation Intensity and Precipitation Efficiency (see Section Precipitation Indices), which only differ in the numerator, these two indexes are highly

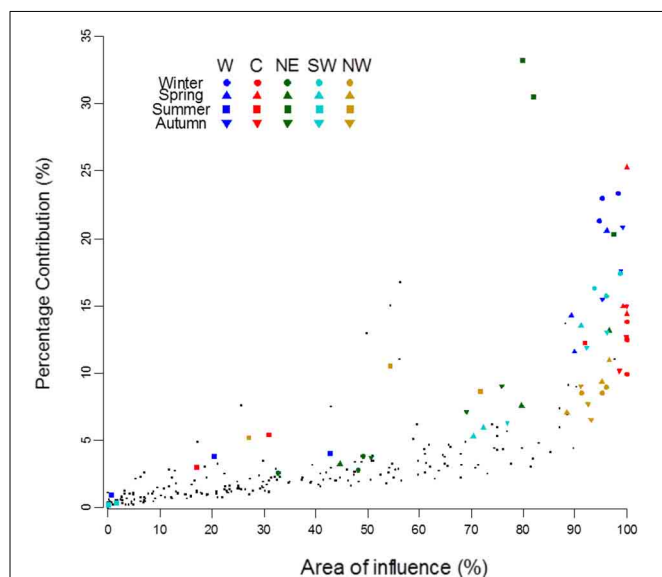**FIGURE 7 | As Figure 5 but relative to the Northeasterly (NE) class.**
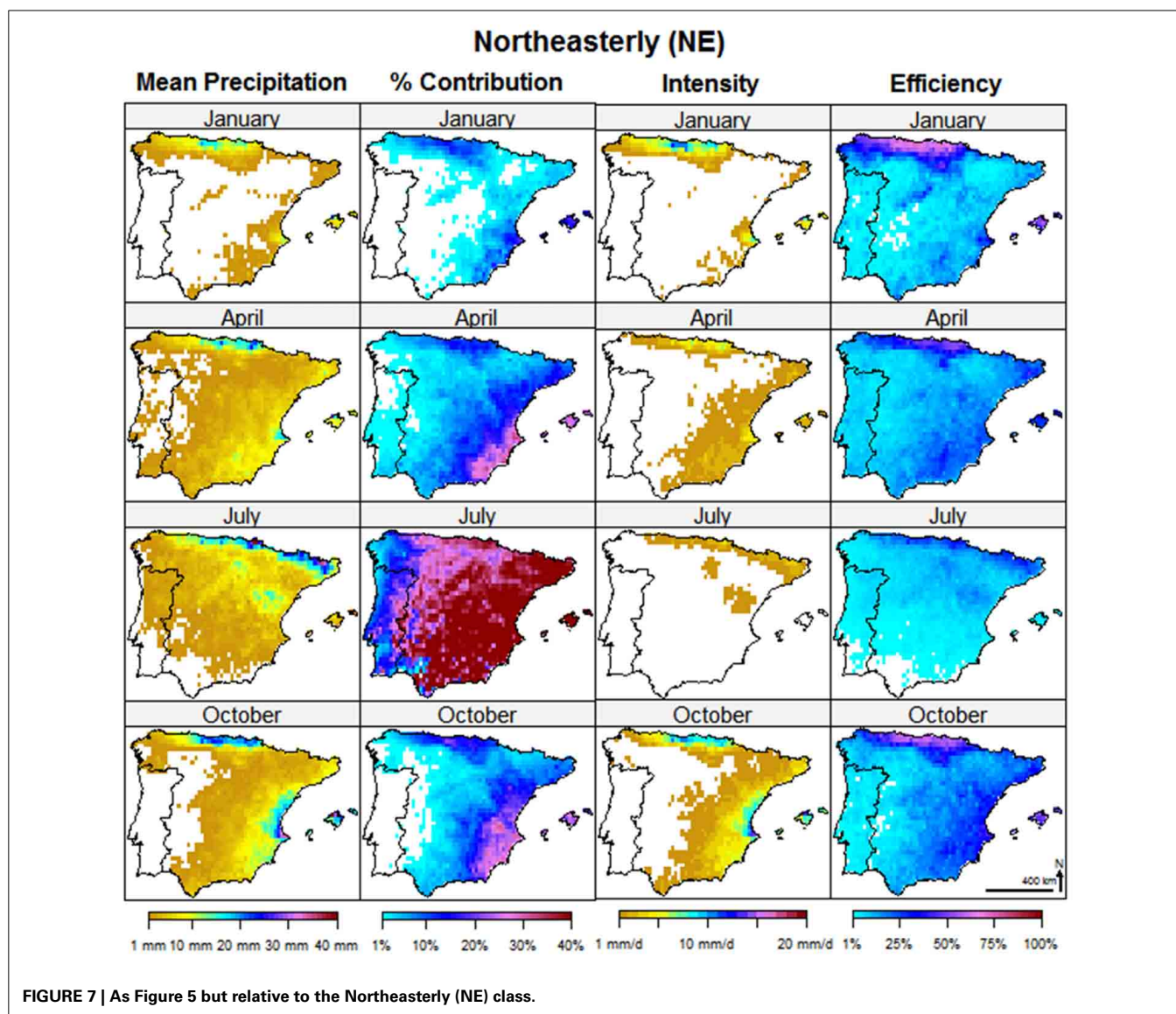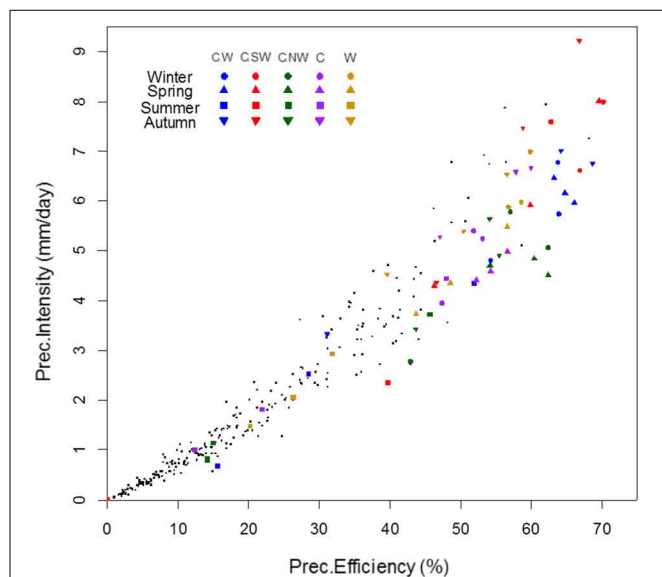
FIGURE 8 | Scatter plot between the Precipitation Intensity and the Precipitation Efficiency. Each point represents a single WT during a specific month (total of 26 × 12 = 312 points). R^2 of the linear fit is 0.94. The five WTs with the highest mean monthly Efficiency are highlighted in color, in order of decreasing Efficiency from left to right. For these five WTs, the three winter months (D-J-F) are shown as circles, the three spring months (M-A-M) as triangles, summer months (J-J-A) as squares, and autumn (S-O-N) as triangles pointing downward.

FIGURE 9 | Scatter plot of the Percentage Contribution as a function of the Area of Influence. The five "wettest" WTs (W, C, NE, SW, and NW) are highlighted in color with a legend similar to **Figure 8**.

FIGURE 10 | Similar to Figure 9 but for Percentage Contribution vs. Precipitation Intensity.

with the highest Precipitation Efficiency are hybrid C types; the fifth is the W type. We should elucidate that these Cyclonic hybrid types tend to occur at much lower rates than most Directional or Anticyclonic types (**Table 1**), often less than 1%, and therefore contribute poorly to the total precipitation. Another interesting aspect results from the apparent existence of two regimes in **Figure 8**, with higher correlation values and lower dispersion at low intensity or efficiencies.

The global high Precipitation Intensity and Efficiency of pure Cyclonic type (C) is also extensive to all hybrid C types. The maximum value of Efficiency is 70.2%, reached by the CSW in January. Each WT presents a seasonal cycle that alternates between minimum Efficiency and Intensity values in summer months, and its maximum in one of the other seasons.

PERCENTAGE CONTRIBUTION vs. AREA OF INFLUENCE

A different measure of the relevance of each WT on IP precipitation regime is given in **Figure 9**, where we present the scatter plot between the Area of Influence for each month and WT and its corresponding Percentage Contribution. The correlation is good but not as high as for the Precipitation Intensity and Efficiency (**Figure 8**) due to the non-linear nature of this relationship, especially for values with very high (>80%) Area of Influence.

The only WT which almost completely affects the IP (>99.9%) is the C type from October to April; its Area of Influence is very high also during September, May, and June (>92%), and only in July and August falls below 31% (see Table S2). The second most widespread WT influential area is the NW, which spreads to over 90% of IP during all non-summer months and March, followed closely by the W, which covers more than 89% of IP during all not-summer months. These three WTs impinge their influence over extended areas of IP, while in general other WTs provide a more localized contribution over relatively narrow areas usually

correlated between them, as can be seen from their scatter plot in **Figure 8**. This fact explains the sequence of the five most intense WTs is very similar to the sequence of the five most efficient ones (from **Figure 8**: CW; CSW; CNW; C; W). Four of the five WTs

with a limited percentage of total monthly precipitation of IP, but locally being important.

The spatial extension of NE and N types is also important but lower than the three previous ones, in any case their global mean monthly extension is over 65% of IP, and during a few months their affected area is larger than 90% (May–June for NE, May for N, October to March for SW). Their seasonal cycle is similar to the most prominent WTs but often affecting considerably smaller areas than those three wet WTs.

It's important to stress that other WTs can affect extended areas but during shorter periods of the year. Among those that are relevant during the warm season we can find (see Table S1 of the Supplementary Material): E (May, June, and September), CNE (April), and CE (May); during autumn many WTs reach their maximum extension, between them 5 Cyclonic and 5 Anticyclonic types: the SE (October), CSE (October), CE (September), CSW (November), CW (October), CNW (November), A (September, with a secondary maximum in January), ANE (September), AS and AE (October), and lastly ASE (November). Even in winter season several extended WTs are visible, such as NW, S, CS, CSW, CNW, AW, ANW, ASW, even if the three last Anticyclonic WTs affect at their maximum less than 70% of IP. Only in spring the Area of Influence is minimum, and it is limited to only the CNE and CE types.

PERCENTAGE CONTRIBUTION vs. PRECIPITATION INTENSITY

As we have shown previously in **Table 3** and **Figures 2**, **3**, just a few "wet" WTs dominate the precipitation over large parts of IP particularly the W, C, SW, NE, and NW. The situation is more varied in case of the Precipitation Intensity. The scatter plot between the Percentage Contribution and the Precipitation Intensity is presented in **Figure 10**. The majority of WTs show low contributions (<3%), but have varying intensities, ranging from near 0 to 9.2 mm/day, typically lower for Anticyclonic types and higher for Cyclonic ones.

Precipitation Intensity of Cyclonic WTs is clearly higher than Directional or Anticyclonic types, as they produce more precipitation when they occur, even if their Percentage Contribution is inferior to the Directional types. For this reason, the C Type is found along the lower right tail of the distribution in **Figure 10**.

The five "wettest" WTs dominate the upper right part of the scatter plot with contribution >3%, always reaching their maximum Precipitation Intensity during autumn or winter, and then falling to a minimum of both Intensity and Contribution during summer (except NE, which in summer reaches the maximum Contribution). The same seasonal pattern is also observed for most other WTs, exceptions being CN during spring and CNE during summer (see Table S3 of the Supplementary Material). The three green squares in the upper left corner of **Figure 10** refer to the high Contribution of NE type during summer, but its Intensity is low because in this period its Frequency is very high ($\approx$25%).

DISCUSSION AND CONCLUSIONS

Climate variability at sub-regional scale is generally higher than on hemispheric or global scale (Giorgi, 2002). This is especially true for precipitation because its variability shows less spatial

averaged predictability and higher temporal variability than any other climate element (Quadrelli et al., 2001; Xoplaki et al., 2004). It also reflects the fact that several different spatial scale processes from hemispheric to local convective, are in one way or another, related to precipitation. Thus, research on precipitation at sub-regional scales depends more than other climate elements on both, (1) the availability of spatially dense databases (Lana and Burgueño, 2000; Huntington, 2006; Trenberth et al., 2007), and (2) the length and completeness of the series (Llasat and Quintas, 2004; Xoplaki et al., 2004). We have applied this approach in the present study to analyze at the highest available spatial detail the relationship between WTs and daily monthly precipitation in the IP.

In a recent paper focused on WTs at general scale of the IP, Cortesi et al. (2013a) stated that the number of WTs that contribute to monthly precipitation decreases from western areas to eastern Mediterranean fringe. The authors concluded that the high variability of precipitation in the eastern areas is due to the dependence on a few number of WTs, while to the west the anomalous behavior of one or two WTs could affect the total amount to a lesser extent.

Some of the results presented in the present work are in accordance with those obtained previously by other researchers for IP using precipitation at the monthly scale (e.g., Paredes et al., 2006; Cortesi et al., 2013a,b). However, the use of a high resolution daily dataset implies much more robust results, in particular we have noticed that the monthly approach has serious limitations, namely positive (negative) bias for the wet (dry) WTs, quite often stating that the contribution from drier WTs is negligible or null while the contribution of wetter WTs is overestimated. For comparison see the large number of zero entrances in the individual WTs contribution in **Table 2** (Cortesi et al., 2013b) that are not negligible at all in the corresponding analysis in the present work (**Table 3**). Additionally we have obtained finer spatial detail results of the WT impact in precipitation and novel results related with combined analysis of precipitation indices related to WTs.

Overall the main results can be summarized as follows:

1. Most of the precipitation is produced by just a few WTs that contribute to a large percentage of the monthly precipitation in most areas of IP; however, their Efficiency varies substantially, being the most efficient WTs the Cyclonic cluster types throughout the year, and the Directional (those with a western component) being also efficient precipitation generators in winter months.

2. The WTs that dominate the precipitation during winter months (D-J-F) in central, western and southwestern areas of IP are pure C, and Directional W and SW. These three WTs have a combined frequency of occurrence of about 15%, but are responsible for up to 50% of the precipitation in winter. This confirms that a small number of WTs indeed captures a high percentage of monthly precipitation variability (Trigo and DaCamara, 2000; Paredes et al., 2006) In the Mediterranean coastland the winter precipitation is linked mostly with easterly flows, noticed by Queralt et al. (2009) and Muñoz-Diaz and Rodrigo (2006).

3. Summer monthly precipitation is usually associated to Northerly or Easterly flows in the IP as suggested by Lorenzo et al. (2011) in northwest areas, or by Muñoz-Diaz and Rodrigo (2006) for the whole IP. During summer months the analyses show that different WTs effects are restricted to relatively narrow areas and during short temporal intervals (one or two months), suggesting that local factors such as relief and deep convection processes could play a major role in precipitation spatial variability.

4. Monthly precipitation during spring and autumn depends mainly from two WTs, namely W and C. We did not observe a clear distinction at IP scale previously noticed between these two seasons as suggested by Lorenzo et al. (2011), Muñoz-Diaz and Rodrigo (2006).

5. Three contrasted areas accordingly WTs can be delimited:

    5.1. Northern Cantabrian coastland, from the sea line to the mountain line, extended from west to the east, where precipitation depends particularly on N and NW.

    5.2. Central-southwest, depending on W, SW, and C, extend from western coastland to the inland mountain line.

    5.3. Mediterranean coastland and Ebro basin, delimited by the Iberian System and Bethic System mountain chain (to the west), the Pyrenees (to the north), and the sea line (to the east). In this area monthly precipitation depends on a variety of WTs, and their effects are confined to very small areas.

6. The geographical disposition of the main mountain chains in the IP, i.e., from west to the east, has been attributed as one of the main factor that promotes the spatial distribution of precipitation and their trends (Gonzalez-Hidalgo et al., 2011), and here we have shown that also they contribute to establish a very well delimited areas accordingly to specific WTs effects.

7. The most efficient WTs corresponds to the CW; CSW; CNW; C; W. However, these Cyclonic hybrid types tend to have low occurrence monthly rates and therefore do not contribute significantly to the total precipitation.

8. The spatial influence of the five "wettest" WTs (W, C, NE, SW, and NW) is particularly large. For the C type, the area of influence is almost 100% of the IP during the extended inter months and decreases for the other months of the year. In addition, the other four WTs impinge their influence over extended areas of IP, while in general the remaining WTs provide a more localized contribution over relatively narrow areas.

All of these aspects are crucial to understand the recent behavior of precipitation in the IP, and form the basis for detailed downscaling analyses for future projections. Finally, this study shows that WTs approach is able to explain at high spatial detail a very high proportion of monthly precipitation variability, and can be a useful argument for precipitation analyses at high resolution in future projections. The results cover also the spring and autumn season less studied until now, and offer information about both seasons in which, for extended areas of IP, the maximum of precipitation are produced (de Luis et al., 2010).

SUPPLEMENTARY MATERIAL

The Supplementary Material for this article can be found online at: http://www.frontiersin.org/journal/10.3389/feart.2014.00025/abstract

REFERENCES

Ansell, T., Jones, P. D., Allan, R. J., Lister, D., Parker, D. E., Brunet-India, M., et al. (2006). Daily mean sea level pressure reconstructions for the European – North Atlantic region for the period 1850–2003. *J. Clim.* 19, 2717–2742. doi: 10.1175/JCLI3775.1

Belo-Pereira, M., Dutra, E., and Viterbo, P. (2011). Evaluation of global precipitation data sets over the Iberian Peninsula. *J. Geophys. Res.* 116, 148–227. doi: 10.1029/2010JD015481

Casado, M. J., Pastor, M. A., and Doblas-Reyes, F. J. (2010). Links between circulation types and precipitation over Spain. *Phys. Chem. Earth* 35, 437–447. doi: 10.1016/j.pce.2009.12.007

Corte-Real, J., Zhang, X., and Wang, X. (1995). Downscaling GCM information to regional scales: a non-parametric multivariate approach. *Clim. Dyn.* 11, 413–424.

Cortesi, N., Gonzalez-Hidalgo, J. C., Trigo, R. M., and Ramos, A. M. (2013b). Weather types and spatial variability of precipitation in the Iberian Peninsula. *Int. J. Clim.* 34, 2661–2677. doi: 10.1002/joc.3866

Cortesi, N., Trigo, R. M., Gonzalez-Hidalgo, J. C., and Ramos, A. M. (2013a). Modelling monthly precipitation with circulation weather types for a dense network of stations over Iberia. *Hydrol. Earth Syst. Sci.* 17, 665–678. doi: 10.5194/hess-17-665-2013

de Luis, M., Brunetti, M., Gonzalez-Hidalgo, J. C., Longares, L. A., and Martin-Vide, J. (2010). Changes in seasonal precipitation in the Iberian Peninsula during 1946–2005. *Global Planet. Change* 74, 27–33. doi: 10.1016/j.gloplacha.2010.06.006

Dünkeloh, A., and Jacobeit, J. (2003). Circulation dynamics of Mediterranean precipitation variability 1948–1998. *Int. J. Clim.* 23, 1843–1866. doi: 10.1002/joc.973

Esteban-Parra, M., Rodrigo, F., and Castro, M. Y. (1998). Spatial and temporal patterns of precipitation in Spain for the period 1880–1992. *Int. J. Clim.* 18, 1557–1574.

Fernández-González, S., del Rio, S., Castro, A., Penas, A., Fernández-Raga, M., Calvo, A., et al. (2012). Connection between NAO, weather types and precipitation in León, Spain (1948–2008). *Int. J. Clim.* 32, 2181–2196. doi: 10.1002/joc.2431

Fernandez-Mills, G. F. (1995). Principal component analysis of precipitation and rainfall regionalization in Spain. *Theor. Appl. Climatol.* 50, 169–183.

Garcia, J. A., Serrano, A., and Gallego, M. D. (2002). A spectral analysis of Iberian Peninsula monthly rainfall. *Theor. Appl. Climatol.* 71, 77–95. doi: 10.1007/s704-002-8209-y

Gimeno, L., Nieto, R., Trigo, R. M., Vicente-Serrano, S. M., and Lopez-Moreno, J. I. (2010). Where does the Iberian Peninsula moisture come from? an answer based on a lagrangian approach. *J. Hydrometeorol.* 11, 421–436. doi: 10.1175/2009JHM1182.1

Giorgi, F. (2002). Variability and trends of subcontinental scale surface climate in the twentieth century. Part I: observatorios. *Clim. Dyn.* 18, 675–691. doi: 10.1007/s00382-001-0204-x

Gonzalez-Hidalgo, J. C., Brunetti, M., and de Luis, M. (2011). A new tool for monthly precipitation analysis in Spain: MOPREDAS database (Monthly precipitation trends December 1945–November 2005). *Int. J. Clim.* 31, 715–731. doi: 10.1002/joc.2115

Goodess, C. M., and Jones, P. D. (2002). Links between circulation and changes in the characteristics of Iberian rainfall. *Int. J. Clim.* 22, 1593–1615. doi: 10.1002/joc.810

Goodess, C. M., and Palutikof, J. P. (1998). Development of daily rainfall scenarios for southeast Spain using a circulation-type approach to downscaling. *Int. J. Clim.* 18, 1051–1083.

Hanggi, P., Jete, M., Kuttel, M., Wanner, H., and Weingartner, R. (2011). Weather type-related trend analysis of precipitation in Switzerland. *Hydrol. Wasserbewirts.* 55, 140–154.

Herrera, S., Gutiérrez, J. M., Ancell, R., Pons, M. R., Frías, M. D., and Fernández, J. (2012). Development and analysis of a 50-year high-resolution daily gridded precipitation dataset over Spain (Spain02). *Int. J. Clim.* 32, 74–85. doi: 10.1002/joc.2256

Huntington, T. G. (2006). Evidence for intensification of the global water cycle: review and synthesis. *J. Hydrol.* 319, 83–95. doi: 10.1016/j.jhydrol.2005.07.003

Jenkinson, A. F., and Collison, F. P. (1977). "An initial climatology of gales over the North Sea," in *Synoptic Climatology Branch Memorandum* (Bracknell: Meteorological Office).

Jones, P. D., Hulme, M., and Briffa, K. R. (1993). A comparison of Lamb circulation types with an objective classification scheme. *Int. J. Clim.* 13, 655–663.

Kostopoulou, E., and Jones, P. D. (2007a). Comprehensive analysis of the climate variability in the eastern Mediterranean. Part I: map-pattern. *Int.J. Clim.* 27, 1189–1214. doi: 10.1002/joc.1467

Kostopoulou, E., and Jones, P. D. (2007b). Comprehensive analysis of the climate variability in the eastern Mediterranean. Part II: relationships between atmospheric circulation patterns and surface climatic elements. *Int. J. Clim.* 27, 1351–1371. doi: 10.1002/joc.1466

Kutiel, H., Maheras, P., and Guika, S. (1996). Circulation indices over the Mediterranean and Europe and their relationship with rainfall conditions across the Mediterranean. *Theor. Appl. Climatol.* 54, 125–138. doi: 10.1007/BF00865155

Lana, X., and Burgueño, A. (2000). Some statistical characteristics of monthly and annual pluviometric irregularity for the Spanish Mediterranean coast. *Theor. Appl. Climatol.* 65, 79–97. doi: 10.1007/s007040050006

Lionello, P., Gacic, M., Gomis, D., Garcia-Herrera, R., Giorgi, F., Planton, S., et al. (2012). Program focuses on climate of the Mediterranean region. *EOS Trans. Am. Geophys. Union* 93, 105–106. doi: 10.1029/2012EO100001

Llasat, M. C., and Quintas, L. (2004). Stationarity of monthly rainfall series since the middle of the XIXth century. Application to the case of Peninsular Spain. *Nat. Hazards* 31, 613–622. doi: 10.1023/B:NHAZ.0000024894.66869.46

Lorenzo, M. N., Ramos, A. M., Taboada, J., and Gimeno, L. (2011). Changes in present and future circulation types frequency in Northwest Iberian Peninsula. *PLoS ONE* 6:e16201. doi: 10.1371/journal.pone.0016201

Lorenzo, M. N., Taboada, J. J., and Gimeno, L. (2008). Links between circulation weather types and teleconnection patterns and their influence on precipitatioon patterns in Galicia (NW Spain). *Int. J. Clim.* 28, 1493–1505. doi: 10.1002/joc.1646

Lorenzo-Lacruz, J., Vicente-Serrano, S. M., López-Moreno, J. I., Gonzalez-Hidalgo, J. C., and Morán-Tejeda, E. (2011). The response of Iberian rivers to the North Atlantic Oscillation. *Hydrol. Earth Syst. Sci.* 15, 2581–2597. doi: 10.5194/hess-15-2581-2011

Martin-Vide, J. (2004). Spatial distribution of a daily precipitation concentration index in peninsular Spain. *Int. J. Clim.* 24, 959–971. doi: 10.1002/joc.1030

Martin-Vide, J., and Gomez, L. (1999). Regionalization of peninsular Spain based on the length of dry spells. *Int. J. Clim.* 19, 537–555.

Martin-Vide, J., and Lopez-Bustins, J. A. (2006). The western Mediterranean oscillation and rainfall in the Iberian Peninsula. *Int. J. Clim.* 26, 1455–1475. doi: 10.1002/joc.1388

Michailidou, C., Maheras, P., Arseni-Papadimititriou, A. F., Kolyva-Machera, A., and Anagnostopoulou, C. (2009). A study of weather types at Athens and Thessaloniki and their relationship to circulation types for the cold-wet period, part I: two-step cluster analysis. *Theor. Appl. Climatol.* 97, 163–177. doi: 10.1007/s00704-008-0057-x

Morata, A., Martin, M. L., Luna, M. Y., and Valero, F. (2006). Self-similarity patterns of precipitation in the Iberian Peninsula. *Theor. Appl. Climatol.* 85, 41–59. doi: 10.1007/s00704-005-0175-7

Muñoz-Diaz, D., and Rodrigo, F. S. (2004). Spatio-temporal patterns of seasonal rainfall in Spain (1912–2000) using cluster and principal component analysis: comparison. *Ann. Geophys.* 22, 1435–1448. doi: 10.5194/angeo-22-1435-2004

Muñoz-Diaz, D., and Rodrigo, F. S. (2006). Seasonal rainfall variations in Spain (1912–2000) and the links to atmospheric circulation. *Atmos. Res.* 81, 94–110. doi: 10.1016/j.atmosres.2005.11.005

Paredes, D., Trigo, R. M., García-Herrera, R., and Trigo, I. F. (2006). Understanding precipitation changes in Iberia in early spring: weather typing and storm-tracking approaches. *J. Hydrometeorol.* 7, 101–113. doi: 10.1175/JHM472.1

Quadrelli, R., Pavan, V., and Molteni, F. (2001). Wintertime variability of Mediterranean precipitation and its links with large-scale circulation anomalies. *Clim. Dyn.* 17, 457–466. doi: 10.1007/s003820000121

Queralt, S., Hernandez, E., Barriopedro, D., Gallego, D., Ribera, P., and Casanova, C. (2009). North Atlantic Oscillation influence and weather types associated with Winter total and extreme precipitation events in Spain. *Atmos. Res.* 94, 675–683. doi: 10.1016/j.atmosres.2009.09.005

Ramos, A. M., Lorenzo, M. N., and Gimeno, L. (2010). Compatibility between modes of low-frequency variability and circulation types: a case study of the northwest Iberian Peninsula. *J. Geophys. Res. Atmos.* 115:D02113. doi: 10.1029/2009JD012194

Ramos, A. M., Trigo, R. M., and Liberato, M. L. R. (2014). A ranking of high-resolution daily precipitation extreme events for the Iberian Peninsula. *Atmos. Sci. Lett.* doi: 10.1002/asl2.507

Rodriguez-Puebla, C., Encinas, A. H., Nieto, S., and Garmenia, J. (1998). Spatial and temporal patterns of annual precipitation variability over the Iberian Peninsula. *Int. J. Clim.* 18, 299–316.

Romero, R., Ramis, C., and Guijarro, J. A. (1999). Daily rainfall patterns in the Spanish Mediterranean area: an objective classification. *Int. J. Clim.* 19, 95–112.

Saaroni, H., Halfon, N., and Ziv, B. (2010). Links between the rainfall regime in Israel and location and intensity of Cyprus lows. *Int. J. Clim.* 30, 1014–1025. doi: 10.1002/joc.1912

Santos, J. A., Corte-Real, J., and Leite, S. M. (2005). Weather regimes and their connections to the winter rainfall in Portugal. *Int. J. Clim.* 25, 33–50. doi: 10.1002/joc.1101

Serrano, A., Garcia, J. A., Mateos, V. L., Cancillo, M. L., and Garrido, J. (1999). Monthly modes of variation of precipitation over the Iberian peninsula. *J. Clim.* 12, 2894–2919.

Spellman, G. (2000). The use of an index-based regression model for precipitation analysis on the Iberian Peninsula. *Theor. Appl. Climatol.* 66, 229–239. doi: 10.1007/s007040070027

Tartaglione, N., Maugeri, M., Dalan, F., Brunetti, M., Nanni, T., and Speranza, A. (2009). Searching for resemblance between large-scale sea level pressure patterns leading to "intense" precipitation events over Italy. *Theor. Appl. Climatol.* 95, 183–196. doi: 10.1007/s00704-007-0374-5

Trenberth, K. E., Jones, P. D., Ambenje, P., Bojariu, R., Easterling, D., Klein Tank, A., et al. (2007). "Observations: surface and atmospheric climate change," in *Climate Change 2007: The Physical Science Basis. Contribution of Working Group I to the Fourth Assessment Report of the Intergovernmental Panel on Climate Change*, eds S. Solomon, D. Qin, M. Manning, Z. Chen, M. Marquis, K. B. Averyt, M. Tignor and H. L. Miller (Cambridge; New York, NY: Cambridge University Press).

Trigo, R. M., and DaCamara, C. C. (2000). Circulation weather types and their impact on the precipitation regime in Portugal. *Int. J. Clim.* 20, 1559–1581. doi: 10.1002/1097-0088(20001115)20:13<1559::AID-JOC555>3.0.CO;2-5

Trigo, R. M., and Palutikof, J. P. (2001). Precipitation scenarios over Iberia: a comparison between direct GCM output and different downscaling techniques. *Int. J. Clim.* 14, 4422–4446. doi: 10.1175/1520-0442(2001)014<4422:PSOIAC>2.0.CO;2

Valero, F., Martín, M. L., Sotillo, M. G., Morata, A., and Luna, M. Y. (2009). Characterization of the autumn Iberian precipitation from long term datasets: comparison between observed and hindcasted data. *Int. J. Clim.* 29, 527–541. doi: 10.1002/joc.1726

Vicente-Serrano, S. M., and Lopez-Moreno, J. I. (2006). The influence of atmospheric circulation at different spatial scales on winter drought variability through a semi-arid climatic gradient in Northeast Spain. *Int. J. Clim.* 26, 1427–1453. doi: 10.1002/joc.1387

Wilks, D. S. (2006). *Statistical Methods in the Atmospheric Sciences: An Introduction.* International Geophysics. Series 59. St. Louis, MO: Academic Press.

Xoplaki, E., González-Rouco, F., Luterbacher, J., and Wanner, A. (2004). Wet season Mediterranean precipitation variability: influence of large scale dynamics and trends. *Clim. Dyn.* 23, 63–78. doi: 10.1007/s00382-004-0422-0

Zhang, X., Wang, X. L., and Corte-Real, J. (1997). On the relationships between daily circulation patterns and precipitation in Portugal. *J. Geophys. Res.* 102, 13495–13507.

Zorita, E., Kharin, V., and von Storch, H. (1992). The atmospheric circulation and sea surface temperature in the North Atlantic area in winter: their interaction and relevance for Iberian precipitation. *J. Clim.* 5, 1097–1108.

The influence of circulation weather patterns at different spatial scales on drought variability in the Iberian Peninsula

Ana C. Russo[1]*, Célia M. Gouveia[1], Ricardo M. Trigo[1], Margarida L. R. Liberato[1,2] and Carlos C. DaCamara[1]

[1] Instituto Dom Luiz, Faculdade de Ciências, Universidade de Lisboa, Lisboa, Portugal

[2] Escola de Ciências e Tecnologia, Departamento de Engenharias, Universidade de Trás-os-Montes e Alto Douro, Vila Real, Portugal

Europe has suffered several extreme weather events which were responsible for considerable ecological and economic losses in the last few decades. In Southern Europe, droughts are one of the most frequent extreme weather events, causing severe damages and various fatalities. The main goal of this study is to determine the role of Circulation Weather Types (CWT) on spatial and temporal variability of droughts by means of the multi-scalar Standardized Precipitation Evapotranspiration Index (SPEI). This study aims also to identify the main CWTs associated with winter and summer droughts over different regions of Iberian Peninsula. During the period between 1950 and 2012, the most frequent CWTs were found to be the Anticyclonic (A), Cyclonic (C), North (N) and Northeast (NE) types. The trend analysis for winter season shows a clear increase of frequency CWTs associated to dry events (A, East and Southeast) and a decrease of frequency of C and northern types while in summer a clear decrease of NE is observed. The spatial patterns of correlation between SPEI and CWT show large patterns of negative correlations with winter frequencies of A and eastern weather types, while the reverse occurs with C and western types. This feature is highlighted on a regional approach. The NE type presents negative correlations in Central, Northwestern and Southwestern regions during winter and positive correlations in Eastern region during summer. In opposition, the West type presents positive correlations in all regions (except Eastern region) during winter and does not present significant correlations during summer. In general, the predominant CWT associated to winter or summer drought conditions differs greatly between regions. The winter droughts are associated mainly with high frequency of E types and low frequency of W types for all areas, while the summer drought in eastern sectors are linked with low frequency of C type, as well as the western regions are related with the N type.

Keywords: circulation weather types, Iberian Peninsula, Standardized Precipitation Evapotranspiration Index (SPEI), winter and summer droughts, spatial scale

INTRODUCTION

In the last decade, Europe has experienced multiple extreme weather (EW) events (Hov et al., 2013), such as the devastating floods in Central Europe in 2002 (Sánchez et al., 2004) and 2013 (Grams et al., 2014) and the severe droughts that hit the Iberian Peninsula (IP) in 2004/2005 (Garcia-Herrera et al., 2007) and 2011/2012 (Trigo et al., 2013) and western Russia and Ukraine in 2010 (Sánchez et al., 2004; Hov et al., 2013). Unprecedented mega heat waves have also struck Western Europe in 2003 (Garcia-Herrera et al., 2007) and Russia/Eastern Europe in 2010 (Barriopedro et al., 2011).

Despite their profound impact in the biosphere, and in built-up areas and transport networks, floods and heatwaves are usually phenomena of relative short duration, lasting in the order of a few days to a few weeks. On the contrary, droughts are characterized by much longer time scales, typically spanning from few months to several years, as the mega droughts of Australia (Delworth and Zeng, 2014) and southwestern USA (Woodhouse

et al., 2010). In Southern Europe, in particular in the IP, droughts are one of the most frequent EW events (Hov et al., 2013), having negative impacts on agriculture (Vicente-Serrano and López-Moreno, 2006), hydroelectric power production (Garcia-Herrera et al., 2007; Trigo et al., 2013), water resources (Vicente-Serrano and López-Moreno, 2006), vegetation activity (Gouveia et al., 2009), net primary production (Bastos et al., 2014), forest growing (Martínez-Villalta et al., 2008) and risk of forest fires (Pausas, 2004).

According to the SREX report on extremes (IPCC, 2012), there are still large uncertainties regarding observed global-scale trends in droughts with no statistically significant changes in observed drought conditions in Europe, except for the Mediterranean region. Despite some contradictory results obtained with different GCMs (Scaife et al., 2012), there are several studies confirming that drought frequency is increasing in the Mediterranean basin (Seneviratne et al., 2006; Sousa et al., 2011; Hoerling et al., 2012), in particular over the IP (Xoplaki et al., 2012; Trigo et al., 2013).

The occurrence of intense droughts in the IP is strongly associated to its precipitation regime, which is characterized by an intense interannual and decadal variability (Garcia-Herrera et al., 2007; Trigo et al., 2013). Taking into account that the largest concentration of rainfall in the IP occurs between October and March (Trigo and DaCamara, 2000; Garcia-Herrera et al., 2007), all major droughts in the IP are therefore characterized by a rainfall shortage during several winter months (Garcia-Herrera et al., 2007; Trigo et al., 2013). Even though precipitation is the main conditioning factor for the occurrence of drought events, temperature has also been identified in several studies as an important factor explaining recent trends in water resources (e.g., Vicente-Serrano et al., 2011, 2014; Schubert et al., 2014). Thus, warming processes may have a negative effect on the availability of surface water resources, mostly driven by higher evapotranspiration rates (Vicente-Serrano et al., 2011).

Drought events and their associated impacts have been systematically studied during the last years, namely in the context of future climate change scenarios. Some types of EW are expected to become more frequent and severe, enhancing the exposure and vulnerability of ecosystems and humans (IPCC, 2014). Moreover, the IP as part of the Mediterranean basin, corresponds to one of the most sensitive areas to current and future climate change, stressing its role as a climate change "hot spot" (Giorgi, 2006; Giorgi and Lionello, 2008), with some of the changes reflecting already an anthropogenic signal (Hoerling et al., 2012; Trigo et al., 2013). Furthermore, most climate change scenarios present a relative consensual evolution of the climate for the Mediterranean, pointing toward a concurrent decrease in precipitation and increase in temperature in Southern Europe (Giorgi, 2006; Giorgi and Lionello, 2008) including more summer heatwaves (Fischer and Schär, 2010). This combined effect of less rainfall and higher temperatures is bound to increase the frequency, magnitude and severity of drought episodes (Vicente-Serrano et al., 2011, 2014). Therefore, it is crucial to understand the spatial and temporal variability of droughts, especially within the framework of future warming scenarios (IPCC, 2014) and risk assessment (IPCC, 2012).

Given the difficulties to objectively identify the onset and end of a drought, and to quantify drought severity, a considerable amount of studies were undertaken in recent years with the aim of developing new drought indicators (e.g., Wells et al., 2004; Vicente-Serrano et al., 2010a,b). Drought analysis and monitoring have been conducted traditionally using either the Palmer Drought Severity Index (PDSI), based on a soil water balance equation (Palmer, 1965), or the Standardized Precipitation Index (SPI), based on a probabilistic approach to precipitation (McKee et al., 1993). However, the original PDSI has notorious problems when used outside USA plains (Wells et al., 2004). This caveat triggered the development of new formulations to adapt the PDSI, namely the so called self-calibrated PDSI (scPDSI) that was used successfully to assess droughts over the Mediterranean region (Wells et al., 2004; Sousa et al., 2011). Vicente-Serrano et al. (2010a) proposed a climatic drought index, the Standardized Precipitation Evapotranspiration Index (SPEI), based on the simultaneous use of precipitation and temperature fields. This new index also holds the advantage of combining a multi-scalar character with the capacity to include the effects of

temperature variability on drought assessment (Vicente-Serrano et al., 2010a). The application of multi-scalar indices to the high-resolution datasets allows identifying whether the IP is in hydric stress and also whether drought and desertification is installed. Traditionally, local risk management strategies focus only on short-term climatic events without considering long-term climate changes (IPCC, 2012). The use of indices which account for different variables and time-scales in their formulation (e.g., SPEI) will fill this gap, especially for applications involving future climate scenarios (Vicente-Serrano et al., 2010a,b, 2011).

Droughts in Europe are closely connected to anomalies of the atmospheric circulation and to circulation features (e.g., Garcia-Herrera et al., 2007; Pfahl, 2014), thus the influence of synoptic atmospheric circulation on the frequency, intensity, severity and the onset and end of drought should be look upon carefully, especially within the framework of future warming scenarios and risk assessment.

The last two decades have witnessed a growing development and application of automated classifications of regional atmospheric circulation patterns, often entitled Circulation Weather Type (CWT) classification. CWTs are a fairly simple method to describe atmospheric circulation variability (Huth et al., 2008; Beck and Philipp, 2010), providing a discrete characterization of the atmospheric conditions for a specific given region. These weather patterns or CWTs result from the automated examination of synoptic weather data [e.g., sea level pressure (SLP) or geopotential height at 500 hPa (HGT500)], usually on regular gridded fields (Huth et al., 2008; Beck and Philipp, 2010). Most classification procedures are based on the application of statistical selection rules or on the determination of physical parameters related with the prevailing atmospheric circulation pattern (Yarnal, 1993; Beck and Philipp, 2010). CWTs have been widely used and the focus tends to be threesome: (i) climatic variability, including trends and extreme years, (ii) environmental and (iii) weather driven natural hazards. Typically, applications to the Iberian Peninsula concentrate on climatic trends (Paredes et al., 2006; Lorenzo et al., 2008), on drought events (Trigo and DaCamara, 2000; Vicente-Serrano and López-Moreno, 2006; Garcia-Herrera et al., 2007), on very wet years (Vicente-Serrano et al., 2011) or to assess the changes in present and future CWTs frequency (Lorenzo et al., 2011). In particular, several authors have applied different methodologies to study the influence of weather-type frequency on precipitation in Iberia using different datasets and periods of study (e.g., Trigo and DaCamara, 2000; Santos et al., 2005; Lorenzo et al., 2008; Cortesi et al., 2013). However, to the best of our knowledge, there is no application for the entire Iberian Peninsula including an analysis of the relationship between the CWT frequencies and the intensity, as well as, the spatial differences of droughts with detailed spatial scales for winter and summer.

The present study's main objectives are to determine the role of CWTs on spatial and temporal variability of droughts allowing to better identify the atmospheric processes associated to severe drought in the Iberian Peninsula. This aim is met through the following specific objectives: (1) to identify the influence of CWTs occurrences on spatial and temporal variability of droughts using the multi-scalar drought index (SPEI) for the study of historical droughts and (2) to identify the main CWTs associated

with winter and summer droughts and (3) to identify the main CWTs associated with drought over different regions of Iberian Peninsula.

DATA AND METHODS

CIRCULATION WEATHER TYPE CLASSIFICATION

Classification procedures based on the determination of CWTs and their applications to environmental analysis have been used frequently in recent decades (e.g., Trigo and DaCamara, 2000; Demuzere et al., 2009; Ramos et al., 2011; Russo et al., 2014). The CWTs are able to capture the multivariate information given by an input dataset, e.g., time series of daily pressure fields, into a univariate time series of type membership, i.e., to a classification catalog (Philipp et al., 2010). Most classification procedures are based on the application of statistical selection rules (e.g., cluster analysis and regression trees) but can also be based on the determination of physical parameters related with the prevailing atmospheric circulation pattern. Traditionally, classification procedures have been divided into manual and automated classifications (e.g., Yarnal, 1993). Alternatively, subjective vs. objective procedures or even hybrid methods have been established (Philipp et al., 2010). For additional information on different CWTs classification procedures and applications throughout Europe please see also Huth et al. (2008); Beck and Philipp (2010) and Philipp et al. (2010).

In the present work, we applied an automated version of the Lamb circulation type's methodology. This classification of atmospheric circulation into CWTs was first developed for the British Isles by Lamb (1972) and, later on, it was improved for an objective automated classification by Jenkinson and Collison (1977). This automated methodology was later applied for different areas in the Iberian Peninsula (e.g., Trigo and DaCamara, 2000; Paredes et al., 2006; Garcia-Herrera et al., 2007; Domínguez-Castro et al., 2014; Russo et al., 2014). In this work, prevailing CWTs at regional scale where determined using the simple Geostrophic approximation according to the methodology proposed by Trigo and DaCamara (2000). Following the referred approach, 26 CWTs are initially identified (10 pure, 8 anticyclonic hybrids and 8 cyclonic hybrids). However, in order to obtain a more structured and statistically representative analyses, the 26 CWTs are reassembled in just 10 classes, not including any undefined class. This was achieved by simply assuming that each of the 16 hybrid types contributes with a weight of 0.5 into the corresponding pure directional and cyclonic/anticyclonic type monthly frequencies (e.g., one case hybrid like the CE is included as 0.5 in C and 0.5 in E types). This assemblage results on that only 10 distinct CWTs are considered from now on, eight of which are driven by the direction of the flow (NE, E, SE, S, SW, W, NW, and N) and two further classes dominated by the shear vorticity (cyclonic C or anticyclonic A). A short description for the observed SLP features of each type, as well as the description of this methodology including the simplification from 26 to 10 classes may be found in Trigo and DaCamara (2000).

The daily CWT for the 1950–2012 periods were computed based on Trigo and DaCamara (2000) approach by means of the daily sea level pressure (SLP) on a 2.5° latitude-longitude grid retrieved from the NCEP/NCAR reanalysis data (Kistler et al., 2001). Afterwards, the corresponding monthly frequencies were computed based on the daily classification. The year was divided in two extended winter (October–March) and summer (April–September) seasons that will be considered for the analysis.

DROUGHT ASSESSMENT

As mentioned before the application of multi-scalar indices will allow to identify if the IP is in hydric stress and also if drought is installed. In order to quantify the evolution of drought for the IP the recently developed SPEI (Vicente-Serrano et al., 2010b) was applied. Choice of SPEI among other drought indices was because SPEI is not only more accurate than the standard precipitation-based indices (such as SPI and PDSI), but also more sensitive to global warming (Vicente-Serrano et al., 2010a); it has also shown to be better associated with hydrological drought in Iberia than SPI or PDSI (Vicente-Serrano et al., 2014). Additionally, SPEI is a standardized measure that is comparable among seasons, enabling the estimation of the duration, magnitude and intensity of drought. The water balance is included in the computation of SPEI by means of the calculation of the difference between monthly precipitation (**Figure 1B**) and the potential evapotranspiration (**Figure 1C**).

The SPEI was computed using the Climatic Research Unit (CRU) TS3.21 High Resolution Gridded Data of Month-by-month Variation in Climate dataset (available online at http://badc.nerc.ac.uk/data/cru/), with a spatial resolution of 0.5 degrees and for the period 1950–2012. The study region of IP corresponds to a square of 30 × 30 grid boxes (**Figure 1B**). We computed the Potential Evapotranspiration (PET), using the Hargreaves equation (Hargreaves and Samani, 1985) and the log-logistic probability distribution. This formulation allows a very good fit to the series of differences between precipitation and PET (Vicente-Serrano et al., 2010b), and using monthly averages of daily maximum and minimum temperature data (**Figures 1D,E**) and also monthly precipitation records. The parameters were estimated by means of the L-moment method.

One of the main advantages of SPEI is that it can be determined for different time scales, which is very useful for monitoring drought impacts on natural and socioeconomic systems (Vicente-Serrano et al., 2010b). Detailed explanation on the meaning of the different drought time scales can be found in Vicente-Serrano et al. (2010a) and Vicente-Serrano et al. (2010b). In the present study, the 6-month time scale was used.

DROUGHT SPATIAL AND TEMPORAL PATTERNS

The precipitation regime in the IP is characterized by high temporal and spatial variability (Lionello, 2012), with the former being related to the intense seasonal cycle and inter-annual variability and the latter driven by the marked topography (**Figure 1A**). Previous studies (e.g., Vicente-Serrano and López-Moreno, 2006) on drought characteristics suggest that it is possible to effectively quantify the hydrological variability over a certain region in terms of the combined monthly temperature and precipitation variability. In order to determine SPEI's general patterns of temporal evolution, a PCA was applied to the SPEI determined over IP for the 1950–2012 period.
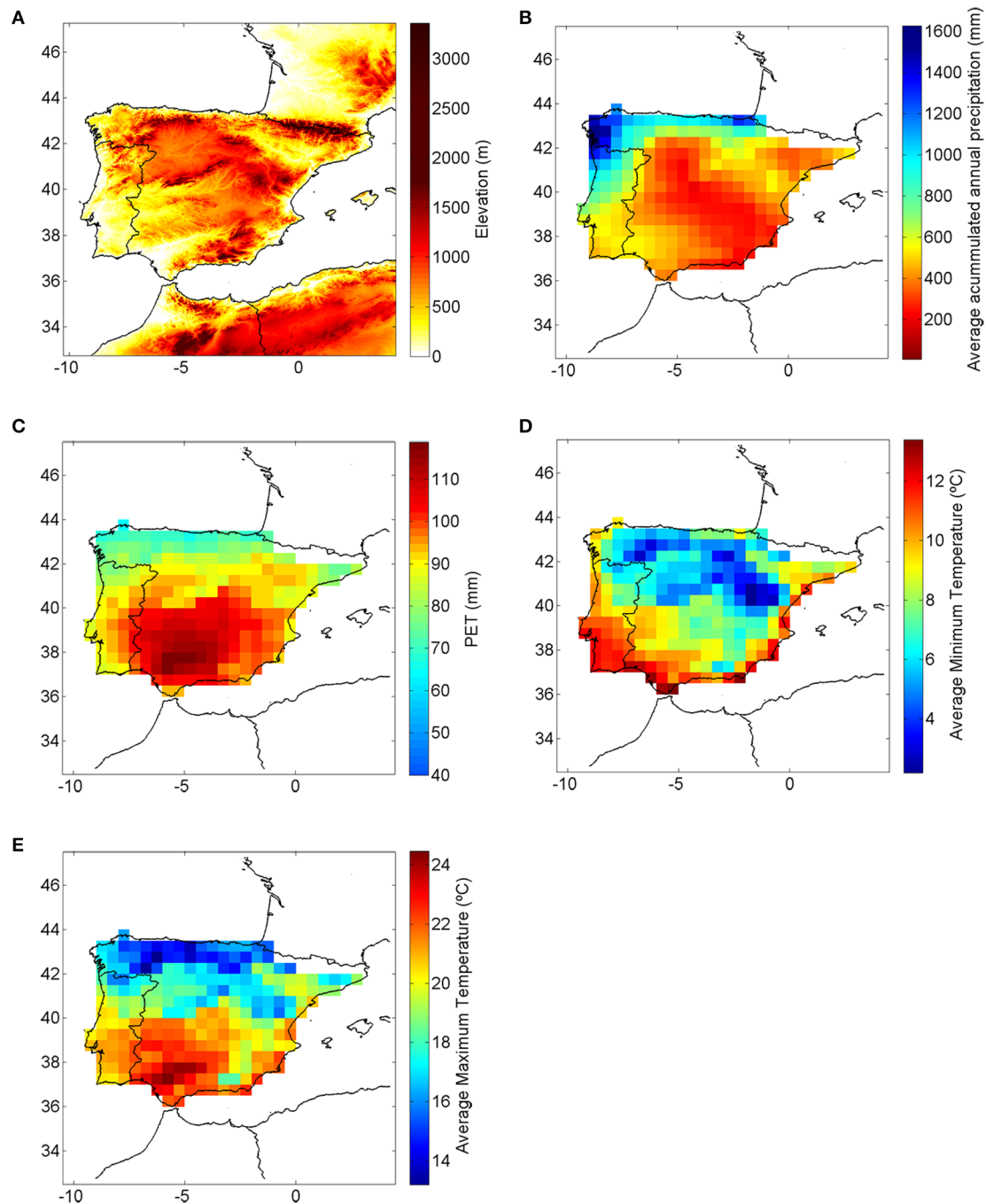
FIGURE 1 | Elevation (A), annual mean accumulated precipitation (B), annual mean PET (C) minimum (D) and maximum temperature (E) in the study area.

To encapsulate the main spatio-temporal patterns of droughts in the study area, we used a PCA in S-mode (Serrano et al., 1999). The S-mode allows the determination of regions in which the structure of evolution of droughts is very similar and we have used the gridded values of SPEI as variables and years as cases. The retained principal components were rotated to redistribute the explained variance, using the

Varimax method (Wilks, 2006). For each season we selected 4 PCs that explains about 80% of the variance (**Table 3**). A cluster analysis was then applied to the eight selected EOFs, representing the variability of the entire year. The clustering method used is the standard k-means clustering algorithm leading to the identification of six spatial clusters, that can be associated with the main homogeneous regions over

Iberia, as obtained by Vicente-Serrano using SPI 6 months (Vicente-Serrano, 2006).

RESULTS AND DISCUSSION
CWT CHARACTERIZATION

As described in Section Drought assessment, the prevailing circulation patterns were identified based on the large-scale standard pressure fields and the relative frequency of each CWT averaged for each month was then estimated for the period 1950–2012 (**Figure 2**). The anticyclonic (A) type is the most frequent circulation pattern throughout the year, except for the summer months of July and August, which are also highly influenced by the northeast (NE), north (N) and east (E) circulation types. The predominance of the A type is associated with the migration of the Azores anticyclone toward the Iberian Peninsula (Tomás et al., 2004). During summer, Portugal is usually under the influence of the Azores anticyclone and while a frequent shallow thermal depression can develop over the central Iberian Peninsula, the A class appears as one of the most frequent CWT affecting Portugal also during summer months (Ramos et al., 2011). The meridional circulation types north (N) and south (S) present very distinct behaviors; N is one of the predominant CWT, particularly during spring and summer months, while S is rather minor, especially from April to August. The directional CWTs with a southern component (i.e., S, SE, SW) are the least frequent CWTs throughout the majority of the year. Moreover, the NW and E circulation types present relatively stable frequencies during most of the year. Throughout the year, the relative frequency of C situations does not change significantly reaching one relative peak in the spring.

The CWTs present an important range of temporal variability behavior, with inter-annual and inter-decadal variance often superimposed on longer trends. The moving average procedure is a conventional approach for temporal change detection in climatology, allowing for filtering the year-to-year variations and revealing more persistent trends (De Luis et al., 2000). Thus, prior to trend analysis, a moving average of 9 years was determined, decreasing the degrees of freedom of the series through the reduction of the number of samples, reducing also the higher frequency variability which can hide existing trends. The datasets

were smoothed using a 9-year moving average, as suggested by De Luis et al. (2000) and Vicente-Serrano and López-Moreno (2006). Trends were then evaluated by means of Spearman's rank correlation (**Figure 3**). **Figure 3** shows the frequency of the A, C, SW, and NE weather types throughout the study period for winter and summer seasons. The red line indicates a moving average for a 9 year window.

Previous works have shown that the most important CWTs associated to the Iberian precipitation regime are C, W, and SW that contribute to the highest fraction of winter, spring and autumn precipitation (Trigo and DaCamara, 2000; Garcia-Herrera et al., 2007). **Figure 3** shows that some of winter CWTs contributing to the highest fraction of winter, spring, and autumn precipitation over Iberia are decreasing (e.g., types C and NE) and those associated with stability are increasing (e.g., types A and E), contributing positively to the intensification of more frequent drought events.
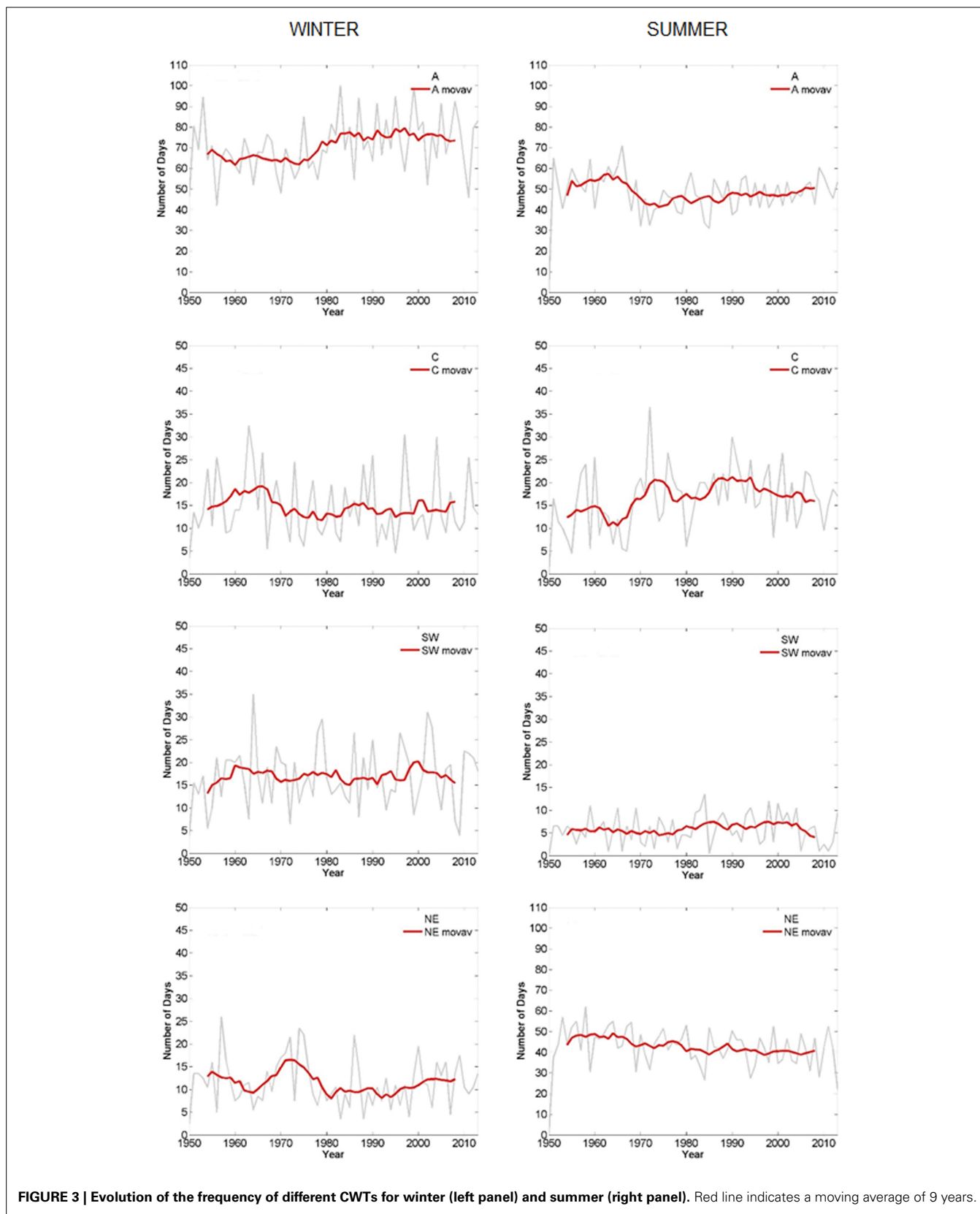
These results are supported by **Table 1** where the statistically significant trends ($\alpha < 0.05$) for the different CWTs in the Iberian Peninsula (1950–2012) are presented. The winter season presents a significant increasing trend in A and a significant decreasing trend in NW, contrasting with summer where significant increases can be observed for types C and NW and W (**Table 1**). The decrease in NW in winter is also observed in the adjacent classes N and W, although being not significant. A significant decrease in NE and significant increases in neighboring types E and SE are also observed in summer. Finally, the winter season shows a significant increase in E type (**Table 1**).

Figure 4 shows the seasonal anomaly composites of pressure (mb) at sea level (SLP) relative to four distinct CWTs, those classified as C, A, SW, and NE. These seasonal anomaly composites were obtained after removing the respective grand means computed for the period 1950–2012 over each season: winter (ONDJFM) and summer (AMJJAS).

In winter the A weather type (**Figure 4A**) which shows a clear increase in the frequency from 1950 to 2012 (**Table 1**), indicates the influence of high pressures centered on the IP. On the other hand the C (**Figure 4B**) and NE (**Figure 4D**) weather types, characterized by a negative and statistically non-significant
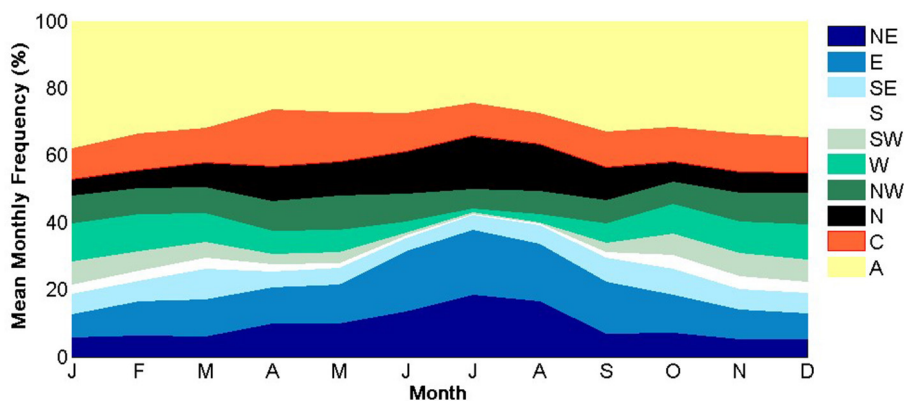
FIGURE 2 | Mean monthly frequency (%) for the 10 CWT during the 1950–2012 period. The circulation patterns are labeled as follows: A, Anticyclonic; C, Cyclonic; N, North; S, South; W, West; E, East; NW, Northwest; NE, Northeast; SW, Southwest and SE, Southeast.

FIGURE 3 | Evolution of the frequency of different CWTs for winter (left panel) and summer (right panel). Red line indicates a moving average of 9 years.

Table 1 | Trends in the different CWTs in the Iberian Peninsula (1950–2012).

	Season	A	C	NE	E	SE	S	SW	W	NW	N
Rho-Spearman	Winter	0.30	−0.06	−0.04	0.21	0.12	−0.01	0.12	−0.16	−0.32	−0.13
	Summer	−0.08	0.28	−0.29	0.25	0.22	0.11	0.06	0.21	0.32	−0.05

The shaded CWTs have a statistically significant trend (α < 0.05).

FIGURE 4 | Anomaly composites of pressure (colorbar; mb) at sea level (SLP) in days classified as A, C, SW, and NE. The anomaly fields are shown for winter **(A–D)** and summer **(E–H)**.
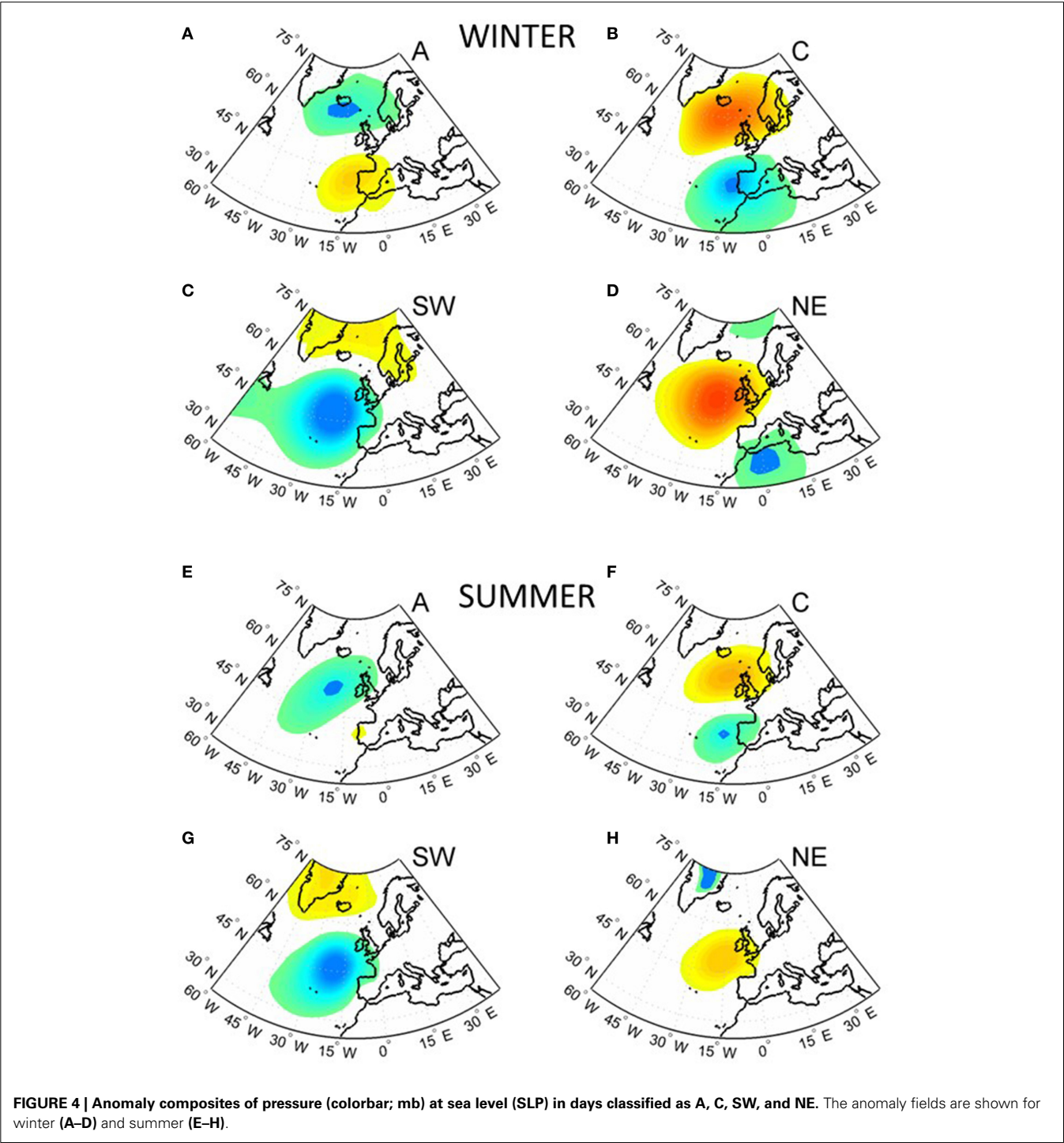
trend in the frequency, show respectively low pressures centered on the IP and a transition from strong high pressures over the Atlantic region extending to the northwestern Iberia and low pressures centered over northwestern Africa. The SW (**Figure 4C**) weather type, which presents very low and non-significant trends, indicates intense low pressures over the Atlantic and affecting the IP.

In summer the patterns are similar, though less intense than in winter. The C (**Figure 4F**) and SW (**Figure 4G**) weather types, which also correspond to low relative pressures over the IP, show an increase in the frequency during the analyzed period (**Table 1**), while the NE (**Figure 4H**) weather type, which shows a clear negative and statistically significant trend in the frequency, still shows a high pressure region over eastern Atlantic and northwestern Iberia. Finally, the A weather type (**Figure 4E**), which presents low and non-significant trends, indicates the influence of high relative pressures centered on the IP.

SPATIAL REGIONALIZATION OF THE IBERIAN DROUGHTS
Having obtained all CWTs patterns and time series for the considered period, their possible associations with observed drought patterns were investigated. This circulation-to-environmental approach (Yarnal, 1993) should allow identifying clear links between circulation and drought patterns. In order to reduce the dimensionality of the problem we have applied a PCA to the SPEI dataset from 1950 to 2012 over Iberia. A selection criteria was used to determine how many principal components should be retained. According to this criteria, one should retain all the components that account for a minimum of 80% of the cumulative temporal variability. Thus, we have selected four principal components as they explain more than 80% of the temporal variability of the SPEI (**Table 2**). Accordingly, the four principal components account for 80.4% of the total explained variance (EV) in the case of winter season and 82.6% in summer. **Figure 5** shows the spatial distribution of the first four PC loadings and it may be noted that the spatial patterns of the four major leading components is similar for winter and summer, although they appear in a different order. Component 1 (55.4% of the EV) for winter and component 2 (12.8% of the EV) for summer reflect the temporal evolution of the SPEI series in the southwestern quadrant, which is influenced by the Atlantic systems. Component 2 (12.1% of the EV) for winter and component 4 (3.4% of the EV) for summer reflect the temporal
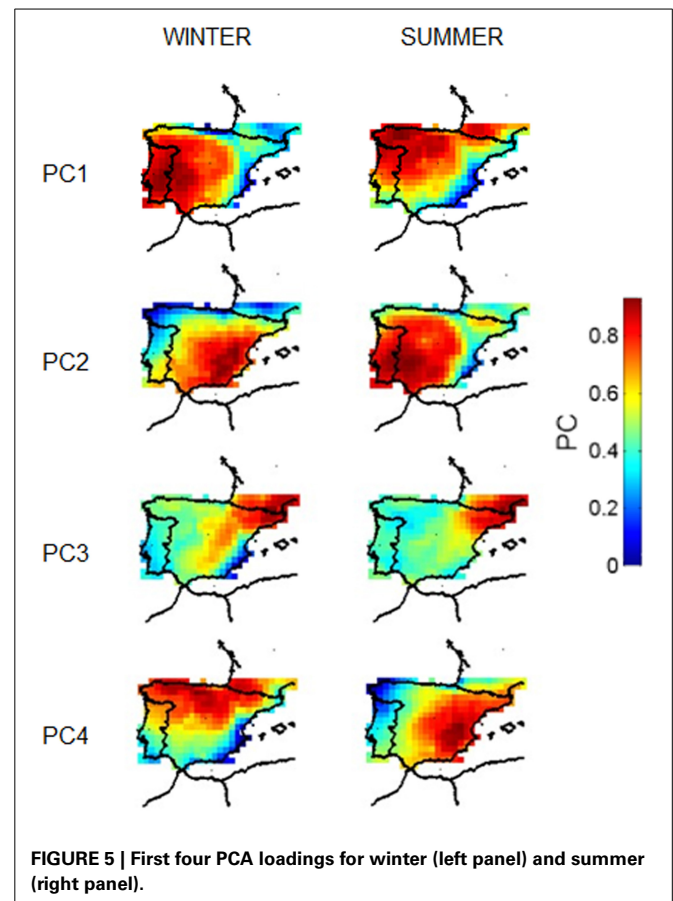
evolution of droughts in the southeastern quadrant, corresponding to the area between Spanish Central System mountain area and the Mediterranean coastland. Component 3 for both winter (10.1% of the EV) and summer (8.5% of the EV) represents the evolution in the northeastern quadrant, a transitional region between the Pyrenees mountain area and the Spanish Central System. Finally, component four for winter (3.8% of the EV) represents the temporal evolution in northern IP, whereas component 1 for summer (57.8% of the EV) reflects the evolution of SPEI in the northwestern quadrant, including the area from the Atlantic to the central Iberia and part of the Pyrenees mountains.

Results obtained suggest that the first and second components, both for summer and winter, are representative of drought evolution for a large spatial fraction of the Iberian Peninsula.

Figure 6 shows the evolution of the four components obtained from the PCA for winter (left panel) and summer (right panel). The winter PC1 does not present a significant trend. However, the temporal evolution of winter PC1, representative of SW Iberia, allows identifying the main drought events in the region, namely the 1975/76, 1981, and 1999 episodes. The summer PC1, representative of the Northwestern IP, shows a sharp and statistically significant decrease in SPEI values (Rho = −0.67, α < 0.05) starting at the beginning of the 1980s, and also allows identifying the 2005 intense drought. Although representative of different areas, component 2 shows marked negative trends in both winter

FIGURE 5 | First four PCA loadings for winter (left panel) and summer (right panel).

Table 2 | Results of principal component analysis for SPEI over Iberia (1950–2012).

Components	Winter		Summer	
	Explained variance (%)	Accumulated explained variance (%)	Explained variance (%)	Accumulated explained variance (%)
1	55.4	55.4	57.8	57.8
2	12.1	66.5	12.8	70.6
3	10.1	76.6	8.5	79.1
4	3.8	80.4	3.4	82.6
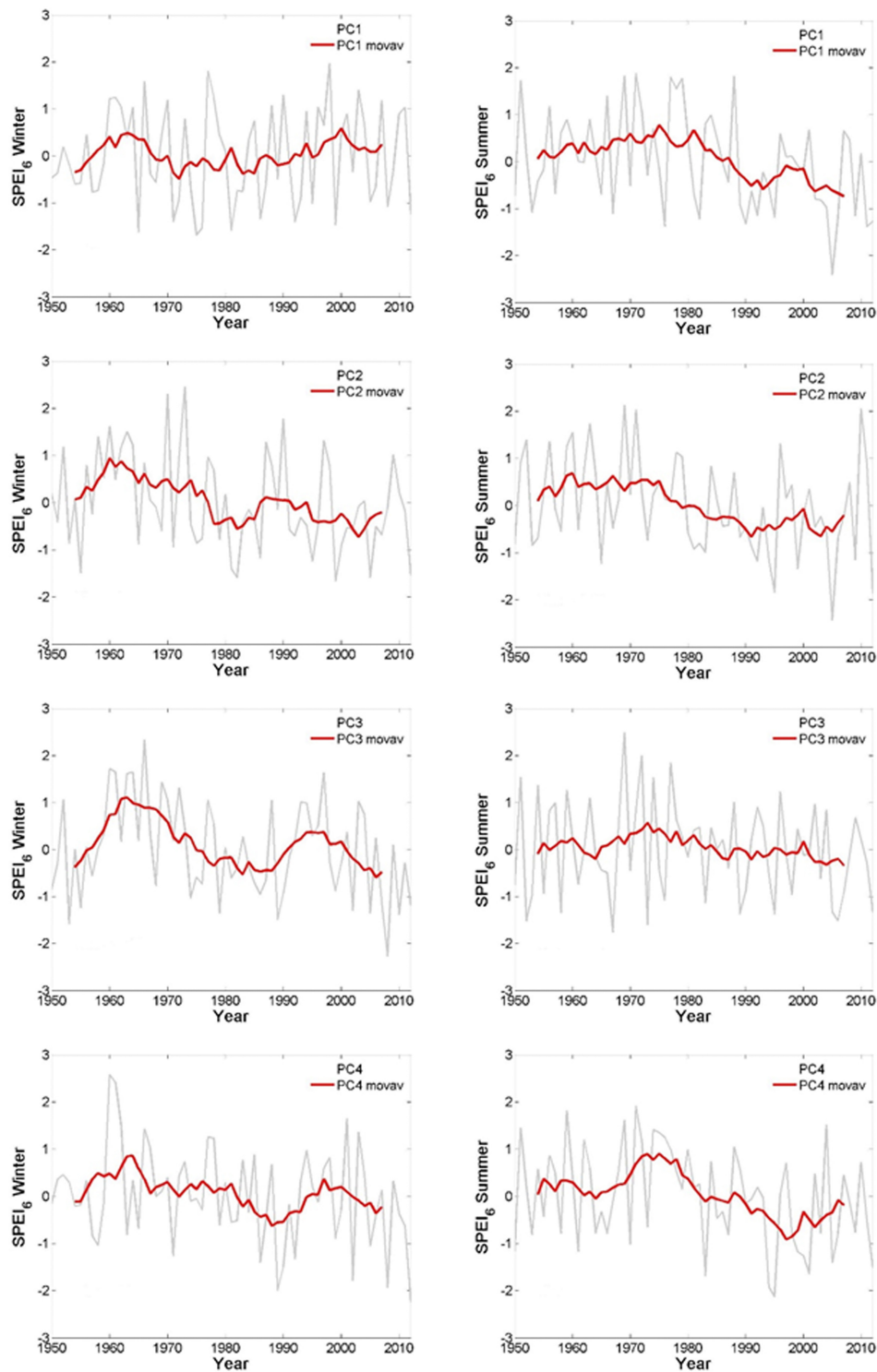
FIGURE 6 | Evolution of the first four principal components (PC1-PC4) in the winter (left panel) and in the summer (right panel). Red line indicates a moving average of 9 years for each PC.

(Rho = −0.76) and summer (Rho = −0.82) particularly noticeable between the 1970s until the 1990s. Component 3, representative of the Pyrenees area both for summer and winter, shows slightly smaller negative trends for winter (Rho = −0.47) and

summer (Rho = −0.53) which are nevertheless statistically significant (α < 0.05). Component 4 also shows negative trends for winter (Rho = −0.57) and summer (Rho = −0.71), both statistically significant (α < 0.05) caused by a sustained and progressive

decrease in the SPEI values since the decade of 1970s until the 1990s.

The negative SPEI trends account for an observed general increase in droughts which agrees with precipitation trends in other Mediterranean regions, namely in Spain (Vicente-Serrano and López-Moreno, 2006), Portugal (Trigo and DaCamara, 2000), and Italy (Brunetti et al., 2001; Ventura et al., 2002). Some studies in the Mediterranean region have shown a general negative trend in precipitation since the 1960s, which is related to the increase in the succession of dry years (Vicente-Serrano and López-Moreno, 2006; Sousa et al., 2011). Our results are in good agreement with the recent work of Vicente-Serrano et al. (2014); using data from ground meteorological stations in the IP to compute SPEI and SPI, the authors confirm that the drought severity has increased in the past five decades, as a consequence of greater atmospheric evaporative demand resulting from temperature rise. They also pointed that this drought severity increase is less intense in SW Iberia, namely in Lisbon, which is in good agreement with the strong negative trends obtained for all the principal components except for the winter PC1, that are representative of the SW sector.

Using cluster analysis, the 8 EOFs of SPEI were aggregated into six main homogeneous regions over the Iberian Peninsula (**Figure 7**): the northwestern region (RNW), the northeastern region (RNE), the central region (RC), the southwestern region (RSW), the southeastern region (RSE) and the eastern region (RE). This classification is especially useful since it summarizes the information on the regionalisation of drought behavior in the Iberian Peninsula and will be used to evaluate drought evolution on each of the determined areas. Results are in accordance with the ones obtained by other authors, using SPI 6 months (Vicente-Serrano, 2006).

FIGURE 7 | Six main homogeneous regions over Iberia.
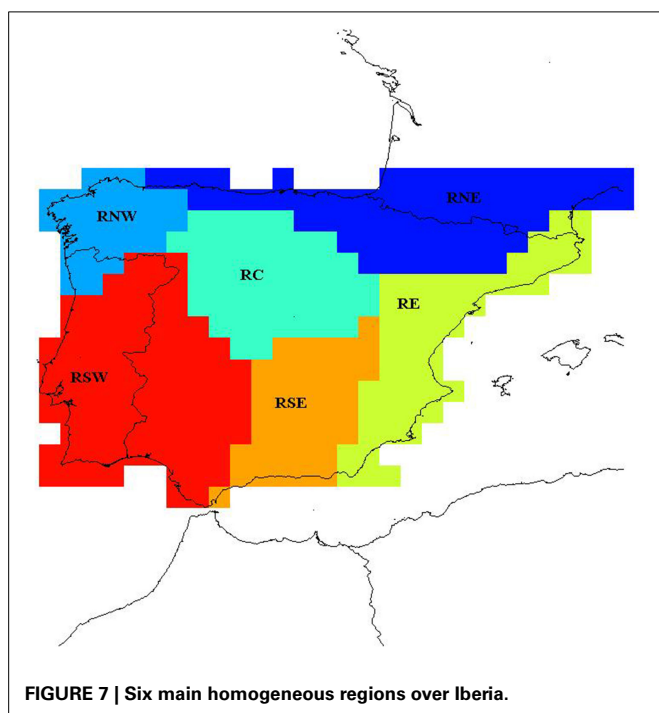
RELATIONSHIP BETWEEN THE CIRCULATION WEATHER TYPES AND DROUGHT—THE CIRCULATION-TO-ENVIRONMENTAL APPROACH

In this section the influence of weather-type frequency on drought spatial and temporal patterns is assessed. First, the correlation matrices between each CWT and the PCs were estimated for the Iberian Peninsula (**Tables 3, 4**). It should be noted that the proposed methodology only accounts for linear relationships although some of the relations could be non-linear. Thus, we acknowledge that some of the results presented in these tables should be considered within this context. Regions affected by droughts are characterized by negative values of SPEI and associated with lower (higher) than usual frequency of "wet" CWTs, such as C (A). Therefore, as expected, all PCs present negative and positive correlations with the frequency of A and C weather types, respectively. The frequency of east weather types (E, SE, NE) during winter shows negative correlations with all PCs except for SE vs. PC2. A similar behavior is found for summer, except for NE which presents very small positive values of correlation with PCs 1 to 4. In opposition, the frequency of west CWTs (W, SW, NW) shows positive correlations with all PCs in winter and with PC1 in summer. Overall, the winter season presents a larger number of statistically significant correlations (at the 5% level) than summer. The obtained results are consistent with the spatial fields of correlation between CWTs frequency and SPEI time series for each grid point (**Figure 8**). Negative correlations may be identified in a large part of the study area of SPEI with the winter frequencies of A, N and eastern weather types (E, SE, NE). Positive correlations are found in the case of winter frequencies of C and western weather types (W, SW, NW). Again, the winter fields present stronger correlations than those of summer and a reverse of signs in the spatial patterns is also conspicuous in some of the CWTs (N, NE, SW, and W) between the two seasons. However, it should be noted the low monthly frequency of some CWTs in summer, namely S, SW, and W.

The structure of some loadings presents similarities with the correlation pattern obtained between several CWTs and seasonal SPEI. In particular, the winter loadings for component 1 (**Figure 5**, top left panel) agrees with spatial impacts of the western types (W, NW, SW). The structure of the winter loadings for component 2 is similar to the correlation pattern between the frequency of the C weather type and the winter SPEI (**Figure 8A**). This behavior was also highlighted by Vicente-Serrano and López-Moreno (2006) for central Spain. Regarding the summer season, the structure of the summer component 1 (top **Figure 5**, right panel) agrees with spatial impacts of the N and NW types. The structure of the summer loadings for component 4 is consistent with the correlation pattern between the frequency of the C weather type and the summer SPEI.

The information above is complemented by the regionalised information on **Tables 5, 6** where the median and interquartile values of significant correlation values ($\alpha < 0.05$) between the CWT frequencies and the winter and summer SPEI for each region of the Iberian Peninsula (**Figure 7**) is presented. The interquartile measure is used to evaluate the range of correlation values within each region. Overall, these values present relatively low inter-regional variability with the exceptions of the cases of the NW type for the RNW area and for the W class for the RSW

Table 3 | Correlation between the winter weather-type frequency and the PC.

	A	C	NE	E	SE	S	SW	W	NW	N
PC1	**−0.40**	**0.33**	**−0.47**	**−0.39**	−0.12	0.19	**0.56**	**0.61**	0.21	−0.22
PC2	**−0.49**	**0.49**	−0.04	−0.01	0.05	0.07	0.13	0.04	0.13	−0.03
PC3	−0.29	**0.47**	−0.18	**−0.39**	−0.27	−0.06	0.06	0.25	**0.43**	0.21
PC4	−0.15	0.15	−0.26	**−0.52**	**−0.51**	−0.03	0.11	**0.58**	**0.60**	0.19

Bold values represent he correlations significant at 5% level.

Table 4 | As in Table 3, but for summer.

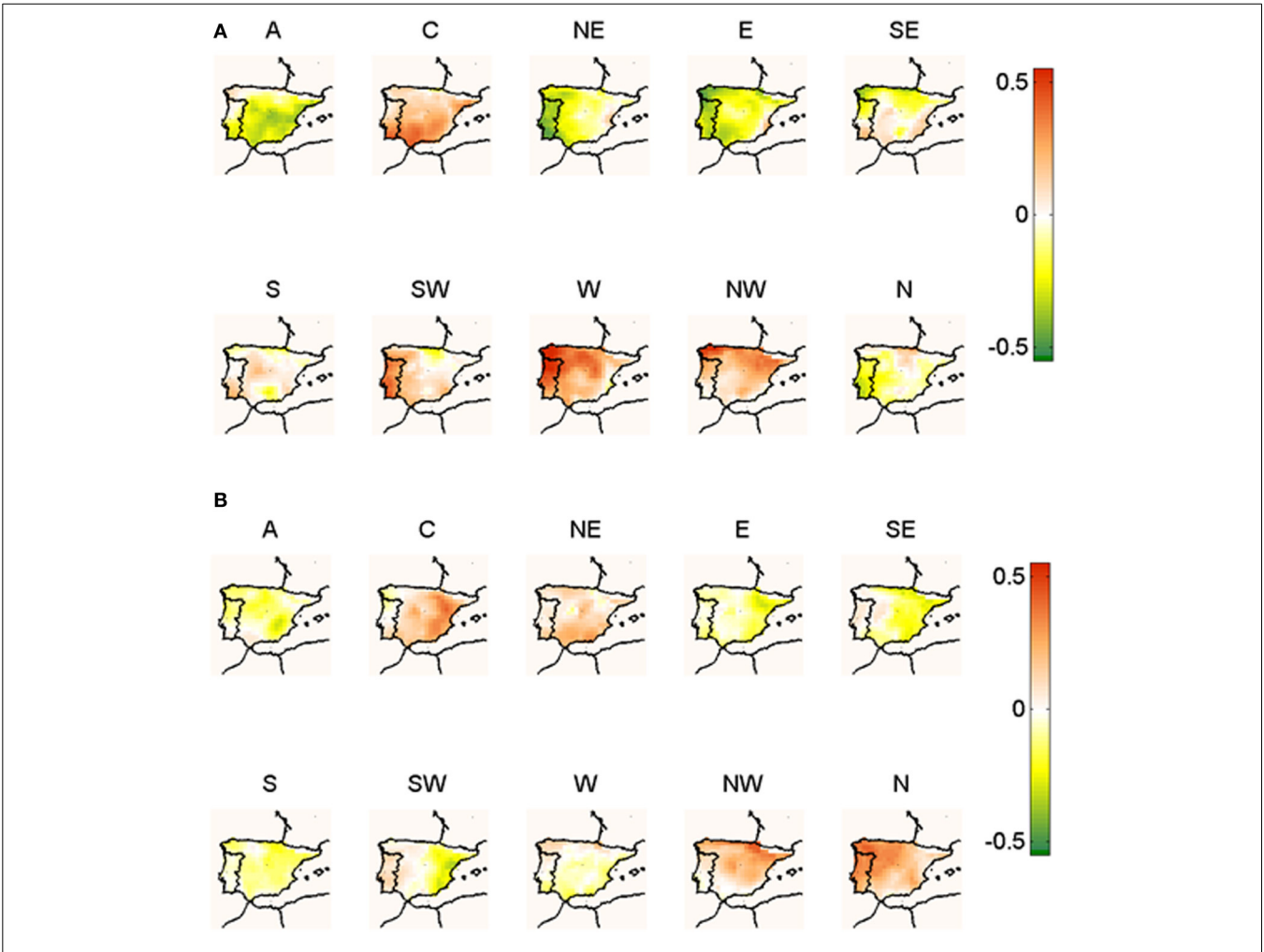|	A	C	NE	E	SE	S	SW	W	NW	N
PC1	−0.30	0.10	0.08	−0.29	**−0.35**	−0.17	0.04	0.26	**0.49**	0.19
PC2	−0.28	0.24	0.17	−0.12	−0.20	−0.06	0.01	−0.01	0.14	0.08
PC3	−0.07	0.25	0.11	−0.24	−0.31	−0.22	−0.13	−0.06	0.28	0.05
PC4	−0.29	**0.45**	0.23	−0.08	**−0.35**	−0.18	−0.24	−0.21	0.19	0.08

FIGURE 8 | Correlation between the (A) winter and (B) summer SPEI and the frequencies of each CWT. Significant correlations correspond to *R*-values higher than 0, 24 or lower than −0,24 (α < 0,05).

Table 5 | Median values of correlation between the weather-type frequency and the winter SPEI in the Iberian Peninsula (1950–2012).

	RNE	RNW	RC	RE	RSE	RSW
A	–	–	−0.31 (0.04)	−0.32 (0.07)	−0.32 (0.06)	−0.28 (0.04)
C	0.27 (0)	–	–	0.30 (0.03)	0.32 (0.06)	0.37 (0.07)
NE	–	−0.32 (0.06)	−0.30 (0.06)	–	−0.29 (0)	−0.35 (0.09)
E	−0.32 (0.06)	−0.41 (0.07)	−0.28 (0.02)	–	−0.28 (0.02)	−0.32 (0.05)
SE	−0.29 (0.10)	−0.31 (0.10)	−0.26 (0)	–	–	–
S	−0.27 (0.01)	–	–	–	–	–
SW	–	0.33 (0.08)	0.29 (0)	–	0.29 (0)	0.35 (0.11)
W	0.35 (0.05)	0.56 (0.10)	0.38 (0.05)	–	0.33 (0.05)	0.38 (0.17)
NW	0.35 (0.08)	0.42 (0.19)	0.31 (0.06)	0.34 (0.06)	0.25 (0.03)	0.27 (0)
N	0.31 (0.04)	–	–	–	–	–

The interquartile range of the correlation values are represented between brackets.

Table 6 | As in Table 5, but for summer.

	RNE	RNW	RC	RE	RSE	RSW
A	–	–	–	−0.27 (0.03)	−0.29 (0.03)	–
C	0.32 (0.05)	–	0.26 (0.04)	0.32 (0.07)	0.30 (0.04)	–
NE	–	–	–	0.30 (0.03)	0.27 (0.03)	0.26 (0.002)
E	−0.27 (0.02)	–	–	−0.27 (0.02)	–	–
SE	−0.28 (0.02)	–	–	−0.26 (0.02)	−0.26 (0)	–
S	–	–	–	–	–	–
SW	−0.25 (0)	–	–	−0.28 (0.03)	–	–
W	–	–	–	–	–	–
NW	0.35 (0.09)	0.27 (0.04)	0.27 (0.03)	0.28 (0.06)	–	–
N	0.29 (0.05)	0.37 (0.05)	0.32 (0.03)	0.26 (0.01)	0.26 (0)	0.32 (0.04)

area during winter. On the other hand **Tables 5**, **6** present relatively small values of interquartile range, thus ensuring a high level of consistency impact of each CWT on the SPEI field within each region. The exceptions to these are the RNW and RSW sectors that present higher average values of interquartile range during winter than the rest of Iberia.
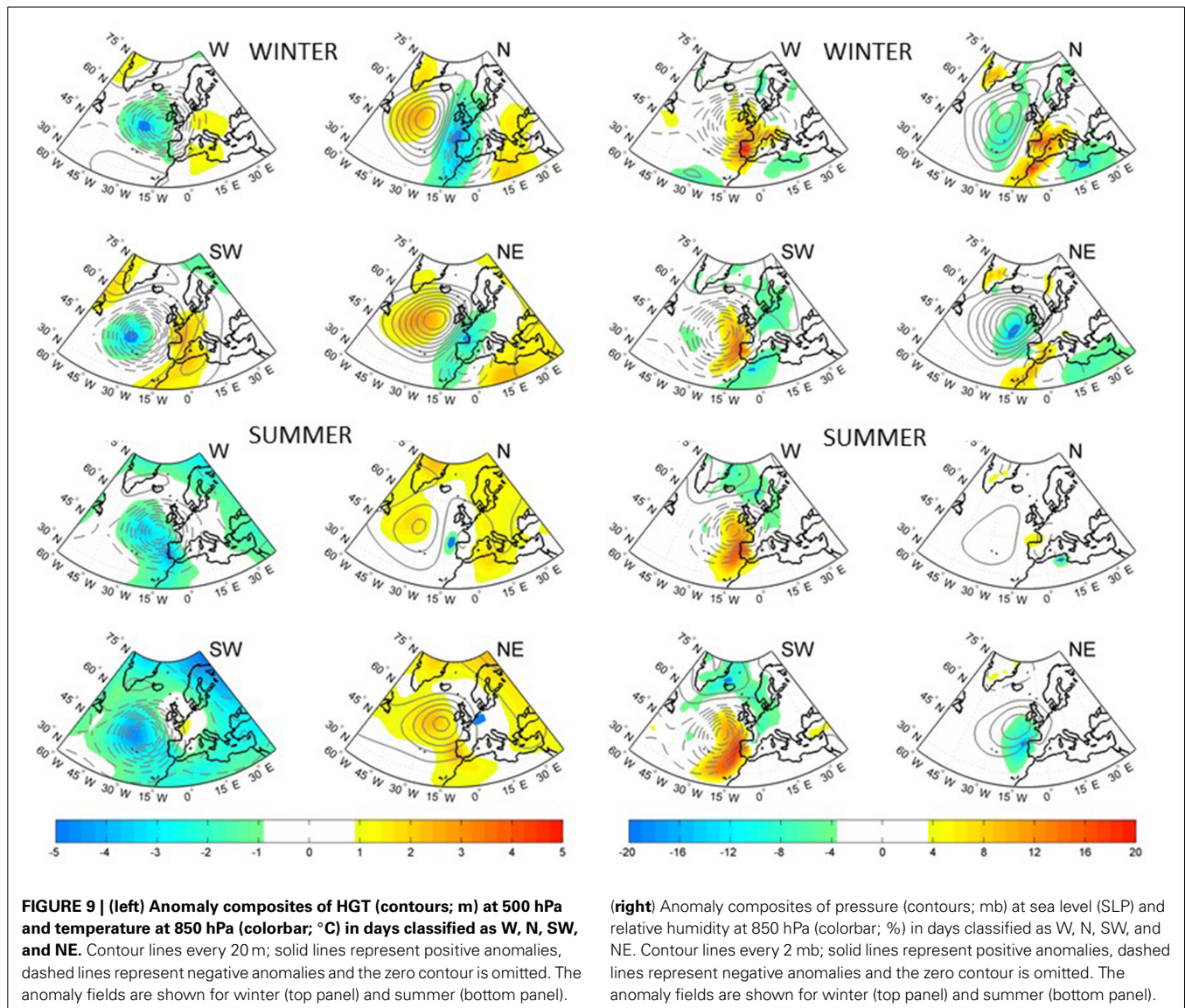
It should be noted that the above mentioned contrasting behavior of NE and W classes between winter and summer is also notorious at regional scale (**Figure 8**). The NE type, which presents statistically significant negative correlations with SPEI values, particularly for RNW, RC and RSW regions during winter (**Table 5**), has statistically significant positive correlations to SPEI values in RE and RSE regions during summer (**Table 6**). In opposition, the W type, which presents statistically significant positive correlations to SPEI values in all regions except for RE during winter (**Table 5**), has no statistically significant negative correlations to SPEI for any Iberian region during summer.

CWTs associated to drought conditions depend on both region and season (**Tables 5**, **6**). In the case of RNE, droughts in winter are associated to CWTs more (less) frequent than average of the lower right (upper left) quadrant, i.e., E, SE, and S (W, NW, and N) whereas in summer droughts are accompanied by a predominance of NW and C types. Winter droughts in RNW are related to higher (lower) than normal frequency of eastern (western) types, i.e., NE, E, and SE (SW, W, NW), whereas in RC they appear to

be related to more (less) frequent NE and A (W and NW) types. Summer droughts are linked to a higher frequency of the N type in both RNW and RC. Winter droughts in both RE and RSE are related to more (less) frequent A (NW and C) types, whereas those in RSW appear associated to higher (lower) than normal frequencies of E and NE (C, W, and SW) types. Finally, summer droughts are associated to lower than normal frequencies of C and NE types in the case of both RE and RSE, and of N type in the case of RSW.

In order to understand how distinct synoptic conditions may differently affect a specific given region, several meteorological fields are evaluated for several CWTs. Thus, **Figure 9** shows anomaly composites of HGT at 500 hPa and temperature at 850 hPa as well as anomaly composites of SLP and relative humidity at 850 hPa, both in days classified as W, N, SW, and NE, for winter and summer seasons. For the sake of simplicity results are only shown for the most relevant CWTs. The contrasting behavior between winter and summer seasons over Iberia is particularly evident (**Figure 9**, left panels) where the winter negative temperature anomalies associated with the N and NE CWTs disappear (N) or even become positive (NE) in summer. Likewise, the winter anomalies in the patterns of W and SW (positive) change to negative in summer. Since, in the case of the W and SW types, there is no inversion on the pattern depicting the relative humidity anomaly fields, these results suggest the overall importance of the

FIGURE 9 | (left) Anomaly composites of HGT (contours; m) at 500 hPa and temperature at 850 hPa (colorbar; °C) in days classified as W, N, SW, and NE. Contour lines every 20 m; solid lines represent positive anomalies, dashed lines represent negative anomalies and the zero contour is omitted. The anomaly fields are shown for winter (top panel) and summer (bottom panel).

(right) Anomaly composites of pressure (contours; mb) at sea level (SLP) and relative humidity at 850 hPa (colorbar; %) in days classified as W, N, SW, and NE. Contour lines every 2 mb; solid lines represent positive anomalies, dashed lines represent negative anomalies and the zero contour is omitted. The anomaly fields are shown for winter (top panel) and summer (bottom panel).

temperature. Winter drought events have been shown above to be associated to the occurrence of NE and N types and these are characterized by negative temperature anomalies and positive relative humidity anomalies (**Figure 9**, top panel). On the contrary, during summer these same CWTs are not associated to cold and wet anomalies, with anomalous fields either disappearing (N) or even reversing the signal (NE).

CONCLUSIONS AND FINAL REMARKS

Prevailing circulation patterns affecting the Iberian Peninsula were identified following the methodology proposed by Trigo and DaCamara (2000). The interannual variability of the 10 resulting CWTs was determined over the period 1950–2012 and the number of days for each CWT and season for the same period was accounted for. The impact of each CWT on drought regime was studied on a monthly basis between 1950 and 2012. During this period, the most frequent CWTs were found to be the anticyclonic (A), the cyclonic (C), the north (N) and the northeast (NE) types, accounting respectively for 30, 11, 9, and 12% of the days.

Drought is associated with synoptic circulation but also with many other factors that are not taken into account in this work. The influence of the atmospheric circulation on spatial and temporal patterns of winter and summer droughts in the Iberian Peninsula was analyzed by means of the SPEI, as obtained using the high resolution CRU TS3.21 gridded monthly data. The potential evapotranspiration was computed using the Hargreaves equation and the log-logistic probability distribution.

The trend analysis for winter season over the period between 1950 and 2012 shows a linear positive trend of CWTs associated with dry events, such as A, E, SE, and SW and a decrease of frequency of C and of the remaining weather types. On the other hand, only the A, E and NW weather types present statistically significant trends. During summer a clear decrease is observed for NE. The A and N weather types present low and non-significant trends and the remaining CWTs presents a clear increase.

The spatial variability of SPEI was analyzed using PCA and four PCs were selected for each season, explaining about 80% of the variance. The first PC, for both winter and summer, explains

more than half of the variability. With exception of the winter PC1, all the remaining components present a negative trend, with higher Rho values ($\alpha < 0.05$) for summer PC1, winter and summer PC2 and summer PC4. The temporal evolution of SPEI indicates a general negative trend, indicative of drier conditions between 1950 and 2012, which is in agreement with the evolution in the Iberian Peninsula and in other Mediterranean regions (Vicente-Serrano and López-Moreno, 2006).

On the other hand droughts show an important spatial and temporal variability within the study area, presenting six well-defined patterns corresponding to the northwestern (RNW), northeastern (RNE), central (RC), eastern (RE), southwestern (RSW) and southeastern (RSE) regions. The correlation between each CWT and the PCs were determined for the Iberian Peninsula showing an opposite behavior for A and C weather types for both seasons. The frequency of weather types with an eastern component during winter months shows negative correlations with all PCs, with exception of PC2. A similar behavior is found for summer months, except for NE. In opposition, the frequency of western CWTs shows positive correlations with PC1 and PC2 during summer and with all PCs during winter. As expected, the higher positive correlation values for PC1 are obtained with SW and W types for winter and for with SE and NW types in summer.

The spatial patterns of correlation between SPEI and CWT show negative correlations in a large part of the study area with the winter frequencies of A and eastern weather types (E, SE, NE), while the reverse occurs with the winter frequencies of C and western weather types (W, SW, NW). The spatial patterns of summer correlations present lower values for the majority of the CWTs, showing particular differences between SPEI and the NE and W influences during summer and winter. This feature is highlighted during the regional analysis of the relation between SPEI and CWTs. The NE type presents negative correlations with SPEI in RNW, RC and RSW regions during winter and positive correlations in RE, RSE, and RSW regions during summer. In contrast, the W type presents positive correlations with SPEI values in all regions (except RE) during winter and non-significant correlations during summer.

In general, the predominant CWT associated to winter or summer drought conditions differs greatly between regions. Over the majority of the areas the winter droughts are associated with high frequency of E types and low frequency of W types. RE and RSE present also a high frequency of A type during winter and a low frequency of C type. On the other hand the summer droughts of eastern regions (RNE, RE, RSE) are usually associated with low frequency of C type, while the western regions (RSW, RNW, RC) are associated with the N type. The NE type is also frequent in RE and RSE areas during winter.

REFERENCES

Barriopedro, D., Fisher, E., Luterbacher, J., Trigo, R. M., and García-Herrera, R. (2011). The hot summer of 2010: redrawing the temperature record map of Europe. *Science* 322, 220–224. doi: 10.1126/science.1201224

Bastos, A., Gouveia, C. M., Trigo, R. M., and Running, S. W. (2014). Analysing the spatio-temporal impacts of the 2003 and 2010 extreme heatwaves on plant productivity in Europe. *Biogeosciences* 11, 3421–3435. doi: 10.5194/bg-11-3421-2014

Beck, C., and Philipp, A. (2010). Evaluation and comparison of circulation type classifications for the European domain. *Phys. Chem. Earth* 35, 374–387. doi: 10.5194/bg-11-3421-2014

Brunetti, M., Mangueri, M., and Nanni, T. (2001). Changes in total precipitation, rainy days and extreme events in northeastern Italy. *Int. J. Climatol.* 21, 861–871. doi: 10.1002/joc.660

Cortesi, N., Gonzalez-Hidalgo, J. C., Trigo, R. M., and Ramos, A. M. (2013). Weather types and spatial variability of precipitation in the Iberian Peninsula. *Int. J. Climatol.* 34, 2661–2677. doi: 10.1002/joc.3866

De Luis, M., Raventós, J., González-Hidalgo, J. C., Sánchez, J. R., and Cortina, J. (2000). Spatial analysis of rainfall trends in the region of Valencia (East Spain). *Int. J. Climatol.* 20, 1451–1469. doi: 10.1002/1097-0088(200010)20:12<1451::AID-JOC547>3.0.CO;2-0

Delworth, T. L., and Zeng, F. (2014). Regional rainfall decline in Australia attributed to anthropogenic greenhouse gases and ozone levels. *Nat. Geosci.* 7, 583–587. doi: 10.1038/ngeo2201

Demuzere, M., Trigo, R. M., Vila-Guerau de Arellano, J., and van Lipzig, N. P. M. (2009). The impact of weather and atmospheric circulation on O3 and PM10 levels at a rural mid-latitude site. *Atmos. Chem. Phys.* 9, 2695–2714. doi: 10.5194/acp-9-2695-2009

Domínguez-Castro, F., Ramos, A. M., García-Herrera, R., and Trigo, R. M. (2014). Iberian extreme precipitation 1855/1856: an analysis from early instrumental observations and documentary sources. *Int. J. Climatolol.* 35, 142–153. doi: 10.1002/joc.3973

Fischer, E. M., and Schär, C. (2010). Consistent geographical patterns of changes in high-impact European heatwaves. *Nat. Geosci.* 3, 398–403. doi: 10.1038/ngeo866

Garcia-Herrera, R., Paredes, D., Trigo, R. M., Trigo, I. F., Hernández, H., Barriopedro, D., et al. (2007). The outstanding 2004-2005 drought in the Iberian Peninsula: associated atmospheric circulation. *J. Hidrometeorol.* 8, 483–498. doi: 10.1175/JHM578.1

Giorgi, F. (2006). Climate change hot-spots. *Geophys. Res. Lett.* 33:L08707. doi: 10.1029/2006GL025734

Giorgi, F., and Lionello, P. (2008). Climate change projections for the Mediterranean region. *Global Planet. Change* 63, 90–104. doi: 10.1016/j.gloplacha.2007.09.005

Gouveia, C., Trigo, R. M., and DaCamara, C. C. (2009). Drought and vegetation stress monitoring in Portugal using satellite data. *Nat. Hazards Earth Syst. Sci.* 9, 185–195. doi: 10.5194/nhess-9-185-2009

Grams, C. M., Binder, H., Pfahl, S., Piaget, N., and Wernli, H. (2014). Atmospheric processes triggering the central European floods in June 2013. *Nat. Hazards Earth Syst. Sci.* 14, 1691–1702. doi: 10.5194/nhess-14-1691-2014

Hargreaves, G. H., and Samani, Z. A. (1985). Reference crop evapotranspiration from temperature. *Appl. Engine Agric.* 1, 96–99. doi: 10.13031/2013.26773

Hoerling, M., Eischeid, J., Perlwitz, J., Quan, X., Zhang, T., and Pegion, P. (2012). On the increased frequency of Mediterranean drought. *J. Clim.* 25, 2146–2161. doi: 10.1175/JCLI-D-11-00296.1

Hov, Ø., Cubasch, U., Fischer, E., Höppe, P., Iversen, T., Gunnar Kvamstø, N., et al. (2013). *Extreme Weather Events in Europe: Preparing for Climate Change Adaptation.* Oslo: Norwegian Meteorological Institute.

Huth, R., Beck, C., Philipp, A., Demuzere, M., Ustrnul, Z., Cahynová, M., et al. (2008). Classifications of atmospheric circulation patterns: recent advances and applications. Trends and Directions in Climate Research: *Ann. N.Y. Acad. Sci.* 1146, 105–152. doi: 10.1196/annals.1446.019

IPCC. (2012). "Managing the risks of extreme events and disasters to advance climate change adaptation," in *A Special Report of Working Groups I and II of the Intergovernmental Panel on Climate Change*, eds C. B. Field, V. Barros, T. F. Stocker, D. Qin, D. J. Dokken, K. L. Ebi, et al. (Cambridge, UK; New York, NY, USA: Cambridge University Press), 582.

IPCC. (2014). *Climate Change 2014: Mitigation of Climate Change.* New York, NY: Cambridge University Press

Jenkinson, A. F., and Collison, F. P. (1977). *An Initial Climatology of Gales Over the North Sea.* London, UK: Synoptic Climatology Branch Memo. 62, Met Office.

Kistler, R., Collins, W., Saha, S., White, G., Woollen, J., Kalnay, E., et al. (2001). The NCEP–NCAR 50–year reanalysis: monthly means CD–ROM and

documentation. *Bull. Am. Meteorol. Soc.* 82, 247–267. doi: 10.1175/1520-0477(2001)082<0247:TNNYRM>2.3.CO;2

Lamb, H. (1972). British isles weather types and a register of daily sequence of circulation patterns. *Geophys. Mem.* 116, 1861–1971.

Lionello, P. (2012). *The Climate of the Mediterranean Region. From the Past to the Future.* London: Elsevier.

Lorenzo, M. N., Ramos, A. M., Taboada, J. J., and Gimeno, L. (2011). Changes in present and future circulation types frequency in northwest Iberian Peninsula. *PLoS ONE* 6:e16201. doi: 10.1371/journal.pone.0016201

Lorenzo, M. N., Taboada, J. J., and Gimeno, L. (2008). Links between circulation weather types and teleconnection patterns and their influence on precipitation patterns in Galicia (NW Spain). *Int. J. Climatol.* 28, 1493–1505. doi: 10.1002/joc.1646

Martínez-Villalta, J., López, B. C., Adel, N., Badiella, L., and Ninyerola, M. (2008). Twentieth century increase of Scots pine radial growth in NE Spain shows strong climate interactions. *Global Change Biol.* 14, 2868–2881. doi: 10.1111/j.1365-2486.2008.01685.x

McKee, T. B. N., Doesken, J., and Kleist, J. (1993). "The relationship of drought frecuency and duration to time scales," in *Eight Conference On Applied Climatology* ed *Nāo encontro em lado nenhum* (Anaheim, CA: Amer. Meteor. Soc.), 179–184.

Palmer, W. C. (1965). *Meteorological Drought.* Office of Climatology, US Weather Bureau Research Paper NO.45, Washington, DC.

Paredes, D., Trigo, R. M., García-Herrera, R., and Trigo, I. F. (2006). Understanding precipitation changes in iberia in early spring: weather typing and storm-tracking approaches. *J. Hydrometeor.* 7, 101–113. doi: 10.1175/JHM472.1

Pausas, J. G. (2004). Changes in fire and climate in the Eastern Iberian Peninsula (Mediterranean Basin). *Climate Change* 63, 337–350. doi: 10.1023/B:CLIM.0000018508.94901.9c

Pfahl, S. (2014). Characterising the relationship between weather extremes in Europe and synoptic circulation features. *Nat. Hazards Earth Syst. Sci.* 14, 1461–1475. doi: 10.5194/nhess-14-1461-2014

Philipp, A., Bartholy, J., Beck, C., Erpicum, M., Esteban, P., Huth, R., et al. (2010). COST733CAT – a database of weather and circulation type classifications. *Phys. Chem. Earth* 35, 360–373. doi: 10.1016/j.pce.2009.12.010

Ramos, A. M., Ramos, R., Sousa, P., Trigo, R. M., Janeira, M., and Prior, V. (2011). Cloud to ground lightning activity over Portugal and its association with Circulation Weather Types. *Atmos. Res.* 101, 84–101. doi: 10.1016/j.atmosres.2011.01.014

Russo, A., Trigo, R. M., Martins, H., and Mendes, M. T. (2014). NO2, PM10 and O3 urban concentrations and its association with circulation weather types in Portugal. *Atmos. Environ.* 89, 768–785. doi: 10.1016/j.atmosenv.2014.02.010

Sánchez, E., Gallardo, C., Gaertner, M. A., Arribas, A., and Castro, M. (2004). Future climate extreme events in the Mediterranean simulated by a regional climate model: a first approach. *Global Planet. Change* 44, 163–180. doi: 10.1016/j.gloplacha.2004.06.010

Santos, J. A., Corte-Real, J., and Leite, S. M. (2005). Weather regimes and their connection to the winter rainfall in Portugal. *Int. J. Climatol.* 25, 33–50. doi: 10.1002/joc.1101

Scaife, A. A., Spangehl, T., Fereday, D. R., Cubasch, U., Langematz, U., Akiyoshi, H., et al. (2012). Climate change and stratosphere–troposphere interaction. *Climate Dyn.* 38, 2089–2097. doi: 10.1007/s00382-011-1080-7

Schubert, S. D., Wang, H., Koster, R. D., Suarez, M. J., and Groisman, P. Y. (2014). Northern eurasian heat waves and droughts. *J. Climate* 27, 3169–3207. doi: 10.1175/JCLI-D-13-00360.1

Seneviratne, S. I., Lüthi, D., Litschi, M., and Schür, C. (2006). Land-atmosphere coupling and climate change in Europe. *Nature* 443, 205–209. doi: 10.1038/nature05095

Serrano, A., García, J. A., Mateos, V. L., Cancillo, M. L., and Garrido, J. (1999). Monthly modes of variation of precipitation over the Iberian Peninsula. *J. Climate* 12, 2894–2919. doi: 10.1175/1520-0442(1999)012<2894:MMOVOP>2.0.CO;2

Sousa, P., Trigo, R. M., Aizpurua, P., Nieto, R., Gimeno, L., and García-Herrera, R. (2011). Trends and extremes of drought indices throughout the 20th century in the Mediterranean. *Nat. Hazards Earth Syst. Sci.* 11, 33–51. doi: 10.5194/nhess-11-33-2011

Tomás, C., de Pablo, F., and Rivas Soriano, L. (2004). Circulation weather types and cloud to-ground flash density over the Iberian Peninsula. *Int. J. Climatol.* 24, 109–123. doi: 10.1002/joc.917

Trigo, R. M., Añel, J., Barriopedro, D., García-Herrera, R., Gimeno, L., Nieto, R., et al. (2013). The record Winter drought of 2011-12 in the Iberian Peninsula, in explaining extreme events of 2012 from a climate perspective. *Bull. Am. Meteorol. Soc.* 94, S41–S45.

Trigo, R. M., and DaCamara, C. C. (2000). Circulation weather types and their impact on the precipitation regime in Portugal. *Int. J. Climate* 20, 1559–1581. doi: 10.1002/joc.917

Ventura, F., Rossi, P., and Ardizzoni, E. (2002). Temperature and precipitation trends in Bologna (Italy) from 1952 to 1999. *Atmos. Res.* 61, 203–214. doi: 10.1016/S0169-8095(01)00135-1

Vicente-Serrano, S. M. (2006). Differences in spatial patterns of drought on different time scales: an analysis of the Iberian Peninsula. *Water Res. Manag.* 20, 37–60. doi: 10.1007/s11269-006-2974-8

Vicente-Serrano, S. M., Beguería, S., and López-Moreno, J. I. (2010a). A Multi-scalar drought index sensitive to global warming: the standardized precipitation evapotranspiration index – SPEI. *J. Climate* 23, 1696–1718. doi: 10.1175/2009JCLI2909.1

Vicente-Serrano, S. M., Beguería, S., López-Moreno, J. I., Angulo, M., and El Kenawy, A. (2010b). A new global 0.5° gridded dataset (1901-2006) of a multiscalar drought index: comparison with current drought index datasets based on the Palmer Drought Severity Index. *J. Hydrometeorol.* 11, 1033–1043. doi: 10.1175/2010JHM1224.1

Vicente-Serrano, S. M., and López-Moreno, J. I. (2006). The influence of atmospheric circulation at different spatial scales on winter drought variability through a semiarid climatic gradient in north east Spain. *Int. J. Climatol.* 26, 1427–1456. doi: 10.1002/joc.1387

Vicente-Serrano, S. M., Lopez-Moreno, J. I., Beguería, S., Lorenzo-Lacruz, J., Sanchez-Lorenzo, A., García-Ruiz, J. M., et al. (2014). Evidence of increasing drought severity caused by temperature rise in southern Europe. *Environ. Res. Lett.* 9:044001. doi: 10.1088/1748-9326/9/4/044001

Vicente-Serrano, S. M., López-Moreno, J. I., Drumond, A., Gimeno, L., Nieto, R., Morán-Tejeda, E., et al. (2011). Effects of warming processes on droughts and water resources in the NW Iberian Peninsula (1930-2006). *Climate Res.* 48, 203–212. doi: 10.3354/cr01002

Wells, N., Goddard, S., and Hayes, M. J. (2004). A self-calibrating palmer drought severity index. *J. Climate* 17, 2335–2351. doi: 10.1175/1520-0442(2004)017<2335:ASPDSI>2.0.CO;2

Wilks, D. (2006). *Statistical Methods in the Atmospheric Sciences. No. 59 in International Geophysics, 2nd Edn.* Burlington, MA: Academic Press.

Woodhouse, C. A., Meko, D. M., MacDonald, G. M., Stahle, D. W., and Cook, E. R. (2010). A 1,200-year perspective of 21st century drought in south-western North America. *Proc. Natl. Acad. Sci. U.S.A.* 107, 21283–21288. doi: 10.1073/pnas.0911197107

Xoplaki, E., Trigo, R., García-Herrera, R., Barriopedro, D., D'Andrea, F., Fisher, E. M., et al. (2012). "Large-scale atmospheric circulation driving extreme climate events in the mediterranean and its related impacts," in *The Climate of the Mediterranean Region: From the Past to the Future*, ed P. Lionello (London: Elsevier), 347–417. doi: 10.1016/B978-0-12-416042-2.00006-9

Yarnal, B. (1993). *Synoptic Climatology in Environmental Analysis: A Primer. Studies in Climatology Series.* London: Belhaven Press.

Conflict of Interest Statement: The authors declare that the research was conducted in the absence of any commercial or financial relationships that could be construed as a potential conflict of interest.

Multi-decadal classification of synoptic weather types, observed trends and links to rainfall characteristics over Saudi Arabia

Ahmed M. El Kenawy[1,2]*, Matthew F. McCabe[1], Georgiy L. Stenchikov[3] and Jerry Raj[3]

[1] Earth System Observations and Modeling Group, Water Desalination and Reuse Center, King Abdullah University of Science and Technology, Thuwal, Saudi Arabia
[2] Department of Geography, Mansoura University, Mansoura, Egypt
[3] Division of Physical Sciences and Engineering, King Abdullah University of Science and Technology, Thuwal, Saudi Arabia

An automated version of the Lamb weather type classification scheme was employed to characterize daily circulation conditions in Saudi Arabia from 1960 to 2005. Daily gridded fields of sea level pressure (SLP) from both the NCEP/NCAR and the European Center for Medium-Range Weather Forecast (ECMWF) reanalysis data (ERA40) were used as input data for this classification. The output catalog included 10 basic types, which describe the direction and vorticity of airflow in the region (i.e., cyclonic, anti-cyclonic, and directional). In general, our findings indicate that cyclonic (C) days represent the most frequent type among all days, with 69.2% of the annual count of days from 1960 to 2005, followed by SE directional flows (21%). It was also determined that airflows originating from the Indian Ocean (i.e., S, SE, and E) are more frequent than those from the Mediterranean and Red Seas (i.e., W, NW, and SW). The defined weather types were assessed for the presence of inter-annual and intra-annual trends using the Mann–Kendall tau statistic. The trend analysis suggests statistically significant changes in the frequencies of a majority of the weather types from 1960 to 2005. The relationship between the daily occurrence of rainfall and the frequency of individual weather types was also described using daily rainfall data from a network of 87 weather observatories. Results demonstrate that increasing frequencies of weather types connected to easterly inflows support higher precipitation amounts over the study domain. Characterizing the association between atmospheric circulation patterns and rainfall in Saudi Arabia is important for understanding potential impacts related to climate variability and also for developing circulation-based downscaling methods.

Keywords: weather types, directional flows, daily rainfall, circulation patterns, extremes, Saudi Arabia

INTRODUCTION

Atmospheric circulations play a critical role in the Earth's climate system and better understanding their links and interactions provides a capacity for assessing regional climate variability, improving characterization of land-atmosphere connections and facilitating new insights into potential impacts of climate changes. In recent years, there has been a growing interest in studying the influence of atmospheric circulations on the surface climate, with a view to enhancing our understanding of dynamic meteorological processes, such as extreme weather events (Vicente-Serrano and López-Moreno, 2006; de Vries et al., under review). A number of studies have sought to provide evidence on the relationships between atmospheric circulation and inter-annual climate fluctuations on different spatial scales, including hemispheric (e.g., Hurrell and Deser, 2009), continental (e.g., Clark and Brown, 2013; Hoy et al., 2014), regional (e.g., Park and Ahn, 2014), and sub-regional (e.g., López-Moreno and Vicente-Serrano, 2007). In addition, possible changes in the recurrence of linked climate variables can be obtained by projecting

changes in the probability of occurrence of atmospheric regimes (Goodess and Palutikof, 1998). Indeed, atmospheric circulations have steadily and increasingly been used for enhancing short-term forecasting of many meteorological variables. In downscaling studies, circulation characteristics can be used as predictors for regional and local climates (Goodess and Palutikof, 1998; Buchanan et al., 2002).

Atmospheric processes are likely to be reflected in the underlying weather types. For example, anti-cyclonic patterns are typically associated with dry conditions and clear skies. For this reason, efforts have been directed over the last few decades to develop schemes that categorize atmospheric circulations into distinct weather types (Huth et al., 2008). The aim of these approaches is to describe the local/regional pressure characteristics, so that each weather type provides a simple configuration of a variety of weather conditions. In this regard, although the results from weather type schemes can vary along prolonged time intervals and in regions with specific climate characteristics, possibly due to the pre-processing procedures such as selection of a "best"

classification scheme, similarity function and number of final types, many authors have found that describing climate variability by means of weather types is advantageous, compared to using circulation indices (e.g., Huth et al., 2008; Jacobeit et al., 2009). This might be because large-scale climate indices (e.g., NAO and ENSO indices) generally focus on just a few atmospheric modes (i.e., positive, neutral and negative), whereas circulation classifications can explain a larger range of climate behavior and variability, particularly at more regional scale.

Generally, weather type classification methods can be classified into two broad groups: statistically-based methods and automated methods. A detailed discussion of the advantages and disadvantages of both methods can be found in Frakes and Yarnal (1997). Overall, the first group relies on statistical techniques for classification, including among others, principal components analysis (Esteban et al., 2005), canonical correlation analysis (Xoplaki et al., 2003), and cluster analysis (Littmann, 2000). For example, Alpert et al. (2004) applied a discriminant-based analysis to classify synoptic conditions over the eastern Mediterranean using NCEP data for 1948–2000. Automated classification approaches, on the other hand, often employ existing circulation-type catalogs, such as the Lamb weather types (Lamb, 1972), the Muller classification (Muller, 1977), or the Grosswetterlagen catalog (Hess and Brezowsky, 1977). While statistically-based approaches may result in many classes and subgroups, weather patterns can be assigned to a specific number of types in automated classification schemes (Linderson, 2001; Goodess and Jones, 2002).

Saudi Arabia is defined as a "typical" arid region (BWh in the Köppen classification, 1936). Nonetheless, it can occasionally be subjected to severe weather phenomena (Deng et al., under review). While rainfall events are infrequent and occasional, intense storms can lead to severe flash-floods, with consequences on infrastructure, property and human settlements. Despite the obvious necessity of studying synoptic-scale atmospheric situations responsible for such events, the atmospheric configurations related to these are generally poorly explained. In contrast to many regions, the links between atmospheric circulation and precipitation in the Middle East and North Africa (including Saudi Arabia) have received minor attention, with regional studies mostly devoted to the Mediterranean countries of the region [e.g., Morocco (Lamb and Peppler, 1987), Turkey (Türkeş and Erlat, 2005), and Israel (Black, 2012) or the Mediterranean mountains (López-Moreno et al., 2011)]. One possible explanation for this deficit is the lack of a complete, reliable and homogenized dataset of rainfall, that also provides a reasonable spatial coverage. Those studies that have sought to describe the spatial patterns of climate in Saudi Arabia have generally relied on a very limited number of observatories of short duration (e.g., Ahmed, 1997; Abdullah and Almazroui, 1998; Rehman, 2010; Almazroui et al., 2012). Among these, Ahmed (1997) employed factor analysis to classify Saudi Arabia into distinct climate regions, using 14 climate variables from a spatially restricted data set. More recently, Almazroui et al. (2012) assessed the observed annual rainfall over Saudi Arabia from 1978 to 2009, using daily records from 27 observatories. In the same context, there have been limited attempts at classification of the main synoptic types over the region, which can be indirectly linked to

regional rainfall patterns. Earlier weather type classifications over the Middle East were restricted to the east Mediterranean (e.g., Alpert et al., 2004; Tsvieli and Zangvil, 2005).

Assessing the spatial and temporal characteristics of weather types in Saudi Arabia is important for two reasons. First, it can enhance our understanding of the possible influences of climate change and variability on atmospheric circulation at the local scale. For instance, as flood events in Saudi Arabia are associated with short duration extreme rainfall, classifying synoptic conditions on a daily basis can be beneficial to improve our understanding of these events and to interpret the physical processes behind them. Second, it is anticipated that large-scale weather patterns are likely to respond to climate changes, particularly in terms of changes in their frequency of occurrence and variability in space and time. As such, characterizing weather types may provide insights into the statistical association between the occurrence of specific weather regimes and rainfall response. This dependency is crucial when examining climate model simulations, as relationships developed via observation based data sets can be used in evaluation and subsequent forecasting of anticipated climate response.

The main objectives of this work are: (1) to categorize weather types in Saudi Arabia on a daily basis by means of an automated version of the Lamb weather types classification; and (2) to establish a connection between weather regimes and the occurrence of wet events in the region during rainy seasons (winter and spring). Apart from providing a description of hydro-climatological interactions in the region, this work represents the first attempt to classify multi-decadal circulation patterns in the region. Thus, this study may provide new insights into the main characteristics of weather types and their linkage with rainfall regimes in Saudi Arabia and the broader region.

STUDY AREA

Saudi Arabia is located in southwestern Asia between latitudes of 15°22′ N and 32°09′ N and longitudes of 34°50′ E and 55°50′ E. It has an area of approximately 2.25 million km^2 and occupies around 80% of the Arabian Peninsula. As shown in **Figure 1**, it is bounded by the Red Sea to the west, the Arab Sea in the south and the Arabian Gulf in the east. The altitude varies from 0 to over 3000 m. Rainfall in the region is characterized by high spatial and temporal variability, as revealed in **Figure 2**. In general, the annual average rainfall over the whole territory is approximately 114 mm/year. The rainy season extends from late October to April, with two peaks in late spring (March and April) and November. However, heating of the dry interior during the summer months may generate sufficient convection to develop cumulus cloud. In rare cases, the Red Sea Trough (RST) extends from East Africa through the Red Sea toward the eastern Mediterranean, allowing for the development of strong depressions over the central Red Sea, which may lead to heavy rainfall (de Vries et al., under review). Spatially, rainfall occurs more often in the southwestern regions, as orographic uplift significantly enhances rainfall on the windward sides of mountain ranges (Najd plateau and Sarawat mountains) along the Red Sea coast (**Figure 2B**). The southeastern region (namely the Rub al Khali, or empty quarter) shows the lowest annual rainfall totals, with almost no precipitation throughout the year.
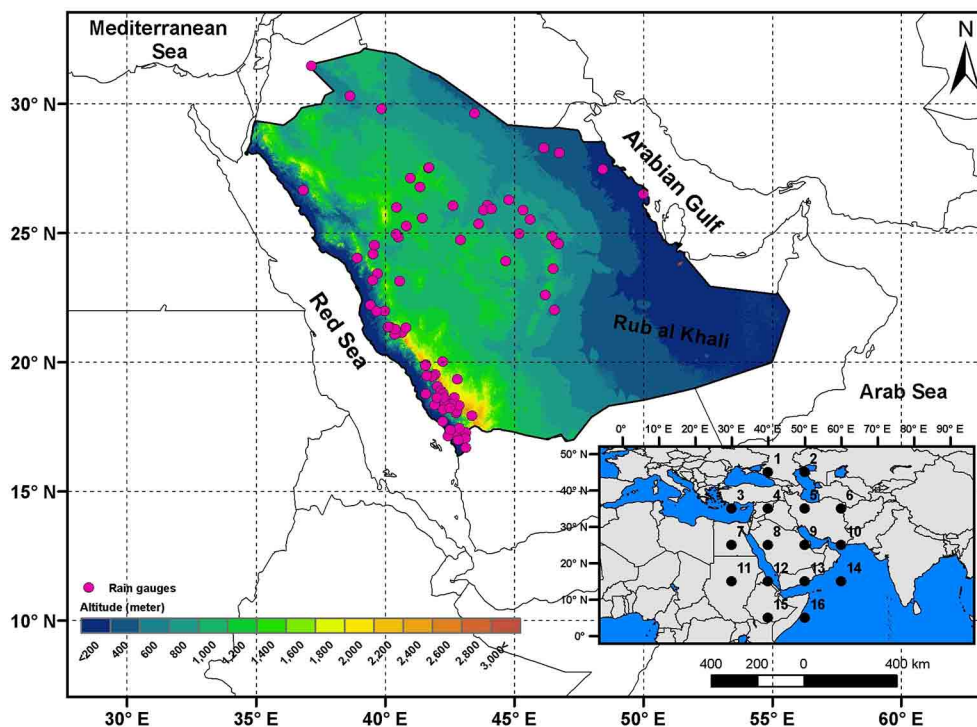
FIGURE 1 | Location of the study domain and the spatial distribution of the meteorological stations together with the 16 grid points (1–16) used in the automated circulation-typing.
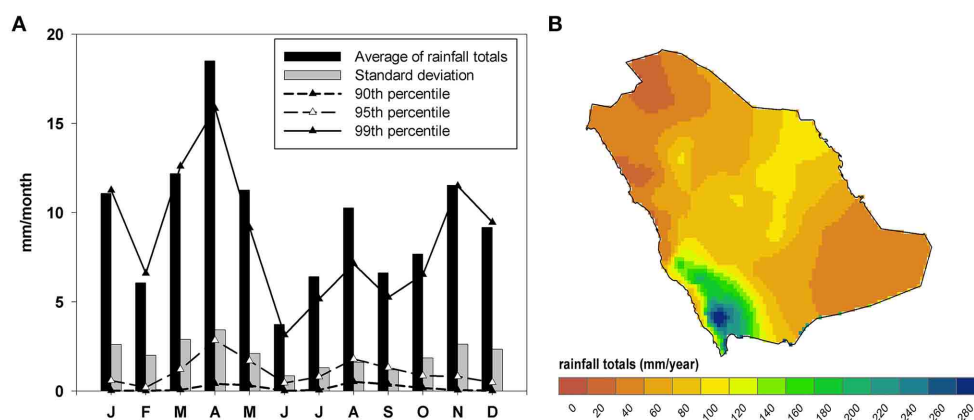
FIGURE 2 | (A) Monthly accumulated rainfall for Saudi Arabia (black bars) and the corresponding standard deviation (gray bar), compared to a set of percentiles (90th, 95th, and 99th) calculated for the 1960–2005 period. Panel **(B)** shows the spatial distribution of the annual rainfall totals (mm) averaged from 1960 to 2005.

In addition to the influence of topography and local convective activity, rainfall regimes are impacted by the location and intensity of large-scale circulations. In particular, the region lies between two important features of the global general circulation: the band of subtropical configurations to the south, and the mid-latitudinal regimes to the north. The subtropical depressions, associated with a complexity of interactions of warm and cold fronts, sometimes shift to the Red Sea, bringing heavy rain to the region. Other configurations (e.g., the Azores High, the Siberian low and the monsoon) may

also have indirect influence on the regional climate in Saudi Arabia.

DATA AND METHODOLOGY
GRIDDED SLP DATA SETS
Here we define the daily synoptic weather types for Saudi Arabia according to the Lamb classification (see Section Circulation-Type Catalog). Weather types following this method are generally obtained using daily gridded data of mean sea level pressure (SLP) rather than air pressure at upper levels (see for example

Goodess and Palutikof, 1998; Trigo and DaCamara, 2000; Vicente-Serrano and López-Moreno, 2006). Pressure data at the surface level are favored because the characteristics of precipitation are generally best described using circulation at the surface or lower levels of pressure (e.g., 850 hPa) (Conway and Jones, 1998; Post et al., 2002). In addition, surface pressure often produces a smaller range of synoptic conditions compared with upper pressure levels (McKendry et al., 2006). To generate the weather types catalog, we use daily SLP data from 16 points derived from the National Center for Environmental Prediction and the National Center for Atmospheric Research (NCEP/NCAR) reanalysis product (http://www.cdc.noaa.gov/cdc/data.ncep.reanalysis.html; Kalnay et al., 1996). The gridded daily SLP data are provided at a spatial resolution of 2.5° latitude × 2.5° longitude for the period 1960–2005. As illustrated in **Figure 1**, the 16 points are selected between 5°–45° N and 30°–60° E, so that the study domain is centered in the grid.

As there is limited access to station-based SLP data in the region, it is important to evaluate the reliability of the NCEP/NCAR SLP data. To accomplish this task, we assess the consistency of the defined weather types based on the NCEP/NCAR data set by comparing them against the European Center for Medium-Range Weather Forecast (ECMWF) reanalysis (ERA40) SLP data set. The ERA40 reanalysis data are supplied on a 1.5° by 1.5° latitude-longitude grid for the period 1960–2002 (Uppala et al., 2005). While some products (e.g., ERA-Interim) have a high spatial resolution (approximately 70 km), they only date back to 1979. Other products (e.g., UCAR ds010.0) present a relatively coarse spatial resolution (5° × 5°). For consistency, we therefore retrieve SLP data from 1960 to 2005 for a spatial domain consistent with the NCEP/NCAR data set.

CIRCULATION-TYPE CATALOG

The Lamb weather type catalog was initially developed for the British Isles using subjective methods (Lamb, 1972). To classify weather types in the study domain, we use the automated version of the Lamb classification following Jenkinson and Collinson (1977). This method is simple, straightforward and likely homogenous over time, regardless of the grid density (Demuzere et al., 2008). Thus, it has been used in several environments with varied climate regimes (e.g., Jones et al., 1993; Goodess and Palutikof, 1998; Trigo and DaCamara, 2000; Linderson, 2001; Vicente-Serrano and López-Moreno, 2006; Lorenzo et al., 2011; Ramos et al., 2011). This method has also been used as a tool for forecasting in a wide range of environmental studies, including analysis of air pollution (Hongisto and Joffre, 2005), ozone concentration (Tang et al., 2009), biometeorology (Laaidi, 2001), health risks (Rusticucci et al., 2002), wildfires (Papadopoulos et al., 2014), floods (Prudhomme and Genevier, 2011), droughts (Vicente-Serrano et al., 2011), and soil erosion (Ekström et al., 2002).

Using calculations of total shear vorticity (Z), the resultant flow strength (F), and direction (with an increment of 45°), the Lamb scheme can provide information on the direction (i.e., N, S, E, W, NE, NW, SE, and SW) and type (i.e., cyclonic, anticyclonic, hybrid) of surface flow. The southerly flow (SF), westerly flow (WF), total flow (F), southerly shear vorticity (ZS), and westerly shear vorticity (ZW) are computed from SLP data at the 16 grid points (P1–P16) shown in **Figure 1**, using the following expressions:

$$SF = 1.35\,[0.25\,(P5 + 2P9 + P13)$$
$$- 0.25\,(P4 + 2P8 + P12)] \quad (1)$$

$$WF = [0.5\,(P12 + P13)\ - 0.5\,(P4 + P5)] \quad (2)$$

$$ZS = 0.85\,[0.25\,(P6 + 2P10 + P14) - 0.25\,(P5 + 2P9 + P13)]$$
$$- 0.25(P4 + 2P8 + P12) + 0.25\,(P3 + 2P7 + P11)] \quad (3)$$

$$ZW = 1.12\,[0.5(P15 + P16) - 0.5\,(P8 + P9)]$$
$$- 0.91[0.5(P8 + P9) - 0.5(P1 + P2)] \quad (4)$$

$$F = (SF^2 + WF^2)^{0.5} \quad (5)$$

$$Z = ZS + ZW \quad (6)$$

As indicated, F is defined as the sum of the westerly component of the geostrophic wind, while Z is computed as the sum of the westerly shear vorticity. The rules described in **Table 1** are then employed to define the typical 26 weather types of the Lamb scheme [10 pure classes (A, C, NE, SE, NW, SW, E, W, N, S), eight cyclonic hybrids (CNE, CSE, CNW, CSW, CE, CW, CN, CS), and eight anti-cyclonic hybrids (ANE, ASE, ANW, ASW, AE, AW, AN, AS)]. The pure directional flow is computed using an eight-point compass, allowing 45° per each direction. Following Goodess (2000), the direction is computed by $\tan^{-1}$ (WF/SF), adding 180° if WF is positive. In this work, the classical 26 weather types are reduced to 10 by eliminating the hybrid types. Days with hybrid types are regrouped between either cyclonic (C) or anti-cyclonic (A) and their directional weather type (NE, SE, NW, SW, E, W, N, S) using a fractional weighting approach. For example, ANE is evenly distributed between A-type and NE-type, with 50% accounted to both. This occurs principally because the frequency of cyclonic and anti-cyclonic hybrid types is relatively small compared with pure synoptic (i.e., cyclonic/anti-cyclonic) or directional types. Numerous studies have aggregated Lamb's circulation types into fewer and more meaningful groups to facilitate inter-comparison (e.g., Trigo and DaCamara, 2000; Demuzere et al., 2008; Lorenzo et al., 2011). From a statistical

Table 1 | The 14 circulation types defined using total shear vorticity (Z) and resultant flow (F).

Description (acronym)	Calculation
Directional (N, NE, E, SE, S, SW, W, NW)	$|Z| < F$
Cyclonic (C)	$|Z| > 2F$, $Z > 0$
Anticyclonic (A)	$|Z| > 2F$, $Z < 0$
Unclassified cyclonic (UC)	$Z <$ mean annual Z, $F <$ mean annual F, $Z > 0$
Unclassified anti-cyclonic (UA)	$Z <$ mean annual Z, $F <$ mean annual F, $Z < 0$
Hybrid cyclonic (HYC)	$F < |Z| < 2F$ and $Z > 0$
Hybrid anti-cyclonic (HYA)	$F < |Z| < 2F$ and $Z < 0$

point of view, a smaller number of weather types ensure a reasonable sample size for each type (Cortesi et al., 2013). To this end, the automated Lamb weather type method generates a daily circulation database (1960–2006) for 10 basic groups (eight directional and two synoptic).

TREND DETECTION AND SLP ANOMALY ANALYSIS

In order to indicate the presence or absence of significant long-term trends in weather types, changes in their frequencies of occurrence are assessed from 1960 to 2005 using the least-squares regression method. The statistical significance of changes is estimated using the non-parametric Mann–Kendall tau statistic at the 95% level (p-value < 0.05). This test is robust to outliers and does not assume any prior distribution of the series (Lanzante, 1996) and has therefore been widely used for analyzing the significance of trends in climate and hydrology studies (e.g., Zhang et al., 2005; Choi et al., 2009; Liu et al., 2013). In this work, trend assessment is undertaken separately for each season. Seasons are defined as winter (DJF), spring (MAM), summer (JJA), and autumn (SON).

Composite maps of mean SLP corresponding to each weather type are also computed for the period from 1960 to 2005. The aim is to explore whether SLP patterns corresponding to each weather type are physically distinct and whether they can produce the expected type and direction of surface flow over the study domain. Here, the daily SLP data are first re-calculated as the deviation between each grid cell and its long-term average (1960–2005). The anomalies are calculated for each month separately, so that the effect of seasonal variability in pressure is minimized while the pressure spatial patterns are retained.

LINKS BETWEEN WEATHER TYPES AND RAINFALL CHARACTERISTICS

To assess the link between weather types and rainfall characteristics in Saudi Arabia, we use a network of 87 daily rainfall observatories, provided by the Saudi Ministry of Water and Electricity (MWE) from 1960 to 2005. The network is considered the most reliable in Saudi Arabia as it was screened for redundancy and the presence of erroneous values and outliers. Thus, it provides the best in-situ based representation of the range of climate regimes experienced across the country (see spatial distribution in **Figure 1**). As a function of altitude, just over 50% of observatories are below 700 m and approximately 25% are above 1000 m. It should be noted that the observatories used in this study are selected from a denser database of 209 stations spanning the period from 1960 to 2013. The selection of these observatories is based on the completeness of the series, as only those stations with relatively few missing values (less than 10% of the entire length of the record) are used. Here, no attempts were made to infill gaps because the time series of rainfall network show low spatial dependence among nearby observatories, even over short distances.

In this research, the development of relationships between weather types and rainfall characteristics focuses not only on mean changes, but also on other important characteristics, such as intensity and frequency of wet events. The aim is to explore whether there are any specific weather types that contribute more (or less) to rainfall in the region. This is particularly important

in Saudi Arabia given the low rainfall totals in the region and the occasional nature of extreme events. Meteorological wet events are identified from the time series using two different indices. First, the most extreme rain-days (hereinafter RD99$_{perc}$) are computed using values with probability of occurrence of 1% or lower. The RD99$_{perc}$ is determined for each observatory independently over the period 1960–2005. For each observatory, we also use a fixed absolute rainfall threshold to define extreme wet events. Rainy events (hereinafter RD30$_{mm}$) are defined as those in which at least 30 mm of daily rainfall is recorded at any meteorological station.

It is inherently challenging to link rainfall amounts to the frequency of weather types in an arid region like Saudi Arabia. The relationship between weather patterns and rainfall characteristics cannot be assessed solely using the frequency of weather types. In Saudi Arabia, the number of rainy days is generally low, which makes it difficult to establish reliable statistics for rainfall characteristics (i.e., intensity and frequency) associated with each type. An alternative statistical approach is to assess the direction and strength of the rainfall-circulation relationship by comparing the frequency of weather types and rainy days with rainfall amount. More specifically, our approach relies on exploring the contribution of each weather type to rainfall totals as well as frequency of rainy days. In this respect, the contribution of a particular weather type to rainfall totals can be attributed to: (i) the proportion of rainy days, and/or (ii) the intensity of rainfall. To assess this association, we compute two indices following the procedure detailed by Goodess and Jones (2002). The first index compares the proportion of rainy days corresponding to each weather type to the proportion of all rainy days, at each observatory. The second index is defined as the ratio of the mean amount of rain that falls on days of a specific weather type to the mean amount of rainfall in all days. Both indices are calculated on a seasonal and annual basis.
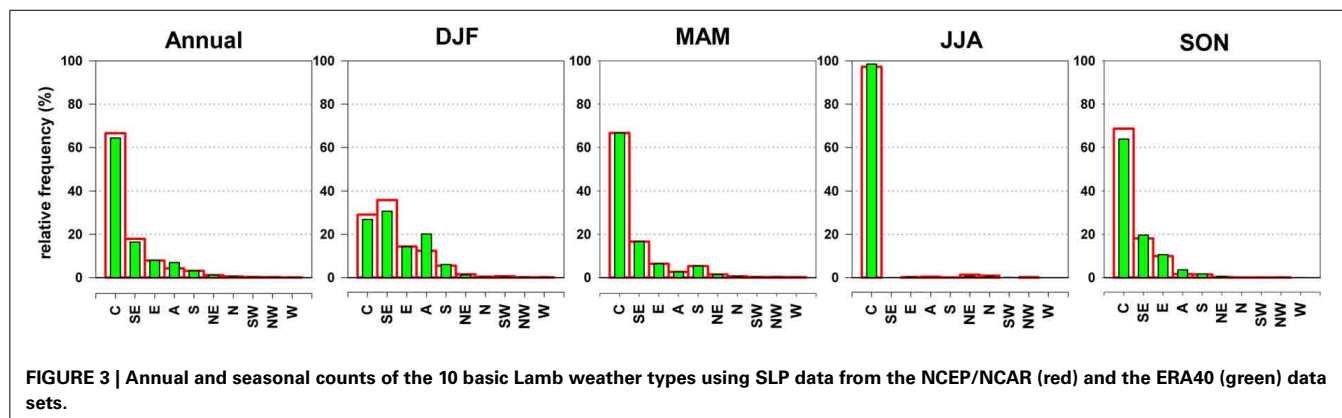
RESULTS AND DISCUSSION
REANALYSIS DERIVED PATTERNS IN WEATHER TYPES

Following the implementation of the Lamb weather type scheme, we calculated seasonal and annual totals for the 10 basic types using SLP from two independent sources (NCEP/NCAR and ERA40 data sets). The relative frequency of weather types obtained from both data sets annually and by season is given in **Figure 3**. A comparison between the defined weather types using the two data sets shows good correspondence. The frequencies of all types are consistent across both data sets and across all seasons. The relative occurrence of C-, SE-, E-, and A-types are well represented across all seasons in both data sets. While still consistent, the remaining weather types show a much lower frequency of occurrence throughout the study period. For example, there is agreement between the annual frequency of C-type in the NCEP/NCAR and ERA40 data sets (64.3% days per year in ERA40 and 66.5% in NCEP/NCAR). The high agreement is also seen for the frequency of C-type during the summer (98.4% summer days in ERA40 and 97.2% in NCEP/NCAR), highlighting the reliability and homogeneity of the NCEP/NCAR SLP data in the region for the considered period.

Figure 3 reveals that C-type is the most frequent at the annual scale, followed by SE- and E-types. Conversely, the occurrence

FIGURE 3 | Annual and seasonal counts of the 10 basic Lamb weather types using SLP data from the NCEP/NCAR (red) and the ERA40 (green) data sets.

of W, NW, and SW weather types is negligible for all periods throughout the year. This clearly suggests a stronger effect of the Indian Ocean wind component (E, SE, and S flows), compared with both the Mediterranean and Saharan influences (W and NW) and Asian continental airflows (N and NE). In winter, winds originating from the easterly quarter (NE, E, and SE) occur 51.6% of the time, followed by C (29%) and A-types (12.3%). In contrast, westerlies (NW, W, SW) show the least frequency during this season (0.7%). The presence of C-days during the winter can be associated with the intrusions of the Mediterranean cyclones, which occur frequently during this season. In winter, the central Mediterranean cyclones shift to the east. These depressions originally develop in the North Atlantic Ocean and the central Mediterranean and then move to the east, enhanced by the deepening upper level trough and the lee-low effect of the Cyprus mountains (Almazroui, 2006). Papadopoulos et al. (2013) indicated that the low pressure originating over both the east Mediterranean and equatorial Africa shifts during winter to be placed over the Red Sea. According to Cullen et al. (2002) and Kahya (2011), the winter cyclones over the Middle East region are significantly impacted not only by changes in the Atlantic westerly heat/moisture transport controlled by the NAO, but also by changes in sea surface temperatures (SSTs) between the Atlantic and the Mediterranean. In their study to assess the connections between atmospheric circulation and interannual variations of rainfall in Israel, Ziv et al. (2006) confirmed that the Cyprus low, a branch of the Mediterranean cyclones, is the main synoptic system affecting the eastern Mediterranean and parts of the Middle East during the winter.

C-type also has the greatest frequency of occurrence in spring, representing about two thirds (66.6%) of the days analyzed. Many studies regard the RST as the dominant circulation feature in the eastern Mediterranean and the Middle East during spring months (Ziv, 1994; Goldreich, 2003). Similar to the winter response, the circulation types driven by airflow with a westerly direction (W, NW, and SW) show lower frequency (0.1, 0.2, and 0.3%, respectively), than the eastern circulation types (SE:16.6%, E:6.3%, and NE:1.4%). A-type only occurs on about 2.6% of the spring days.

As depicted in **Figure 3**, the most obvious result during summer months is that the cyclonic (C) type has the greatest frequency of occurrence (97.2%), indicating that summer presents the least variations of weather types in Saudi Arabia. The relative

frequencies of SW, NW, and W days are almost zero between late May and September. The relative frequency of A-days is also minimized (0.35%). This finding agrees well with Zarrin et al. (2010) who noticed that the frequency of the anti-cyclone centers over the Arabian Peninsula during the summer is negligible at all levels, except for the 500 hPa. The dominance of C-days during the summertime can be explained by the frequent low pressures at surface level during this season (Almazroui, 2006). Similarly, Littmann (2000) found that the Arabian Low deepens to its maximum in early summer (June and July). A large number of the cyclones are thermal lows, resulting from the high thermal contrast between the hot air over land and the colder maritime air in adjacent seas. Some authors (e.g., Chen, 2005) considered the thermal lows that develop over the Arabian desert as a westward extension of the Indian Monsoon trough. This can be linked to the extension of the intensified Persian Gulf Trough to the west in the period from June to September (Maheras et al., 2001). Similar to other seasons, both cyclonic conditions and easterly flows (E and SE) prevail 96.7% of the time over autumn compared with 1.6 and 1.4% of the time under anti-cyclonic and SFs, respectively. Likewise, SW, W, and NW days present very low relative frequencies.

Figure 3 also shows that the seasons that contribute most to annual rainfall totals (i.e., winter and spring) are characterized by a greater variety of weather types. Indeed, winter is the only season that generally shows a more balanced frequency distribution of weather types. For example, 96.9% of days are allocated to five weather types (C, SE, E, A, and S) in winter. By contrast, the driest seasons (i.e., autumn and summer) exhibit fewer weather types. This clearly suggests that rainfall in both the dry and wet seasons is largely influenced by variations in the number of weather types dominating in each season.

The results demonstrate that the Lamb scheme does not allow for defining how the cyclones are formed (i.e., thermal/synoptic). Therefore, it is quite difficult to evaluate the ability of the Lamb scheme to distinguish between cyclones associated with convective processes, which are more likely to occur at a very localized scale, and synoptic cyclones that extend largely over space. One explanation of this failure is that the Lamb weather type assumes that each day is dominated by a single synoptic type across the whole domain. In a country like Saudi Arabia, with an area of 2.25 million km^2, a particular weather type may not characterize
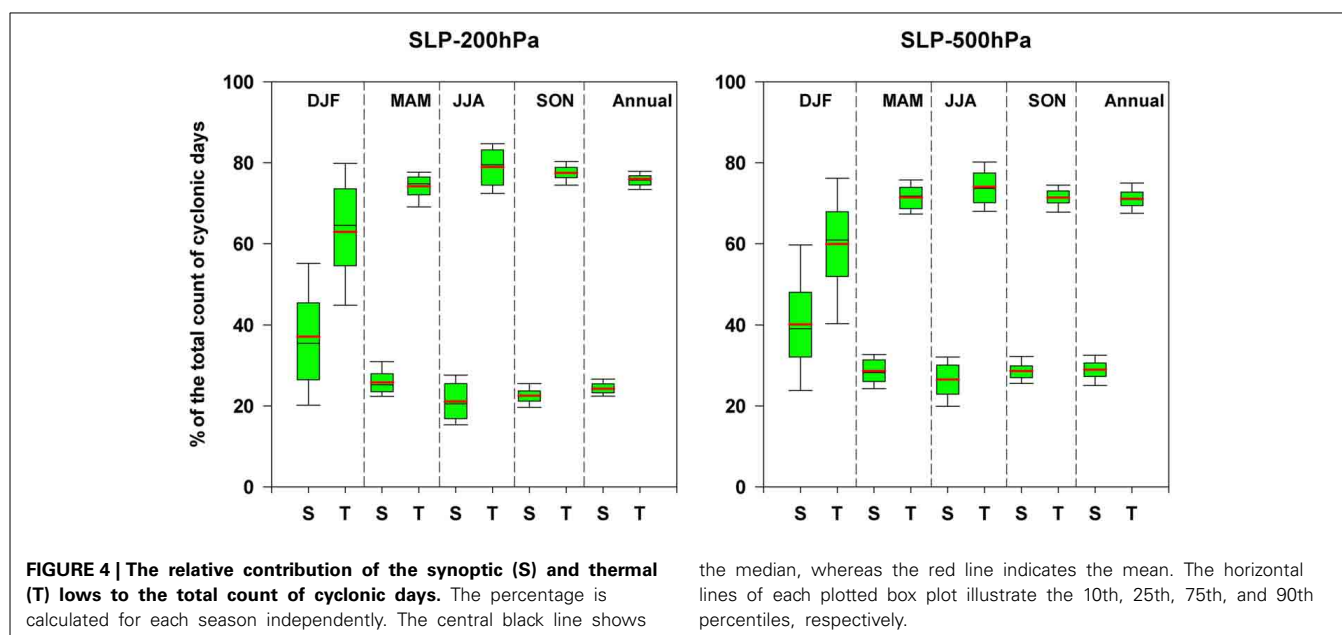
identical weather conditions on the same day across the whole country. For instance, while the northern and southern sides of the cyclone are devoted to the same weather type according to the Lamb classification, their weather conditions might be completely different. For this reason, these days cannot be easily attributed to a unique synoptic condition over the whole domain. Another reason is that the area of influence of thermal heating cyclones is usually small in terms of its size (i.e., very localized) compared with other synoptic patterns (e.g., anti-cyclones). Therefore, they are less well represented by the coarse resolution of the SLP gridpoint data. Previous works (e.g., Goodess, 2000; Martin-Vide, 2001) found that the coarse resolution of the NCEP/NCAR SLP data fails to capture more local scale atmospheric configurations. Unfortunately, the availability of data sets of pressure with fine spatial resolution is not limited to this region alone.

In an attempt to distinguish between thermal lows and cyclones originating from synoptic conditions, we incorporated pressure data at the surface level with data of geopotential fields at low (500 hPa) and mid (200 hPa) troposphere fields. The chosen height levels are proven to be among the best predictors of climate variability in many regions worldwide (Pozo-Vázquez et al., 2001; Xoplaki et al., 2003; Vicente-Serrano et al., 2011). The use of geopotential data at different heights can determine whether anomalous low pressure at the surface during cyclonic days are forced by similar or different modes of pressure at mid and shallow troposphere. In particular, synoptic cyclones are expected to be accompanied by a dominant low pressure anomaly, not only at the surface, but also at upper air levels. Meanwhile, thermal lows resulting from convective activity often occur at the surface level and at a very local scale. To accomplish this task, daily data of geopotential fields are obtained from the NCEP/NCAR reanalysis on a regular grid of 2.5° × 2.5° resolution. Here, we first computed the daily anomalies of pressure at each grid using the long-term means calculated for each month independently from 1960 to 2005. Afterwards, the rank of pressure anomaly on

each cyclonic day is obtained as a quantile, relative to all cyclonic days. For each cyclonic day, the quantile of pressure at the surface is then compared with that of the 200 and 500 hPa fields. When values are below the second quartile at the surface and above the second quartile at the height level, cyclonic condition on this day are assigned to thermal. In contrast, when values are below the second quartile at both surface and upper levels, the day is classified as synoptically cyclonic. **Figure 4** depicts the relative contribution of the thermal and synoptic lows to the overall count of cyclonic days for each season. It can be clearly seen that the thermal lows dominate in all seasons, relative to synoptic lows. For example, a comparison of pressure anomaly at the surface and 200 hPa level suggests that 78.9% of cyclones during the summer are originating from convective activity, whereas only 21.1% have a synoptic origin. However, recalling that cyclonic days show the maximum frequency in the study domain throughout the year, with greater occurrence in spring and summer, more information about the positions and tracks of the cyclones is still needed. Therefore, it is probably prudent to rely on more sophisticated approaches to include the pressure at upper levels, which can be a useful tool for grouping cyclonic days into sub-types of circulation. Such classification may represent better dynamic frontal depressions and thermal cyclones in the region, which the Lamb scheme fails to clearly identify.

Trend analysis in observed weather types

Both the direction and the magnitude of the trends in mean annual frequency of the 10 circulation types are illustrated in **Figure 5**. The trends were estimated using the least-squares linear regression method and their statistical significance assessed at the 95% level using the Mann–Kendal tau statistic. Over the 46-year assessment, the time series analysis shows positive changes in the frequency for the majority of weather types, with a negative trend observed only for C- and S-types. Given the existence of these significant trends, the analysis may imply that all weather types

FIGURE 4 | The relative contribution of the synoptic (S) and thermal (T) lows to the total count of cyclonic days. The percentage is calculated for each season independently. The central black line shows the median, whereas the red line indicates the mean. The horizontal lines of each plotted box plot illustrate the 10th, 25th, 75th, and 90th percentiles, respectively.

are being influenced by potential changes in the mean climate state, regardless of their relative frequency. The strongest change was found for C-type, with a decrease of −5.1 days per decade. The observed decrease in the yearly frequencies of C-days suggests a decrease in low pressure events in the region. As shown in **Figure 5**, it seems that C- and E-types show reverse annual trends relative to each other. This suggests that years of high frequency of C and S regimes correspond to low frequency of flows from the east.

Table 2 summarizes linear trends in the seasonal frequencies of weather types from 1960 to 2005. The largest changes tend to occur for those types with high frequency (e.g., C, SE, and E). In winter, A, E, NE, and SE days exhibited an increase in their frequencies, while C and S days show a downward trend. This

response is typically revealed in spring and autumn, with a greater increase in the frequency of A, E, NE, and SE-types relative to other types. **Table 2** also indicates that there is a tendency toward an increase in the frequencies of weather types associated with low-rainfall (e.g., A and N). In the case of A-days (blockings), an increasing trend of 0.75 days/decade was found during winter, compared with an increasing trend of 0.48 days/decade in spring. In contrast, the high-rainfall types (e.g., C) tend to decrease. Almazroui et al. (2012) found a statistically significant decrease (47.8 mm/decade) in the annual rainfall over Saudi Arabia from 1978 to 2009. It can therefore be implied that the dry periods in the last decades can be related to a weakening of the cyclonic conditions and intensification of the anti-cyclones. Vicente-Serrano and López-Moreno (2006) indicate that the synoptic conditions
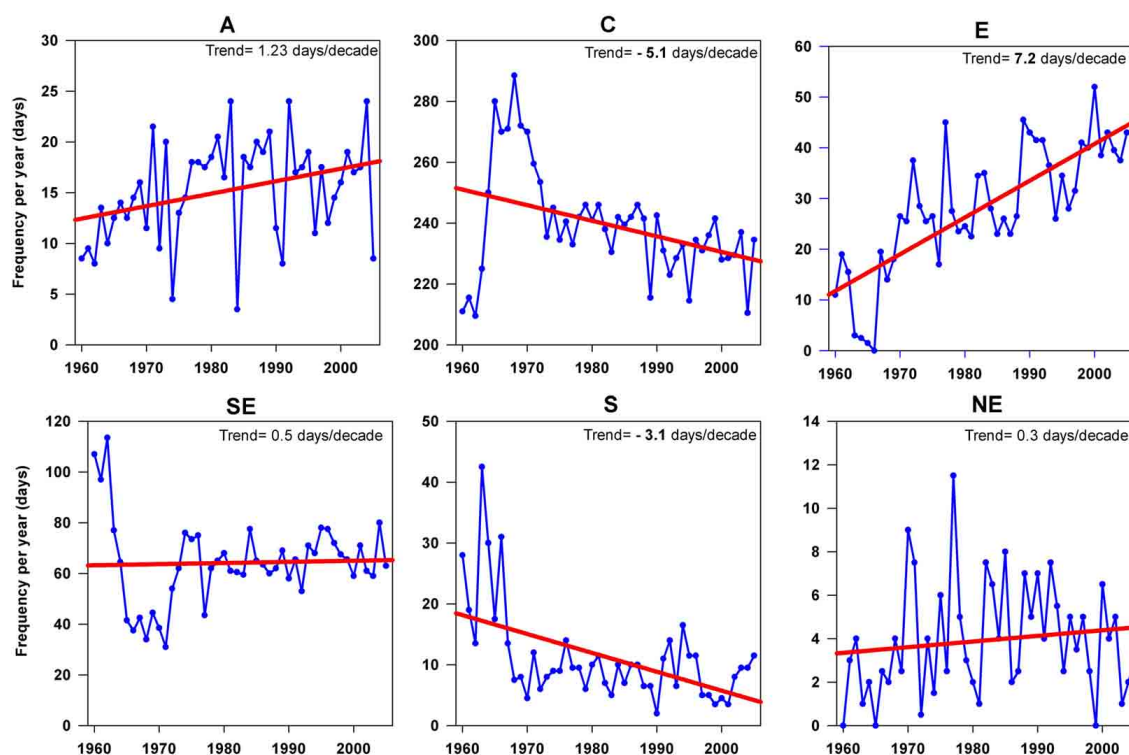
FIGURE 5 | Temporal evolution of the annual frequency of the defined weather types during the period 1960–2005. Magnitudes of trends given in bold are statistically significant at the 95% level.

Table 2 | Linear trends of the defined weather types using the SLP fields from the NCEP/NCAR reanalysis data.

	A	C	E	N	NE	NW	S	SE	SW	W
Winter (DJF)	0.75	−2.38**	3.05**	0.07**	0.20	−0.02**	−1.10**	0.59	−0.26**	−0.04**
Spring (MAM)	0.48	−1.59*	1.86**	0.02**	0.23	−0.11**	−1.45**	0.82	−0.16**	−0.08**
Summer (JJA)	0.04**	0.48	0.00	−0.22**	−0.15**	−0.11**	−0.04**	–	–	–
Autumn (SON)	0.12	−1.40**	2.33**	0.00	0.01**	−0.02**	−0.47**	−0.56	−0.02**	–

Trends were calculated for the period 1960–2005 and given in days per decade. The statistical significance was assessed at the 95% level using Mann–Kendall tau statistic.

*Significant at the 95% level.

**Significant at the 99% level.

that usually cause droughts correspond to the persistency of different anti-cyclonic configurations.

## QUALITATIVE ASSESSMENT OF LAMB SCHEME OUTPUTS USING SLP CONFIGURATIONS

Composites of the average SLP corresponding to each weather type for the 1960–2005 period are shown in **Figure 6**. The composite maps provide an indication on whether the circulation patterns support airflows from the direction defined by the Lamb classification in the previous section. They can also show whether SLP patterns associated with each weather type are distinct and physically meaningful, compared with other types. This is important because it determines whether each weather type is unique or whether it can be combined with other types with similar surface configurations when assessing the dependency between weather types and rainfall characteristics. A description of the SLP configurations associated with each weather pattern is provided, as follows:

- C-type configurations are characterized by two low-pressure centers, with the first developed over the Sahara to the west of the study area, while the second is placed over Southwest Asia and the Arabian Sea. Over the Arabian Peninsula, the mean frequency of the low pressure is enhanced by the frequent intrusions of the Persian Gulf Trough during the summer and the east Mediterranean cyclones during winter. The East European High is already established over continental Europe. This situation enhances moisture transfer from the tropical section of the Indian Ocean into the study domain, particularly in winter and spring.
- SE-type formations are characterized by a displacement of the cyclones to the north of the study domain. This situation is also accompanied by a negative mode of the NAO over the mid-latitudes and northern Atlantic and significant intrusions of the Siberian Anticyclone over mainland Asia. The spatial component of the SLP anomaly enhances advection of warm and humid air, accompanied by a cyclonal curvature of isobars over the study domain.
- E-type patterns are associated with the dominance of the anti-cyclonic system over central and eastern Europe, having a maximum intensity over the Black Sea. The East European High is established and extends southward toward the Balkan, eastern Mediterranean and large parts of North Africa and the Middle East. At the same time, the Azores High tends to be over the Western Mediterranean. Two well developed negative anomaly systems are positioned over the Indian Ocean and the Arabian Sea and large parts of Eurasia.
- A-type systems are characterized by the presence of a well-developed anti-cyclonic center over the Arabian Peninsula. The frequent high pressure at surface level, enhanced by the thermal heating, leads to a significant SLP gradient over the Arabian Peninsula. This synoptic condition is characterized by statically stable inversions with calm or weak winds. As illustrated in **Figure 6**, A-type over Saudi Arabia corresponds to a weakening of the Azores high (pressure) and a dominance of cyclones over Europe and the Mediterranean region.

- S-type circulations are generally associated with the formation of a cyclonic system placed over the eastern Mediterranean and western Asia. The anti-cyclones developed over the Arabian Sea are still weak. Therefore, the wind is generally weak, with a southerly component.
- NE-type systems are associated with a distinct west-to-east pressure gradient, with higher pressure throughout northern Africa and lower pressure over the southwest of Asia. The positive anomaly over north Africa is an extension of the subtropical high to the north, while the low pressure is an extension of the Indian Monsoon in the east. The boundary between the high-pressure and low-pressure anomalies lies over the Red Sea and allows for dry airflow originating over continental Asia.
- N-type flows are mainly enhanced by the absence of blocking activity over eastern Europe and western Asia. This configuration is governed by two pressure systems: the Siberian high and the eastern Mediterranean depressions. These air masses are typical for continental air masses, which are generally drier and not associated with rainfall, particularly from late autumn until the end of spring.

As illustrated in **Figure 6**, A- and N-types are associated with intensification of the negative NAO in the north and central Atlantic. In contrast, the E-type corresponds to the NAO positive mode, in which above-normal SLP anomalies are located over the British Isles and below-normal anomalies are positioned over the mid-latitudes of the Atlantic Ocean. SW-, NW-, and W-types show fairly similar SLP anomaly patterns, although the anomalies of W- and NW-types are somewhat smaller in their magnitude (hPa), which leads to a weak pressure gradient over North Africa and the Middle East. These patterns are generally characterized by an intensified extension of the Persian Gulf Trough to the eastern Mediterranean. Correspondingly, there is a clear absence of the Azores High anti-cyclonic.

Figure 6 indicates that when high-pressure systems reach their greatest intensity over the Arabian Peninsula (e.g., A and N), the synoptic conditions are likely favored for significant low rainfall throughout the country. Conversely, when the high pressure anomalies are much further north, as in the case of E-type, the easterlies tend to be displaced well to the south of the country. Easterly airflows are associated with advection of moist air from the Indian Ocean, which often produces rainfall. On the other hand, rainfall tends to be relatively higher when the depressions are displaced over the Arabian Peninsula. These depressions can originate from different sources, including the migration of the East Mediterranean depressions in winter (e.g., Cyprus low), the RST in spring, and the Persian Gulf Trough and local thermal heating in summer. However, the wind directions corresponding to a cyclonic synoptic condition and their influence on rainfall in the study area varies markedly, depending on the intensification of the cyclones, their position, as well as the position of the high pressure anomaly. By comparison, when the positive anomalies are centered east of the Arabian Sea and over equatorial sections of the Indian Ocean, the rainfall is likely to be much higher in the region. In such situations, maritime air masses move from the Indian Ocean toward the Persian Gulf coasts and the Arabian Peninsula. However, it should be emphasized here that no single
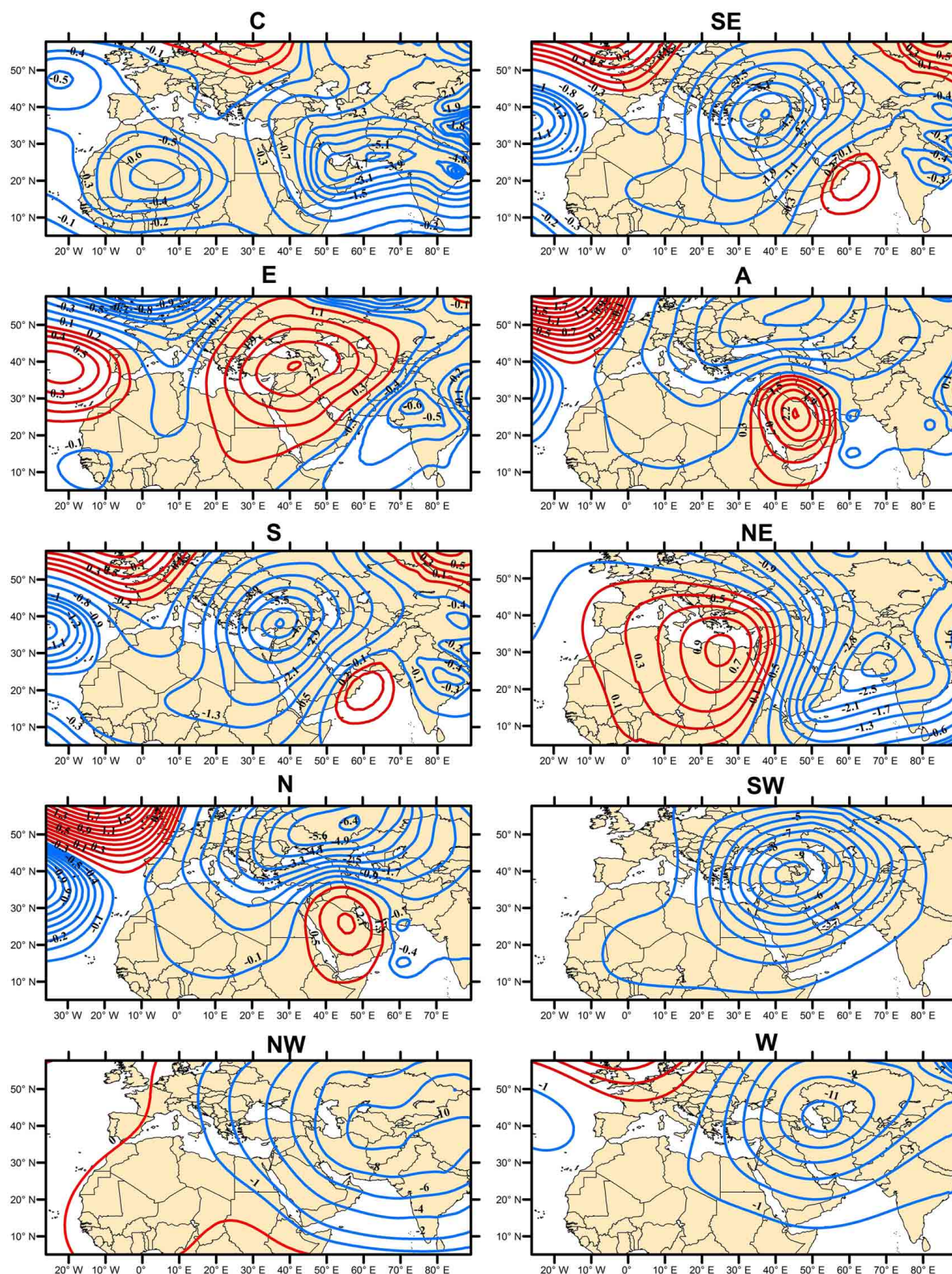
FIGURE 6 | Composite maps of anomaly SLP fields for the 10 weather types calculated for the 1960–2005 period. Positive (negative) anomalies are shown in red (blue). Daily anomalies were computed by subtracting the daily long-term mean (1960–2005) of SLP from the mean of all days corresponding to a particular type.

type can completely describe changes in rainfall characteristics in the region. This is simply because there are always some transitional cases, in which different configurations can interact with each other. Almazroui (2006) highlighted the role of the interaction between the RST and the southeastern flows on rainfall in the central Red Sea region.

For the majority of weather types, the composite maps of SLP are physically distinct, showing the expected type and direction of surface flow over the study area, as predicted by the Lamb classification scheme. For particular patterns (e.g., W and NW), the composite maps reveal similar underlying pressure patterns. They show very small differences in the positions of synoptic centers, although the frequencies of these patterns differ. However, even for those patterns, they are relatively distinct in the sense that their pressure gradients vary over space. For S-type, high pressures are almost in the same place as in SE cases, but with lower pressures, become established in eastern Europe. This finding implies that the results of the automated Lamb weather types in the study domain can be used to explore the association between defined weather types and rainfall in the region—the focus of the following section.

OBSERVATION BASED RELATIONSHIPS BETWEEN WEATHER TYPES AND RAINFALL

Local measurements from 87 observatories spanning the period from 1960 to 2005 were used to establish relationships between weather types and rainfall characteristics. **Figure 7** (left) shows the contribution of each weather type to the annual rainfall in the region. The aim here is to identify those types which contribute greater (or less) than average to the annual rainfall totals for each observatory. As illustrated, SE-, E-, S-, and NW-types favor above normal rainfall across Saudi Arabia. While SE-, E-, and S-type events occur quite frequently throughout the year, NW-types occur infrequently. Conversely, A, NE, SW, and W patterns are responsible for below-average rainfall. This implies that weather types can generally be grouped into "wetter" (C, SE, E, S, and NW) and "drier" (A, N, NE, SW, and W).

It should be emphasized that the results also suggest higher deviations for the patterns with the least frequency (e.g., S, SW, and NW) compared with those of the maximum frequency of

occurrence (e.g., C, SE, E, and A). This demonstrates that the influence of some weather types on the intensity of rainfall is very significant for some observatories, although these types rarely occur all year round. For example, the contribution to the annual rainfall from the rain-days classified as cyclonic is close to the annual rainfall totals of all rain-days for all observatories, with the greatest deviation of around $15.4 \pm 19.1\%$. By contrast, though being favored for below normal rainfall, the NE, SW, and W regimes account in some observatories for rainfall totals much greater than their annual totals in all rain-days (e.g., 109.8% of deviation from the average rainfall totals for W days). Here, it should be noted that the negative deviations found for some of the types responsible for above-normal rainfall (e.g., SE, E, and NW) may be linked to the influence of topography or distance to water bodies (e.g., the Red Sea, the Arabian Sea), which can modulate the influences of these airflows over space. For example, NW flow brings rain to the western portions of Saudi Arabia, but not to the far eastern and southeastern regions.

To distinguish between the influence of weather types on both average rainfall and extreme rain events, we looked for the contribution of each weather type to the frequency of extreme wet events. Here, we defined the extreme rainy day by using an absolute (30 mm) and percentile-based (99th) threshold. As shown in **Figure 7** (middle and right panels), C, SE, and E weather types contribute more to extreme wet events in Saudi Arabia throughout the year. C-type events contribute about 61.9 and 58.6% of the annual frequency of $RD99_{perc}$ (rainy days exceeding the 99th percentile of rainfall distribution) and $RD30_{mm}$ (days receiving 30 mm of rainfall or above), respectively. Approximately 30.0% of $RD99_{perc}$ and 31.6% of $RD30_{mm}$ events are associated with intensification of SE flows.

Several studies have sought to investigate the relationships between changes in precipitation and the frequency of different weather types in many regions. Trigo and DaCamara (2000) concluded that the decrease in the frequency of C-type contributed significantly to the decrease in precipitation during the second half of the 20th century in Portugal. In the eastern Mediterranean, Maheras et al. (2001) investigated the connection between precipitation and the frequency of cyclonic type over the last decades of the 20th century, concluding that high

FIGURE 7 | Box plots showing the ratio of the average of rainfall totals falling during days of each weather type and those falling in all rainy days (left). Also, the relative frequency (%) of $RD99_{perc}$ days (middle) and $RD30_{mm}$ days (right) corresponding to each weather type is plotted. All calculations were made using daily data from 87 observatories from 1960 to 2005. The black central line of each box denotes the median. Red line indicates identical changes (no differences) between the rainfall totals falling during days of a particular weather type and those of all rainy days.

precipitation was associated with intensification of cyclones. In contrast, the contribution from NE, N, SW, NW, and W weather types to the occurrence of both $RD99_{perc}$ and $RD30_{mm}$ is considerably lower than for other weather types. In this study, a quick comparison of the panels in **Figure 7** reveals the low number of extreme rain-days ($RD99_{perc}$ and $RD30_{mm}$) associated with N and NW days, although these types are denoted as favorable for higher than average rainfall. Taken together, this may suggest an increase in the contribution of moderate rainfall events to total rainfall during these types.

A comparison between changes in precipitation amounts and frequencies and changes in the frequency of synoptic types was also examined. The analysis was predominantly restricted to winter (DJF) and spring (MAM), as most rainfall falls within these two seasons (roughly 65% of the annual rainfall totals) in Saudi Arabia. As shown in **Figure 8** (upper panels), C, SE, and E regimes contribute to the vast majority of both rain-days and total amount of rainfall, with smaller contributions from N, NE, NW, SW, and W regimes. This offers some insight into the higher contribution of the Indian Ocean (i.e., SE, E, and S) to the annual fraction of

rainfall in the region. The frequency of wet events and changes in rainfall intensity in Saudi Arabia seems to be conditioned by the phase of the intra-seasonal oscillation over the Indian Ocean and the Arabian Sea. **Figure 8** also reveals that C-type contributes, on average, to 63.4% of the annual count of rain-days (>1 mm) and 61.8% of the annual rainfall sums.

Recalling that C-type represents roughly 65.6% of the days count per year, we may infer that it is the key circulation type influencing rainfall regimes in the region all year round. As illustrated in **Figure 8**, rainfall amounts corresponding to C-type are strongly correlated with the count of rainy days classified as cyclonic ($r = 0.96$). This clearly implies that rainfall amounts during these days show a regular distribution, with less intense wet events. Similarly, SE- and E-types are responsible for 28.5 and 10.5% of the count of rain-days, 29.2 and 10.9% of the total rainfall, but only 17.6 and 7.7% of days in the year, respectively. This indicates that SE and E days are more likely to be rainy within the year, relative to days with predominantly cyclonic conditions.

If we consider these relationships for the rainy seasons in **Figure 8** (middle and lower panels), we can see that the main
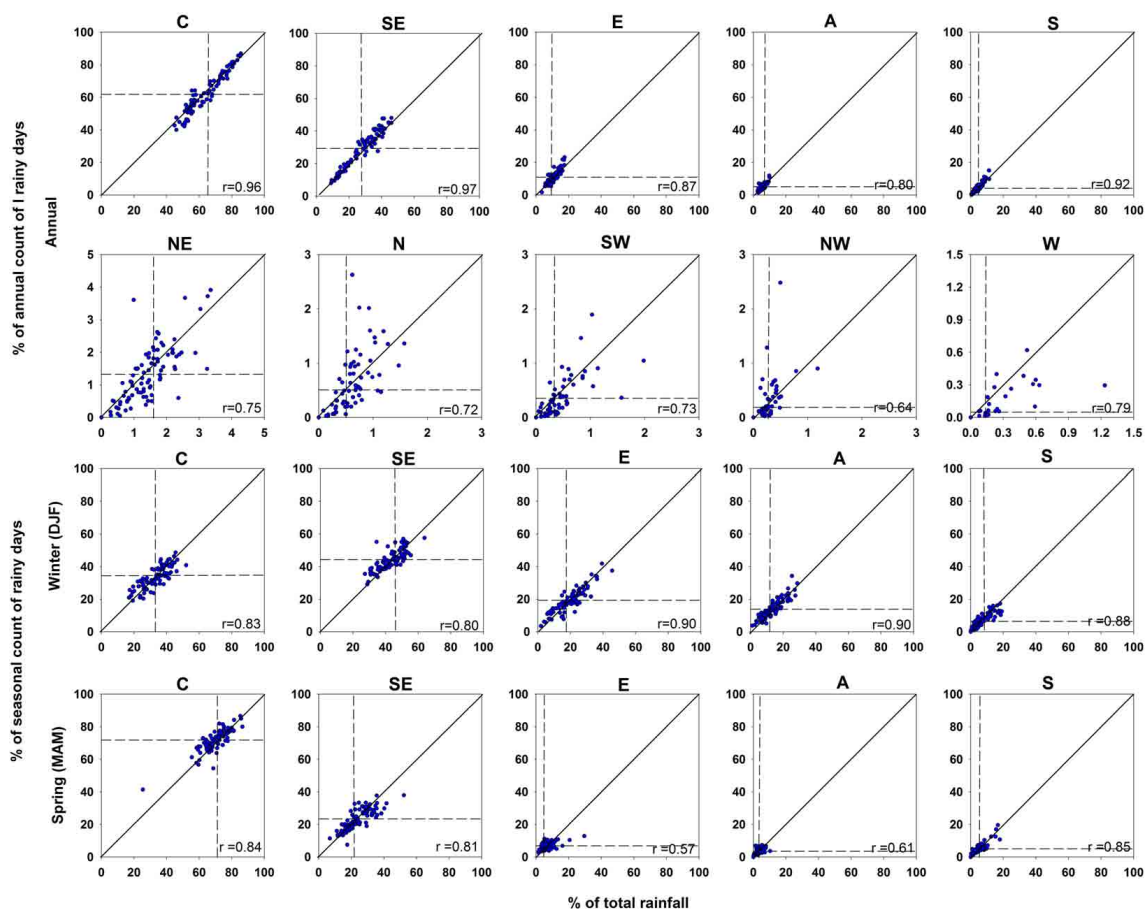
FIGURE 8 | Scatter plots between the ratio of total rainfall corresponding to each weather type and the total rainfall of all rain-days (>1 mm) for each observatory (X-axis) against the ratio of the count of rain-days corresponding to each weather type and the count of all **rain-days for each observatory (Y-axis).** Dashed lines indicate the mean. The X and Y axes were re-scaled for the NE, N, SW, NW, and W annual types to improve their readability. Relationships were calculated for the annual and rainy season (winter and spring) periods.

weather types follow a different distribution to that found on the annual scale. In winter, it seems that no single type can completely describe changes in rainfall characteristics in the region. The C-type explains 33.2% of the winter total amounts of rainfall, compared with 43.3% for SE-type. Similarly, 33.4 and 44.2% of the total rain-days during the winter months are associated with C- and SE-types, respectively. Remaining types (e.g., E, A, and S) also contribute to either the rainfall totals or the seasonal count of rain-days during this season. In winter, it seems that the most intense rainfall is associated with days experiencing southerly (S) flows. However, although these days represent only 2.4% of the winter days, they contribute to more than 8.3% of the total rainfall and 6.4% of the count of rain-days. In spring, the maximum contribution to the rainfall totals and the highest frequency of rain-days are primarily allocated to C-type. A lower proportion of the rainfall totals and the count of rain-days are contributed by E, A, and S patterns. On average, 70.1% of rainfall during the spring months are linked to cyclonic conditions, compared with 24.2% for the southeasterly flows.

As depicted in **Figure 8**, the high percentage of rainfall contribution from C and SE weather types during the winter and spring is mainly due to the high proportion of rain-days of these types. This can be revealed in the strong correlation between the percentage of rain-days and their contribution to the total rainfall. The Pearson coefficient was found to be 0.96 for C- and 0.97 for SE-types, while it varies from 0.80 (SE) to 0.83 (C) in winter and 0.81 (SE) to 0.84 (C) in spring. The association is weaker for other types (e.g., E and A in spring). This suggests that more rainy days may contribute to smaller amounts of rainfall and vice versa, a response that is evident in **Figure 9**. Pearson correlation coefficients calculated between circulation-type frequency during the spring and rainfall totals (mm) from 1960 to 2005 are negative for

A-type and positive for E-type. This implies that rainfall intensity tends to show higher variations among stations, compared with their differences in terms of the ratio of wet days to all considered days.

CONCLUSIONS

A comprehensive analysis of the seasonal characteristics of weather types in Saudi Arabia and their links with rainfall regimes has been performed. An attempt was made to apply an automated version of the Lamb weather type classification scheme in Saudi Arabia, which is a region influenced by the tropical and extratropical teleconnections of the northern Hemisphere. Using daily SLP data at 16 grid points, the direction and type of surface winds were computed from 1960 to 2005. The analysis revealed that the most common weather types in any part of the year are the cyclonic, southeastern, eastern, and anti-cyclonic types. Westerly, southerly and northerly flows were the least frequent. The results also demonstrate that the cyclones associated with thermal convectivity are significantly more frequent compared with the cyclones of synoptic origin. For the studied period, trend analysis of the defined weather types indicated a generally positive trend in the frequency of types associated with dry conditions (e.g., A, SE, and E) and a general negative trend in patterns favoring above-normal rainfall (e.g., C).

To provide an assessment of inter-annual variations of weather types and explore their association with wet events over Saudi Arabia, we employed daily rainfall totals (mm) from a network of observatories ($N = 87$). The synoptic patterns of SLP associated with the defined circulation in the region were identified and described over the period 1960–2005. The results indicate that weather types contributing to the highest fraction of winter (DJF) and spring (MAM) rainfall are C-type and also those with a predominant directional flow from the Indian Ocean (i.e., SE, E, and S).

The relationships described in this paper advance the understanding of the large-scale processes that contribute to the climate of Saudi Arabia and the results enhance our current understanding of pressure–rainfall dependency over the region. The results obtained by the Lamb weather type scheme may serve as a basis for informing the parameterization of climate models operating in the region, particularly on the seasonal scale. The relationships between atmospheric regimes and wet events may also be used for downscaling purposes, as they offer a potential for statistical description of the occurrence of extreme event in the region. Although rainfall changes in Saudi Arabia may be driven in part by changes in the circulation, observed changes in rainfall cannot be explained by changes in the circulation alone. The results of this work motivate future efforts to examine whether other synoptic classification techniques can be applied. Indeed, it might be informative to incorporate upper-air trough (e.g., 500 and 1000 hPa) in order to improve the prediction of rainfall in the region. In the same regard, although the spatial resolution of the NCEP/NCAR SLP data is satisfactory for downscaling purposes (as it is generally comparable with the spatial interval of GCMs), an improvement in the SLP grid resolution might be more appropriate for capturing important mesoscale or convective processes in the region.
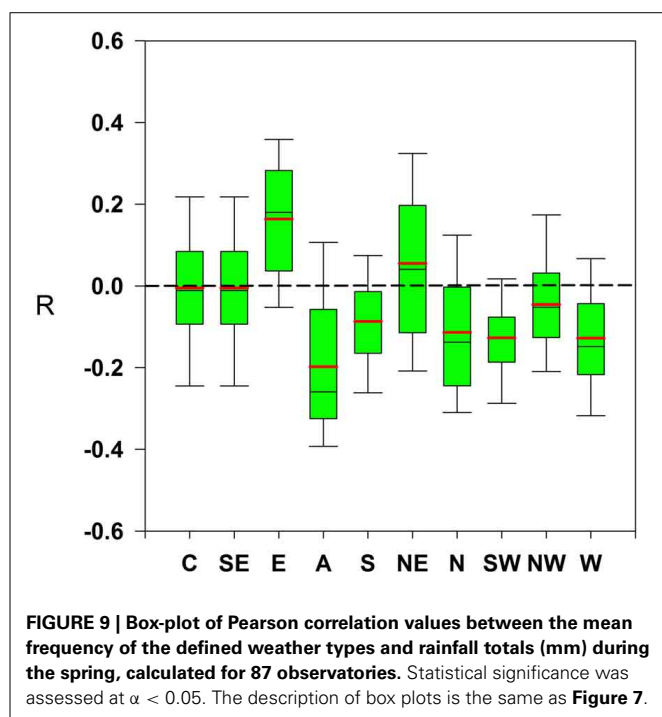
FIGURE 9 | Box-plot of Pearson correlation values between the mean frequency of the defined weather types and rainfall totals (mm) during the spring, calculated for 87 observatories. Statistical significance was assessed at $\alpha < 0.05$. The description of box plots is the same as **Figure 7**.

REFERENCES

Abdullah, M. A., and Almazroui, M. (1998). Climatological study of the southwestern region of Saudi Arabia. I. Rainfall analysis. *Climate Res.* 9, 213–223.

Ahmed, B. Y. M. (1997). Climatic classification of Saudi Arabia: an application of factor-cluster analysis. *GeoJournal* 41, 69–84.

Almazroui, M. (2006). *The Relationships Between Atmospheric Circulation Patterns and Surface Climatic Elements in Saudi Arabia.* Unpublished Ph.D. thesis, Climate Research Unit, University of East Angelia, 433.

Almazroui, M., Islam, M. N., Athar, H., Jones, P. D., and Rahman, M. A. (2012). Recent climate change in the Arabian peninsula: annual rainfall and temperature analysis of Saudi Arabia for 1978–2009. *Int. J. Climatol.* 32, 953–966. doi: 10.1002/joc.3446

Alpert, P., Osetinsky, I., Ziv, B., and Shafir, H. (2004). Semi-objective classification for daily synoptic systems: application to the eastern mediterranean climate change. *Int. J. Climatol.* 24, 1001–1011. doi: 10.1002/joc.1036

Black, E. (2012). The influence of the North Atlantic Oscillation and European circulation regimes on the daily to interannual variability of winter precipitation in Israel. *Int. J. Climatol.* 32, 1654–1664. doi: 10.1002/joc.2383

Buchanan, C. M., Beverland, I. J., and Heal, M. R. (2002). The influence of weather-type and long range transport on airborne particle concentrations in Edinburgh, UK. *Atmos. Environ.* 36, 5343–5354. doi: 10.1016/S1352-2310(02)00579-4

Chen, T. C. (2005). Maintenance of the midtropospheric North African summer circulation: saharan high and African Easterly Jet. *J. Climate* 18, 2943–2962. doi: 10.1175/JCLI3446.1

Choi, G., Collins, D., Ren, G., Trewin, B., Baldi, M., Fukuda, Y., et al. (2009). Changes in means and extreme events of temperature and precipitation in the Asia-Pacific Network region (1955)–(2007). *Int. J. Climatol.* 29, 1906–1925. doi: 10.1002/joc.1979

Clark, R. T., and Brown, S. J. (2013). Influences of circulation and climate change on European summer heat extremes. *J. Climate* 62, 9621–9632. doi: 10.1175/JCLI-D-12-00740.1

Conway, D., and Jones, P. D. (1998). The use of weather types and air flow indices for GCM downscaling. *J. Hydrol.* 213, 348–361.

Cortesi, N., Trigo, R. M., González-Hidalgo, J. C., and Ramos, A. M. (2013). Modelling monthly precipitation with circulation weather types for a dense network of stations over Iberia. *Hydrol. Earth Syst. Sci.* 17, 665–678. doi: 10.5194/hess-17-665-2013

Cullen, H. M., Kaplan, A., Arkin, P., and deMenocal, P. B. (2002). Impact of the North Atlantic oscillation on middle Eastern climate and streamflow. *Clim. Change* 55, 15–338. doi: 10.1023/A:1020518305517

Demuzere, M., Werner, M., van Lipzig, N. P. M., and Roeckner, E. (2008). An analysis of present and future ECHAM5 pressure fields using a classification of circulation patterns. *Int. J. Climatol.* 29, 1796–1810. doi: 10.1002/joc.1821

Ekström, M., Jönsson, P., and Bärring, L. (2002). Pressure patterns associated with wind erosion events in S. Sweden. *Clim. Res.* 23, 51–66. doi: 10.3354/cr023051

Esteban, P., Jones, P. D., Martin-Vide, J., and Mases, M. (2005). Atmospheric circulation patterns related to heavy snowfall days in Andorra, Pyrenees, *Int. J. Climatol.* 25, 319–329. doi: 10.1002/joc.1103

Frakes, B., and Yarnal, B. (1997). A procedure for blending manual and correlation-based synoptic classifications. *Int. J. Climatol.* 17, 1381–1396.

Goldreich, Y. (2003). The Climate of Israel. Observation, Research and Applications. New York, NY: Kluer Academic/Plenum Publishers.

Goodess, C. M. (2000). *The Construction of Daily Rainfall Scenarios for Mediterranean Sites Using a Circulation-Type Approach to Downscaling.* Ph.D. thesis, University of East Anglia, Norwich.

Goodess, C. M., and Jones, P. D. (2002). Links between circulation and changes in the characteristics of Iberian rainfall. *Int. J. Climatol.* 22, 1593–1615. doi: 10.1002/joc.810

Goodess, C. M., and Palutikof, J. P. (1998). Development of daily rainfall scenarios for southeast Spain using a circulation-type approach to downscaling. *Int. J. Climatol.* 18, 1051–1083. doi: 10.1002/joc.810

Hess, P., and Brezowsky, H. (1977). "Katalog der Grosswetterlagen Europas 1881–1976," in *Berichte des Deutschen Wetterdienst, No. 113* (Offenbach am Main: Selbstverlag des Deutschen Wetterdienstes).

Hongisto, M., and Joffre, S. (2005). The influence of meteorological conditions affecting transport and deposition of nitrogen compounds over the Baltic Sea area. *Boreal Environ. Res.* 10, 1–17.

Hoy, A., Schucknecht, A., Sepp, M., and Matschullat, J. (2014). Large-scale synoptic types and their impact on European precipitation. *Theor. Appl. Climatol.* 116, 19–35. doi: 10.1007/s00704-013-0897-x

Hurrell, J. W., and Deser, C. (2009). North Atlantic climate variability: the role of the North Atlantic Oscillation. *J. Mar. Syst.* 78, 28–41. doi: 10.1016/j.jmarsys.2008.11.026

Huth, R., Beck, C., Phillipp, A., Demuzere, M., Ustrnul, Z., Cahynová, M., et al. (2008). Classifications of atmospheric circulation patterns: recent advances and applications. Trends and directions in climate research. *Ann. N.Y. Acad. Sci.* 1146, 105–152. doi: 10.1196/annals.1446.019

Jacobeit, J., Rathmann, J., Philipp, A., and Jones, P. D. (2009). Central European precipitation and temperature extremes in relation to large-scale atmospheric circulation types. *Meteorol. Z.* 18, 397–410. doi: 10.1127/0941-2948/2009/0390

Jenkinson, A. F., and Collinson, P. (1977). "An initial climatology of gales over the North Sea," in *Synoptic Climatology Branch Memorandum No. 62* (Bracknell: Meteorological Office), 18.

Jones, P. D., Hulme, M., and Briffa, K. R. (1993). A comparison of Lamb circulation types with an objective classification scheme. *Int. J. Climatol.* 13, 655–663.

Kahya, E. (2011). "The impacts of NAO on hydrology of the East Mediterranean," in *Hydrological, Socioeconomic and Ecological Impacts of the North Atlantic Oscillation in the Mediterranean Region, Advances in Global Change Research*, Vol. 46, eds S. M. Vicente-Serrano and R. M. Trigo (Zaragoza: Springer). doi: 10.1007/978-94-007-1372-7_5

Kalnay, E., Kanamitsu, M., Kistler, R., Collins, W., Deaven, D., Gandin, L., et al. (1996). The NCEP/NCAR 40-year reanalysis project. *Bull. Am. Meteorol. Soc.* 77, 437–471.

Köppen, W. (1936). "Das geographisca System der Klimate," in *Handbuch der Klimatologie*, Vol. 1, eds W. Köppen and G. Geiger (Berlin: C. Gebr. Borntraeger), 1–44.

Laaidi, K. (2001). Predicting days of high allergenic risk during Betula pollination using weather types. *Int. J. Biometeorol.* 45, 124–132. doi: 10.1007/s004840100096

Lamb, H. H. (1972). "British Isles weather types and a register of daily sequence of circulation patterns 1861–1971," in *Geophysical Memoir 116* (London: HMSO), 85.

Lamb, P. J., and Peppler, R. A. (1987). North Atlantic oscillation: concept and an application. *Bull. Amer. Meteorol. Soc.* 68, 1218–1225.

Lanzante, J. R. (1996). Resistant, robust and non-parametric techniques for the analysis of climate data: theory and examples, including applications to historical radiosonde station data. *Int. J. Climatol.* 16, 1197–1226.

Linderson, M. (2001). Objective classification of atmospheric circulation over southern Scandinavia. *Int. J. Climatol.* 21, 155–169. doi: 10.1002/joc.604

Littmann, T. (2000). An empirical classification of weather types in the Mediterranean basin and their interrelation with rainfall. *Theor. Appl. Climatol.* 66, 161–171. doi: 10.1007/s007040070022

Liu, Y. Y., van Dijk, A. I. J. M., McCabe, M. F., Evans, J. P., and de Jeu, R. A. M. (2013). Global vegetation biomass change 1988–2008 and attribution to environmental and human drivers. *Global Ecol. Biogeogr.* 22, 692–705. doi: 10.1111/geb.12024

López-Moreno, J. I., and Vicente-Serrano, S. M. (2007). Atmospheric circulation influence on the interannual variability of snowpack in the Spanish Pyrenees during the second half of the twentieth century. *Nord. Hydrol.* 38, 33–44. doi: 10.2166/nh.2007.030

López-Moreno, J. I., Vicente-Serrano, S. M., Moran-Tejeda, E., Lorenzo-Lacruz, J., Kenawy, A., and Beniston, M. (2011). Effects of the North Atlantic Oscillation (NAO) on combined temperature and precipitation winter modes in the Mediterranean mountains: observed relationships and projections for the 21st century. *Global Planet. Change* 77, 62–76. doi: 10.1016/j.gloplacha.2011.03.003

Lorenzo, M. N., Ramos, A. M., Tabuada, J. J., and Gimeno, L. (2011). Changes in present and future circulation types frequency in northwest Iberian Peninsula. *PLoS ONE* 6:e16201. doi: 10.1371/journal.pone.0016201

Maheras, P., Flocas, H. A., Patrikas, I., and Anagnostopoulou, C. (2001). A 40 year objective analysis of surface cyclones in the Mediterranean region: spatial and temporal distribution. *Int. J. Climatol.* 21 359–367. doi: 10.1002/joc.599

Martin-Vide, J. (2001). Limitations of an objective weather-typing system for the Iberian peninsula. *Weather* 56, 248–250. doi: 10.1002/j.1477-8696.2001.tb06585.x

McKendry, I. G., Stahl, K., and Moore, R. D. (2006). Synoptic sea-level pressure patterns generated by a general circulation model: comparison with the types derived from NCEP/NCAR re-analysis and implications for downscaling. *Int. J. Clim.* 26, 1727–1736. doi: 10.1002/joc.1337

Muller, R. A. (1977). A synoptic climatology for environmental baseline analysis: New Orleans. *J. App. Meteorol.* 16, 20–33.

Papadopoulos, A., Paschalidou, A. K., Kassomenos, P. A., and McGregor, G. (2014). On the association between synoptic circulation and wildfires in the Eastern Mediterranean. *Theor. Appl. Climatol.* 115, 483–501. doi: 10.1007/s00704-013-0885-1

Papadopoulos, V. P., Abualnaja, Y., Josey, S. A., Bower, A., Raitsos, D. E., Kontoyiannis, H., et al. (2013). Atmospheric forcing of the winter air-sea heat fluxes over the Northern Red Sea. *J. Clim.* 26, 1685–1701. doi: 10.1175/JCLI-D-12-00267.1

Park, Y. J., and Ahn, J. B. (2014). Characteristics of atmospheric circulation over East Asia associated with summer blocking. *J. Geophys. Res. Atmos.* 119, 726–738. doi: 10.1002/2013JD020688

Post, P., Truija, V., and Tuulik, J. (2002). Circulation weather types and their influence on temperature and precipitation in Estonia. *Boreal Environ. Res.* 7, 281–289.

Pozo-Vázquez, D., Esteban-Parra, M. J., Rodríguez, F. S., and Castro-Diez, Y. (2001). A study of NAO variability and its possible non-linear influences on European surface temperature. *Climate Dyn.* 17, 701–715. doi: 10.1007/s003820000137

Prudhomme, C., and Genevier, M. (2011). Can atmospheric circulation be linked to flooding in Europe? *Hydrol. Process.* 25, 1180–1190. doi: 10.1002/hyp.7879

Ramos, A. M., Ramos, R., Sousa, P., Trigo, R. M., Janeira, M., and Prior, V. (2011). Cloud to ground lightning activity over Portugal and its association with circulation weather types. *Atmos. Res.* 101, 84–101. doi: 10.1016/j.atmosres.2011.01.014

Rehman, S. (2010). Temperature and rainfall variation over Dhahran, Saudi Arabia, 1970–2006. *Int. J. Climatol.* 30, 445–449. doi: 10.1002/joc.1907

Rusticucci, M., Bettolli, M. L., and Harris de los Angeles, M. (2002). Association between weather conditions and the number of patients at the emergency room in an Argentine hospital. *Int. J. Biometeorol.* 46, 42–51. doi: 10.1007/s00484-001-0113-z

Tang, L., Karlsson, P. E., Gu, Y., Chen, D., and Grennfelt, P. (2009). Synoptic weather types and long-range transport patterns for ozone precursors during high-ozone events in Southern Sweden. *Ambio* 38, 459–464. doi: 10.1579/0044-7447-38.8.459

Trigo, R. M., and DaCamara, C. C. (2000). Circulation weather types and their influence on the precipitation regime in Portugal. *Int. J.*

Climatol. 20, 1559–1581. doi: 10.1002/1097-0088(20001115)20:13<1559::AID-JOC555>3.0.CO;2-5

Tsvieli, Y., and Zangvil, A. (2005). Synoptic climatological analysis of "wet" and "dry" Red Sea Troughs over Israel. *Int. J. Climatol.* 25, 1997–2015. doi: 10.1002/joc.1232

Türkeş, M., and Erlat, E. (2005). Climatological responses of winter precipitation in Turkey to variability of the North Atlantic Oscillation during the period 1930-2001. *Theor. Appl. Climatol.* 81, 45–69. doi: 10.1007/s00704-004-0084-1

Uppala, S. M., Allberg, K., Simmons, P. W., Andrae, A. J., Da Costa, U., Bechtold, V., et al. (2005). The ERA40 re-analysis. *Q. J. R. Meteorol. Soc.* 131, 2961–3012. doi: 10.1256/qj.04.176

Vicente-Serrano, S. M., and López-Moreno, J. I. (2006). The influence of atmospheric circulation at different spatial scales on winter drought variability through a semiarid climatic gradient in north east Spain. *Int. J. Climatol.* 26, 1427-1456. doi: 10.1002/joc.1387

Vicente-Serrano, S. M., Trigo, R. T., López-Moreno, J. I., Liberato, M. L. R., Lorenzo-Lacruz, J., Beguería, S., et al. (2011). The 2010 extreme winter north hemisphere atmospheric variability in Iberian precipitation: anomalies, driving mechanisms and future projections. *Clim. Res.* 46, 51–65. doi: 10.3354/cr00977

Xoplaki, E., Gonzalez-Rouco, F. J., Gyalistras, D., Luterbacher, J., Rickli, R., and Wanner, H. (2003). Interannual summer air temperature variability over Greece and its connection to the large-scale atmospheric circulation and Mediterranean SSTs 1950–1999. *Clim. Dyn.* 20, 537–554. doi: 10.1007/s00382-002-0291-3

Zarrin, A., Ghaemi, H., Azadi, M., and Farajzadeh, M. (2010). The spatial pattern of summertime subtropical anti-cyclones over Asia and Africa: a climatological review. *Int. J. Climatol.* 30, 159–173. doi: 10.1002/joc.1879

Zhang, X., Aguilar, E., Sensoy, S., Melkonyan, H., Tagiyeva, U., Ahmed, N., et al. (2005). Trends in middle East climate extreme indices from 1950 to 2003. *J. Geophys. Res. Atmos.* 110, D22104. doi: 10.1029/2005JD006181

Ziv, B. (1994). "The weather in Israel," in *Introduction to Meteorology, Unit 5*, eds B. Ziv, Y. Yair (Tel Aviv: The Open University Press), 8–59.

Ziv, B., Dayan, U., Kushnir, Y., Roth, C., and Enzel, Y. (2006). Regional and global atmospheric patterns governing rainfall in the southern Levant. *Int. J. Climatol.* 26, 55–73. doi: 10.1002/joc.1238

From daily climatic scenarios to hourly atmospheric forcing fields to force Soil-Vegetation-Atmosphere transfer models

Julia Hidalgo[1,2]*, Valéry Masson[2] and Christophe Baehr[2]

[1] Laboratoire Interdisciplinaire Solidarités, Sociétés et Territoires, CIEU Department, Université Toulouse – Jean Jaurès, Centre National de la Recherche Scientifique, École des Hautes Etudes en Sciences Sociales, Toulouse, France

[2] Groupe d'Etudes de l'Atmosphère Météorologique, Centre National de Recherches Météorologiques, Météo-France Centre National de la Recherche Scientifique, Toulouse, France

This paper presents a method to produce long term climatic forcing fields to force Soil-Vegetation-Atmosphere transfer (SVAT) models in off-line mode. The objective is to increase the temporal frequency of existent climate projections databases from daily frequency to hourly time step to be used in impact climate studies. A statistical clustering *k*-means method is used. A tens of clusters seems to be enough to describe the climate variability in term of wind regimes, precipitation and thermal and humidity amplitude. These clusters are identified in the future projections of climate and reconstructed sequences at hourly frequency are obtained for all the forcing variables needed by a SVAT model, typically: air temperature, specific humidity, wind speed and direction, precipitation, direct short-wave radiation, downward long-wave radiation, and scattered short-wave radiation. Eleven years of observations from two sites in France are used to illustrate the method: the Chartres station (Paris) and Blagnac station (Toulouse). The reconstruction algorithm is able to produce diurnal cycles that fits well with hourly series from observations (1998–2008; 1961–1990) and from climatic scenarios (1961–2100). The diurnal amplitude and mean value is well represented for variables with marked daily cycle as temperature or humidity. Changes in the mean wind direction are represented and, to a certain extent, changes in wind intensity are also retained. The mean precipitation is conserved during the day even if the method is not able to reproduce the short rain picks variability. Precipitation is used as input in the clusterization process so in clusters representative of rainy days some diurnal variability is nevertheless retained.

Keywords: downscaling, regional climate models, SVAT, atmospheric forcing, climate change impact

INTRODUCTION

Investigations on climate change impact often requires projections of climate at the local scale to be used to force a Soil-Vegetation-Atmosphere transfer (SVAT) model[1] in offline mode. The easier way to obtain long term databases for the atmospheric parameters used to force SVAT models, would be to directly[2] use climate simulations from General Circulation Models or Regional Climate Models when those datasets are available with a high temporal frequency (1–3 h). Due to computational storage limitations, often this product is only available over a restricted area, during short periods of time and emission or land use scenarios available are limited. One example is the study of Tanaka et al. (2006) that estimates the impact on hydrological variables of the

Seyhan River basin, Turkey, through off-line simulations for the periods 1994–2003 and 2070–2080.

Future climate projections databases currently available for the whole Europe area that includes different emission scenarios and an ensemble of models have daily frequency, as PRUDENCE (http://prudence.dmi.dk/), ENSEMBLES (http://www.ensembles-eu.org/), or those from the Climatic Research Unit of the New Anglia University (http://www.cru.uea.ac.uk/cru/data/hrg/). This means that, for a grid point, only the daily mean or at the best the maximum and minimum values are available. In this case, an increase in the temporal frequency of the variables from daily to hourly time step is needed.

One way to do that is to obtain relationships between large scale circulation patterns and local variables through a classification based on atmospheric circulations or weather types. This classification is determined in a high resolution hourly reanalysis database and projected in to a daily database of climate scenarios. These climate scenarios are then reconstructed at high temporal frequency using mean (or a representative) diurnal cycles from the same weather types in the reanalysis database (see Huth et al., 2008 for a deep review of this method). This approach was used by Quintana-Seguí et al. (2010, 2011), Querguiner et al. (2012)

---

[1] SVAT models simulate micro-scale energy and matter exchange processes between land surface and the atmospheric layer near the ground level. They are used by meteorologists, climatologists, ecologists, and biogeochemists to study the radiative transfer, the energy balance, the turbulent and diffusive transfer, the stomatal function, the photosynthesis and respiration, or the liquid phase water flow.

[2] A previous bias correction should be performed using observed climate data in order to remove systematic errors from Global and Regional Climate models.

and during the RexHySS project (Ducharne et al., 2009) to study the impact of climate change on some French basins. Recently it was used by Lemonsu et al. (2012) to study climate change impact over Paris region and by Déqué et al. (2011) for mountainous zones.

This approach has two limitations: first it needs a previous large scale weather type classification at synoptic scale. This kind of product is not available everywhere and it demands high amount of data and validation time. It is only after a recent COST action 733 (Philipp et al., 2010) that were developed for the European regions tools to simply overview of the existing circulation classification catalogs. The second limitation is that the method, as applied in the studies cited before, cannot produce extremes higher than those observed during the period used to construct the weather type classification.

The methodology presented here allows to generate climatic input databases, based on past near surface observations, for SVAT models that need high-resolution atmospheric forcing inputs. In fact, observational data at hourly frequency is available from the operational network of surface stations with large coverage around the world (http://worldweather.wmo.int/). The idea here is to use single-site observations from a sufficiently long period (so all the diversity of weather types affecting the site will be represented) and apply a cluster analysis using only the mean, maximum, and minimum daily data, that are the only one available for modeled future scenarios, to classify the data in function of the type of the diurnal cycle for each variable.

These mean meteorological characteristics are identified in the future projections of climate from Regional Climate Models. A cluster number is then attributed and a reconstructed sequence for the future projections at hourly frequency is obtained.
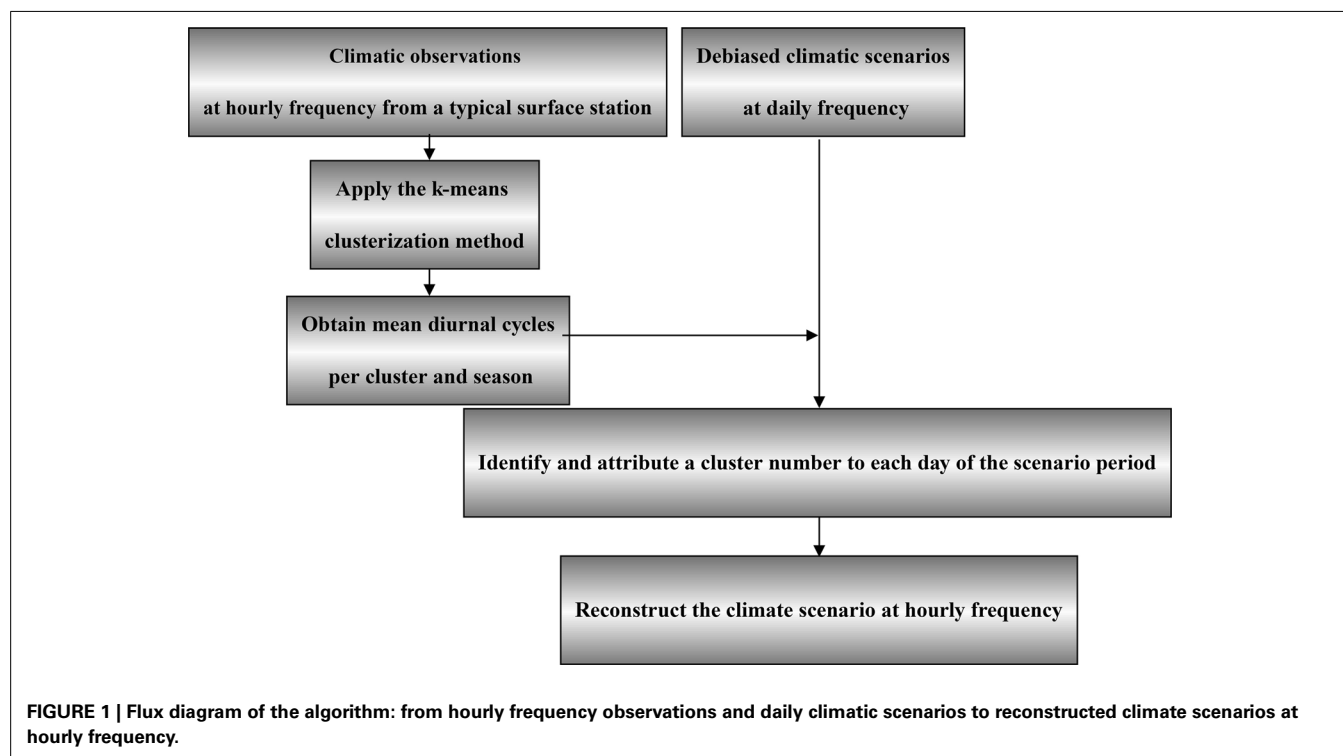
Figure 1 represent the flux diagram of the algorithm and describes the methodology.

Two sites are selected to prove the feasibility of the method. The Chartres station close to Paris and Blagnac station close to Toulouse were used to perform a *k*-means cluster classification for the *construction period* 1998–2008 (Section Materials and Methods). A validation analysis is performed for reconstructed series for the construction period and the climatic *reference period* 1961–1990. Near-surface atmospheric outputs from seven Regional Climate Models from the EU-FP6 ENSEMBLES (Hewitt, 2005) are reconstructed at hourly frequency from 1961 to 2100 and the method is validated using hourly climate projections provided by the Marx-Planck-Institute (Section Results). The statistics are shown for both areas in Section Materials and Methods but to limit the number of figures and, as the objective of the paper, is to illustrate the methodology, the results of validation and application to climatic scenarios in Section Results are shown only for Paris area. Nevertheless, a complete documentation of results, figures, and analyses of the types of diurnal cycles for both sites can be found, in French, on Hidalgo (2012a,b).

MATERIALS AND METHODS

HOURLY CLIMATIC DATA FROM A TYPICAL METEOROLOGICAL STATION

Data from two meteorological stations are used due to specific needs on projections of climate at the local scale on two French National projects on climate change impact on Paris [MUSCADE (http://www.cnrm.meteo.fr/ville.climat/spip.php?article85)] and Toulouse [ACCLIMAT (http://www.cnrm.meteo.fr/ville.climat/spip.php?rubrique47)] areas. Air temperature, specific humidity, wind speed and direction and precipitation from the operational network of Meteo-France were extracted from: Blagnac station
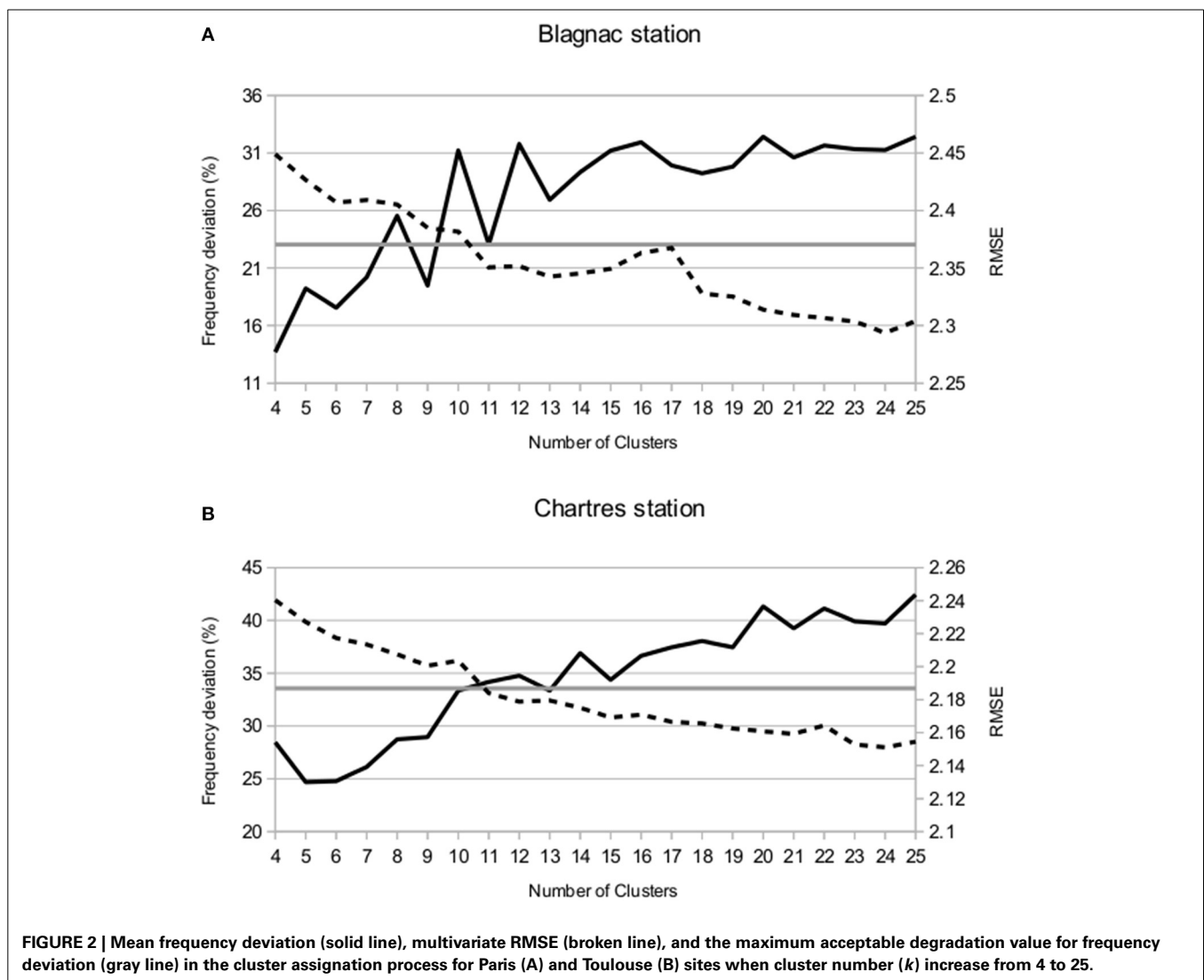
FIGURE 1 | Flux diagram of the algorithm: from hourly frequency observations and daily climatic scenarios to reconstructed climate scenarios at hourly frequency.

(Toulouse) located at (43°′12″N, 1°22′42″E). This station is situated over grass inside the airport at 6 km in the North-West of Toulouse city and from Chartres station (Paris) situated also over grass at 155 m over the sea level at (48°27′ 36″N, 1°30′00″E) at 80 km at the South-West of Paris. As far as possible, it is convenient to use observations from meteorological stations representative of rural areas because scenarios of climate change do not consider the influences of urban areas on their own local climates.

STATISTICAL METHOD

The statistical k-means method is applied for the *construction period* (1998–2008, 4018 days) to obtain a set of clusters that represents the plurality of weather situations representative of Paris and Toulouse local climates. To define the cluster structure the following variables are used, the daily: diurnal thermal amplitude (ΔT, °C), mean wind speed (ff, m s^{-1}) and direction [dd (four quadrants were defined for the 1–90; 91–180; 181–270 and 271–360 wind direction)], mean precipitation (pp, mm), and mean specific humidity (q, gr kg^{-1}). In the method the distance measure determines how the similarity of two elements is calculated when forming the clusters. Here the Euclidean distance is used. To avoid differences in scale among the variables the standard deviation is used to normalize their values.

An important question that needs to be tackled before applying the k-means clustering algorithm is how many clusters (k) are in the dataset. This is not known a priori and often the strategy is to perform an iterative exercise increasing the number of clusters. There are different means to evaluate the resulting clustering quality in a quantitative manner (He et al., 2002). For us the objective is to obtain the best reconstructed series for all variables once the attribution method is applied. Two parameters are used to evaluate the resulting series. The first represents how well the resulting mean diurnal cycles from clusters serves to identify and attribute a cluster number for a particular day. In others words, for the construction period, the frequency distribution of clusters issue from the attribution process is evaluated against those obtained directly from the k-means clustering method. The second one is the multivariate Root Mean Square Error of the reconstructed and original observed series. The magnitudes evaluated

FIGURE 2 | Mean frequency deviation (solid line), multivariate RMSE (broken line), and the maximum acceptable degradation value for frequency deviation (gray line) in the cluster assignation process for Paris (A) and Toulouse (B) sites when cluster number (k) increase from 4 to 25.

are the hourly near surface temperature, relative humidity, wind u-v components and precipitation from observations.

Figure 2 shows the mean frequency deviation (solid line) and the mean RMSE (broken line) for 10^3 repetitions of the iterative exercise where k increase from 4 to 25 clusters. In both locations Paris and Toulouse, the frequency deviation increase (solid line) and the RMSE decrease (broken line) when k increases. The reason is that a high number of clusters results in mean diurnal cycles of temperature, humidity, wind, and precipitation that could be very similar for some seasons resulting in a degradation in the inter-cluster separation making difficult the cluster attribution process.

The choice of an optimal number of clusters is here done as follows. The range (Freq$_{max}$ − Freq$_{min}$) is calculated. A threshold of 50% of this quantity is fixed as a maximum acceptable degradation in the cluster assignation process (gray line in **Figure 2**). The number of clusters that produces relative Freq$_{min}$ values under this threshold are identified. For this cluster numbers, RMSE is computed. The number of clusters relative to the minimum RMSE is kept. For Paris and Toulouse, thresholds are 33.56 and 23.05% respectively. Two relative minimums at $k = 5$ and 9 are identified for Paris and three at $k = 6$, 9, and 11 for Toulouse. RMSE is minimum at $k = 9$ and $k = 11$ for Paris and Toulouse respectively. Nine and eleven clusters are respectively retained as an optimum number for the cluster analysis and further development.

TYPES OF DIURNAL CYCLES FROM CLUSTERS

Table 1 summarizes the values of centroids for each variable. Those are the values that characterize each type of day obtained from the clustering process for Paris (nine clusters) and Toulouse (11 clusters) respectively. They will be used to classify days in periods outside of the *construction period* 1998–2008 [as explained in Section First validation: cluster attribution and hourly reconstruction for the construction period (1998–2008)]. **Figure 3** presents the occurrence frequency (number of days belonging to a cluster) in total percentage and per season.

In Paris region predominant winds flow from the south-west (mainly in winter and autumn, clusters 1, 3, 5, and 7) and the north and north-east (mainly in winter and summer, clusters 6 and 8). Humid winds from the west are also frequents (clusters 0 and 2). Winds from south and south-east (cluster 4) are infrequent and normally it corresponds to temporary phases before a perturbation. Even if the clusters are present in almost all seasons, predominant winter clusters are 1, 5, and 6 and summertime clusters are 2, 4, and 7. The mean daily thermal amplitude varies between 4°C (for cluster 1) and 13°C (for cluster 8) and the daily amplitude in relative humidity varies between 5 and 50%. Precipitation is concentrated on clusters 4, 5, and 7 for all seasons.

In Toulouse dominant winds are, in descending order of importance, the humid westerly wind from the Atlantic Ocean [represented here by clusters 0, 3, 4, 6, 8, 9 (the more frequent), and 10], moderate south-easterly wind (cluster 1 and 7) that can be very strong (called the Autan wind, cluster 2) and finally the southerly wind (cluster 5). Predominant winter clusters are 0, 3,

[3]Similar results where obtained for repetition number of 5 and 30.

Table 1 | Values for the clusters centroids of the diurnal amplitude of air temperature and daily mean values for wind speed, wind direction (expressed in quadrants for wind direction inside of the following ranges 1–90; 91–180; 181–270; and 271–360 wind direction), precipitation, and specific humidity.

Cluster number	Tmax-Tmin (°C)	ff (m/s)	dd (quadrants)	pp (mm)	q (kg/kg)
PARIS					
0	5.32	1.49	3.5	0.020	0.00631
1	4.05	2.66	3.0	0.049	0.00472
2	11.81	1.59	3.5	0.028	0.00582
3	7.76	4.59	2.9	0.036	0.00725
4	6.70	2.17	2.8	0.832	0.00888
5	5.02	5.46	3.0	0.343	0.00689
6	6.84	3.16	1.1	0.004	0.00406
7	7.08	2.29	2.8	0.309	0.00885
8	13.78	1.61	1.5	0.012	0.00715
TOULOUSE					
0	5.60	1.43	3.7	0.071	0.00507
1	7.31	2.59	2.0	0.297	0.00842
2	6.19	6.25	2.1	0.016	0.00709
3	3.43	4.27	3.9	0.065	0.00507
4	6.44	3.13	3.6	1.003	0.00942
5	9.75	2.37	1.9	0.012	0.00567
6	5.05	4.56	3.7	0.436	0.00721
7	11.08	2.62	1.9	0.014	0.01045
8	7.23	2.38	3.6	0.089	0.01082
9	12.49	1.80	3.8	0.059	0.00703
10	4.15	5.01	3.1	1.938	0.00903

and 5. Representative summertime clusters are 7, 8, and 9. The daily thermal amplitude varies between 3 and 12°C and the daily amplitude in relative humidity between 10 and 50%. Precipitation is concentrated on clusters 1, 4, 6, and 10.

Seasonal intra-cluster differences in the mean hourly cycles where found for both, Paris and Toulouse locations. Some are related to the large-scale seasonal forcing as for example the seasonal delay in the daybreak or a higher thermal amplitude for warm seasons that for the cold ones. For example cluster 6 for Paris (**Figure 4A**) presents a high thermal amplitude variability 5°C in winter and 10°C in summer. In consequence the same relation is found for the relative humidity. Even though, the rest of variables for this cluster (the precipitation rate, the wind speed and wind direction) are very consistent between seasons. Other are related to differences in the circulations at the synoptic scale. For example again in Paris, hourly mean temperature for cluster 4 (**Figure 4B**), decrease during winter days from 10°C in the morning to 5°C in the afternoon. This type of day corresponds to a low pressure (985 hpa) situation with quasi-constant relative humidity (98%) and stronger winds during the morning (4.5 m s^{-1} instead 2–3 m/s for other seasons). In Toulouse, cluster 10 (**Figure 4C**) corresponds to rainy days. In Winter (blue line) this situation describes days with south westerly winds and storms during the afternoon (15–20 h UTC). This type of day has temperatures around 10°C and very low
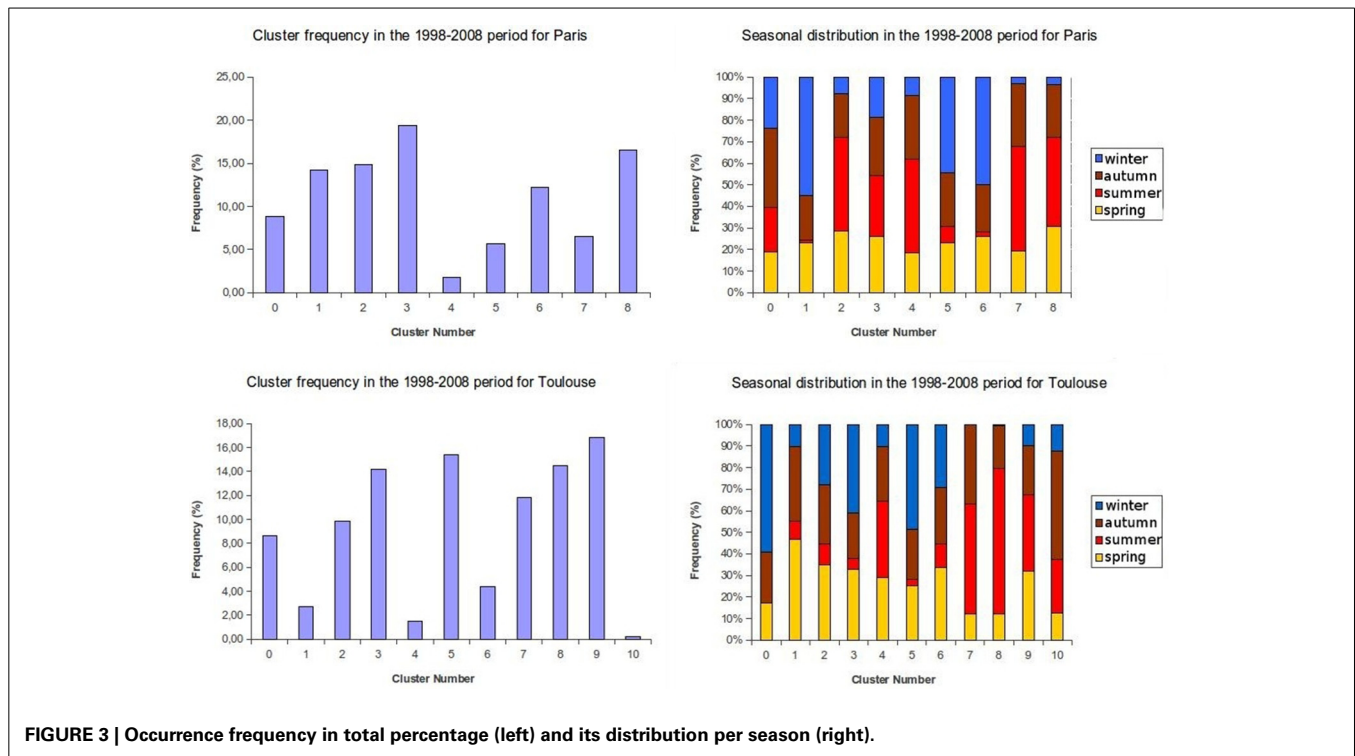
FIGURE 3 | Occurrence frequency in total percentage (left) and its distribution per season (right).

thermal amplitude. Humidity increase during the day ($q = 0.006$ to $0.008\,\mathrm{kg\,kg^{-1}}$) being the atmosphere close to saturation at the end of the afternoon (Hu = 99%).

RESULTS

FIRST VALIDATION: CLUSTER ATTRIBUTION AND HOURLY RECONSTRUCTION FOR THE CONSTRUCTION PERIOD (1998–2008)

The cluster methodology aims to represent the climatic variability of a site using a finite set of daily mean cycles. For that, a cluster number is associated by the k-means method to each day of the period and a series that maintains the climatic features and variability of the site can be directly reconstructed using the seasonal diurnal mean cycles associated to each cluster (hereafter direct method). When working with an alternative period in the past (observations or model outputs) or in the future (model outputs) where the clustering process is not possible, it is necessary to attribute a type of day (cluster number) to each day of the alternative period.

The attribution method is here based on variables that are available at daily frequency in climate scenarios databases: the mean, max, and min values for temperature and relative humidity; the daily mean values of u-v wind components and precipitation.

These values are obtained for the *construction period*. The deviation between those values for a day of the alternative series and from each cluster is computed and summed for each cluster (S_K). All the data is normalized with its standard deviation. The cluster number with the minimum value of S_K is attributed to the day.

A hourly reconstructed series is obtained for all the observables using the observed mean daily value and the shape of the cluster diurnal cycle for the season of this particular day. For

temperature and relative humidity, maximum and minimum values are available so the shape amplitude of the cluster diurnal cycle is modulated as follows:

$$T(h)_i = \overline{T_i} + (\Delta T(h)_{season\_mean})_k {}^* Cte$$

$$Cte = \frac{(T_{\max} - T_{\min})_{obs}}{(T_{\max} - T_{\min})_k}$$

Where i is the day number and k the cluster number. $T_{\max}$ and $T_{\min}$ are the maximum and minimum values of the observed (or modelized) field. For a cluster k, $\Delta T(h)_{season\_mean}$ is the seasonal mean hourly cycle of $\Delta T(h)$ being $\Delta T(h) = T(h)_j - \overline{T}(h)_j$. Over all days ($j$) of the season.

The performance of the attribution method to produce hourly reconstructed series close to observations is presented and discussed in next section where the method is applied to the WMO *reference climate period* 1961–1990.

We want to focus here on the differences found on the occurrence frequency when the reconstruction is performed using the direct method and the attribution method.

When analyzing the number of days affected to each cluster number for both methods, differences between 0.02 and 7.7% for Toulouse and 0.2 and 8.7% for Paris are found resulting in a total of 24 and 30% of the days that are affected to an annex cluster. Most of those differences are concentrated in summer and autumn. This is due to the fact that for each cluster four seasonal hourly cycles are obtained. Some, for the same season, are very similar so the method is not able to attribute the exact cluster number. This has not a big impact on the reconstructed series because the method attributes a mean cycle very close to the original one (**Figures 5**, **6**), one must be prudent exploring changes

FIGURE 4 | Mean diurnal cycles of temperature, relative humidity, wind speed and precipitation for Paris (A,B), and Toulouse (C). Seasonal intra-clusters differences for spring, summer, autumn, and winter are in black, red, green, and blue lines respectively.
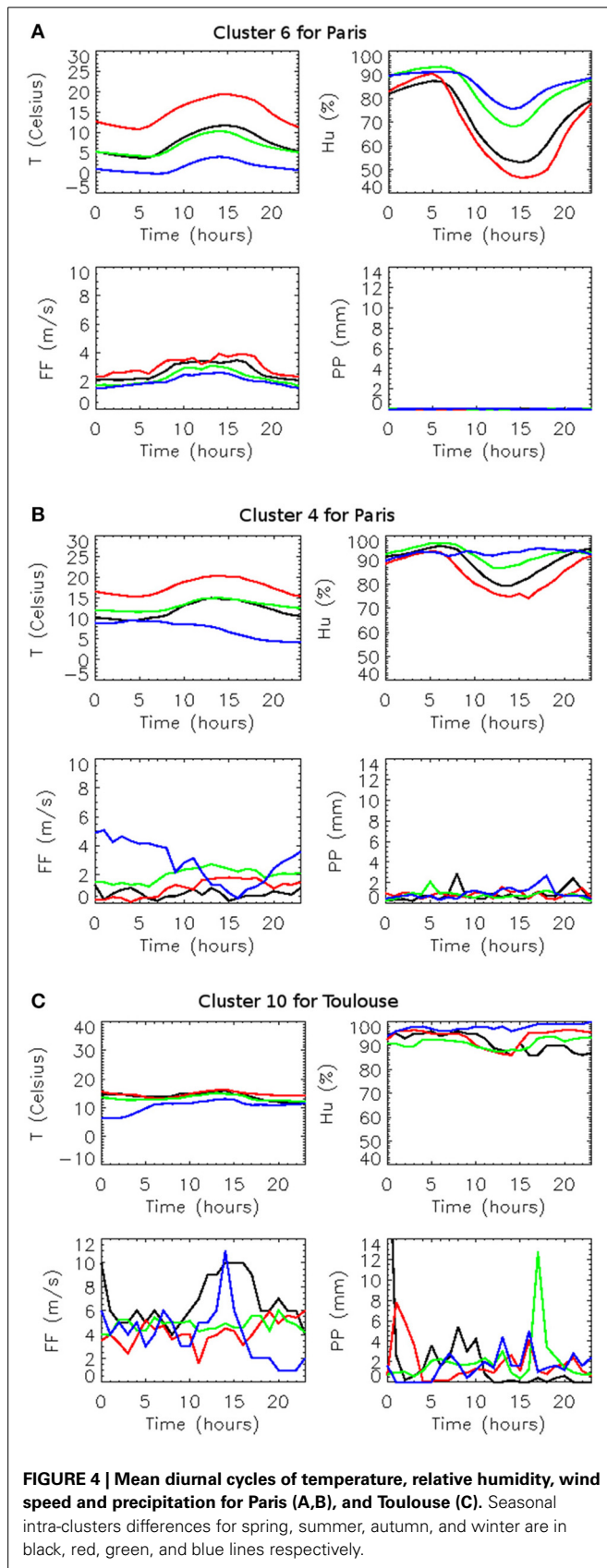
in the frequency of the clusters occurrence in future projections because this may be an artifact of the attribution methodology.

SECOND VALIDATION: APPLYING THE ATTRIBUTION METHOD TO AN ALTERNATIVE OBSERVATIONAL PERIOD

The objective here is to show the feasibility of the method for an alternative period in the past where the clustering process is not possible and attribution of a cluster number is mandatory. The attribution method is applied for the WMO *reference climate period* 1961–1990 where at Chartres (Paris) and Blagnac (Toulouse) locations three-hourly observations are available.

Values of the mean, max and min values for temperature and relative humidity; the daily mean values of u-v wind components and precipitation are obtained from the 1961–1990 three-hourly observed series after a spline function reconstruction that provides hourly disaggregation.

The hourly reconstructed 1961–1990 series are compared to observations of Chartres station by means of the scatter-plot and the linear Pearson correlation coefficient (represented by $\rho_{x,y}$ in the figures) (**Figure 7**) and the temporal evolution of each variable (**Figure 8**, a random period of 10 consecutive days in summer and winter is shown). The reconstruction algorithm is able to produce diurnal cycles that fits well with observations during different seasons. The diurnal amplitude and mean value is well represented for variables with marked daily cycle as temperature ($\rho_{x,y} = 0.97$) or relative humidity ($\rho_{x,y} = 0.91$). For temperature, there is a jump in the intersection between 2 days that is more or less pronounced in function of the cycle features[4], for example during the night from 7th to 8th August (**Figure 8**). Changes in the mean wind direction are well represented and, to a certain extent, changes in wind intensity are also retained ($\rho_{x,y} = 0.76$). The mean precipitation is conserved during the day but the method is not able to reproduce the short rain picks variability ($\rho_{x,y} = 0.52$). However precipitation is used as input in the clusterization process and some variability is retained in clusters that are representative of rainy days. For example days of autumn with precipitation during the late afternoon (**Figure 4C**, cluster 10 for Toulouse, green line).
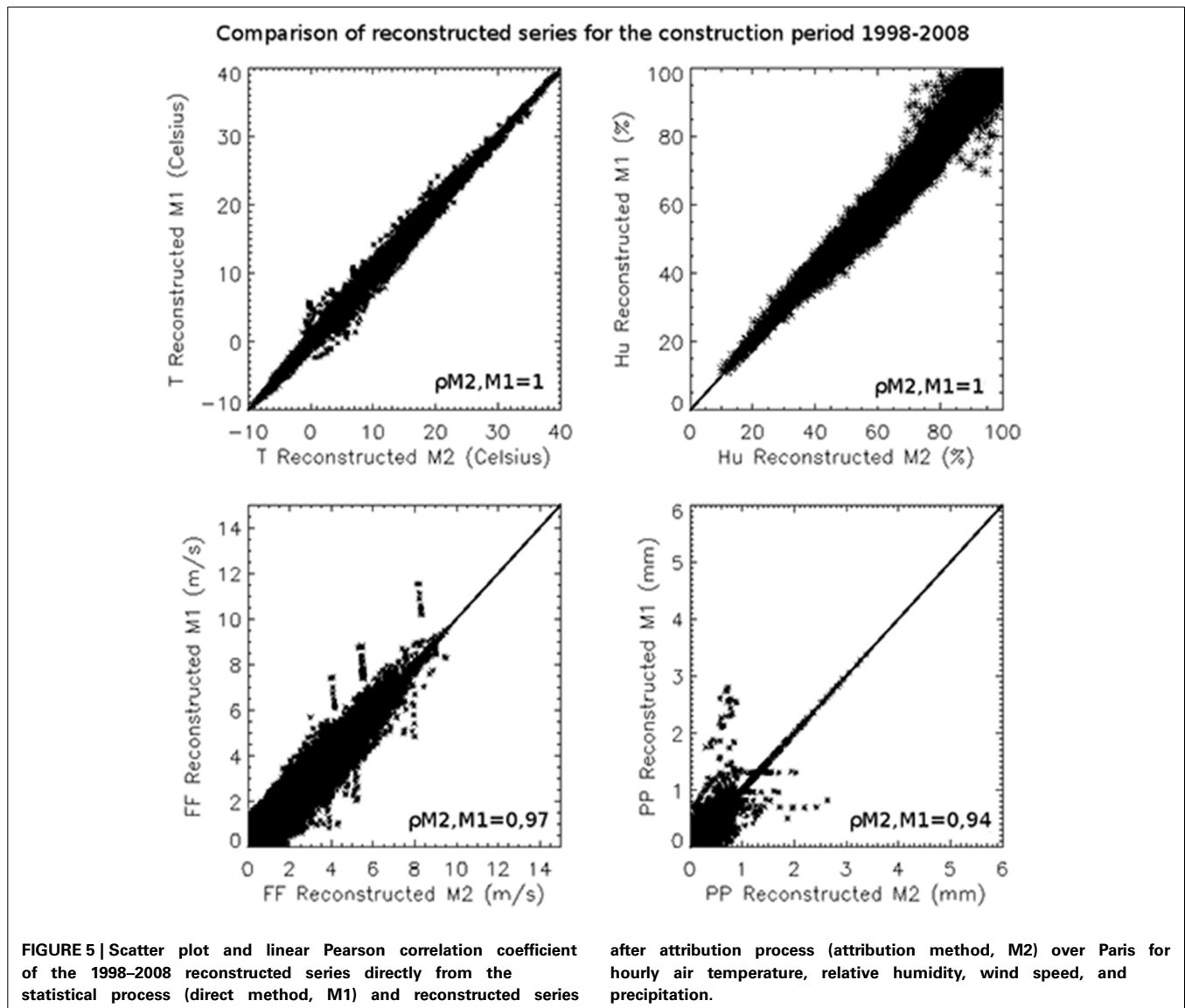
VALIDATION AND APPLICATION TO CLIMATE SCENARIOS FROM REGIONAL CLIMATE MODELS SIMULATIONS

To explore the applicability of the method to future scenarios, the Climate Service Center of the Max Planck Institute for Meteorology provided for validation time-series at the nearest grid point for near-surface hourly temperature, specific humidity, u- and v-velocities, net surface solar radiation and downward, long-wave radiation from REMO simulations.

Three kinds of simulations were available in function of the emission scenario (Nakicenovic et al., 2000): A1B, B1, and E1. A common control period run (1961–2000) was performed for A1B and B1 scenarios and a single one for E1 scenario. Three projections from 2001 to 2100 were performed for A1B and B1 and from 2001 to 2099 for E1 scenario.

---

[4]A fit function should be applied before long term simulations to avoid propagation of this signal to diagnosed fields.

FIGURE 5 | Scatter plot and linear Pearson correlation coefficient of the 1998–2008 reconstructed series directly from the statistical process (direct method, M1) and reconstructed series after attribution process (attribution method, M2) over Paris for hourly air temperature, relative humidity, wind speed, and precipitation.
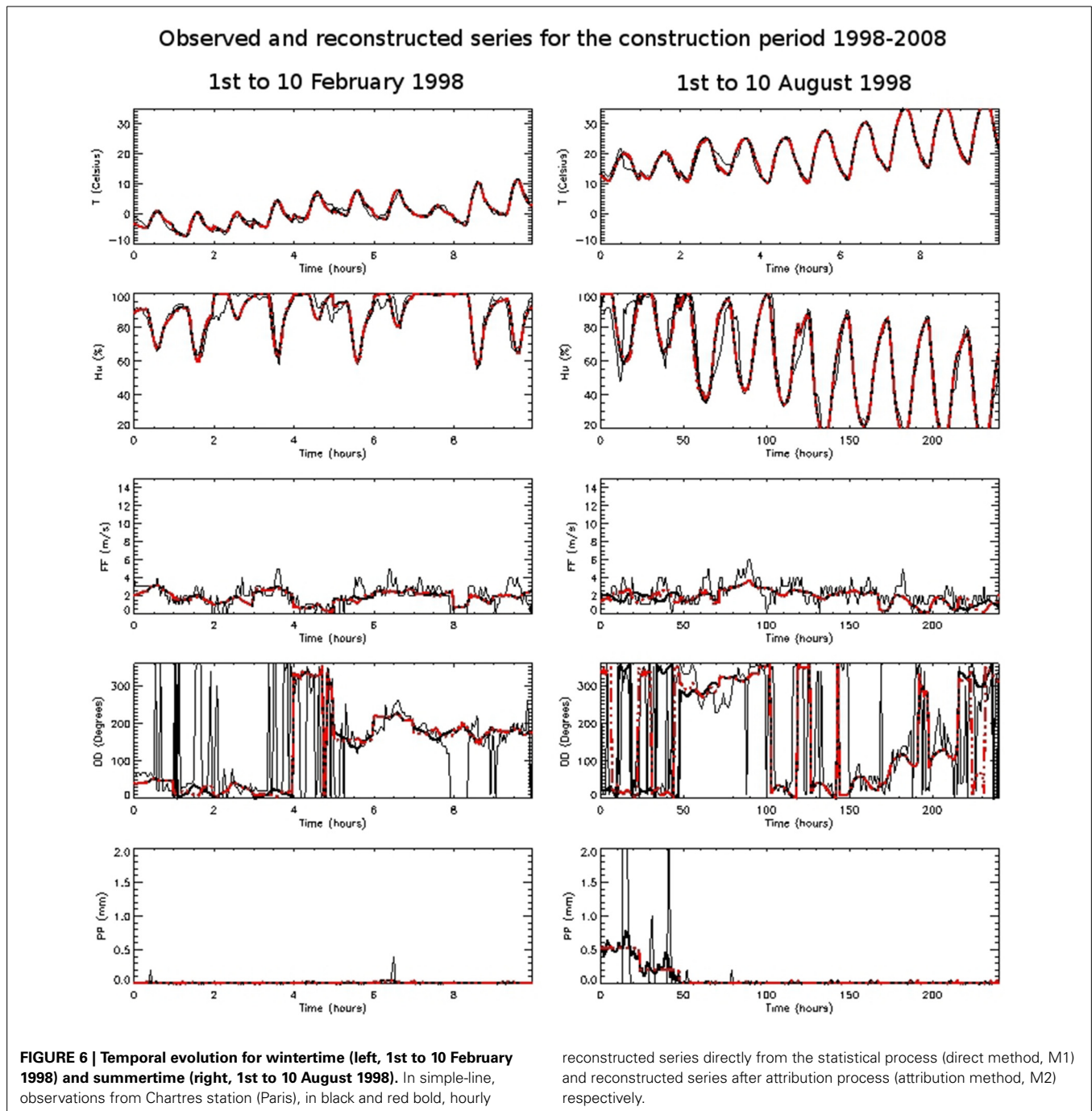
Systematic errors from Global and Regional Climate models are too large to allow for direct use of the outputs in the attribution process so a previous bias correction using observed climate data during a control period (1961–1990) is performed before to apply the attribution methodology. Here this bias is calculated in base to the percentile differences between the mean daily value for modeled and observed series during the reference period as explained in Gonzalez-Aparicio and Hidalgo (2012). This technique, uses a correction function that restores model percentiles in present time to those from observations. This means that it is supposed that the model is able to reproduce the distribution of climatic variables but not their exact value of the percentile. The strongest hypothesis of the method is to consider that model errors are stationary so that it is possible to use the correction function for future projections. Once the mean daily value is corrected the diurnal cycle is reproduced using the original hourly anomaly to the original mean value.

Afterwards, hourly reconstructed series for the three future projections are obtained for all the variables as explained in Section First validation: cluster attribution and hourly reconstruction for the construction period (1998–2008). Precipitation was not available in this database so this variable was not used as a prescriptor in the attribution process. The application of the attribution method to climate projections is possible assuming that under future climate conditions the occurrence frequencies of clusters might be modified but their dynamical characteristics remain unchanged. It is the same hypothesis as for methodologies based on weather classes and this approach is supported by studies as those from Corti et al. (1999) and Stone et al. (2001) which suggested that anthropogenic climate change may manifest itself as a projection onto the pre-existing natural modes of variability of the climate system (Najac et al., 2011).

Figure 9 shows the performance of the methodology to reconstruct 10 consecutive days in February and August 2061 for the A1B scenario for Paris. In this case reconstruction for surface
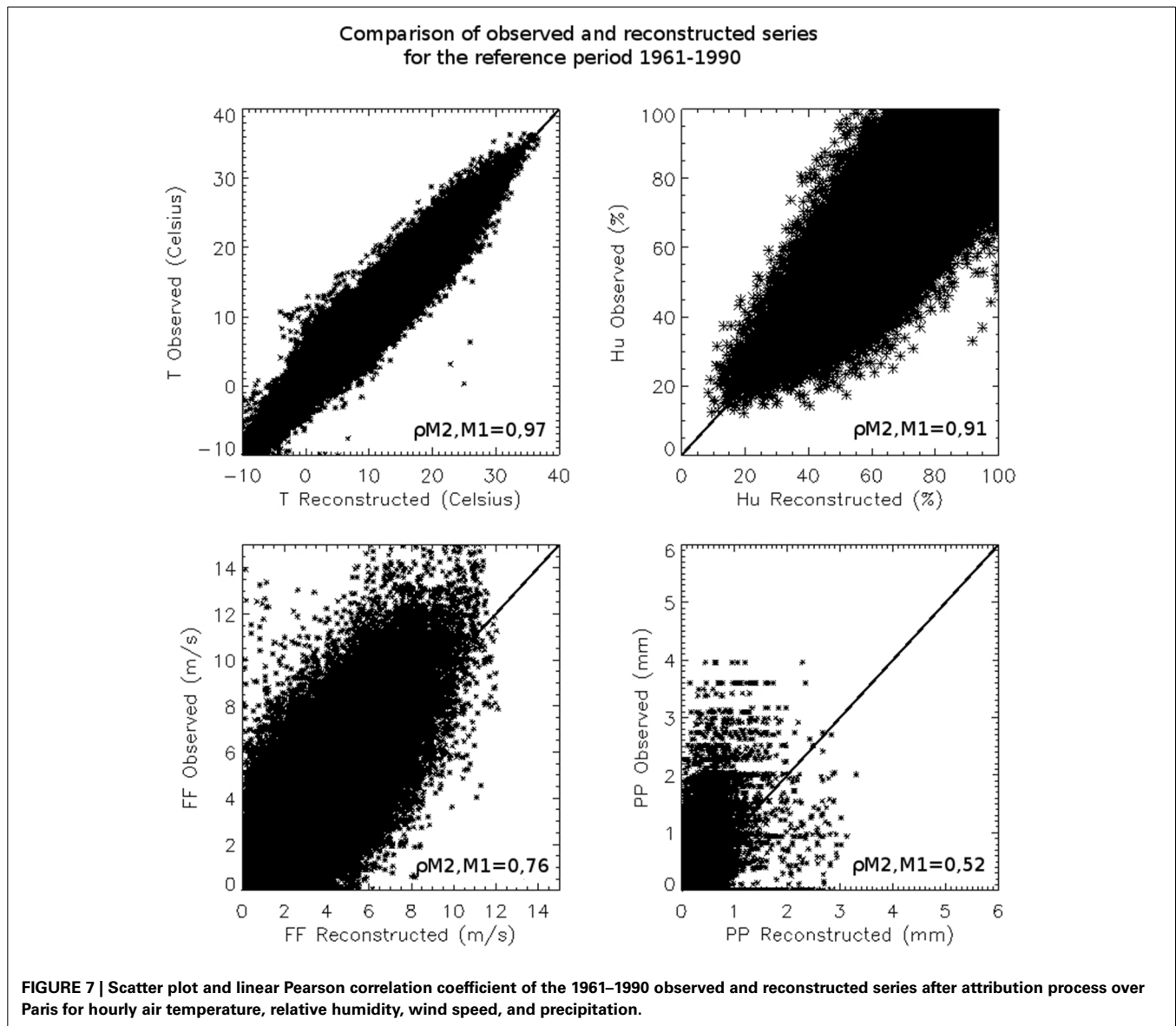
FIGURE 6 | Temporal evolution for wintertime (left, 1st to 10 February 1998) and summertime (right, 1st to 10 August 1998). In simple-line, observations from Chartres station (Paris), in black and red bold, hourly reconstructed series directly from the statistical process (direct method, M1) and reconstructed series after attribution process (attribution method, M2) respectively.

solar radiation (*RG*) and downward, long-wave radiation (*RA*) is shown. The methodology to calculate and reconstruct the temporal series for the radiative variables is explained in Appendix 1 in Supplementary Material. It could be seen that the daily maximum value of *RG* is slightly underestimated in reconstructed series but the cycle conserves the integral sum over the day. The linear Pearson correlation coefficient is calculated for a 30 years window (2061–2090) to maintain the statistical significance of comparison with values obtained for the *reference period*. **Table 2** shows that the performance of the method is very similar for the three simulations A1B, B1, and E1. The impact of leaving out

precipitation from the attribution process seems to have more impact over the wind speed reconstruction that over other variables. The score for linear Pearson correlation coefficient for the wind speed is lower ($\rho_{x,y}$ varies from 0.30 to 032 in function of the scenario) than for the *reference period* ($\rho_{x,y} = 0.76$). This is due to an underestimation of wind gusts mainly in the ranges of 7–10 m s^{-1}.

DISCUSSION
When dynamical downscaling is needed in impact or adaptation studies high temporal frequency atmospheric fields are required

FIGURE 7 | Scatter plot and linear Pearson correlation coefficient of the 1961–1990 observed and reconstructed series after attribution process over Paris for hourly air temperature, relative humidity, wind speed, and precipitation.

to force SVAT models. Future climate projections databases currently available for the whole Europe area have often daily frequency and for a grid point they provide only the daily mean or at the best the maximum and minimum values of atmospheric fields. This study presents a method to increase the temporal frequency of these variables from daily to hourly time step based on past near surface observations from a typical operational surface station. A statistical *k*-means method is applied to a construction period to classify observations in function of the type of the diurnal cycle for each variable. These clusters are identified in the future projections of climate and reconstructed sequences at hourly frequency are obtained.

Two sites in France were selected for this analysis, the Chartres station close to Paris (North-West of France) and Blagnac station close to Toulouse (South-West of France). The *construction period* was 1998–2008, the choice is based on the availability of hourly observations. Nine and eleven clusters were respectively

identified for Paris and Toulouse. This number of clusters are considered enough to describe the climate variability in term of wind regimes, precipitation and thermal and humidity amplitude for both sites. Seasonal intra-cluster differences in the mean hourly cycles and differences in the circulations at the synoptic scale are also well represented.

Hourly reconstruction of 1961–1990 fields are compared to observations by means of the temporal evolution for a random period of 10 consecutive days for winter-time and summer-time, the scatter-plot and the linear Pearson correlation coefficient. The reconstruction algorithm is able to produce diurnal cycles that fits well with observations. The diurnal amplitude and mean value is well represented for variables with marked daily cycle as temperature or humidity. Changes in the mean wind direction are represented and, to a certain extent, changes in wind intensity are also retained. The mean precipitation is conserved during the day even if the method is not able to reproduce the short rain picks

FIGURE 8 | Temporal evolution for wintertime (left, 1st to 10 February 1961) and summertime (right, 1st to 10 August 1961). In simple-line observations from Chartres station (Paris) and in bold hourly reconstructed series after attribution process.
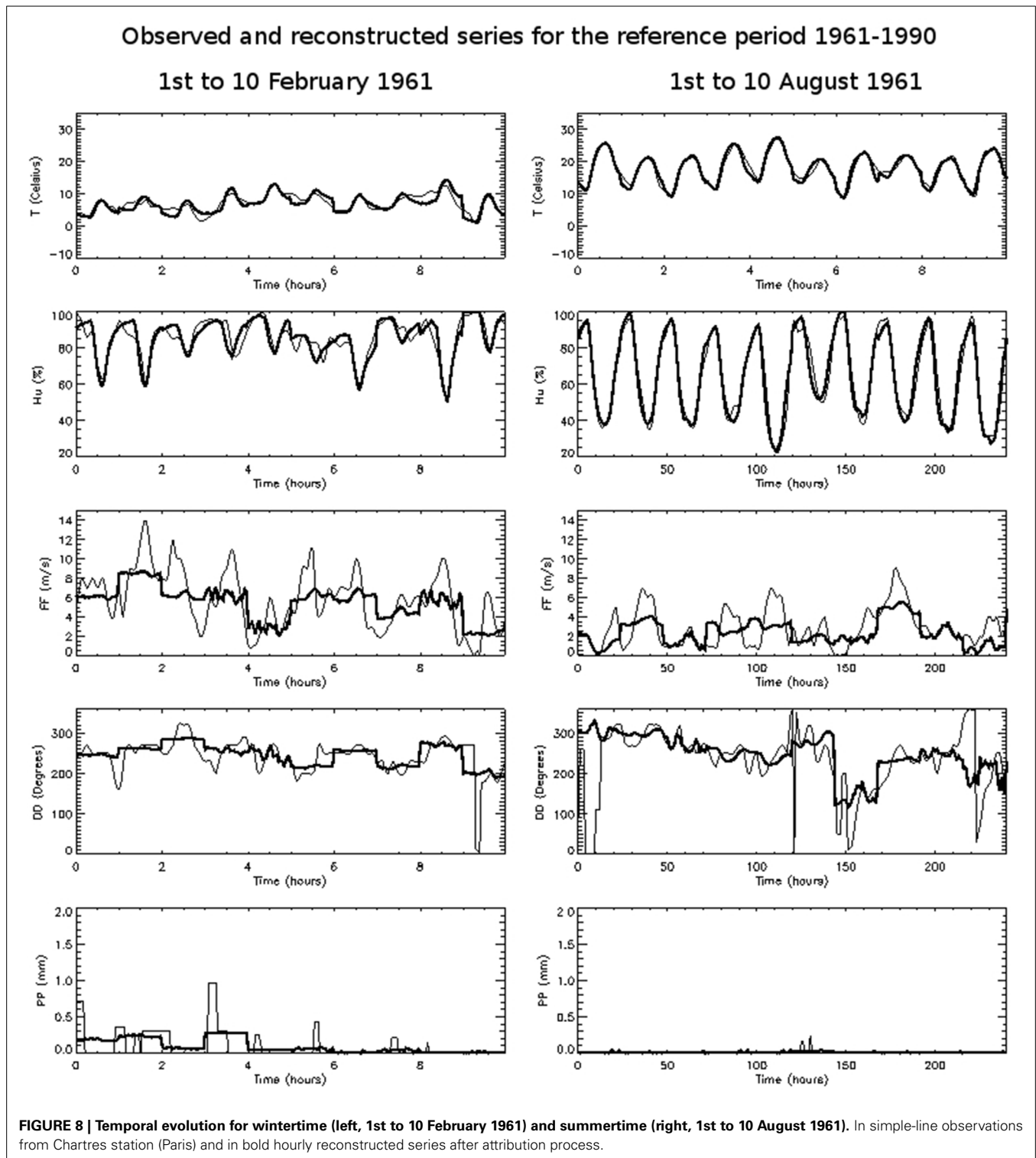
variability. Precipitation is used as input in the clusterization process and in clusters representative of rainy day some variability is in to a certain extent retained.

Finally, near-surface atmospheric outputs from Regional Climate Models have been reconstructed. Three runs from the MPI-REMO model at hourly frequency have been used to show

the feasibility of the method for future projections of climate and pointed out the impact of omitting precipitation in the attribution process.

Six model outputs from the EU-FP6 ENSEMBLES were also reconstructed during the project at hourly frequency from the daily database. The ENSEMBLES database is a good example of

FIGURE 9 | Temporal evolution for wintertime (left, 1st to 10 February 2061) and summertime (right, 1st to 10 August 2061). In simple-line debiased REMO projections for the A1B scenario over Paris and in bold hourly reconstructed series after attribution process.
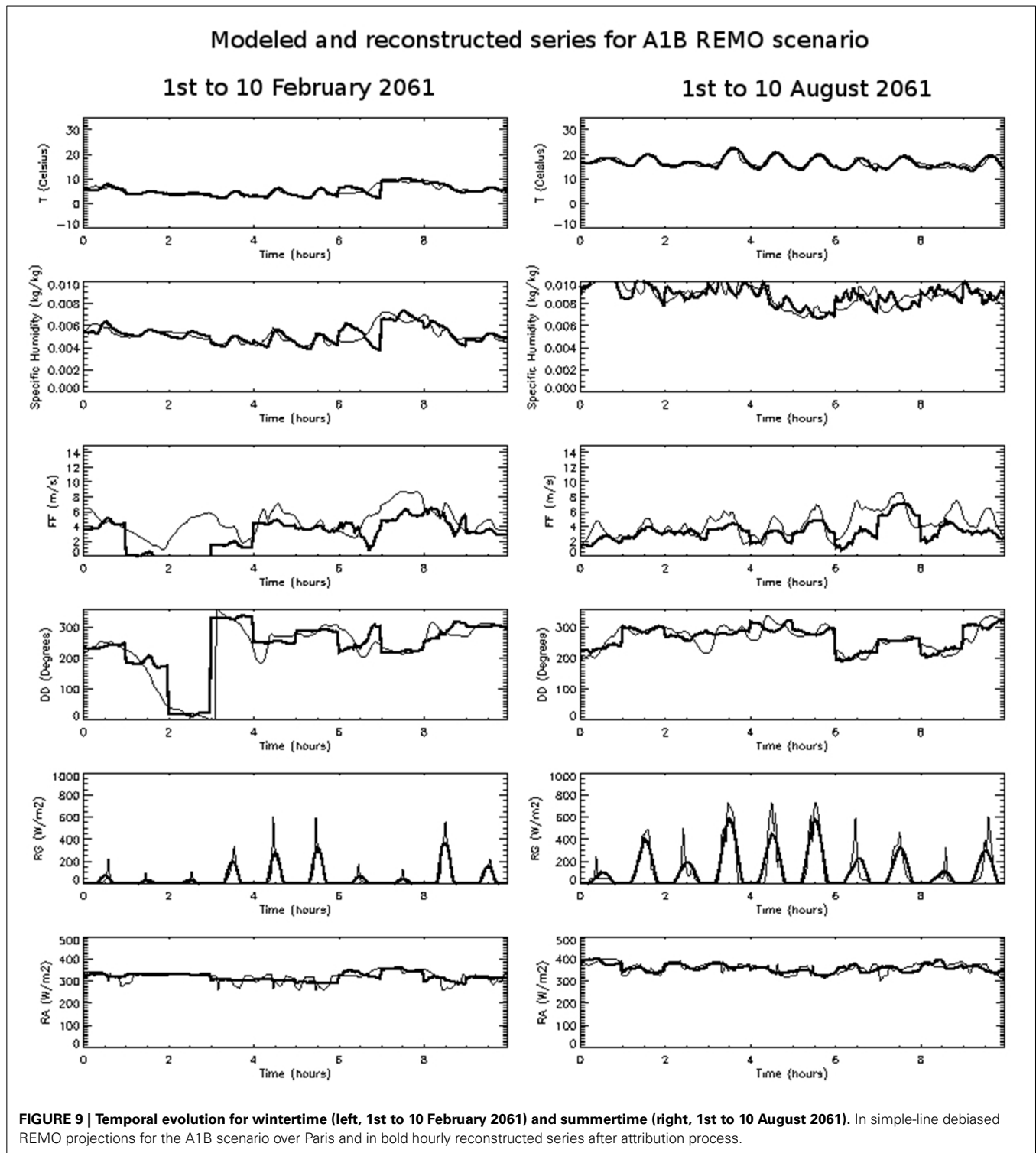
a rich RCM scenarios database that are difficult to be exploited in the framework of off-line SVAT simulations for impact studies due to its temporal resolution. During the ENSEMBLES project climate groups from different countries performed ensemble simulations for Europe at 25×25 km^2 horizontal resolution for the A1B emission scenario. Seven model outputs were retained:

ECHAM5-r3–RCA, ECHAM5-r3–RACMO, ECHAM5-r3–REMO; HadCM3Q0–CLM, HadCM3Q0–HadRM3Q0; BCM–RCA and BCM-DMI–HIRHAM5 (first name correspond to the forcing Global Climate model, the second name to the Regional Climate model). This choice was done in function of the availability of the following daily variables used in the attribution process

Table 2 | Linear Pearson correlation coefficient for A1B, B1, and E1 scenarios for the period 2061–2090 for temperature, specific humidity, wind speed, surface solar radiation, and downward long-wave radiation.

Scenario	T	q	ff	RG	RA
A1B	0.98	0.92	0.32	0.94	0.87
B1	0.99	0.92	0.31	0.94	0.87
E1	0.99	0.93	0.30	0.94	0.86

(maximum, minimum and mean temperature and relative humidity, mean wind speed and direction, and mean precipitation) and period (at least runs from 1961 to 2090). Output time-series of daily modeled data are extracted at nearest grid point.

After a bias correction, a cluster number was attributed to every day of climate scenarios produced by these seven models using the method explained in Section First validation: cluster attribution and hourly reconstruction for the construction period (1998–2008).

From a statistical point of view mean values and climate variability are represented by Regional Climate Models but they do not reproduce the chronology of fields. For this reason, in absence of hourly scenarios, validation of reconstructed series from the ENSEMBLES database cannot be done with a day by day comparison as shown in Section Validation and Application to climate scenarios from Regional Climate Models simulations and only a statistical analysis makes sense. As modeled mean (and if available maximum and minimum) values are directly used, the hourly reconstructed series reproduce intensity of extreme events predicted by climate models and the temporal trends explored in typical climatic analysis as daily, seasonal or annual mean values. For impact studies where an accurate value of the length and intensity of extreme precipitation or gusts is needed, as for example in some hydrological or wind farms production impact studies, a complementary analysis of the clusters could be performed in order to obtain clusters where the precipitation or wind field has higher weight in the statistical analysis.

The main advantage of the method with regard to others cited in the introduction are the availability and light computing treatment of the data. The large coverage around the world of the meteorological stations makes the data collection easy and free available to anyone. The k-clustering algorithm is implemented in a variety of free programming languages and can be run in a simple computer or laptop. The attribution method is based on variables that are also available at daily frequency in climate scenarios databases so it is directly applicable to this kind of climate projections. Hourly reconstructed series are obtained using the observed (or modeled) mean value. If maximum and minimum values are also available, the shape of the cluster diurnal cycle is modulated in amplitude accordingly allowing extremes higher than those observed during the construction period if those are represented in the climate projections.

Even though interesting applications can be developed from the cluster attribution, for example to relate a kind of type of meteorological situation with impact factors in health as pollutants concentrations or thermal stress or to contextualize single field campaign days within a larger climatology. Also, with the aim of improve Regional Climate models parameterizations, it is possible to relate a type of day with strong biases in the RCM projections for a reference period to identify the physical process involved in this type of meteorological situations.

This method has been developed for local climate impact studies. In this case numerical simulations are performed over an area of some tenths of kilometers and, normally, only one site of observations is used to force the SVAT model at certain height over the canopy. It is during the numerical simulation that diagnostic atmospheric fields near the surface reproduces spatially the heterogeneity of the terrain. For bigger domains two types of strategies can be used to take into account observations (or model data) from a plurality of points. If the climatology of the area can be represented by a single set of clusters then one classification is done. In the attribution process, logically, the same type of day should be found for all sites and the reconstructed series for each site will reproduce the heterogeneity of observed (or simulated) fields. If in the attribution process there is no coherence between the sites, then, the domain should be divided into regions where the clustering method will be applied separately.

SUPPLEMENTARY MATERIAL

The Supplementary Material for this article can be found online at: http://www.frontiersin.org/journal/10.3389/fenvs.2014.00040/abstract

REFERENCES

Corti, S., Molteni, F., and Palmer, T. N. (1999). Signature of recent climate change in frequencies of natural atmospheric circulation regimes. *Nature* 398, 799–802. doi: 10.1038/19745

Déqué, M., Martin, E., and Kitova, N. (2011). *Response of the Snow Cover over France to Climate Change*. Internal Communication. SCAMPEI project. Available online at: http://www.cnrm.meteo.fr/scampei/

Ducharne, A., Habets, F., Déqué, M., Evaux, L., Hachour, A., Lepaillier, et al. (2009). *Impact du Changement Climatique sur les Ressources en eau et les Extrêmes Hydrologiques dans les Bassins de la Seine et la Somme, Rapport Final du Projet RExHySS, Programme GICC*, 62. Available online at: http://www.sisyphe.jussieu.fr/~agnes/rexhyss/documents_rapport.php

Gonzalez-Aparicio, I., and Hidalgo, J. (2012). Dynamically based daily and seasonal future temperature scenarios analysis for the northern of Iberian Peninsula. *Int. J. Climatol.* 32, 1825–1833. doi: 10.1002/joc.2397

He, J., Tan, A. H., Tan, C. L., and Sung, S. Y. (2002). "On quantitative evaluation of clustering systems," in *Information Retrieval and Clustering*, eds W. Wu and H. Xiong (Kluwer Academic Publishers).

Hewitt, C. D. (2005). The ENSEMBLES Project: providing ensemble-based predictions of climate changes and their impacts. *EGGS newsletter*. 13, 22–25. Available online at: http://www.the-eggs.org/?issueSel=24

Hidalgo, J. (2012a). *Scénarios Climatiques Pour le Projet ACCLIMAT*. Toulouse: Scientific report (in French).

Hidalgo, J. (2012b). *Scénarios Climatiques Pour le Projet MUSCADE*. Toulouse: Scientific report (in French).

Huth, R., Beck, C., Philipp, A., Demuzere, M., Ustrnul, Z., Cahynová, M., et al. (2008). Classifications of atmospheric circulation patterns: recent advances and applications. *Ann. N.Y. Acad. Sci.* 1146, 105–152. doi: 10.1196/annals.1446.019

Lemonsu, A., Kounkou-Arnaud, R., Desplat, J., Salagnac, J. L., and Masson, V. (2012). Evolution of the Parisian urban climate under a global changing climate. *Clim. Change* 116, 679–692. doi: 10.1007/s10584-012-0521-6

Najac, J., Lac, C., and Terray, L. (2011). Impact of climate change on surface winds in France using a statistical-dynamical downscaling method with mesoscale modeling. *Int. J. Climatol.* 31, 415–430. doi: 10.1002/joc.2075

Nakicenovic, N., Alcamo, J., Davis, G., de Vries, B., Fenhann, J., Gaffin, S., et al. (2000). *IPCC Special Report on Emissions Scenarios*. Cambridge: Cambridge University Press.

Philipp, A., Bartholy, J., Beck, C., Erpicum, M., Esteban, P., Fettweis, X., et al. (2010). Cost733cat - A database of weather and circulation type classifications. *Phys. Chem. Earth* 35, 360–373. doi: 10.1016/j.pce.2009.12.010

Querguiner, S., Martin, E., Lafont, S., Calvet, J. C., Faroux, S., and Quintana-Seguí, P. (2012). Uncertainties associated to the representation of land surface processes in climate change impact studies: a case study for French Mediterranean regions. *Nat. Hazards Earth Syst. Sci.* 11, 2803–2816. doi: 10.5194/nhess-11-2803-2011

Quintana-Seguí, P., Ribes, A., Martin, E., Habets, F., and Boé, J. (2010). Comparison of three downscaling methods in simulating the impact of climate change on the hydrology of Mediterranean basins. *J. Hydrol.* 383, 111–124. doi: 10.1016/j.jhydrol.2009.09.050

Quintana-Seguí, P., Habets, F., and Martin, E. (2011). Comparison of past and future Mediterranean high and low extremes of precipitation and river flow projected using different statistical downscaling methods. *Nat. Hazards Earth Syst. Sci.* 11, 1411–1432. doi: 10.5194/nhess-11-1411-2011

Stone, D. A., Weaver, A. J., and Stouffer, R. J. (2001). Projection of climate change onto modes of atmospheric Variability. *J. Clim.* 14, 3551–3565. doi: 10.1175/1520-0442(2001)014%3C3551:POCCOM%3E2.0.CO;2

Tanaka, K., Yoichi, F., Tsugihiro, W., Toshiharu, K., and Shuichi, I. (2006). Projection of the impact of climate change on the surface energy and water balance in the Seyhan River Basin Turkey. *Annu. J. Hydraul. Eng.* 50, 31–36. doi: 10.2208/prohe.50.31

Cold surge activity over the Gulf of Mexico in a warmer climate[1]

Edgar P. Pérez[1], Víctor Magaña[2]*, Ernesto Caetano[2] and S. Kusunoki[3]

[1] Colegio de Ciencia y Tecnología, Universidad Autónoma de la Ciudad de México, Mexico City, Mexico
[2] Geografía Física, Clima y Sociedad, Instituto de Geografía, Universidad Nacional Autónoma de México, Mexico City, Mexico
[3] Climate Research Department, Meteorological Research Institute, Tsukuba, Japan

Cold surges are a dominant feature of midlatitude tropical interaction. During the North Hemisphere (NH) winter, midlatitude waves propagating from the Rocky Mountains into the Gulf of Mexico result in cold surges, also known as Nortes or Tehuantepecers, associated with severe weather over the southern part of Mexico. The magnitude of their intense surface winds, precipitation and drops in surface temperature depends on the characteristics of the midlatitude wave propagating into the tropics. The high spatial resolution (20 × 20 km) version of the TL959L60-AGC Model of the Meteorological Research Institute of Japan is used to examine changes in cold surge activity under the A1B greenhouse gas emission scenario for the 2080–2099 period. The model realistically reproduces the spatial and temporal characteristics of cold surges for the 1980–1989 control period. The effect of changes in baroclinicity, static stability and mean flow over North America suggest that in a warmer climate, increased cold surge activity over the Gulf of Mexico would occur. However, these systems would have shorter wavelength (higher phase speeds) and shorter lifespans that could reduce the total amount of winter precipitation. The increased frequency of cold surges over the Gulf of Mexico would be a consequence of weaker baroclinicity and static stability in the lower troposphere over the cold surge genesis region, along with more dominant westerly winds, resulting from ENSO-like conditions in the atmospheric circulations over North America.

Keywords: cold-surge, midlatitude-tropical interaction, climate change, El Niño, Gulf of Mexico

INTRODUCTION

Tropical and subtropical regions are frequently affected by winter surges of cold air that propagate from the midlatitudes, as a form of atmospheric midlatitude-tropical interactions (Colle and Mass, 1995). Cold surges over the Gulf of Mexico, also known as *Nortes* (Magaña et al., 2003) or Tehuantepecers (Trasviña et al., 1995), are related to masses of cold air and high surface pressure that originate over the northwestern parts of the Rocky Mountains (their genesis region) and move southeastward into the tropics. They produce air surface temperature drops as large as 20°C in 24 h, in the Veracruz region (**Figure 1**) and precipitation of up to 200 mm day^{-1} along the coastal zone of eastern Mexico, as well as intense gap winds over the Tehuantepec Isthmus (Henry, 1979; Schultz et al., 1997, 1998). Reding (1992) estimates that 70–90% of winter precipitation in the southern Mexico—Central American region is related to these phenomena. The strong winds associated with the cold surge over the Tehuantepec Isthmus may be between 10 to 20 ms^{-1}, but with gust winds of up to 60 ms^1, that result from the large meridional pressure gradient between the Gulf of Mexico and the northeastern tropical Pacific.

Their effects may last between 2 to 6 days, depending on the phase speed (wavelength) of the system (Schultz et al., 1998). On the average, 20–25 cold surges affect the Gulf of Mexico from October through March. However, there is substantial interannual variability in cold surge activity, mainly in relation to El Niño/Southern Oscillation (ENSO) (Magaña et al., 2003). During El Niño (La Niña), more (less) cold surges, with shorter (longer) than average wavelengths affect Mexico and faster (slower) phase speeds, leading to less (more) winter precipitation. The more frequent passage of cold surges over the Gulf of Mexico during El Niño is related to changes in the mean flow induced by the Pacific North American (PNA) pattern that affects the subtropical jet stream, forcing the mean flow into a more westerly state over this region (Magaña and Ambrizzi, 2005). This allows transients, such as cold surges, to propagate deep into lower latitudes, as in a westerly duct (Webster and Holton, 1982). Cold surges with higher phase speed (Vazquez, 1999) may result in negative precipitation anomalies during the Northern Hemisphere (NH) winter over southeastern Mexico. Slower cold surges (longer wavelengths), produce precipitation for a longer period that frequently result in more rainfall, as in 1999 or 2007 (Landa et al., 2009).

As a result of climate change, the mean atmospheric meridional temperature gradient, the baroclinicity, the static stability and the mean flow are to be affected (e.g., Teng et al., 2008). These changes may have important consequences in climate at

---

[1]The first author, Edgar P. Pérez, died in December 2010, after the first draft of this manuscript was completed. This work is now published as a memorial to him.
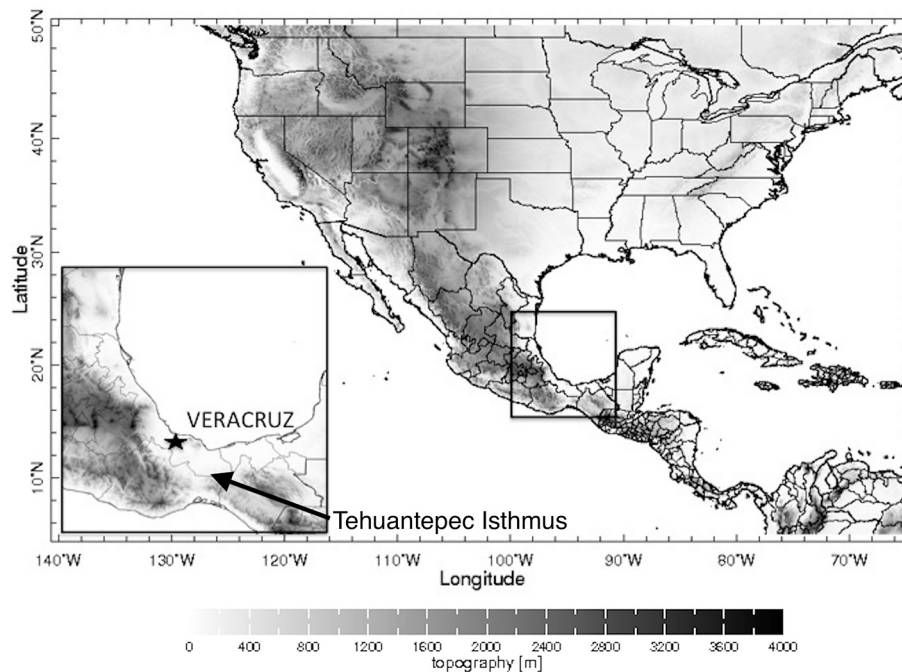
FIGURE 1 | Topography over North America. The location of the city of Veracruz, Mexico and the Tehuantepec Isthmus are indicated.

the regional level (IPCC, 2013) for instance, in the tropical Americas (Karmalkar et al., 2011), as they alter cold surge activity. Considering the importance of these phenomena for the winter climate in the Mesoamerica region, it is interesting to examine the dynamics involved in cold surge activity in a warmer climate. By means of climate change experiments baroclinicity, static stability and the mean flow over North America are diagnosed to determine how this may affect cold surge activity. The regional climate model TL959L60 AGCM from the Earth Simulator of the Meteorological Research Institute (MRI) of Japan, is a state of the art model that has proven to be an adequate tool to examine regional climate change signals (Kusunoki et al., 2006). In particular, it has shown high skill to reproduce present climate features over the tropical Americas (Perez et al., 2007), which makes it a valuable tool to interpret climate change simulations based on physical principles. Therefore, the main goal in the present paper is to explore changes in the mean atmospheric state of North America in order to determine the large-scale factors that control cold surge activity in a warmer climate and examine regional climate change signals.

In Section Data and Methodology, the paper describes the data and methodology used in the study. The main results of this work are given in Section Changes in Cold Surge Activity over the Gulf of Mexico in a Warmer Climate. Section Discussion presents a brief discussion of the results and conclusions are given in Section Conclusions.

DATA AND METHODOLOGY

THE TL959L60 AGCM

The TL959L60 AGC regional climate model is part of the Earth Simulator and its characteristics, as well as its skill to simulate various atmospheric processes has been discussed in detail by

Mizuta et al. (2006). Kusunoki et al. (2006) have examined a very high spatial resolution (20 × 20 km, 60 vertical levels) control run for the present climate and for a climate under the IPCC SRES A1B greenhouse gas emissions scenario for the end of the twenty-first century. Their TL959L60-AGC present climate experiment was conducted with observed climatological SSTs averaged from 1982 to 1993 and for the future climate experiment, the simulation was done using SSTs, projected with the MRI-CGCM2.3 (Yukimoto et al., 2006). Although they did only one climate change realization with this spatial resolution, they results serve for a process study to analyze regional climate change signals. The main goal of the present study is to examine the dynamical mechanisms that result in diminished NH winter precipitation over the central southern part of Mexico in relation to changes in cold surge activity.

In the preset study, 10 years of data of the TL959L60-AGC control (1980–1989) and future climate (2080–2089) experiments (Kusunoki et al., 2006) from October to March have been used to examine cold surge activity over the IAS. The model skill to simulate climate over Mexico has been examined by means of a comparison between present day simulations and gridded observed data (Perez et al., 2007). For instance, the orographic effect on the mean winter precipitation pattern for the present climate (**Figure 2A**) is reasonably reproduced by the model (**Figure 2B**). Winter precipitation over Mexico for the future climate (not shown) maintains the same spatial distribution, but compared with the present climate simulations it shows a reduction over the Veracruz region of the order of 0.5 mm/day (around 10%) (**Figure 2C**). Since cold surge events produce most of the winter precipitation over the southern part of the Gulf of Mexico, it is likely that changes in such systems be responsible for such regional climate change.
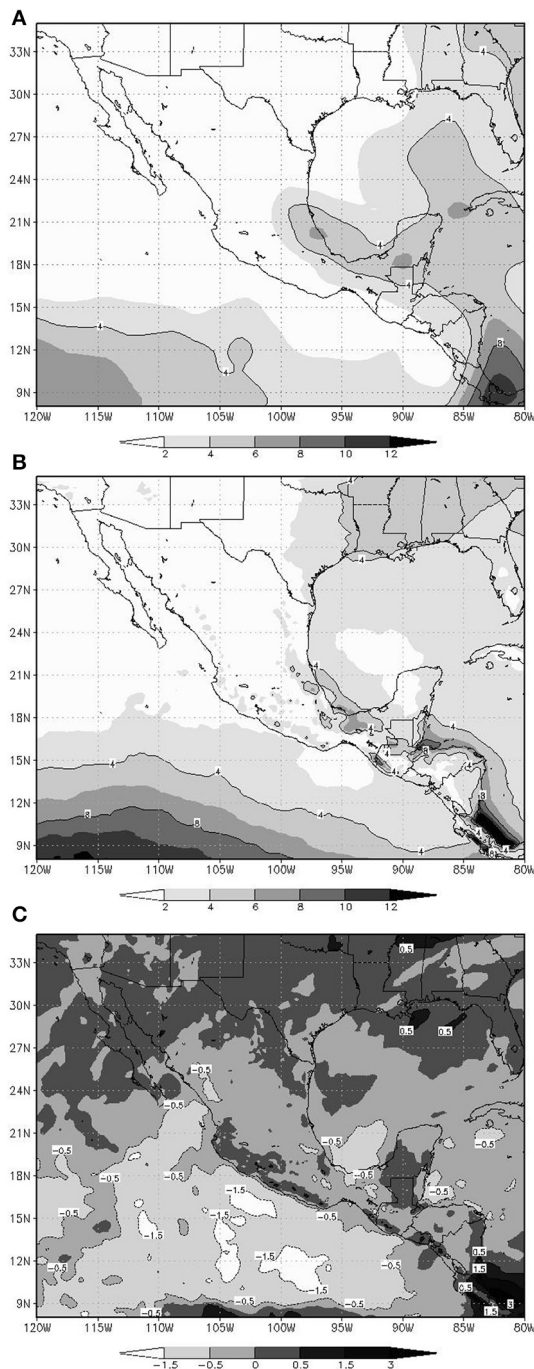
FIGURE 2 | Mean NH winter precipitation (mm day⁻¹). (A) Obtained from the NCEP/NCAR reanalysis for the 1980-1988 period, **(B)** as in **(A)**, but obtained with the TL959L60 AGC model for the 1980–1989 period, and **(C)** Change in NH winter precipitation (mm day⁻¹) for the 2080–2088, relative to 1980–1989 simulated with the TL959L60 AGC Model.

COLD SURGE ACTIVITY OVER MEXICO

Cold surges over the Gulf of Mexico have been characterized by means of various meteorological parameters such as surface pressure, intense winds, surface temperature

drops or intense precipitation events (Reding, 1992; Schultz et al., 1997, 1998). Most of these meteorological signals are related to the meridional propagation of cold anticyclones that lead to intense northerly and northeasterly winds, large temperature drops and precipitation over the southern part of the Gulf of Mexico, as in Veracruz. Following Magaña (1999), a cold surge may be identified since it produces:

(1) Intense winds (>10 m/s) with a northerly component over the Gulf of Mexico,
(2) temperature drops of 2°C or more in 24 h over the southeast coast of the Gulf of Mexico,
(3) precipitation over the southern Gulf of Mexico states.

Indices of these meteorological parameters over southern Mexico serve to construct composite maps of atmospheric patterns associated with the evolution of cold surges for the present and future climate. The model patterns of cold surges adequately compare with those obtained by Vazquez (1999) with NCAR/NCEP reanalysis data (Kalnay et al., 1996). Even more, the number of cold surge events compares well between with the observed one, i.e., around 25 events between October and March (Magaña, 1999).

In the present day experiment, cold surges present spatial and temporal characteristics similar to the observed ones. In this way, 2 days prior to the impact of a cold surge over Veracruz, there is a high-pressure system over the Rocky Mountains and dominant easterly flow over the Gulf of Mexico (**Figure 3A**). Gap flow over the Tehuantepec Isthmus is weak. As the midlatitude wave and the associated high-pressure system move southeastwards into the Gulf of Mexico, the mass of cold air interacts with the warm moist air of the Gulf of Mexico, resulting in a cold surge (Schultz et al., 1997). The anticyclonic circulation produces winds over the Gulf of Mexico, with a northerly component, that impacts the region of Veracruz (**Figure 3B**). The meridional pressure gradient between the high pressure in the northern part of the Gulf of Mexico and the lower surface pressure in the northeastern tropical Pacific generates intense gap winds across the Tehuantepec Isthmus, in southern Mexico. Mean maximum surface wind intensity over the southern Gulf of Mexico may exceed $15\,\mathrm{ms}^{-1}$. The cold surge produces intense precipitation along the frontal zone and along the eastern coast of Mesoamerica due to the orographic effect of the eastern Sierra Madre. As the midlatitude wave propagates eastwards (**Figure 3C**), the cold surge affects part of the Yucatan peninsula, Central America and the Caribbean Sea, but their effects weaken over the Veracruz region. The winds over the southern part of the Gulf of Mexico change from northerly to northeasterly.

Given the close resemblance between the cold surge (i.e., *Norte*) composite pattern produced by the regional climate model, in the present and future climate, and the observed patterns, it is feasible to examine the mean large scale atmospheric conditions in a future (warmer) climate that may affect the activity of such systems.
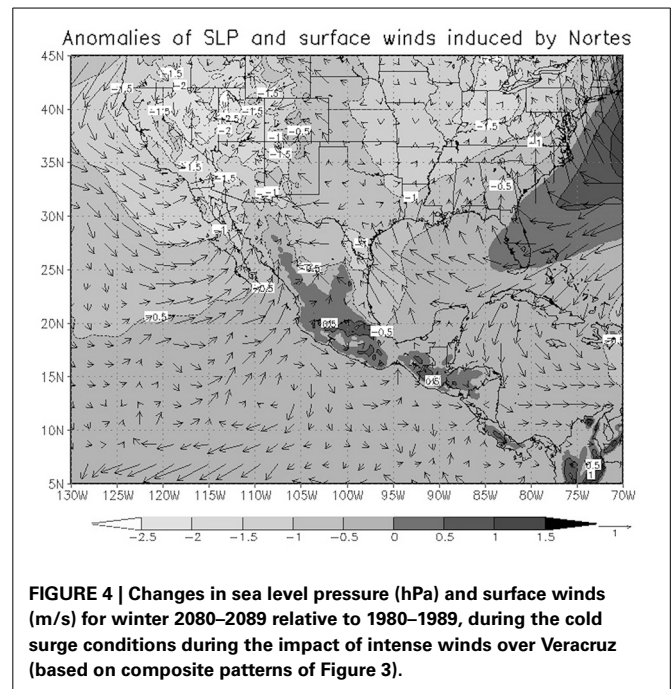
FIGURE 4 | Changes in sea level pressure (hPa) and surface winds (m/s) for winter 2080–2089 relative to 1980–1989, during the cold surge conditions during the impact of intense winds over Veracruz (based on composite patterns of Figure 3).

FIGURE 3 | Composite pattern of surface pressure and surface winds. (A) Two days prior to the impact of the cold surge over Veracruz, (B) during the impact, and (C) 2 days after the impact of a cold surge in Veracruz, Mexico.

CHANGES IN COLD SURGE ACTIVITY OVER THE GULF OF MEXICO IN A WARMER CLIMATE
CHANGES IN COLD SURGE ACTIVITY
The TL959L60-AGC model generates around 252 cold surge events for the 10 years period of the control run (around 25 per year), which compares fairly well with the 23 cases/year obtained with the NCAR/NCEP reanalysis (Kalnay et al., 1996)for the same 1980–1989 period (Magaña et al., 2003). For the future climate simulation, the model generates around 283 cold surges in 10 years (around 28 cold surges per year), which shows a slight increase of the synoptic wave activity over the Gulf of Mexico in a warmer climate. This increase in the number of cold surges may seem relatively small (around 10%), but it is comparable to the interannual variability (Vazquez, 1999). Even more, the interannual variations in the number of cold surges may result in changes in winter precipitation in southern Mexico of 10–15%, between dry and wet winters, as during El Niño and La Niña years. Since winter precipitation over the southern Gulf of Mexico region is less than average during El Niño, it is not only the number these systems, but also their characteristics what determine the amount of rainfall. For instance, in the warmer climate experiment, there is a tendency for the cold surge northerly winds to be weaker (**Figure 4**) which might reduce orographically forced precipitation. Cold surge precipitation also depends on the duration of the event, which in turns depends on the phase speed of the system.

Cold surge properties, such as their lifespan, intensity and surface temperature drops over the Gulf of Mexico, are related to changes in the characteristic wavelength of the associated mid-latitude system that propagates into the tropics. Lifespan of a cold surge may be defined as the number of consecutive days during which the criteria defined in Section Data and Methodology for the impact over Veracruz are met. In the future (warmer) climate, cold surges are expected to be more frequent, but with shorter lifespans (**Figure 5A**). The percentage of systems inducing low temperature decreases ($<5°C$) might increase, but a few more events with large temperature drops ($>8°C$) might also occur (**Figure 5B**). The number of extremely intense northerly winds would also tend to decrease in a warmer climate (**Figure 5C**) with
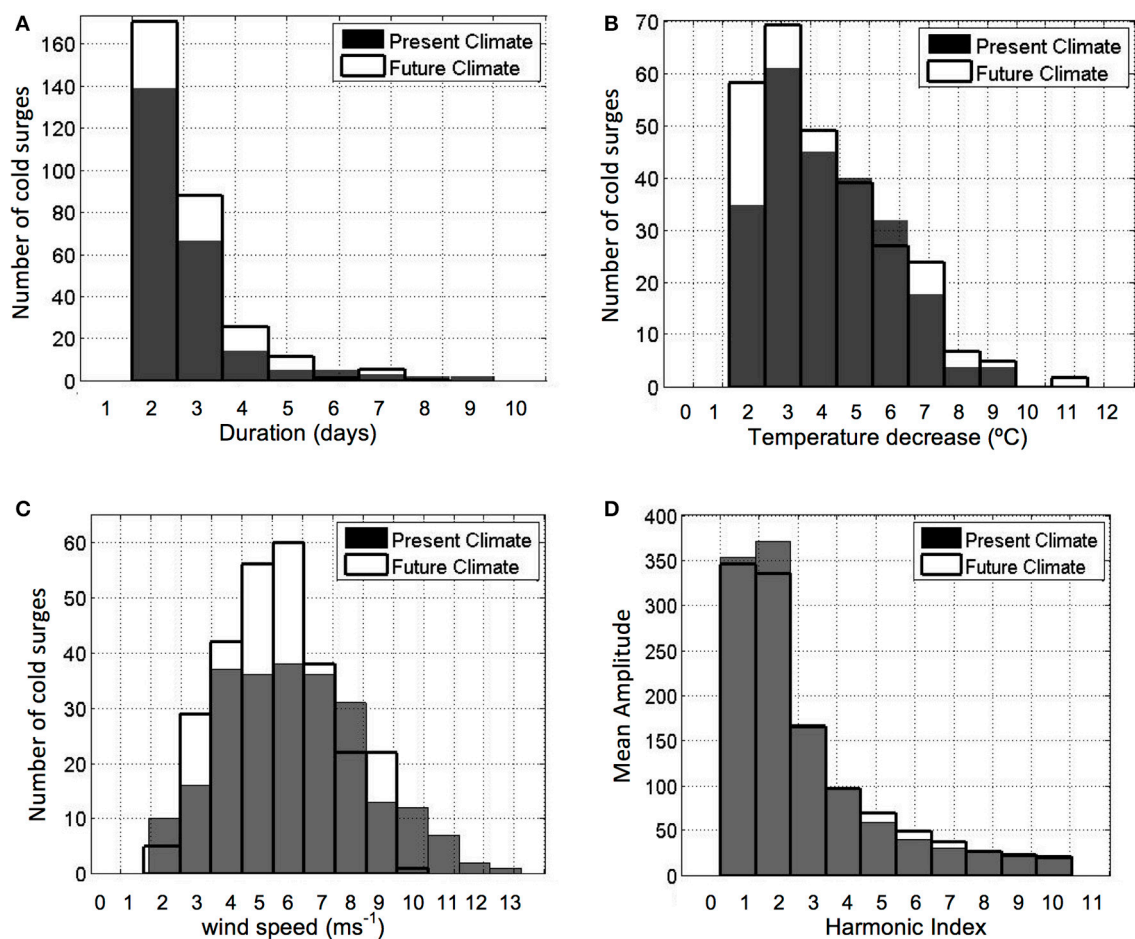
FIGURE 5 | Frequency of cold surges, computed from the TL959L60-AGCM for present and future (warmer) climate conditions, as a function of: (A) duration (days). (B) The associated temperature decreases (°C), and **(C)** mean *Norte* surface winds (ms^{-1}). **(D)** Mean amplitude of the midlatitude wave at 500 hPa (geopotential meters) associated with the cold surge as a function of the dominant wavelengths.

wind speeds larger than $10\,\mathrm{ms}^{-1}$ becoming less frequent. The characteristic wavelength of the systems may be obtained by harmonic analyzing geopotential height at 500 hPa over the domain of study (18–29°N, 170–50°W). This analysis suggests for future climate conditions a decrease in the dominant zonal wavenumbers (1–2) within the domain, corresponding to wavelengths of approximately 12,200–6600 km of wavelength respectively. In the future climate, and a slight enhancement of the zonal wavenumbers 5–7, corresponding to zonal wavelengths of around 2000 km is expected (**Figure 5D**). Shorter wavelengths mean faster phase speeds and consequently shorter system lifespans (**Figure 5A**), and reduced precipitation periods. A dominance of shorter wavelength systems in the atmosphere is consistent with the dynamical response of a rotating flow, when the pole-equator temperature gradient is decreased (Hide et al., 1977). The tendency to have negative NH winter precipitation anomalies over the southern part of the Gulf of Mexico, is related to shorter wavelength systems propagating more rapidly from mid latitudes into the tropics with weaker *Norte* winds, as during an El Niño event (Magaña, 1999). Some of the driest winters in the southern part of Mexico
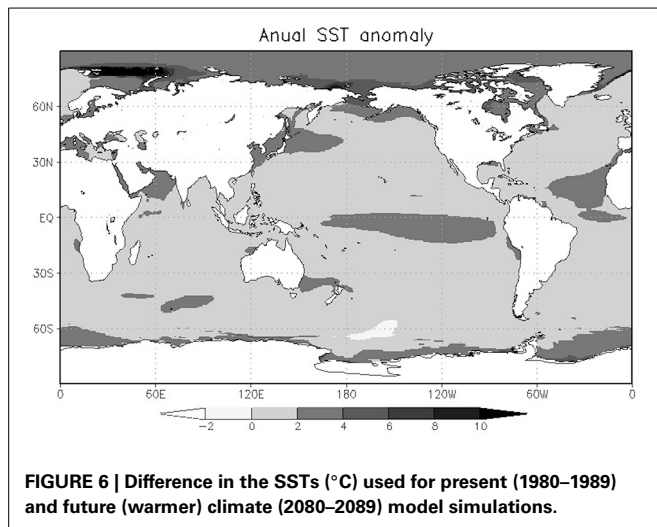
tend to occur under El Niño conditions (Halpert and Ropelewski, 1992).

CHANGES IN THE MEAN SST CONDITIONS

In the climate change experiment with the TL959L60 AGC Model the imposed surface boundary conditions are important. The SST pattern in the future climate experiment (**Figure 6**) resembles El Niño conditions, with a dominant warm anomaly over the central eastern Pacific. This SST anomaly reflects in changes in the mean atmospheric state and consequently, in changes in cold surge activity in a similar way as during El Niño NH winter (Magaña et al., 2003).

The flow regimes that appear in a differentially heated rotating fluid are constrained mainly by the magnitudes of the thermal Rossby and Taylor numbers (Hide et al., 1977). If the pole-equator temperature difference ΔT decreases, while the other system parameters remain unchanged, the configuration in the fluid's regime diagram tends to shift to smaller thermal Rossby numbers, favoring weaker waves of higher wave numbers (i.e., shorter wavelengths). The mean temperature gradient in the

FIGURE 6 | Difference in the SSTs (°C) used for present (1980–1989) and future (warmer) climate (2080–2089) model simulations.

FIGURE 7 | Mean meridional temperature gradient (°C/1000 km) over the domain, for every year of integration.

numerical experiments shows a decrease in intensity as determined in the meridional temperature gradient over the domain of study (**Figure 7**).

This condition tends to produce a change in the dominant zonal wave numbers to shorter wavelengths (higher phase speed), which could explain the increased number of cold surges or *Nortes* in a warmer climate, as well as their shorter lifespans. However, the number of systems that form in the midlatitudes and propagate into the tropics, also depend on the atmospheric static stability, their evolution on the Eady growth rate and their propagation into the tropics in the characteristics of the mean flow.

BAROCLINICITY AND ATMOSPHERIC STATIC STABILITY

Baroclinic instability is the main source of energy for synoptic midlatitude systems. According to Van Loon (1967), a weaker meridional gradient of temperature, as that projected for a global warming scenario, would manifest in a local lower atmospheric baroclinic response with a consequent diminished midlatitude wave activity (Geng and Sugi, 2008). However, along with the meridional temperature gradient, the stability structure of a baroclinic atmospheric is relevant in inducing wave activity. Following Walland and Simmonds (1999), the baroclinicity of the atmosphere for present and future conditions, may be examined in terms of the meridional temperature gradient and the static stability of the atmosphere, considering the amplification rate of the most unstable baroclinic wave in the lower troposphere. Teng et al. (2008) found in one CCSM3 twenty-first century A1B scenario that there was significant increase in the extratropical cyclone frequency on the US west coast and decrease in Alaska. Lindzen and Farrell (1980), Walland and Simmonds (1999), and Teng et al. (2008), suggest that the baroclinicity of the atmosphere for present and future climate conditions can be determined considering the atmospheric static stability and the maximum Eady growth rate at the lower and middle troposphere.

Some theoretical experiments tend to show that waves belonging to the short-wave part of the spectrum of unstable waves are more sensitive to changes in the static stability parameter than waves belonging to the long-wave part of the spectrum
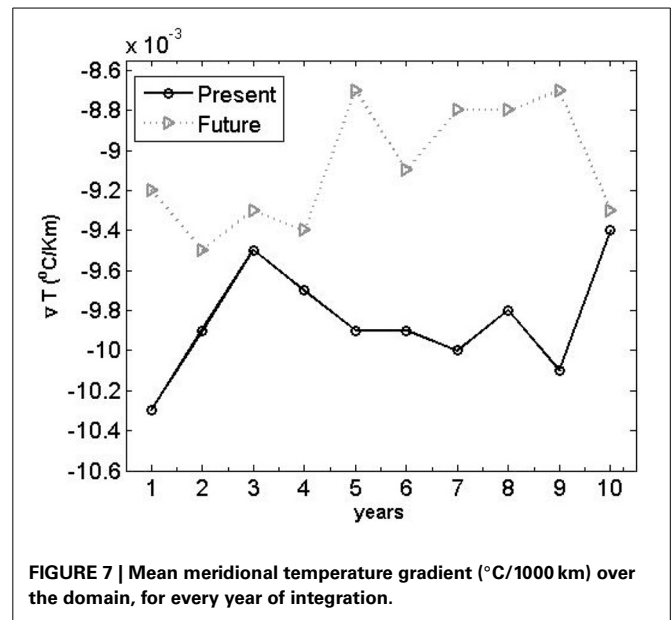
(Soldatenko and Tingwell, 2013). The model experiment for the future climate indicates that during the NH winter the static stability will decrease polewards and increase equatorwards in the lower troposphere (**Figure 8**). In particular, there is a decrease in static stability over the northern Rocky Mountains region, i.e., the cold surge genesis region. A lower vertical stability condition implies that a given meridional temperature gradient, even if weak, would have greater impacts, in terms of baroclinic instability, than a stronger gradient would have in the presence of higher atmospheric static stability conditions. In other words, contrary to the present climate conditions where both, the meridional temperature gradient and the atmospheric static stability are high, over the cold surge genesis region the increasing frequency of *Nortes* in a warmer climate may follow from a weaker atmospheric stability in midlatitudes even with a weaker meridional temperature gradient.

Since the wavelength of maximum instability is proportional to the ratio of static stability to the square of the rotation rate (Holton, 1992), lower static stability conditions north of 50°N mean that the wave number of maximum instability increases over that region (i.e., the wavelength decreases) and then shorter life-span systems would dominate at the cold surge genesis region. Furthermore, since baroclinic waves with shorter wavelengths are rather inefficient for the vertical and horizontal transport of heat, they feed back to the mean flow the weaker static stability conditions where they onset. The Eady growth rate (σ) may be expressed as (Eady, 1949):

$$\sigma = 0.3098\, f\, |\partial U(z)/\partial z|\, N^{-1},$$

where N is the Brunt-Vaisala frequency, 0.3098 is a nondimensional coefficient, f is the Coriolis parameter, and $U(z)$ is the vertical structure of the zonal wind. This expression of the maximum Eady growth rate is similar to Teng et al.'s (2008). In the TL959L60-AGC model, baroclinicity changes in the future
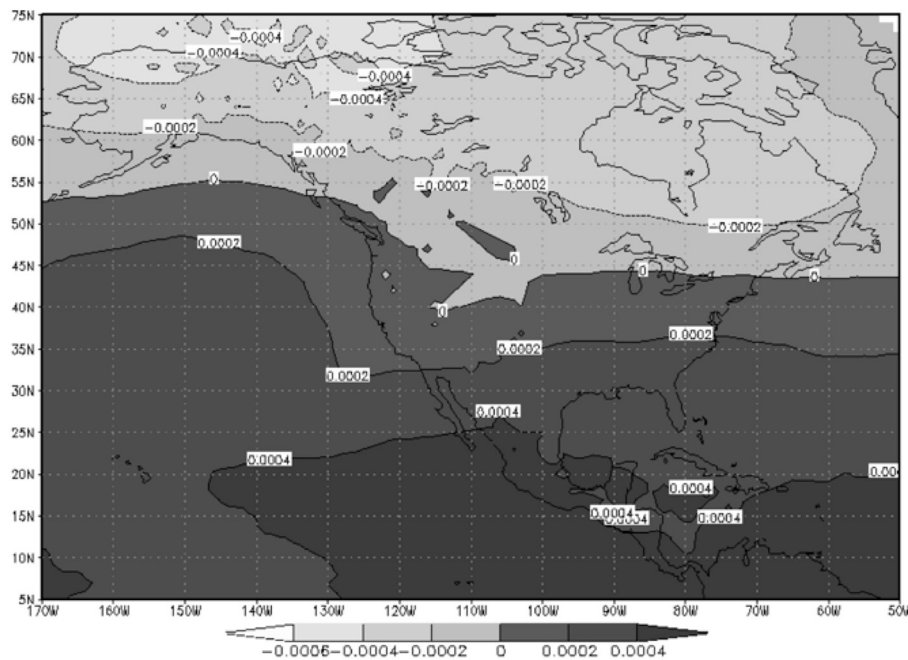
FIGURE 8 | Change of static stability (K hPa^{-1}) between 850 and 500 hPa for the NH winter (2080–2089) conditions minus (1980–1989) conditions.

climate simulation are small over the most of North America (**Figure 9**). In the warmer climate, baroclinicity tends to be weaker over western Canada and most of the US, along the path followed by synoptic waves that penetrate into the Gulf of Mexico. In this region, weaker baroclinicity but weaker static stability favors the more frequent genesis of shorter wavelengths that move into the Gulf of Mexico at higher phase speeds, as diagnosed (**Figure 5**).

The alterations to the atmospheric baroclinic instability resulting from the relationship between lower temperature gradients and weaker vertical stability conditions are such that the perturbations in the zonal flow tend to shift to higher frequencies and shorter wavelengths. The Eady growth rate how well deep pressure systems can develop in a weather situation over a specific area. Over most of North America, it tends to decrease (**Figure 9**) indicating more favorable conditions for the development of midlatitude waves of the kind that result in cold surges over the Gulf of Mexico.

CHANGES IN THE MEAN FLOW

Most model projections of climate change agree that there is a southeastward extension of the upper troposphere Pacific jet stream at the jet exit region, triggered by a sort of PNA pattern (**Figure 10**). This El Niño-like anomalous pattern might be responsible of the significant impacts on the West Coast midlatitude wave activity (Teng et al., 2008). The change of the 500 hPa wind field in winter 2080–2089 relative to 1980–1989 (**Figure 10**) resembles some of the changes observed under El Niño conditions (Magaña et al., 2003). During El-Niño years, the anomalous convective heating over the central/eastern Pacific also generates a quasi-stationary Rossby wave known as the Pacific North America

(PNA) pattern (Horel and Wallace, 1981), with cyclonic circulations off the coast of California and the northern coast of the Gulf of Mexico. A PNA pattern appears to form during the NH winter season in the global warming TL959L60-AGC experiment. This pattern enhances the subtropical jet-stream, with a westerly anomaly over the Gulf of Mexico that allows the propagation of Rossby waves deep into the tropics (Webster and Holton, 1982). In the present case, the changes in the atmospheric circulation would favor the intrusion of cold surges over the IAS.

The change in the mean winter circulation at 500 hPa under climate change conditions is qualitatively similar to the winter anomalous circulation observed during the El Niño in which the PNA pattern dominates and the subtropical jet stream shifts southwards and extends eastward promoting that more frontal systems and cold surges propagate to the Gulf of Mexico states and the Caribbean Sea.

DISCUSSION

Relating projected changes in regional climate to those associated with global warming requires a study of dynamical processes. The TL959L60-AGC climate model shows skill in reproducing the atmospheric circulations that result in the winter precipitation patterns over Mexico, mainly in relation to cold surge activity. A global warming projection experiment during the NH winter season has been analyzed and compared with a present climate control run to explain changes in precipitation over southern Mexico by means of examining changes in the midlatitude waves that propagate into the tropics over the Gulf of Mexico. The precipitation scenario suggests a decrease in NH winter precipitation in a warmer climate in the southern part of the Gulf of Mexico. In the future (warmer) climate scenario, midlatitude
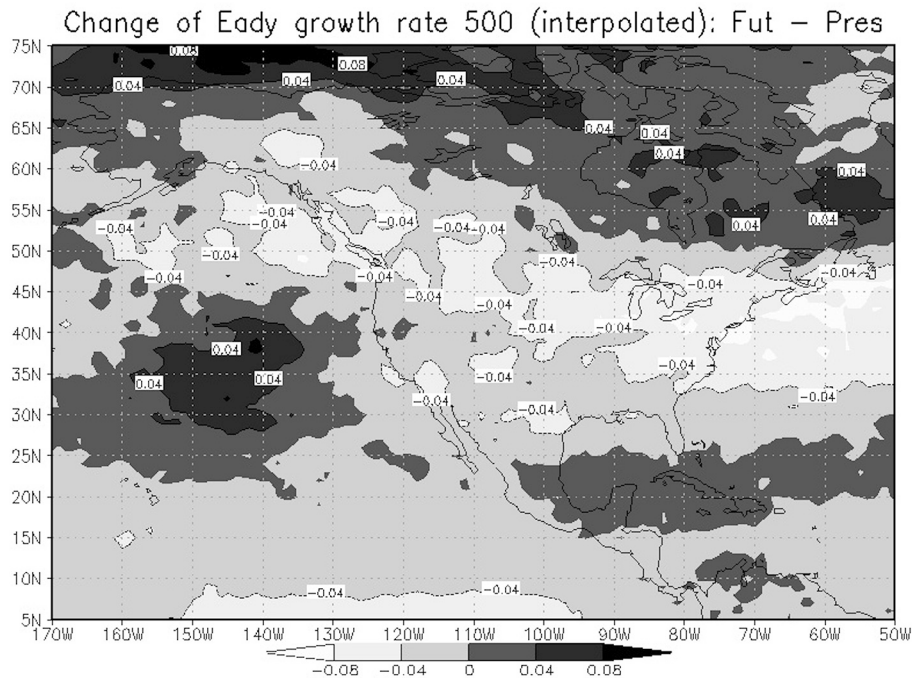
FIGURE 9 | Change of maximum Eady growth rate (day^{-1}) at 500 hPa for the NH winter (2080–2089) minus (1980–1989).
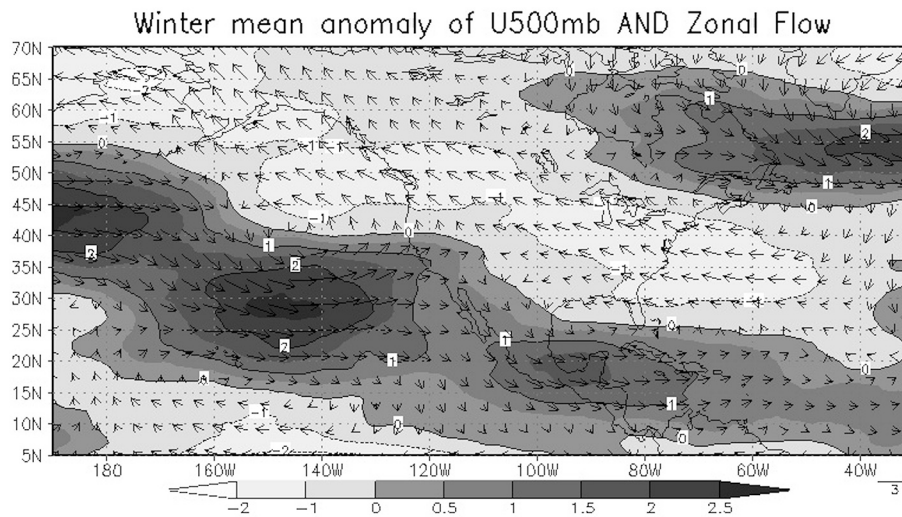
FIGURE 10 | Change of the 500 hPa wind (ms^{-1}) field for the NH winter 2080–2089 relative to 1980–1989. Shades indicate the corresponding anomalies in the 500 hPa zonal flow.

waves propagating into the IAS with shorter wavelengths become more frequent than in present climate and result in shorter lifespans of the systems, as they have a faster phase speed over the Gulf of Mexico. The more frequent occurrence of faster moving cold surges appears to reduce the duration of winter rainfall and translates in less winter precipitation.

The projected characteristics of the midlatitude waves are due to changes in the meridional temperature gradient and the atmospheric static stability. With lower baroclinicity and lower

static stability in the cold surge genesis region, shorter wavelength systems tend to develop and are favored by a lower Eady growth rate. On the other hand, the ENSO like condition used in the future climate experiment results in anomalous westerly atmospheric circulations over the IAS that favor the propagation of more (faster) cold surges into the tropics. The increasing activity of cold surges in the global warming projection tends to produce less winter precipitation in the southern part of the Gulf of Mexico. Trend analyses of precipitation for the twentieth century

indicate a slight decrease in precipitation over the southern part of Mexico. However, the present study does not constitute an attribution experiment.

CONCLUSIONS

In the present study, a robust large-scale response of the atmosphere to increased radiative forcing, which corresponds to a warmer global climate, has been used to provide support to the regional signal of projected decrease in winter precipitation at the regional level in southern part of Mexico. The generation of local or regional climate change scenarios has been one of the main goals in the climate community to build a bridge with those interested in climate change impact scenarios. It is by means of dynamical analyses that relate the local characteristics of climate to large scale processes, that confidence may be gained in climate change projections at the regional level.

The present study takes advantage of the skill of the high spatial resolution model in simulating present day winter climate to analyze how large scale processes may determine climate change at the regional level. It is clear that for a more conclusive answer to the challenge of regional climate change scenarios, one should explore an ensemble of experiments. Such set of realizations with the Earth Simulator is available at a coarser spatial resolution and it may be worth exploring the robustness of the signal examined in this work. There are several studies that address the issue in midlatitude wave activity under climate change (Meehl et al., 2007; Teng et al., 2008), but only a few examine the potential changes in tropical midlatitude interactions in a warmer climate as a process study. This type of analyses may serve to gain confidence in the elements that may determine the signals of climate change in particular regions.

ACKNOWLEDGMENTS

REFERENCES

Colle, B. A., and Mass, C. F. (1995). The structure and evolution of could surges east of the Rocky mountains. *Mon. Weather Rev.* 123, 2577–2610.

Eady, E. (1949). Long waves and cyclone waves. *Tellus* 1, 33–52. doi: 10.1111/j.2153-3490.1949.tb01265.x

Geng, Q., and Sugi, M. (2008). Possible change of extratropical cyclone activity due to enhanced greenhouse gases and sulfate aerosols –Study with a high-resolution AGCM. *J. Climate* 16, 2262–2274. doi: 10.1175/1520-0442(2003)162.0.CO;2

Halpert, M. S., and Ropelewski, C. F. (1992). Surface temperature patterns associated with the Southern Oscillation. *J. Climate* 5, 577–593.

Henry, W. K. (1979). Some aspects of the fate of cold fronts in the Gulf of Mexico. *Mon. Weather Rev.* 107, 1078–1082.

Hide, R., Mason, P. J., and Plumb, R. A. (1977). Thermal convection in a rotating fluid subject to a horizontal temperature gradient: spatial and temporal characteristics of the fully-developed baroclinic waves. *J. Atmos. Sci.* 34, 930–950.

Holton, J. R. (1992). *An Introduction to Dynamic Meteorology, 3rd Edn.* New York, NY: Academic Press.

Horel, J. D., and Wallace, J. M. (1981). Planetary-scale atmospheric phenomena associated with the Southern Oscillation. *Mon. Weather Rev.* 109, 813–829.

IPCC. (2013). "Climate change 2013: the physical science basis," in *Contribution of Working Group I to the Fifth Assessment Report of the Intergovernmental Panel on Climate Change*, eds T. F.Stocker, D. Qin, G.-K. Plattner, M. Tignor, S. K. Allen, J. Boschung, et al. (Cambridge; New York: Cambridge University Press), 1535.

Kalnay, E., Kanamitsu, M., Kistler, R., Collins, W., Deaven, D., Gandin, L., et al. (1996). The NCEP/NCAR 40-year reanalysis project. *Bull. Am. Meteorol. Soc.* 77, 437–471. doi: 10.1175/1520-0477(1996)077%3C0437:TNYRP%3E2.0.CO;2

Karmalkar, A. V., Bradley, R. S., and Diaz, H. F. (2011). Climate change in Central America and Mexico: regional climate model validation and climate change projections. *Clim. Dyn.* 37, 605–629. doi: 10.1007/s00382-011-1099-9

Kusunoki, S., Yoshimura, J., Yoshimura, H., Noda, A., Oouchi, K., and Mizuta, R. (2006). Change of Baiu rain band in global warming projection by an atmospheric general circulation model with a 20-km gris size. *J. Meteorol. Soc. Jpn.* 84, 581–611 doi: 10.2151/jmsj.84.581

Landa, R., Magaña, V., and Neri, Y. C. (2009). *Clima y Agua: Elementos Para la Adaptación al Cambio Climático.* Mexico City: SEMARNAT

Lindzen, R. S., and Farrell, B. F. (1980). A simple approximate result for maximum growth rate of baroclinic instabilities. *J. Atmos. Sci.* 37, 1648–1654.

Magaña, R. V. (1999). *Los Impactos del El Niño en México.* Mexico City: SEP-CONACYT.

Magaña, V., and Ambrizzi, T. (2005). Dynamics of subtropical vertical motions over the Americas during El Niño boreal winters. *Atmosfera* 18, 211–234.

Magaña, V., Vázquez, J., Pérez, J. L., and Pérez, J. B. (2003). *The Impact of El Niño on precipitation in Mexico. Geofísica Int.* 42, 313–330.

Meehl, G. A., Covey, C., Taylor, K. E., Delworth, T., Stouffer, R. J., Latif, M., et al. (2007). THE WCRP CMIP3 Multimodel Dataset: a new era in climate change research. *Bull. Am. Meteorol. Soc.* 88, 1383–1394. doi: 10.1175/BAMS-88-9-1383

Mizuta, R., Oouchi, K., Yoshimura, H., Noda, A., Katayama, K., Yukimoto, S., et al. (2006). 20 km-mesh global climate simulations using JMA-GSM model –Mean Climate States-. *J. Meteor. Soc. Japan,* 82, 1187–1211.

Perez, E., Méndez, J. M., and Magaña, V. (2007). "High spatial resolution climate change scenarios for Mexico based on experiments conducted with the Earth simulator," in *Visualizing Future Climate in Latin America: Results From the Application of the Earth Simulator, Latin America and Caribbean Region Sustainable Development Working Paper 30,* ed W. Vergara (Washington, DC: The World Bank Latin America and the Caribbean Region Sustainable Development Department (LCSSD)).

Reding, P. J. (1992). *The Central American Cold Surge: an Observational Analysis of the Deep Southward Penetration of North America Cold Fronts.* MSc. thesis, Department of Meteorology, Texas A&M University. Available online at: http://www.dtic.mil/dtic/tr/fulltext/u2/a268592.pdf

Schultz, D. M., Bracken, W. E., and Bosart, L. F. (1998). Planetary and synoptic scale signatures associated with Central American cold surges. *Mon. Weather Rev.* 126, 5–27.

Schultz, D. M., Bracken, W. E., Bosart, L. F., Hakim, G. J., Bedrick, M. A., Dickinson, M. J., et al. (1997). The 1993 superstorm cold surge: Frontal structure, gap flow, and tropical impact. *Mon. Weather Rev.* 125, 5–39.

Soldatenko, S., and Tingwell, C. (2013). The sensitivity of characteristics of large scale baroclinic unstable waves in southern hemisphere to the underlying climate. *Adv. Meteorol.* 2013, 981271. doi: 10.1155/2013/981271

Trasviña, A., Barton, E. D., Brown, J., Velez, H. S., Kosro, P. M., and Smith, R. L. (1995). Offshore wind forcing in the Gulf of Tehuantepec, Mexico: the asymmetric circulation. *J. Geophys. Res.* 100, 20649–20663.

Teng, H., Washington, W. M., and Meehl, G. A. (2008). Interannual variations and future change of wintertime extra-tropical cyclone activity over North America in CCSM3. *Clim. Dyn.* 30, 673–686. doi: 10.1007/s00382-007-0314-1

Van Loon, H. (1967). The half yearly oscillations in middle and high southern latitudes and the coreless winter. *J. Atmos. Sci.* 24, 472–486.

Vazquez, A. J. (1999). *Caracterización Objetiva de Los Cold Surges Del Golfo de México y su Variabilidad Interanual.* BSc. thesis, Universidad Veracruzana.

Walland, D., and Simmonds, I. (1999). Baroclinicity, meridional temperature gradients, and the southern semiannual oscillation. *J. Clim.* 12, 3376–3382.

Webster, P. J., and Holton, J. R. (1982). Wave propagation through a zonally varying basic flow: the influences of mid-latitude forcing in the equatorial regions. *J. Atmos. Sci.* 39, 722–733.

Yukimoto, S., Noda, A., Kitoh, A., Hosaka, M., Yoshimura, H., Uchiyama, T., et al. (2006). Present-day climate and climate sensitivity in the Meteorological Research Institute Coupled GCM version 2.3 (MRI-CGCM2.3). *J. Meteorol. Soc. Jpn.* 84, 333–363. doi: 10.2151/jmsj.84.333

Conflict of Interest Statement: The authors declare that the research was conducted in the absence of any commercial or financial relationships that could be construed as a potential conflict of interest.

A climatology of low level wind regimes over Central America using a weather type classification approach

Fernán Sáenz[1]* and Ana M. Durán-Quesada[1,2]

[1] Centre for Geophysical Research, University of Costa Rica, San José, Costa Rica, [2] Department of Atmospheric, Oceanic and Planetary Physics, School of Physics, University of Costa Rica, San José, Costa Rica

Based on the potential of the weather types classification method to study synoptic features, this study proposes the application of such methodology for the identification of the main large scale patterns related with weather in Central America. Using ERA Interim low-level winds in a domain that encompasses the intra-Americas sea, the eastern tropical Pacific, southern North America, Central America and northern South America, the K-means clustering algorithm was applied to find recurrent regimes of low-level winds. Eleven regimes were identified and good coherency between the results and known features of regional circulation was found. It was determined that the main large scale patterns can be either locally forced or a response to tropical-extratropical interactions. Moreover, the local forcing dominates the summer regimes whereas mid latitude interactions lead to winter regimes. The study of the relationship between the large scale patterns and regional precipitation shows that winter regimes are related with the Caribbean-Pacific precipitation seesaw. Summer regimes, on the other hand, enhance the Caribbean-Pacific precipitation with contrasting distribution as a function of the dominant regimes. A strong influence of ENSO on the frequency and duration of the regimes was found. It was determined that the specific effect of ENSO on the regimes depends on whether the circulation is locally forced or lead by the interaction between the tropics and the mid-latitudes. The study of the cold surges using the information of the identified regimes revealed that three regimes are linkable with the occurrence of cold surges that affect Central America and its precipitation. As the winter regimes are largely dependent of mid-latitude interaction with the tropics, the effect that ENSO has on the Jet Stream is reflected in the winter regimes. An automated analysis of large scale conditions based on reanalysis and/or model data seems useful for both dynamical studies and as a tool to support forecasting. The application of the approach implemented in this study may be promising to improve current understanding on how large scale conditions affect regional weather.

Keywords: Central America, precipitation, weather type, wind, cold surge

Introduction

Central America is a narrow portion of land surrounded by the Caribbean Sea and the Eastern tropical Pacific (ETPac). Regional weather and climate are strongly influenced by warm SSTs, easterly

winds, large tropospheric moisture content and steep topography. The regional SST features warm waters phased sequentially from the Eastern North Pacific and west of Central America to the Intra Americas Sea (IAS). This distribution is known as the Western Hemisphere Warm Pool (WHWP) and traditionally, it is defined as enclosed by the 28.5 C isotherm (Wang and Enfield, 2001). The WHWP is highlighted for its potential role to force local winds, precipitation and hurricanes (Wang et al., 2007). The main feature of the regional winds is the Caribbean Low Level Jet (CLLJ). The CLLJ exhibits its primary maximum during summer (zonal wind speed up to 18 m/s) and a secondary maximum in winter (Amador, 1998, 2008; Wang et al., 2007). The CLLJ is important due to its relationship with the regional distribution of precipitation (Magaña et al., 1999), inhibition of deep convection organization and cyclones activity (Wang and Lee, 2007). The CLLJ contributes to the generation of orographic precipitation and the enhancement of the eastward divergence of the moisture flux (Amador, 2008; Muñoz et al., 2008; Cook and Vizy, 2010; Durán-Quesada et al., 2010). Regional distribution of precipitation shows a bimodal behavior. The decrease of precipitation during summer, known as the Mid Summer Drought (MSD) is related with the low level wind regime and SST distribution (Magaña et al., 1999; Small et al., 2007). The cyclone activity, both in the tropical Atlantic and the ETPac (Amador et al., 2010), as well as the less studied intrusion of cold air masses (Schultz et al., 1998; Zárate, 2013) are also part of regional weather and climate.

On the interannual scale, regional variability is lead by the effect of modes at different scales. The North Atlantic Oscillation (NAO, Rogers, 1984) is associated with SST in the Tropical North Atlantic (TNA), the size of the WHWP and the CLLJ. According to Malmgren et al. (1998), the seasonal variations of the NAO may influence the IAS easterly winds and precipitation. Warm Pacific Decadal Oscillation (PDO, Mantua et al., 1997) phases have been found associated with anomalously dry periods in the eastern coast of Central America (Méndez and Magaña, 2010). The Atlantic Multi-Decadal Oscillation (AMO, Kerr, 2000; Knight et al., 2006) signal has been found to be linked with precipitation variations in the Caribbean (Giannini et al., 2003). Gamble and Curtis (2008) suggested that the decrease in the moisture transport from the Gulf of Mexico to northwestern Mexico during positive AMO may be related with a reduction in precipitation. Wetter (drier) conditions over Central America (north-east Brazil) during JJA (DJF) were also found by Zhang and Delworth (2006) for positive AMO. The most studied variability mode in the regional context is the El Niño-Southern Oscillation (Cane et al., 1986 and references therein). Global scale studies show that ENSO is strongly linked with interannual variability of global rainfall (Dai and Wigley, 2000). Regional studies on the Caribbean relate an increase (decrease) of precipitation with cold (warm) ENSO events. Goldenberg and Shapiro (1996), Bell and Chelliah (2006) among others, reported a decrease in the intensity of Atlantic cyclones during warm ENSO events. Schultz et al. (1998) presented results supporting the hypothesis that the number of cold surges penetrating Mexico and Central America is more likely to increase during warm ENSO events.

Unlike for the tropics, the influence of the large scale processes on the high frequency variability at regional scales has been studied thoroughly for mid and high latitudes (e.g., Lamb, 1950; Trigo and DaCamara, 2000; Cortesi et al., 2013). Despite weather phenomena affecting the Intra Americas Seas, such as tropical cyclones have been widely studied, the intrusion of cold air masses into the tropics requires more research. Cold surges are observed confined to the lower troposphere to the east of the main mountain ranges, with a north-south oriented axis and duration between 2 days and 1 week (Garreaud, 2001). Cold surges in Central America and the Intra Americas Sea region have been identified by González (1999), Magaña and Vázquez (2000), Brenes et al. (2003) and more recently Zárate (2013). Reding (1992) presented a climatological study of Central American Cold Surges (CACS hereafter) using surface analysis and satellite imagery. Schultz et al. (1997) analyzed the development of a cold surge associated with a super storm in the eastern United States of America in 1993, which largely affected Central America and Mexico. Schultz et al. (1998) proposed five categories of cold surges for winters between 1978 and 1989 based on observational data from surface stations and upper air measurements. In their classification, each category is linked with a different wind regime, temperature drop and southernmost penetration.

The analysis of circulation patterns is useful to study regions like Central America, as the identification of atmospheric flow regimes performs a reasonable characterization of the large scale circulation on a predefined geographic domain. According to Molteni et al. (2006), these regimes can be regarded as points of statistical equilibrium, in which, the dynamical tendencies of the large scale flow are balanced by the non-linear interactions of the high-frequency transients. Clustering analysis can be used to identify a limited number of partitions of the phase space. Therefore, the variability of each partition is small compared to the variability of the mean state of the partitions. There are some applications of this approach for tropical regions. Moron et al. (2008) identified daily weather types in western Africa from ERA-40 wind fields and related them to precipitation over Senegal. Moron et al. (2010) associated daily weather types to monsoonal rainfall over Indonesia and Qian et al. (2010) linked those clusters to the diurnal cycle of precipitation on Java Island.

This work is motivated by the importance of day to day variability for regional weather and climate and the reduced number of studies in this subject over the region of interest in this study. The proposed work explores the reliability of the application of weather type analysis to study the main large scale patterns that characterize regional circulation over the region of interest in this study. The identification of main synoptic patterns, the evolution of large scale conditions and the relationship between the synoptic patterns and regional precipitation are the focus of this study. This research presents the application of a simple automated classification method to study the large scale circulation that affects the Central American region, the existence of recurrent low-level wind patterns and their effect on regional weather. A special focus is given to the intrusion of cold air masses. As the effect of ENSO is of particular importance, this work also aims to explore the response of the identified patterns to ENSO,

in terms of both intensity and frequency. The study is organized as follows, an introduction with background information on regional weather, climate and their variability that may be useful for reference was given in Section Introduction; Section Data and Methods describes the data and method used. The results are provided in 4 sub sections; the description of the weather types identified and the relationship between the patterns and precipitation are provided in Section Description of the Main Circulation Patterns and Relationship between the Identified Regimes and Precipitation in Central America respectively, the analysis of the response of the weather patterns to ENSO is given in Section Response of the Circulation Regimes to ENSO and Section Inferring the Intrusion of Cold Surges to Central America from Large Scale Patterns contains a detailed analysis of the case of the cold surges. The discussion is provided in Section Discussion and Section Conclusions presents a summary of the analysis, conclusions and further proposed research work.

Data and Methods

Data

Reanalysis Data

The signature of regional climatic features such as the CLLJ (Amador, 2008), MSD (Karnauskas et al., 2013) and cold surges (Garreaud, 2001) is strong at the low-levels. Wind fields at 925 and 850 hPa were extracted from de ERA-Interim reanalysis (Dee et al., 2011) as descriptors of the low-level atmospheric circulation. Complementary, geopotential height at 500 hPa was also retrieved from the ERA-Interim dataset. The daily data spans from 1979 to 2012 and encompasses an area from 8 N to 25 N and from 260 E to 295 E (see the white box in **Figure 1**).

Low-level wind data were normalized subtracting the time series mean to each grid point and dividing it by its standard deviation. In search of computational efficiency, Principal

FIGURE 1 | Region of interest. Geographic domain for the ERA-interim data used in the clustering algorithm is enclosed by the white box.

Components Analysis (PCA) was applied to the data. The 62 first components accounted for 95% of the variance; this implied a significant reduction in data dimensionality, computing time and resources. As the objective of the work is to describe large scale features, the decomposition procedure serves to filter noise that could affect the cluster analysis. To analyze the atmospheric configuration related to mean state of each cluster, composites of wind fields and geopotential height at 925 hPa were computed. Seasonal frequency charts were also drawn in order to analyze if there was a seasonal preference in regime occurrence (not shown).

Precipitation Data

Tropical Rainfall Measuring Mission (TRMM, Simpson et al., 1988) Multi-Satellite Precipitation Analysis (TMPA, Huffman et al., 2010) was used as an approximate of daily precipitation. We are aware that this data is not homogeneous and its quality depends on the availability of source data of high quality rain gage data for the rescaling. However, due to the lack of good quality and long term precipitation observation networks in the region and the known biases for this variable in the reanalyses, the 3B42 version 7 dataset, in a $0.25° \times 0.25°$ grid with 3-h temporal resolution for the 1998–2012 period was consider fair enough to be used to compute daily aggregates.

Method

Cluster analysis has been widely used for circulation patterns recognition (ej. Cheng and Wallace, 1993; Straus and Molteni, 2004; Casola and Wallace, 2007). This method divides a set of N-dimensional data vectors by grouping them into categories. The distance of the vector to the center of each group in an N-dimensional space is the criterion used to assign a vector to a category. Distance can be measured in multiple ways, being the Euclidean distance the simplest. The k-means clustering method (see MacQueen, 1967 for more details) is herein implemented. One of the major draw backs of the k-means algorithm is that the number of categories or clusters, k, must be specified a priori. To find a suitable number of clusters reducing the subjectivity, a combination of methods proposed by Michelangeli et al. (1995) and Cheng and Wallace (1993) was applied. This procedure has been previously used by Moron et al. (2008) and follows the general five-step procedure described by Molteni et al. (2006). The method employed by Michelangeli et al. (1995) relays on the fact that k-means results could be dependent on initial seeds and uses the similarity between the results of different clustering repetitions (partitions) to assess this dependency. To measure the similarity between partitions, Cheng and Wallace (1993) proposed a method based on centroid correlations. Following Cheng and Wallace (1993):

(a) Given two partitions P1 and P2, of k clusters, correlations between centroids are placed in a matrix

(b) For the ith row the maximum is computed and saved as B(i), this value is the correlation between the ith cluster in P1 and its analog in P2

(c) The minimum value in vector B is taken as the pattern correlation between P1 and P2 and denoted c(P1,P2). To generalize this procedure to M partitions in the same k number of
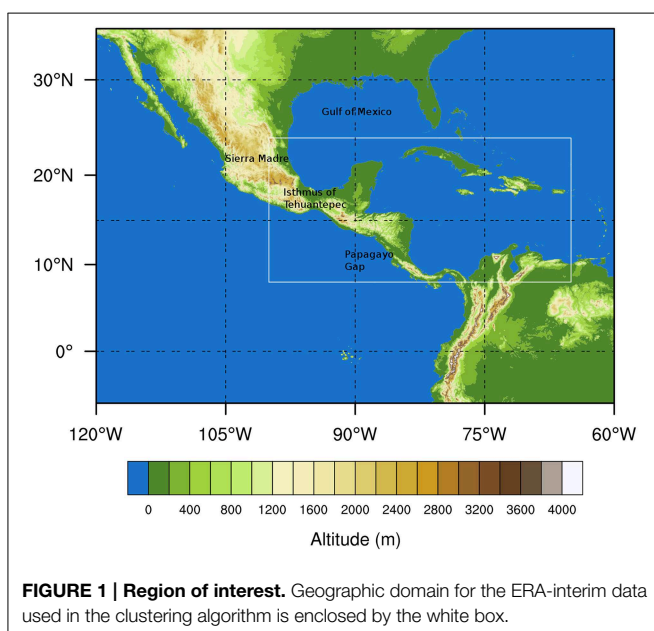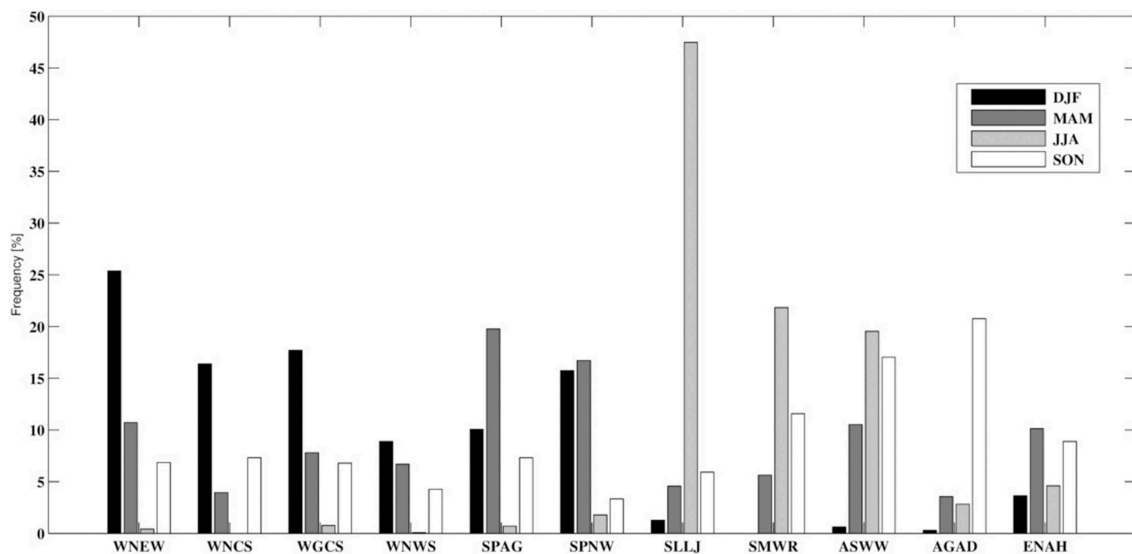
FIGURE 2 | Relative seasonal frequencies showing the dominance of the 11 regimes found. For each season all regime frequencies should sum up to a 100%.

clusters, Michelangeli et al. (1995) defined the classifiability index CI(k):

$$CI\left(k\right) = \frac{1}{M(M-1)} \sum_{1:m \neq m'}^{M} C(Pa_m\left(k\right), Pa_{m'}\left(k\right))$$

The classifiability index varies between 0 and 1. A value of 1 means that M partitions with fixed k produce exactly the same k clusters. For different values of k, the more reliable as predefined number of clusters, is the one that produces the highest CI while maintaining statistical significance.

In this work, the number M of different partitions was set to 100 and CI (k) was computed for $k = 2,..,15$. To assess statistical significance, CI (k) was computed 100 times for every k using quasi-random red-noise data drawn from the original data set. The highest, statistically significant at 99% according to the red-noise test, CI value from the observed data set was found $k = 5$, same as the number of clusters used by Schultz et al. (1998). However, a classification in such small number of clusters would result in very general circulation patterns, mainly considering that a number of 5 patterns of CACS were found by Schultz et al. (1998) while classifying only winter circulation. Therefore, the value $k = 11$, which ensured a high significance (83.5% in this case), was used instead; using an a priori number of 11 clusters assures high statistical significance and is not as small so that only broad general circulations patterns can be identified.

Results

Description of the Main Circulation Patterns

Two large categories can be used to group the 11 circulation patterns found as pure seasonal or transitional patterns. No pure seasonal patterns were found for spring, suggesting that those

months are dominated by transition signals. The names are based on the dynamical features of the regimes, **Figure 2** shows the frequency of each regime, from which the seasonality of the regimes can be noticed. **Figure 1** shows some of the more relevant topographic features of the study area for reader's reference.

Winter North Eastern Winds (WNEW)

This is the most frequent regime during winter; it is likely to occur, on average, up to 10 days per month during winter time. The persistence of this pattern is typically 3 days. The circulation linked to this pattern is featured by northeasterly winds over the Caribbean, which is related to a geopotential maximum off the East coast of the United States of America (USA). These winds cross the Central American Isthmus and reach the ETPac (**Figure 3A**). The large scale features of this regime are typically observed during the winter maximum of the CLLJ. The transisthmic flow is enhanced mainly through the Papagayo gap. The 500 hPa geopotential height, depicted in **Figure 4A**, shows a mid-tropospheric trough over the North Atlantic and USA region, in contrast with relatively quiescent weather conditions over the Gulf of Mexico.

Winter Northern Cold Surge (WNCS)

Each episode of the WNCS regime tends to last between 1 and 2 days (maximum duration, up to 3 days is found in November). This regime is characterized by an eastward displacement of the North Atlantic Subtropical High (NASH) and a geopotential maximum centered at the southeast USA coast. This maximum extends into the sea and is bounded to the West by the Sierra Madre mountain range (**Figure 3B**). The mean low-level wind field features an anti cyclonic gyre in which the winds converge with the weakened trade winds; this enhances winds over the Central American Isthmus from North to the northeast. The intensified flow crosses the continent through the topographic
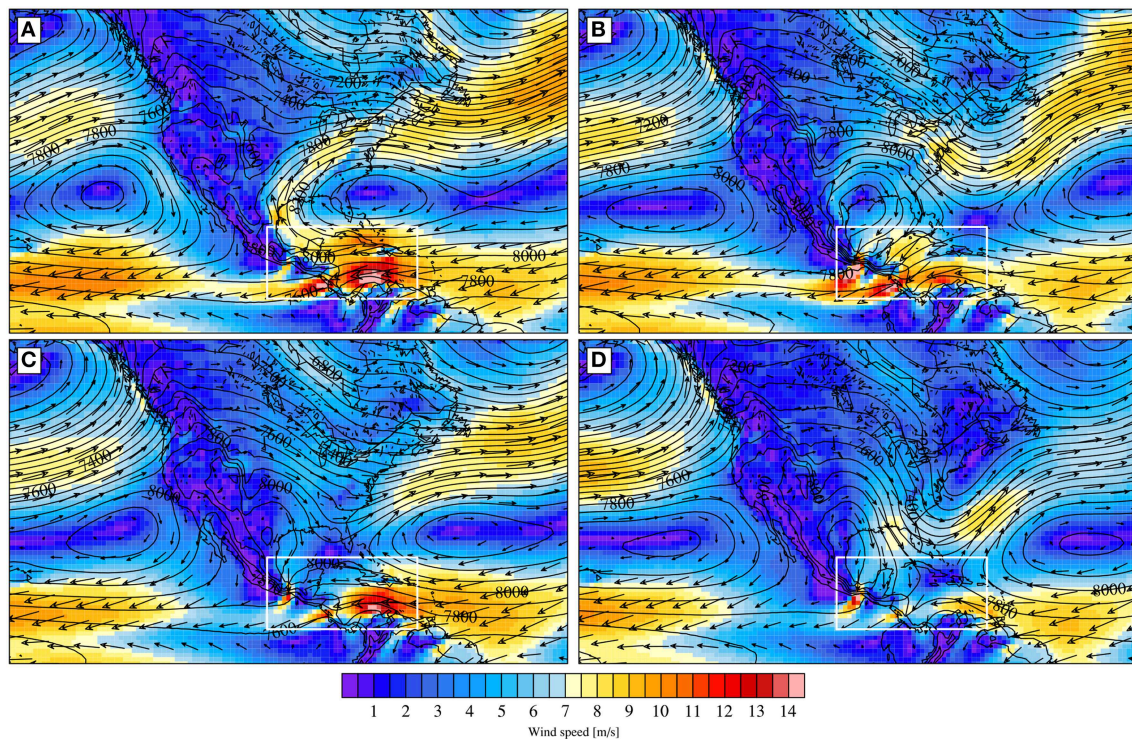
FIGURE 3 | Composited large-scale patterns at 925 hPa associated with (A) WNEW, (B) WNCS, (C) WGCS, and (D) WNWS regimes. Geopotential height [m²/s²] (black contours), wind speed [m/s] (colored pixels) and wind vectors. Geographic domain for the ERA-interim data used in the clustering algorithm is enclosed by the white box.

passes, producing gap winds over the Papagayo and Tehuantepec regions (**Figure 3B**). The mean horizontal low-level fields of this regime are coherent with the low level structure of a typical cold surge entering the Gulf region from central Canada (Henry, 1979; Schultz et al., 1998). In this regime, the trough penetrates into the Gulf of Mexico and the anticyclonic gyre in the Gulf of Mexico is more defined. The easterly flow is even more confined than for WNEW, enhancing trans-isthmic transport through the Gulf of Tehuantepec, in good agreement with observations as reported by Chelton et al. (2000). **Figure 4B** shows cyclonic anomalies at 500 hPa over Central America and the adjacent Pacific Ocean.

Winter Gulf Cold Surge (WGCS)

Observed during winter, this regime appears nearly 17% of the days (**Figure 2**), with a duration between 1 and 2 days. Two geopotential height maxima are observed for this regime, one east of the Sierra Madre and the other related to a westward displacement of the NASH (**Figure 3C**). The low-level wind field is lead by anticyclonic winds related to the NASH, northerly winds over the Gulf region and gap winds off the Central America's Pacific coast (**Figure 3C**). In this regime, the trans-isthmic flow is reduced compared to previous regimes. As the anticyclonic gyre in the Gulf of Mexico is not fully developed, the wind field is not strongly constrained. A mid tropospheric trough enters the east coast of North America, with the divergence

field stretching along the storm track (**Figure 4C**). This regime is only related to cold surges that do not reach the Central American region; this because the NASH constrains the southward displacement of the cold air that is channeled by the topography.

Winter North Western Surge (WNWS)

WNWS is more frequent during spring and winter (**Figure 2**), its mean duration ranges between 1 and 2 days and is also important in November. Even though the distribution of geopotential is similar to the WGCS regime, WNWS differs in the following aspects: (a) the western limit of the NASH is located to the east of the Hispaniola island, allowing the formation of a trough off the USA east coast and (b) a southward displacement of the geopotential maximum is located east of the Sierra Madre mountain range. The main features of the low-level wind are weakened trades, enhanced gap winds at the Yucatan peninsula and northerlies that reach as far south as Costa Rican Caribbean coast (**Figure 3D**). Low level wind over the Central Caribbean is minimum as the Central Caribbean is featured by divergent wind flow. In the mid troposphere, the westerly flow is dominant (**Figure 4D**). These conditions provide an environment that allows the entrance of Pacific cold surges. The large scale features of this regime resemble the structure of cold surges moving from the east Pacific and reaching Central America (Henry, 1979; Schultz et al., 1998).
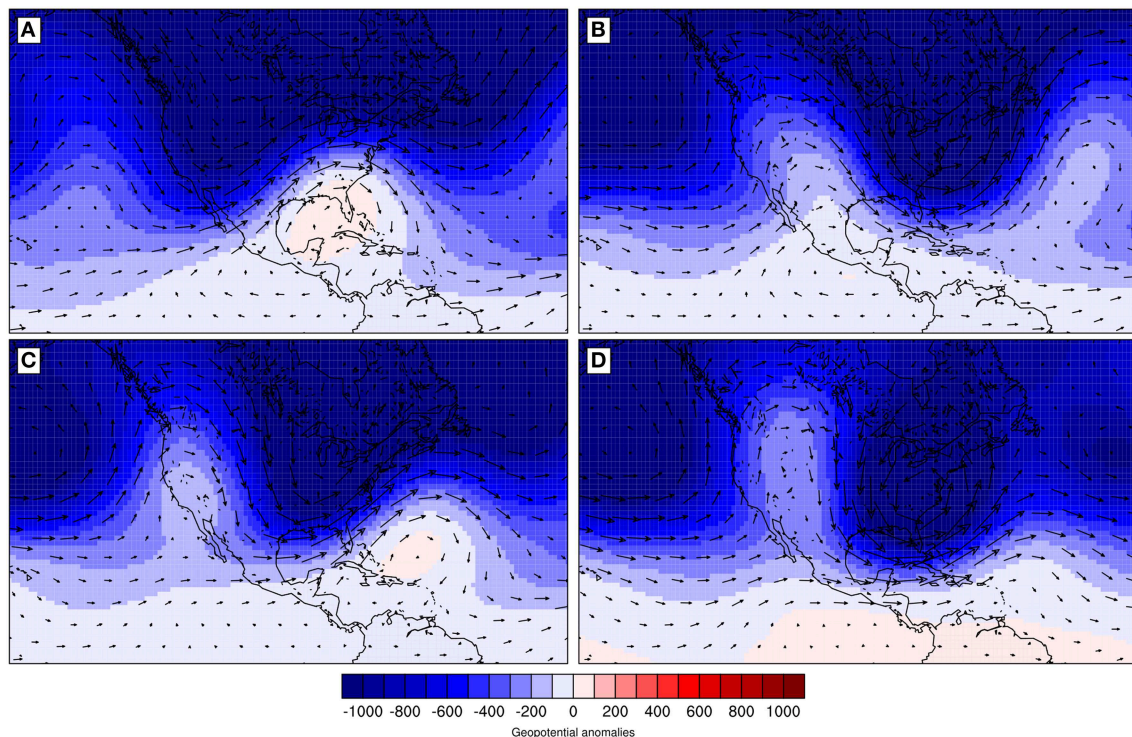
FIGURE 4 | Composited large-scale anomalies at 500 hPa associated with (A) WNEW, (B) WNCS, (C) WGCS, and (D) WNWS regimes. Geopotential anomalies (colored pixels) and anomalous wind field (vectors).

Spring Anti Cyclonic Winds at the Gulf (SPAG)

This regime is more frequent during March and April (even when observed during winter and autumn). The largest persistence in the number of days is 3 (during April). The mean geopotential field of this regime shows a marked eastward displacement of the NASH (**Figure 5A**). Such displacement allows the establishment of a geopotential maximum centered over Florida. The latter induces an anticyclonic gyre with low-level easterlies over the northern portion of the Caribbean Sea. The anticyclonic gyre reinforces the weakened trades, forming a shear line off the coast of Honduras and Nicaragua. For this regime, isolated mid-tropospheric troughs over the Rocky Mountains and the Atlantic off the east coast of USA are well defined (**Figure 5A**). A mid-tropospheric anomalous ridge over the Gulf of Mexico inside a wave train is clear in **Figure 6A**.

Spring NASH West (SPNW)

Almost equally frequent during spring and winter (**Figure 2**), the SPNW regime dominates the seasonal transition and it is the most frequent regime during February and March. Maximum of persistence is found to have an average duration of 2–3 days. A more developed NASH that penetrates into the Gulf of Mexico induces a low-level wind circulation with south easterlies in the Gulf region and enhanced trades over the Caribbean with intensified activity of the CLLJ (**Figure 5B**). A large mid-tropospheric ridge over the western North Atlantic and North America is the main feature of the 500 hPa geopotential height anomalies field

(**Figure 6B**). The large anomalies observed suggest a favorable environment for storm development.

Summer Low Level Jet (SLLJ)

SSLJ is the dominant summer regime (**Figure 2**). It exhibits the largest frequency (up to 47%) of the observed patterns during the summer months (observed up to 22 days in July). This regime has the largest persistence of the identified regimes as an event can last up to 10 consecutive days. Low level flow for this regime shows a reinforcement and increase in the zonal extension of the NASH. Low level winds linked to the geopotential field of this pattern feature enhanced trades over the Caribbean Sea. A low-level jet like structure is observed off the northern coast of South America and enhanced southerlies entering the Great Plains region from the Gulf coast (**Figure 5C**). The structure shown by the low level winds of this regime is consistent with the primary maximum of intensity of the CLLJ. Mid troposphere geopotential height anomalies suggest quiescent conditions for this regime (**Figure 6C**).

Summer Monsoonal Winds Regime (SMWR)

This summer regime, more frequent in early and late summer, can be also observed during autumn and less frequently in spring (**Figure 2**). The geopotential distribution features a NASH similar as for the SLLJ regime, but with a smaller maximum shifted to the East. This configuration may produce a northward veering of the trades over the Caribbean. Such veering, added to the effect
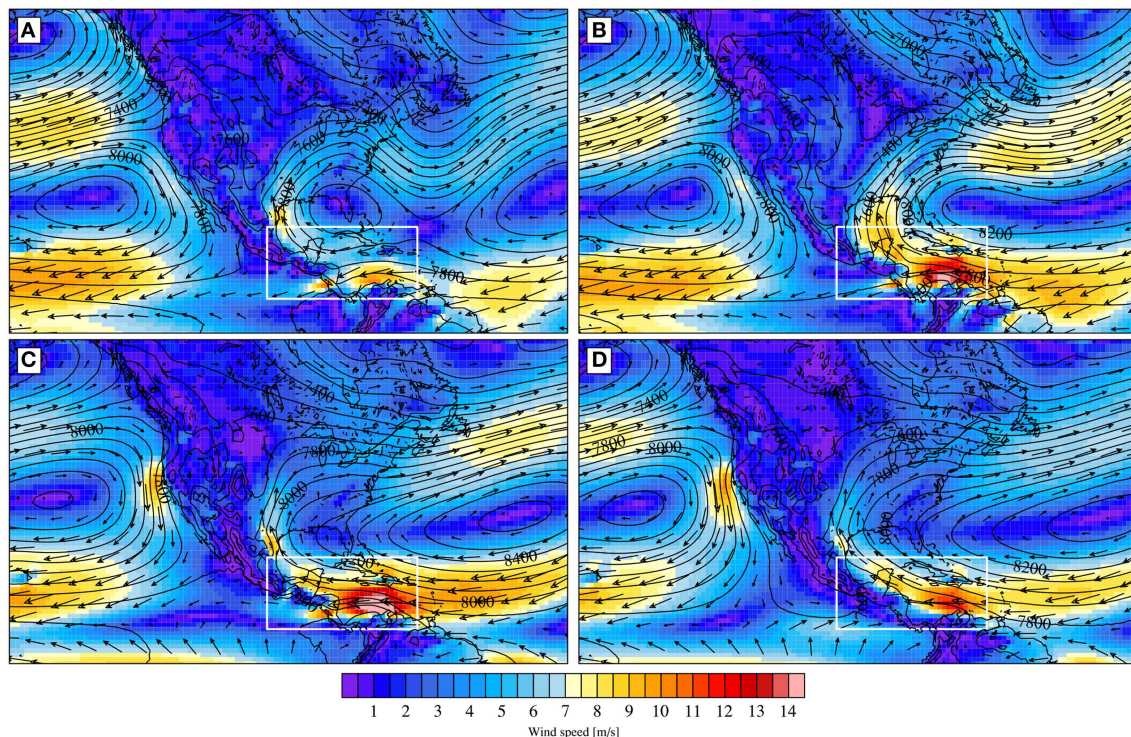
FIGURE 5 | Composited large-scale patterns at 925 hPa associated with (A) SPAG, (B) SPNW, (C) SLLJ, and (D) SMWR regimes. Geopotential height [m²/s²] (black contours), wind speed [m/s] (colored pixels) and wind vectors. Geographic domain for the ERA-interim data used in the clustering algorithm is enclosed by the white box.

of thermal forcing by the Central American isthmus, the WHWP and the enhancement of the southerly trades may induce low-level southwesterly winds that reach the Central American Pacific coast (**Figure 5D**). A mid tropospheric ridge over the west coast of North America along with the development of a cyclonic circulation west off Central American coast is observed for this regime (**Figure 6D**).

Autumn South Westerly Winds (ASWW)

ASWW is frequent during late spring, summer and early autumn (**Figure 2**). Its occurrence peaks in August and September and events last between 1 and 4 days. The mean geopotential field is characterized by a NASH displaced to the East and a secondary geopotential maximum centered over the Gulf coast of the United States. The confluence of the Trades and the easterlies related to the anticylonic gyre induced by the secondary geopotential maximum (**Figure 7A**) enhances trade winds over the Caribbean. The mid troposphere geopotential height anomalies suggest steady weather conditions (**Figure 8A**).

### Autumn Geopotential Dipole Anomalies (AGAD)

AGAD is the most frequent regime during autumn and it is rarely seen in any other season (**Figure 2**). Geopotential mean field shows a weakened NASH displaced to the East. This configuration produces a geopotential anomalies field dipole. Negative anomalies are observed over the Gulf, the Caribbean and the

western tropical Atlantic (**Figure 6B**), whereas, positive anomalies are centered over the Canadian eastern coast (not shown). Reduced trade winds, that barely reach the Caribbean coast of Central America, may allow the continental thermal forcing to induce westerly winds that reach its Pacific coast (**Figure 7B**). From **Figure 8B**, it can be observed that the 500 hPa geopotential height anomalies suggest relatively positive anomalies in the eastern portion of North America. The latter is in contrast with negative values that may suggest storm activity in the Caribbean.

East North Atlantic High (ENAH)

This regime is almost equally important during spring, summer and autumn (**Figure 2**). This pattern does not persist longer than 4 days. The mean geopotential distribution of this regime shows and eastward displaced NASH. The effect on the wind patterns over the Pacific is similar to those of the SMWR regime, but with a well-defined anticyclonic structure over the tropical Atlantic-Caribbean sector (**Figure 7C**). This regime presents a unique mid tropospheric structure in which negative anomalies amplify strongly north of the Gulf of Mexico, TNA and with smaller magnitudes over the north-east Pacific (**Figure 8C**). These negative anomalies contrast with the positive anomalies all over North America. The conditions from the mid tropospheric geopotential height may suggest suitable conditions for storm development.
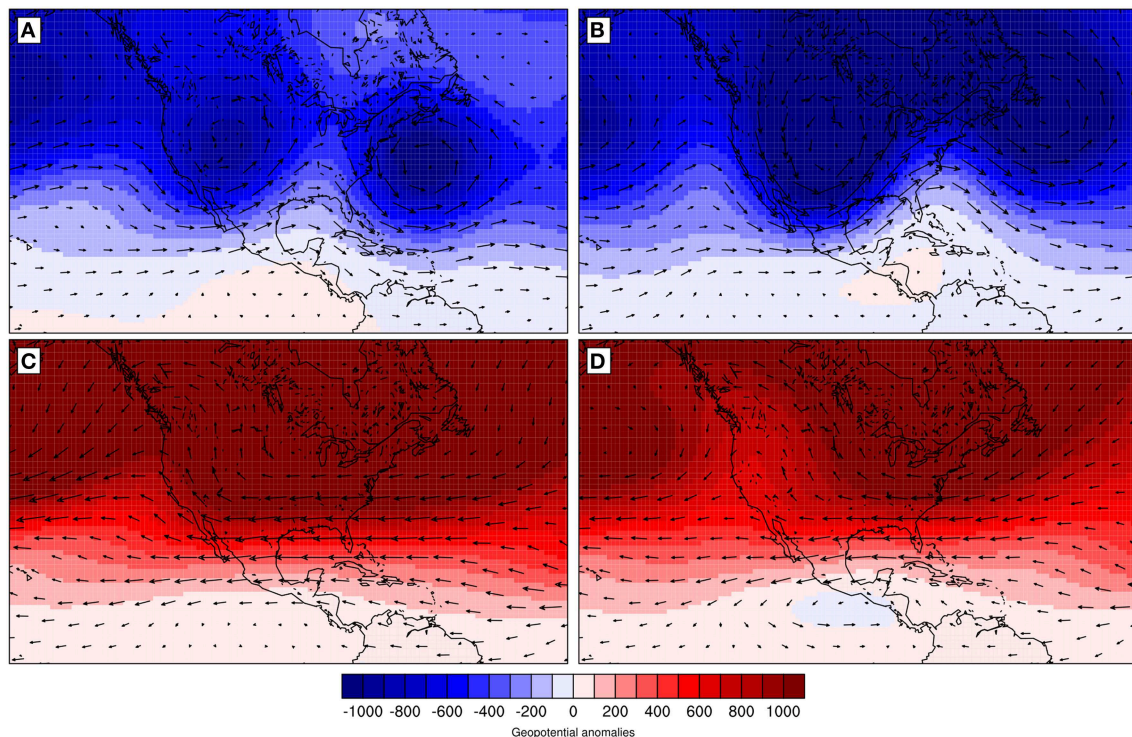
FIGURE 6 | Composited large-scale anomalies at 500 hPa associated with (A) SPAG, (B) SPNW, (C) SLLJ, and (D) SMWR regimes. Geopotential anomalies (colored pixels) and anomalous wind field (vectors).

Relationship between the Identified Regimes and Precipitation in Central America

Precipitation associated with each regime is fairly consistent with the known seasonal precipitation distribution. Marked differences in precipitation fields associated with regimes that are characteristic of the same season were found. Winter months are commonly dry in most of Central America, except for some areas in the Caribbean side (Alfaro, 2000). **Figure 9** shows that, for the winter regimes, less precipitation is observed over the Pacific side of the isthmus. In contrast, more intense precipitation is observed on the Caribbean slope due to topography-forced ascend. Under WNEW conditions (**Figure 9A**), Caribbean precipitation is maximum to the east of Costa Rica and Panama. A similar pattern is observed during WNCS events, but it differs from WNEW because a secondary precipitation maximum in the east coast of Honduras is observed under the WNCS regime. When cold surges reach the Central American region (WNCS and WNWS) rainfall increases over the Caribbean shores of Honduras and Costa Rica. When cold surges reach the Gulf of Mexico, but do not move further south (WGCS), Central America is drier. Despite winter precipitation in the Caribbean slope is mainly forced by topographic effects, wind shear is important over the Isthmus when surges reach the region as will be later discussed.

Spring months are dry in Central America, consistently with the reduction in precipitation for the SPAG (**Figure 9E**) and SPNW (**Figure 9F**) regimes. Nevertheless, regimes that can be also found in spring such as WNEW (**Figure 9A**)

and WNWS (**Figure 9C**) are linked with wetter conditions in the Caribbean slope and southernmost Central America. The ASWW (**Figure 9I**) and ENAH (8.k) regimes are also related to more intense precipitation in the Pacific side. The ENAH regime, with its anomalous westerly flow, could be associated with the beginning of the rainy season in the Central American Pacific slope (Alfaro, 2000; Cortez, 2000); a reduction of atmospheric stability due to an increase in coastal ETPac SST (via latent heating) characterizes the rainy season onset for this region.

The mean conditions for the SLLJ, SMWR, and ASWW regimes are consistent with the large scale conditions that provide the environment for precipitation intensification in the region (**Figure 9I**). Those conditions are northward veering of the trades, enlargement of the WHWP with its consequent reduction of stability due to the exponential relation between SST and large low level moisture content. The dynamic fields for the SLLJ regime show the enhancement of the easterly flow along with a deeper NASH, a clear fingerprint of the CLLJ. When this regime is present, a reduction in precipitation is seen all over the Pacific side of the Isthmus. In contrast, over the Caribbean side of Costa Rica and Nicaragua, Belize and Tehuantepec, precipitation is increased (**Figure 9G**). When the SMWR regime dominates, a cyclonic wind anomaly is present at 500 hPa over Central America and its adjacent Pacific Ocean. This anomaly, which acts in conjunction with low-level convergence to enhance vertical moisture transport, is consistent with the intensification of precipitation observed in that region (**Figure 9H**).
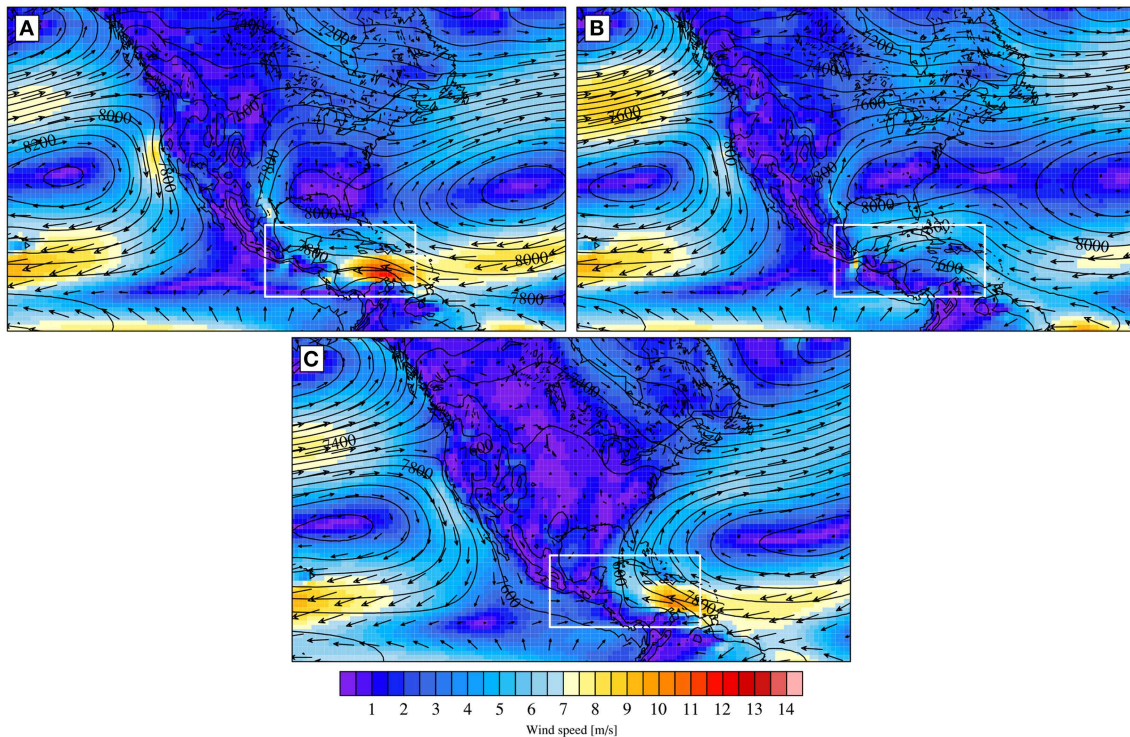
FIGURE 7 | Composited large-scale patterns at 925 hPa associated with (A) ASWW, (B) AGAD, and (C) ENAH regimes. Geopotential height [m²/s²] (black contours), wind speed [m/s] (colored pixels) and wind vectors. Geographic domain for the ERA-interim data used in the clustering algorithm is enclosed by the white box.

The autumn months are the rainiest in Central America (Alfaro, 2000). During this season, the weakening of the NASH, the establishment of the WHWP (in the Central America Pacific coastal areas and the Caribbean) and a maximum tropical cyclone activity over the Caribbean (Wang and Lee, 2007) act together to enhance rainfall in the Pacific slope. **Figure 9** shows that, for the pure autumnal regime AGAD (**Figure 9J**) as well as other regimes frequent during this season, Pacific precipitation is larger. The AGAD regime features a cyclonic anomaly at 500 hPa over the Central America and both adjacent water bodies. The mid tropospheric signal reflects a conductive environment for an intensification of precipitation over the Caribbean Sea and the Pacific coast of Central America as there is a thick layer of moisture convergence (**Figure 9J**). When ASWW is present, precipitation in Nicaragua shows a different pattern, with more (less) rain over the Caribbean (Pacific) side. The latter may be related with the presence of disturbances over the southern Caribbean such as easterly waves or tropical depressions.

Response of the Circulation Regimes to ENSO

ENSO is regarded as the strongest climate variability mode for the tropics (Pezzi and Cavalcanti, 2001; Turner et al., 2005). It is regionally known to modulate variations in precipitation (Ropelewski and Halpert, 1987). Therefore, understanding how ENSO may affect the large scale regimes found is of particular importance. Using the frequency information for the regimes and the Multivariate ENSO Index (MEI, Wolter and Timlin, 2011) as a measure of ENSO intensity, the monthly frequency for each regime was composited for warm and cold ENSO as well as for neutral conditions according to the moderate or stronger MEI ENSO events classification. The likelihood of a regime to occur is reported as a probability ranging from 0 to 1, where 1 is equivalent to the 100% of probability to observe a determined regime.

Results shown in **Figure 10**, suggest that cold ENSO increases the probability of the WNEW (**Figure 10A**) and WNCS (**Figure 10B**). In contrast, warm ENSO phase increases the probabilities of occurrence for WGCS (**Figure 10C**) and WNWS (**Figure 10D**). The increase in the frequency of the WNWS regime (**Figure 10D**) under El Niño conditions is a response to the intensification of the wind flow through the Gulf of Mexico, suggesting the intensification of cold air intrusions. The latter is in agreement with findings by Schultz et al. (1998) that report an anomalously larger number of strong cold surges into Central America for El Niño events. Composites for precipitation (**Figure 11**) show negative anomalies up to 12 mm/day, linked with the occurrence of WNWS during warm ENSO. The increase in the number of CACS under warm ENSO leaves a drier than normal Caribbean. Pérez et al. (2014) suggest that, an increase in CACS frequency accompanied by a shortening of wavelength and lifespan, typical of positive ENSO conditions, could lead to a reduction in the precipitation caused by CACS.
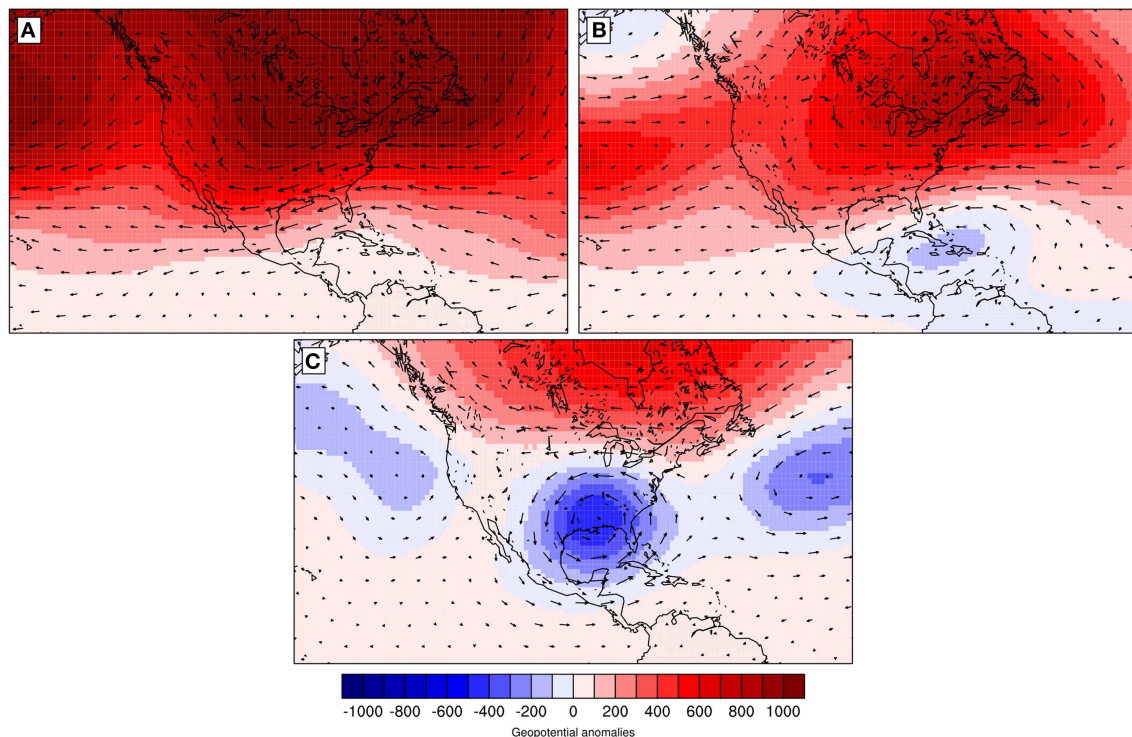
FIGURE 8 | Composited large-scale anomalies at 500 hPa associated with (A) ASWW, (B) AGAD, and (C) ENAH regimes. Geopotential anomalies (colored pixels) and anomalous wind field (vectors).

The occurrence of SPAG regime is increased as warm ENSO is linked with the intensification of the easterly flow. Despite the increase in the probability for SPAG, non-significant changes in precipitation for this regime, associated with the effect of ENSO, were found. The largest variations (up to 30%) are observed for the SLLJ during El Niño events (**Figure 10G**). The results shown are in good agreement with the fact that El Niño is linked with a stronger CLLJ (Wang, 2007; Amador, 2008). As this phase favors the intensification and expansion of the WHWP (Wang and Enfield, 2003) as well as the strengthening of the NASH, the large scale features of SLLJ are also intensified. The intensification of the CLLJ is known to be related with drier (wetter) conditions over the Caribbean (Pacific). The increase of days with a dominant SLLJ regime may be expected to be related with drier conditions. Composites for precipitation under the positive and negative phases of ENSO (**Figure 11**) show the drying of Central America (mostly over the Caribbean slope) for warm ENSO. In contrast, west off Central America, precipitation is intensified under the same ENSO phase, as shown in the anomalies (**Figure 11**). This result has a direct implication on the assessment of drier than normal summer periods and hence, a deeper MSD under El Niño. An enhanced CLLJ produces descending motion over the Pacific side which inhibits deep convection.

The response of the SMWR regime to ENSO is the most extreme of all the regimes. During July and August, the probabilities of the mode to occur increase by 40% from El Niño to La Niña conditions. For the SMWR regime (**Figure 10H**), La

Niña has been associated with the intensification of the occurrence of this regime. This implies that, cold ENSO phase provides conditions that allow the enhancement of the northward veering of the Trades. An increased northward flow is known to occur under cold ENSO conditions (Yu and Wallace, 2000). The latter, in agreement with the findings that suggest a larger frequency of the pattern linked to the summer monsoonal flow during La Niña events. This result may suggest that, precipitation increases during La Niña, favored by the intensification of the monsoonal flow, mainly in northern Central America. The difference between precipitation for El Niño and La Niña, results in negative anomalies with maximum values in northern Central America. Therefore, rainfall is likely to be more intense for La Niña events during summer in dominance of the SMWR regime. This shows coherence with the expected conditions of rainfall when the monsoonal flow is enhanced, as reported by Yu and Wallace (2000).

The results found are indicative of the response of the large scale circulation linked to regional phenomena to the ENSO variability mode. Such results are relevant as they provide an important input for weather analysis and may be useful for seasonal precipitation forecasting ahead of the development of a particular ENSO phase. Note that an analysis on how the precipitation responds to the variability of the patterns due to ENSO is not presented in full detail; TRMM precipitation record is rather short for a detailed study of the interannual variability. However, a further study on this issue will be raised in a future study using a
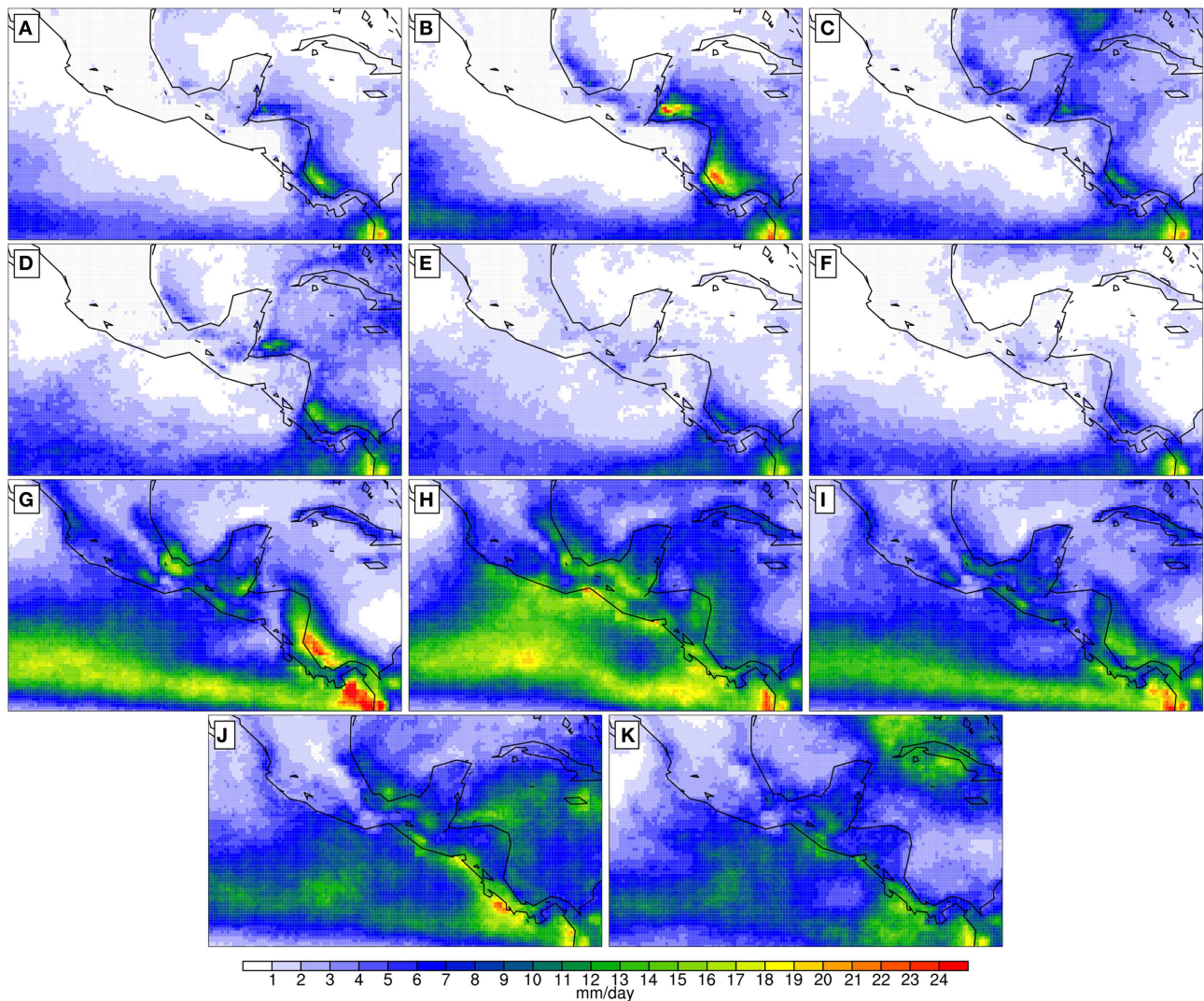
FIGURE 9 | Composited TRMM 3B42 precipitation fields [mm/day] for (A) WNEW, (B) WNCS, (C) WGCS, (D) WNWS, (E) SPAG, (F) SPNW, (G) SLLJ, (H) SMWR, (I) ASWW, (J) AGAD, and (K) ENAH regimes.

longer time span when a new high resolution blended precipitation dataset becomes available at the required time scales for such task.

Inferring the Intrusion of Cold Surges to Central America from Large Scale Patterns

The intrusion of cold extratropical air into the tropical regions is a phenomenon constrained to the eastern slope of major mountain ranges (Garreaud, 2001). The low-level dynamic fingerprint of cold surges located east of the Sierra Madre is used here to identify them. Previous CACS climatologies were developed using stations data, satellite imagery and rawinsonde data (Reding, 1992; Schultz et al., 1998). Those studies are suitable to test the ability of the k-means classification method to detect CACS. Reding (1992) includes a table with the onset date and duration for each of his classified CACS for the October to March season

for the period of 1979–1990. This information was used to construct a time series of days where CACS were present and used as a test bed for a time series of CACS days from the k-means method applied in this work. For this comparison, CACS days are defined as days when WNCS and WNWS regimes are present; WGCS regime days were not taken into account because when this regime is present CACS reach as south as the Gulf of Mexico, this creates inconsistencies with Reading definition of CACS. The automated classification based on large scale patterns, herein used, is able to capture up to 78% of the overlapping days in which Reding (1992) detected cold surges. Differences in the nature of the data as well as the spatial and temporal resolution could justify the difference between the numbers of days with CACS identified for the two methods.

As mentioned before, the three regimes related to cold CACS reproduce the structure of surges of different origins, based on
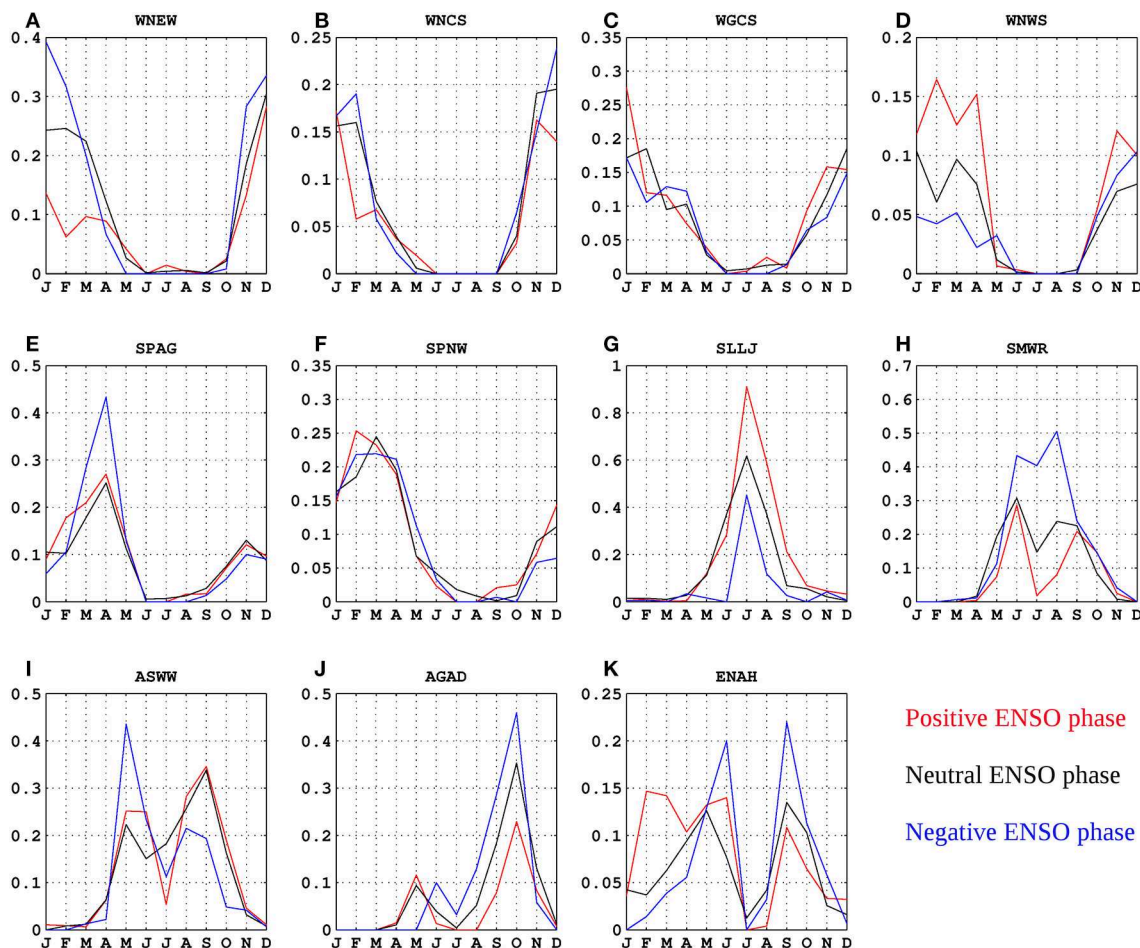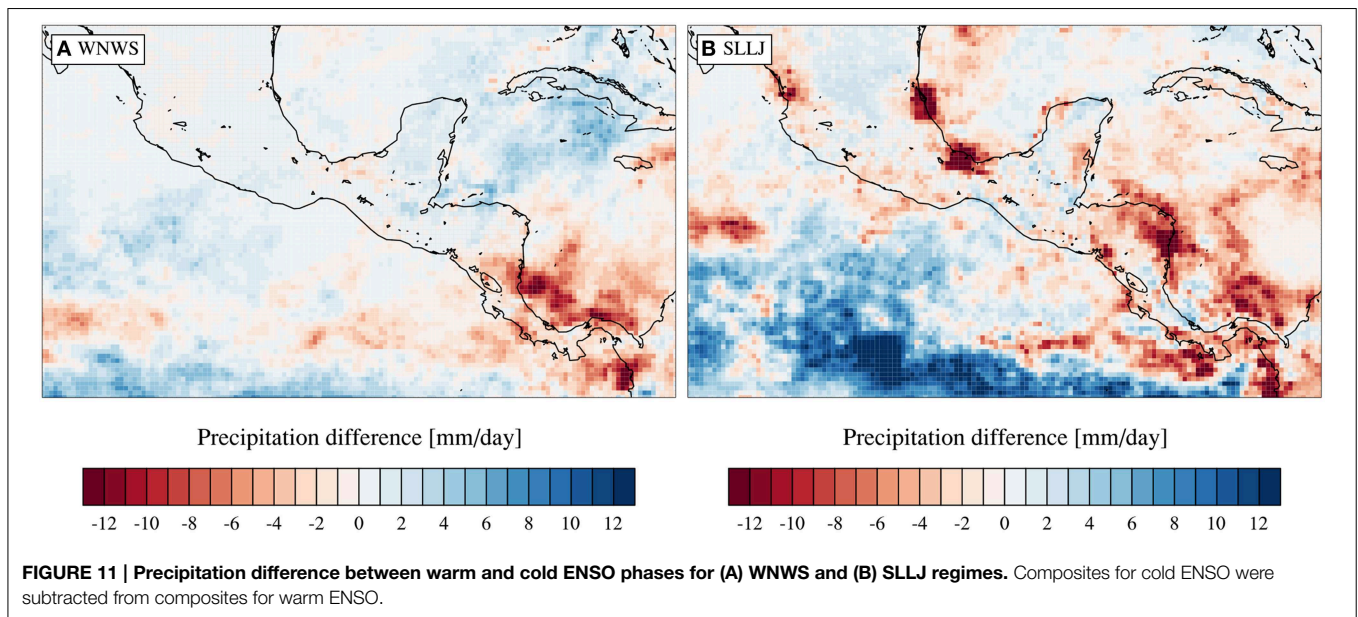
FIGURE 10 | Monthly probabilities of occurrence under each ENSO phase for every regime. Ordinate axis scales are not the same for every subplot.

previous works by Schultz et al. (1998) and Henry (1979). The Winter North Western Surge (WNWS) was found to reproduce the structure of cold surges from the East Pacific that reach Central America, the Winter Northern Cold Surge (WNCS) was found to reproduce the structure of cold surges reaching Central America from continental North America and the Winter Gulf Cold Surge (WGCS) was linked to surges that do not reach southward of the Gulf of Mexico. Therefore, the WNWS regime is herein used as an example to study the features, evolution and effect on precipitation of CACS entering Central America. The most prominent characteristics of the WNWS regime can be summarized as: (a) west limit NASH east of the Hispaniola island, (b) trough off the United States east coast, (c) geopotential maximum east of the Sierra Madre, (d) weak trade winds and (e) enhanced gap winds at the Yucatan Peninsula and northerlies. The analysis of the WNWS events revealed that, on average, a 3 days persistence pattern of this type is preceded by WGCS like large scale conditions and that after the third day of WNWS; the following conditions do not have a determined structure. Low level winds and geopotential height depicted in **Figure 12** show the sequence associated with the development of the WNWS

pattern (11.a WGCS; 11.b, c, and d WNWS 3 day evolution). During the transition from WGCS to WNWS conditions, the low level flow through the Yucatan Peninsula is intensified. This intensification is supported by the development of a low level anticyclone in the tropical Atlantic and a cyclone in the North Atlantic. The 500 hPa fields (**Figure 13**) show how this transition is accompanied by eastward displacement of a ridge. This suggests that the west coast of North America, initially experiencing cold air advection, starts to receive warmer air. It can be also noticed how this pattern seems to be strongly linked with the subtropical jet stream. Therefore, it may be expected that this regime would be sensitive to variations in the Pacific North American region and ENSO. As the WNWS develops (**Figures 12B,C**), the intensity of the cyclone in the North eastern Pacific decreases and the winds through the topographic gaps are more intense. The flow north of the Yucatan Peninsula moves from the Tehuantepec to the Papagayo gap. The funneling due to local topography, sustains the intense westward flow over Tehuantepec. In this process, the cold surge interacts with local topography as highlighted by Steenburgh et al. (1998). The intensification of the winds west off Papagayo results from the

FIGURE 11 | Precipitation difference between warm and cold ENSO phases for (A) WNWS and (B) SLLJ regimes. Composites for cold ENSO were subtracted from composites for warm ENSO.

northerly flow, in agreement with the difference in the mechanisms that generate the Tehuantepec and Papagayo jets (see e.g., Chelton et al., 2000 and Romero-Centeno et al., 2007). In the upper levels (**Figure 13**), the ridges and troughs progress to the east, increasing the warm air advection until the cold air is reduced by far and the cold surge declines (**Figure 13D**).

When the northerly trades are more intense and the cold surge is developing, the circulation patterns enhance the inland transport of moisture to Central America. This moisture transport has been related to increased winter precipitation in some locations of Central America (Romero-Centeno et al., 2007). During the winter months, southernmost west coast of Central America is featured by the low level convergence.

During the stage previous to the development of the WNWS, most of the precipitation is constrained between the Yucatan and Florida Peninsulas (**Figure 14A**), alike the precipitation pattern for WGCS. As the WNWS regime develops, ITCZ precipitation increases and the nuclei of precipitation moves to the east and increases its magnitude. Precipitation is fully developed in the Caribbean coast of southern Central America and Honduras (**Figure 14B**) following the WNWS precipitation average distribution. As the system propagates to the East, the precipitating system is displaced from the Gulf of Mexico to Cuba. The eastward propagation continues as the WNWS regime reaches a mature state (**Figure 14C**). In this, precipitation has reached the Greater Antilles and is maximum over southern Central America. As the WNWS dissipates, the remaining precipitating systems leave rain in the southernmost portion of Central America (**Figure 14D**).

Discussion

The application of a weather typing approach to the classification of large scale patterns that affect Central America yielded to 11 main circulation patterns. The classification obtained is dominated by the fingerprints of wintertime circulation. This result claims winter to provide a larger variety of weather phenomena. Indeed, weather during the other seasons, particularly summer, are featured by more constrained large scale conditions. The method allowed to separate identification of the three Cold Surge patterns that are climatologically typical of the region. Namely, surges entering mostly through the Gulf of Mexico, coming from the Pacific that do not reach Central America and that can go further to Central America. Spring conditions are defined, mostly, by the position of the NASH. The eastward dislocation of the NASH induces an anticyclonic circulation over the Gulf of Mexico. Meanwhile, a more developed NASH penetrating into the Gulf is responsible for enhancement of the Trades and the development of stormy weather. Summer circulation is constrained by two of the most important features of the region, which are not necessarily independent, the monsoon regime in North America and the CLLJ.

An important link between the identified circulation types and regional precipitation was found. As the regional distribution of precipitation is characterized by a Pacific-Caribbean seesaw, each slope responds differently to the occurrence of the weather regimes. Most of winter regimes depict particular conditions of cold surges in the region. Those regimes were found to be associated with more precipitation in the Caribbean side of the isthmus. The difference among the regimes, is their ability to modify the meridional distribution of rainfall depending on their location. The drying of Central America during spring was found in consistency with reductions of precipitation under SPAG and SPNW regimes. The persistence of the ENAH regime during spring was determined to be able to trigger the onset of the rainy season in the Pacific region. Note that this regime features an eastward dislocated NASH, reducing its stabilizing impact on convective activity and low-level winds reaching the Pacific coast of Central America, thus, allowing the transport
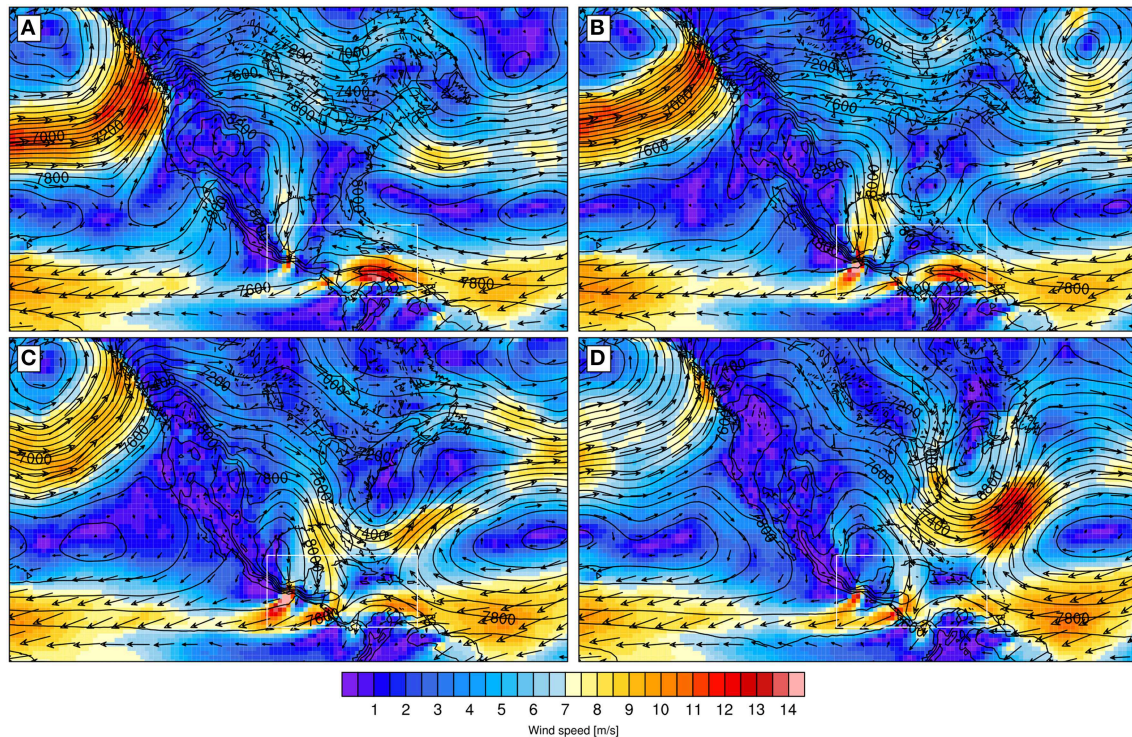
FIGURE 12 | Time evolution of a canonical WNWS event lasting 3 days. Composites for the large-scale patterns at 925 hPa for geopotential height [m/s] (black contours), wind speed [m/s] (colored pixels) and wind vectors are shown. **(A)** shows fields typical for the day previous to the onset. **(B–D)** show fields typical of days 1, 2 and 3 respectively.

of moisture from the Pacific side of the WHWP and reducing static stability.

Summer regimes were found to be consistent with the intensification of regional precipitation. Herrera et al. (2014) highlighted the importance of the CLLJ as a teleconnection mechanism between the Caribbean and the ETPac. Their analysis showed that the CLLJ is related, but not totally attached, to the NASH and other unknown mechanisms regulate its occurrence and intensity. SLLJ reflects the CLLJ peak of intensity; under this condition, convective activity at the CLLJ exit produces descending motion and dry conditions over the Pacific slope of Central America and its adjacent ocean due to adiabatic warming. Meanwhile during autumn regimes, especially AGAD, precipitation over the southwestern Caribbean increases. During this season tropical disturbances are frequent in the above mentioned Caribbean region and are likely to develop as tropical cyclones, relying on how the SST distribution and reduced vertical wind shear enhance organized deep tropical convection. Note that due to data filtering applied and the pattern-producing algorithm these tropical disturbances do not feature as particular regimes.

The ENSO mode was found to affect the frequency of occurrence of the regimes. WNEW and WNCS regimes become more frequent during cold ENSO while WGCS and WNWS are less frequent under the same ENSO phase. Under El Niño, the stronger wind flow over the Gulf of Mexico provides a more suitable environment for conditions featuring WNWS circulation to develop.

Therefore, cold air intrusions are expected to increase for warm ENSO. As shown, precipitation associated with WNWS pattern decreases for warm ENSO. According to Pérez et al. (2014) CACS occurring during warm ENSO, are related to midlatitude wave activity with shorter than typical wave lengths. This might limit the amount of time scale for orographically forced precipitation to build up and the amount of moisture the CACS can acquire from the underlying tropical ocean.

SPAG regime was determined to be more frequent during warm ENSO; however no significant precipitation changes related with this variation were detected. In contrast, the SLLJ becomes much more frequent, dominating strongly the summer circulation. Such enhancement of the CLLJ known for El Niño is fundamental to explain the interannual variability signal of drying in the Central American Pacific slope. On the Caribbean, for the same events, precipitation is intensified, suggesting a deepening of the MSD for warm ENSO.

The regime linked with the monsoonal circulation shows a strong ENSO response as the difference on its frequency for the warm and cold phases of ENSO is 2 to 1. La Niña events provide conditions to increase the veering of the Trades and favor the monsoonal moisture flow to the northern regions. Therefore, rainfall becomes more intense as enhanced low-level moisture converge reduces stability in an ambient which is already conductive for convection due to the absence of a large scale stabilizing mechanism.
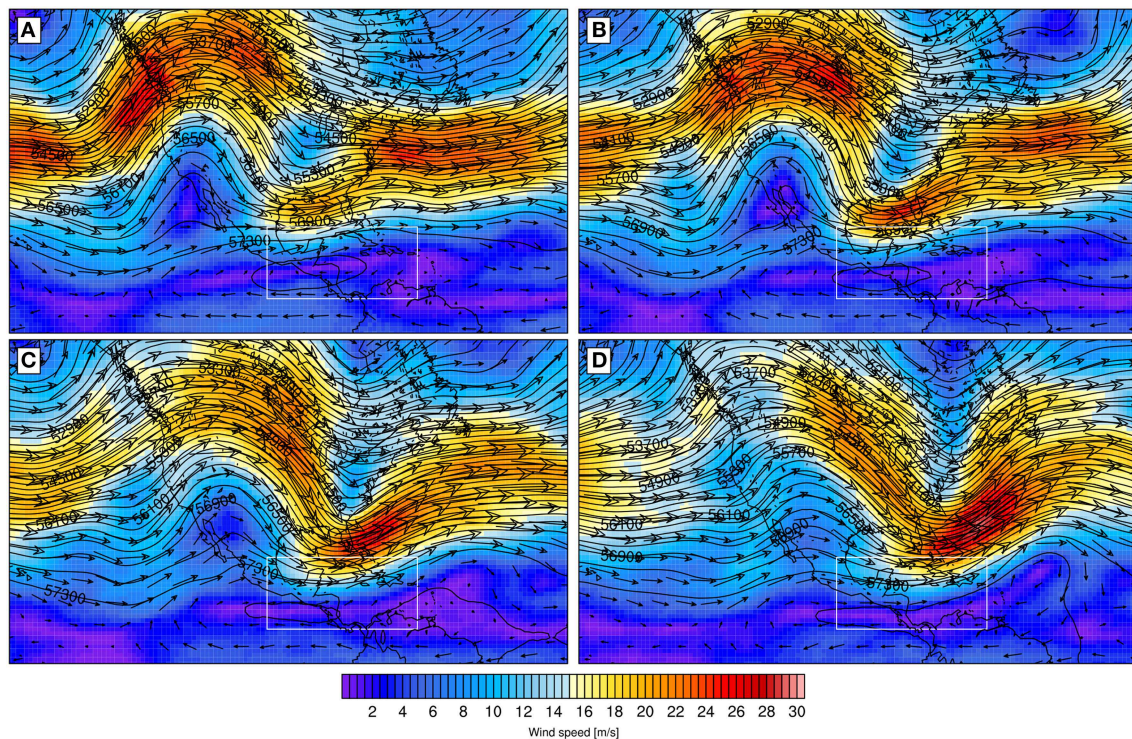
FIGURE 13 | Same as Figure 12 for 500 hPa fields. (A) shows fields typical for the day previous to the onset. **(B–D)** show fields typical of days 1, 2 and 3 respectively.

With the application of the weather types approach, the diagnostics of CACS from large scale patterns was also possible. A comparison of overlapping events detected with a previous climatological study and the present work, showed an agreement of 78%. The WNWS regime was used to study the features, evolution and effect on precipitation of CACS entering Central America. The main features of the pattern that characterizes this evolution can be listed as: (A) west limit NASH east of the Hispaniola island, (B) trough off the United States east coast, (C) geopotential maximum east of the Sierra Madre, (D) weak trade winds and (E) enhanced gap winds at the Yucatan Peninsula and northerlies.

It was determined that the development of CACS reaching Central America is composed of a transition between WGCS and WNWS conditions. For such CACS to fully develop, a 3 day persistent WNWS following WGCS was found on average.

Conclusions

This work presents the application of a weather typing approach to determine the main large scale regimes within the IAS region using publicly available data. The k-means clustering algorithm was applied to find recurrent regimes of low-level winds in this region. The number of clusters for data partitioning was selected using a criterion that measures dependency on initialization and reproducibility of the partition and 11 regimes were selected. There are recurrent low-level circulation regimes in the ERA-Interim data for the study region. Most of the regimes found were consistent with known features of the regional climate (CLLJ,

MSD, and CACS), their spatial and temporal distribution as well as their relationship with ENSO. Some of these regimes are result of regional forcing while others respond to tropical-extratropical interactions. Winter regimes are more sensitive to mid latitude forcing while summer regimes are mostly locally forced. The influence of ENSO on the regimes comes both from the tropical and extratropical response to ENSO. Winter regimes related to CACS are modulated by the effect that ENSO has on the Jet Stream, while summer regimes respond to ENSO effects on WHWP and CLLJ.

A strong link between the identified regimes and precipitation was found. Winter regimes tend to dry the Central American Pacific slope and increase precipitation on the coastal area of the Caribbean slope. Summer precipitation is highly dependent on the dominant regime; SMWR (SLLJ) favors wetter (drier) conditions to the Pacific slope while the opposite effect was found for the Caribbean. Regimes related to easterlies or North easterlies reaching Central America, produce wetter (drier) conditions on the Caribbean (Pacific). Meanwhile, regimes related with westerlies or south westerlies have the opposite effect on precipitation. Friction-induced convergence and topographic interactions are the dynamical mechanisms behind this behavior.

Three of the found regimes reflect the effect CACS have on the low-level circulation over the IAS and therefore, on precipitation. A comparison with a previous CACS climatology (Reding, 1992) was made and despite the differences found, there is a good agreement in the number of events identified as well as their duration. The identification performed in this work detected less
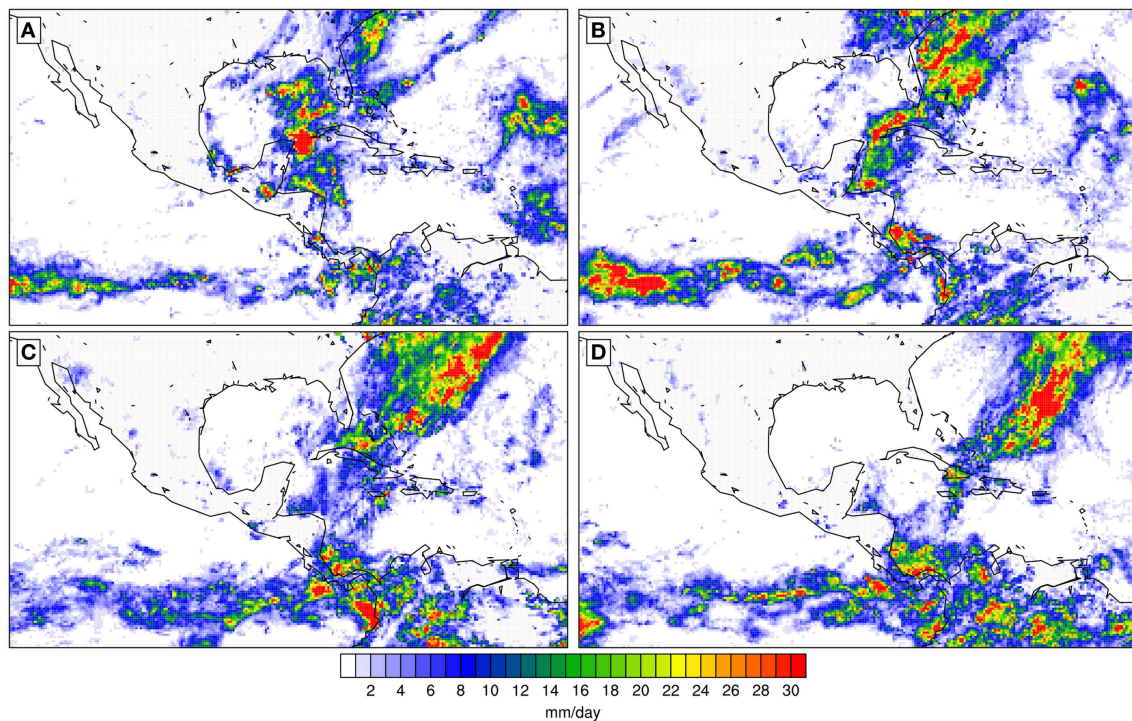
FIGURE 14 | Composited TRMM 3B42 precipitation estimates [mm/day] for the time evolution of a canonical 3-days WNWS event. (A) shows fields typical for the day previous to the onset. **(B–D)** show fields typical of days 1, 2 and 3 respectively.

days with CACS, these differences could be due to disparities in the data nature, spatial-temporal resolution and spatial-temporal research domain. For instance, it is known that the temperature drop precedes the arrival of the anticyclonic winds in CACS. Hence, a detection method based on sub daily station data could make an earlier detection of CACS, nevertheless, an automated based on reanalysis (model) data can be used for dynamical studies and forecasting support.

The use of a weather types approach for studying circulation in the analysis domain was determined to be reliable. However, this method is largely dependent on the availability of daily data for the region and moreover, on the availability of in situ observations for validation. With the advent of new daily regional datasets in the future, we expect the application of such methods to be extremely valuable to support forecasting. Further, work is proposed to study in more detail the relationships between the large scale patterns, local forcing such as orography and observed precipitation from the point of view

of the interannual variability features mentioned in the introduction. The next step of this research would be to tag the large scale features of the tropics-extra tropics interaction via CACS development, the development of forecasting tools based on the circulation types and a proper study on the response of regional precipitation to the effect ENSO has on the large scale patterns found.

Acknowledgments

References

Alfaro, E. J. (2000). Some characteristics of the annual precipitation cycle in central america and their relationships with its surrounding tropical oceans. *Tópicos Meteorológicos y Oceanográficos* 9, 88–103.

Amador, J. (1998). A climatic feature of the tropical Americas: the trade wind easterly jet. *Tópicos Meteorológicos y Oceanográficos* 5, 91–102.

Amador, J. (2008). The intra-americas seas low-level jet (IALLJ): overview and future research. *Ann. N.Y. Acad. Sci.* 1146, 153–188. doi: 10.1196/annals.1446.012

Amador, J., Alfaro, E., Rivera, E., and Calderon, B. (2010). "Climatic features and their relationshipwith tropical cyclones over the intra-Americas Seas," in *Hurricanes and Climate Change,* Vol. 2, eds J. B. Elsner, R. E. Hodges, J. C. Malmstadt, and K. N. Scheitlin (Dordrecht: Springer Science+Bussiness Media B.V.), 149–173.

Bell, G. D., and Chelliah, M. (2006). Leading tropical modes associated with inter-annual and multidecadal fluctuations in North Atlantic hurricane activity. *J. Climate*. 19, 590–612. doi: 10.1175/JCLI3659.1

Brenes, C. L., Coen, J. D., Chelton, D. B., Enfield, D. B., Léon, S., and Ballestero, D. (2003). Wind driven upwelling in the Gulf of Nicoya, Costa Rica. *Int. J. Remote Sens*. 24, 1127–1133. doi: 10.1080/0143116021000028632

Cane, M. A., Zebiak, S. E., and Dolan, S. C. (1986). Experimental forecasts of El Nino. *Nature* 321, 827–832. doi: 10.1038/321827a0

Casola, J. H., and Wallace, J. M. (2007). Identifying weather regimes in the winter-time 500-hPa geopotential height field for the Pacific-North American sector using a limited-contour clustering technique. *J. Appl. Meteor. Climatol*. 46, 1619–1630. doi: 10.1175/JAM2564.1

Chelton, D. B., Freilich, M. H., and Esbensen, S. K. (2000). Satellite observations of the wind jets off the Pacific coast of Central America. Part I: case studies and statistical characteristics. *Mon. Wea. Rev*. 128, 1993–2018. doi: 10.1175/1520-0493(2000)128%3C1993:SOOTWJ%3E2.0.CO;2

Cheng, X., and Wallace, J. M. (1993). Cluster analysis of the northern hemisphere wintertime 500-hPa height field: spatial patterns. *J. Atmos. Sci*. 50, 2674–2696. doi: 10.1175/1520-0469(1993)050<2674:CAOTNH>2.0.CO;2

Cook, K. H., and Vizy, E. K. (2010). Hydrodynamics of the Caribbean low-level jet and its relationship to precipitation. *J. Climate* 23, 1477–1494. doi: 10.1175/2009JCLI3210.1

Cortesi, N., Trigo, R. M., Gonzalez-Hidalgo, J. C., and Ramos, A. M. (2013). Modelling monthly precipitation with circulation weather types for a dense network of stations over Iberia. *Hydrol. Earth Sys. Sci*. 17, 665–678. doi: 10.5194/hess-17-665-2013

Cortez, M. (2000). Variaciones intraestacionales de la actividad convectiva en México y América Central. *Atmósfera* 13, 95–108.

Dai, A., and Wigley, T. M. L. (2000). Global patterns of ENSO induced precipitation. *Geophys Res Lett*. 27, 1283–1286. doi: 10.1029/1999GL011140

Dee, D. P., Uppala, S. M., Simmons, A. J., Berrisford, P., Poli, P., Kobayashi, S., et al. (2011). The ERA-Interim reanalysis: configuration and performance of the data assimilation system. *Q. J. R. Meteorol. Soc*. 137, 553–597. doi: 10.1002/qj.828

Durán-Quesada, A. M., Gimeno, L., Amador, J. A., and, Nieto, R. (2010). Moisture sources for Central America: identification of moisture sources using a Lagrangian analysis technique. *J. Geophys. Res*., 115, D05103. doi: 10.1029/2009JD012455

Gamble, D. W., and Curtis, S. (2008). Caribbean precipitation: review, model and prospect. *Prog. Phys. Geogr*. 32, 265–276. doi: 10.1177/0309133308096027

Garreaud, R. D. (2001). Subtropical cold surges: regional aspects and global distribution. *Int. J. Climatol*. 21, 1181–1197. doi: 10.1002/joc.687

Giannini, A., Saravanan, R., and Chang, P. (2003). Oceanic forcing of sahel rain-fall on interannual to interdecadal time scales. *Science* 302, 1027–1030. doi: 10.1126/science.1089357

Goldenberg, S. B., and Shapiro, L. J. (1996). Physical mechanisms for the association of El Nino and West African rainfall with Atlantic major hurricane activity. *J. Clim*. 9, 1169–1187.

González, C. (1999). Climatología de los frentes fríos que han afectado a Cuba desde 1916-1917 hasta 1996-1997. *Rev. Cubana de Meteorol*. 6, 15–19.

Henry, W. K. (1979). Some aspects of the fate of cold fronts in the Gulf of Mexico. *Mon. Wea. Rev*. 107, 1078–1082. doi: 10.1175/1520-0493(1979)107<1078:SAOTFO>2.0.CO;2

Herrera, E., Magaña, V., and Caetano, E. (2014). Air–sea interactions and dynamical processes associated with the midsummer drought. *Int. J. Climatol*. doi: 10.1002/joc.4077

Huffman, G. J., Adler, R. F., Bolvin, D. T., and Nelkin, E. J. (2010). "The TRMM Multi-satellite Precipitation Analysis (TMPA)," in *Satellite Rainfall Applications for Surface Hydrology*, eds F. Hossain and M. Gebremichael (Dordrecht: Springer Science+Bussiness Media B.V), 3–22.

Karnauskas, K. B., Giannini, A., Seager, R., and Busalacchi, A. J. (2013). A simple mechanism for the climatological midsummer drought along the Pacific coast of Central America. *Atmósfera* 26, 261–281. doi: 10.1016/S0187-6236(13)71075-0

Kerr, R. A. (2000). A north atlantic climate pacemaker for the centuries. *Science* 288, 1984–1986. doi: 10.1126/science.288.5473.1984

Knight, J. R., Folland, C. K., and Scaife, A. A. (2006). Climate impacts of the Atlantic multidecadal oscillation. *Geophysi. Res. Lett*. 33:L17706. doi: 10.1029/2006GL026242

Lamb, H. H. (1950). Types and spells of weather around the year in the British Isles: annual trends, seasonal structure of the year, singularities. *Q. J. R. Meteorol. Soc*. 76, 393–429. doi: 10.1002/qj.49707633005

MacQueen, J. (1967). "Some methods for classification and analysis of multivariate observations," in *Fifth Berkeley Symposium on Mathematics, Statistics and Probability* (University of California Press). 281–297.

Magaña, V., Amador, J., and Medina, S. (1999). The Midsummer Drought over Mexico and Central America. *J. Climate*. 12, 1577–1588. doi: 10.1175/1520-0442(1999)0122.0.CO;2

Magaña, V., and Vázquez, J. (2000). "Interannual variability of Northern activity over the Americas," in *Reprints of the 24th Conference on Hurricanes and Tropical Meteorology*. (Ft. Lauderdale, FL), 116–111.

Malmgren, B. A., Winter, A., and Chen, D. (1998). El Niño-southern oscillation and North Atlantic oscillation control of climate in Puerto Rico. *J. Clim*. 11, 2713–2717.

Mantua, N. J., Hare, S. R., Zhang, Y., Wallace, J. M., and Francis, R. C. (1997). A Pacific interdecadal climate oscillation with impacts on salmon production. *Bull. Amer. Meteor. Soc*. 78, 1069–1079.

Méndez, M., and Magaña, V. (2010). Regional aspects of prolonged meteorological droughts over Mexico and Central America. *J. Clim*. 23, 1175–1188. doi: 10.1175/2009JCLI3080.1

Michelangeli, P. A., Vautard, R., and Legras, B. (1995). Weather regimes: recurrence and quasi stationarity. *J. Atmos. Sci*. 52, 1237–1256. doi: 10.1175/1520-0469(1995)052<1237:WRRAQS>2.0.CO;2

Molteni, F., Kucharski, F., and Corti, S. (2006). "On the predictability of flow-regime properties on interannual to interdecadal timescales," in *Predictability of Weather and Climate*, eds T. Palmer and R. Hagedorn (Cambridge: Cambridge University Press), 365–390.

Moron, V., Robertson, A. W., and Qian, J.-H. (2010). Local versus regional-scale characteristics of monsoon onset and post-onset rainfall over Indonesia. *Clim Dyn*. 34, 281–299. doi: 10.1007/s00382-009-0547-2

Moron, V., Robertson, A. W., Ward, N., and Ndiaye, O. (2008). Weather types and rainfall over senegal. Part I: observational Analysis. *J. Clim*. 21, 266–287. doi: 10.1175/2007JCLI1601.1

Muñoz, E., Busalacchi, A. J., Nigam, S., and Ruiz-Barradas, A. (2008). Winter and summer structure of the Caribbean low-level jet. *J. Clim*. 21, 1260–1276. doi: 10.1175/2007JCLI1855.1

Perez, E., Magaña,V., Caetano E., and Kusunoki, S. (2014). Cold surge activity over the Gulf of Mexico in a warmer climate. *Front. Earth Sci*. 2:19. doi: 10.3389/feart.2014.00019

Pezzi, L. P., and Cavalcanti, I. F. A. (2001). The relative importance of ENSO and tropical Atlantic sea surface temperature anomalies for seasonal precipitation over South America: a numerical study. *Clim. Dyn*. 17, 205–212. doi: 10.1007/s003820000104

Qian, J.-H., Robertson, A. W., and Moron, V. (2010). Interactions among ENSO, the Monsoon, and Diurnal Cycle in Rainfall Variability over Java, Indonesia. *J. Atmos. Sci*. 67, 3509–3524. doi: 10.1175/2010JAS 3348.1

Reding, P. J. (1992). *The Central American Cold Surge: an Observational Analysis of the Deep Southward Penetration of North America Cold Fronts*. MSc. thesis, Department of Meteorology, Texas A&M University, Rogers.

Rogers, J. C. (1984). The association between the North Atlantic oscillation and the Southern oscillation in the Northern Hemisphere. *Mon. Wea. Rev*. 112. 1999–2015.

Romero-Centeno, R., Zavala-Hidalgo, J., and Raga, G. B. (2007). Midsummer gap winds and low-level circulation over the eastern tropical Pacific. *J. Clim*. 20, 3768–3784. doi: 10.1175/JCLI4220.1

Ropelewski, C. F., and Halpert, M. S. (1987). Global and regional scale precipitation patterns associated with the El Nino/ Southern Oscillation. *Mon. Wea. Rev*. 115, 1606–1626.

Schultz, D. M., Bracken, W. E., and Bosart, L. F. (1998). Planetary- and synoptic-scale signatures associated with Central American Cold Surges. *Mon. Wea. Rev*. 126, 5–27. doi: 10.1175/1520-0493(1998)126<0005:PASSSA>2.0.CO;2

Schultz, D. M., Bracken, W. E., Bosart, L. F., Hakim, G. J., Bedrick, M. A., Dickinson, M. J., et al. (1997). The 1993 superstorm cold surge: frontal structure, gap flow, and tropical impact. *Mon. Wea. Rev*. 12, 5–39. doi: 10.1175/1520-0493(1997)125<0005:TSCSFS>2.0.CO;2

Simpson, J., Adler, R. F., and North, G. R. (1988). A proposed tropical rainfall measuring mission (TRMM) satellite. *Bull. Amer. Meteor. Soc.* 69, 278–295.

Small, R. J. O., De Szoeke, S. P., and Xie, S. P. (2007). The Central American Midsummer Drought: regional aspects and large-scale forcing*. *J. Clim.* 20, 4853–4873. doi: 10.1175/JCLI4261.1

Steenburgh, W. J., Schultz, D. M., and Colle, B. A. (1998). The structure and evolution of gap outflow over the Gulf of Tehuantepec, Mexico. *Mon. Wea. Rev.* 126, 2673–2691.

Straus, D. M., and Molteni, F. (2004). Circulation regimes and SST forcing: results from large GCM ensembles. *J. Clim.* 17, 1641–1656. doi: 10.1175/1520-0442 (2004)017<1641:CRASFR>2.0.CO;2

Trigo, R. M., and DaCamara, C. C. (2000). Circulation weather types and their influence on the precipitation regime in Portugal. *Int. J. Climatol.* 20, 1559–1581. doi: 10.1002/1097-0088(20001115)20:13%3C1559::AID-JOC555%3E3.0.CO;2-5

Turner, A. G., Inness, P. M., and Slingo, J. M. (2005). The role of the basic state in the ENSO–monsoon relationship and implications for predictability. *Q. J. R.* 131, 781–804. doi: 10.1256/qj.04.70

Wang, C. (2007). Variability of the Caribbean low-level jet and its relations to climate. *Clim Dyn.* 29, 411–422. doi: 10.1007/s00382-007-0243-z

Wang, C., and Enfield, D. B. (2001). The tropical Western Hemisphere warm pool. *Geophys. Res. Lett.* 28, 1635–1638. doi: 10.1029/2000GL011763

Wang, C., and Enfield, D. B. (2003). A further study of the tropical Western Hemisphere warm pool. *J. Clim.* 16, 1476–1493. doi: 10.1175/1520-0442-16.10.1476

Wang, C., and Lee, S.-K. (2007). Atlantic warm pool, Caribbean low-level jet, and their potential impact on Atlantic hurricanes. *Geophys. Res. Lett.* 34, L02703. doi: 10.1029/2006GL028579

Wang, C., Lee, S. K., and Enfield, D. B. (2007). Impact of the Atlantic warm pool on the summer climate of the Western Hemisphere. *J. Clim.* 20, 5021–5040. doi: 10.1175/JCLI4304.1

Wolter, K., and Timlin, M. S. (2011). El Niño/Southern Oscillation behaviour since 1871 as diagnosed in an extended multivariate ENSO index (MEI. ext). *Inter. J. Climatol.* 31, 1074–1087. doi: 10.1002/joc.2336

Yu, B., and Wallace, J. M. (2000). The principal mode of interannual variability of the North American monsoon system. *J. Clim.* 13, 2794–2800. doi: 10.1175/1520-0442(2000)013%3C2794:TPMOIV%3E2.0.CO;2

Zárate, E. (2013). Climatología de masas invernales de aire frío que alcanzan Centroamérica y el Caribe y su relación con algunos índices Árticos. *Tópicos Meteorológicos y Oceanográficos* 12, 35–55.

Zhang, R., and Delworth, T. L. (2006). Impact of Atlantic multidecadal oscillations on India/Sahel rainfall and Atlantic hurricanes. *Geophys. Res. Lett.* 33:L17712. doi: 10.1029/2006GL026267

Circulation patterns identified by spatial rainfall and ocean wave fields in Southern Africa

András Bárdossy [1,2]*, Geoffrey Pegram [2], Scott Sinclair [2], Justin Pringle [2] and Derek Stretch [2]

[1] Institute for Modelling Hydraulic and Environmental Systems, Universität Stuttgart, Stuttgart, Germany, [2] Civil Engineering, University of KwaZulu-Natal, Durban, South Africa

This paper presents the application of Fuzzy Rule Based Circulation Patterns (CPs) classification in the description and modeling of two different physical processes: rainfall regimes and ocean waves. Large ocean waves are typically generated over fetches of the order of thousands of kilometers far off shore, whereas rainfall is generated by local atmospheric variables including temperature, humidity, wind speed, and radiation over the area of concern. The spatial distribution of these variables is strongly dependent on regional pressure patterns, which are similar for associated weather and wind behavior on a given day. The choice of the CP groupings is made by searching for those CPs which generate (i) different daily rainfall patterns over mesoscale regions and (ii) wave heights from different directions at chosen shoreline locations. The method used to choose the groupings of CPs is a bottom-up methodology using simulated annealing, ensuring that the causative CPs are responsible for the character of the results. This approach is in marked distinction to top-down approaches such as k-means clustering or Self Organizing Maps (SOMS) to identify several classes of CPs and then analysing the effects of those CPs on the variables of choice on given historical days. The CP groups we define are often different for the two phenomena (rainfall and waves) simply because different details of the pressure fields are responsible for wind and for precipitation. The region chosen for the application is the province of KwaZulu-Natal in South Africa, using the same set of raw geopotential heights to represent the pressure patterns, but selecting from the set those typical patterns affecting ocean waves on the one hand and regional rainfall on the other.

Keywords: circulation patterns, rainfall, waves, classification, South Africa

1. Introduction

Local weather (precipitation, temperature wind) and related phenomena such as floods, storm, and waves are strongly dependent on atmospheric processes. These processes are very complex and highly non-linear. On the other hand due to the continuity of the atmospheric conditions these local phenomena are imbedded into large scale features. It is both of theoretical and practical importance to understand these links. Among the atmospheric variables, pressure is the driver for flow and transport. Air pressure at the land surface is a variable which can be measured simply and with good accuracy. Selected observations and meteorological models provide information on high

altitude pressure conditions. Air pressure and geopotential heights are among the best modeled quantities. Therefore, it is reasonable to use them as a basis to describe atmospheric circulation.

The relationship between local variables and atmospheric circulation described with the help of pressure conditions is a complicated and highly non-linear one. On the other hand it reasonable to assume that similar circulation conditions cause similar local meteorological conditions. Therefore, an appropriate classification can help to quantify the relationship between local variables, such as amount of rain on a day in a region or wave height and period on a shoreline, and circulation. The intention is to define classes on the basis of the circulation and the local variables via conditional distributions. The behavior of the local variable described for example using the conditional distribution should be different for the different classes from the unconditional distribution of the variable. A comprehensive summary of classification methods can be found in Jacobeit (2010).

There are different ways one can define groups of circulation patterns (CPs):

1. to define CPs using atmospheric variables only
2. to define CPs using atmospheric variables by taking the local variable into account for setting up the patterns
3. to define CPs using a combination of atmospheric variables and local variables

The first method intends to find typical distinct patterns of the atmospheric variables. The patterns differ in their defining space. Their link to local variables is determined after the classification and might for some variables yield a good distinction in the behavior while for others not.

The second method acknowledges the fact that relatively small differences of the atmospheric variables might lead to very different behavior of the local variables. This means that the classification should not intend to distinguish the patterns by producing very different CPs but to group CPs which to some extent are similar but explain the target variable as well as possible. On the other hand it is important that the classification is done on the basis of the atmospheric variables only so that the classification can be used for time periods lacking the observation of the local variables.

The goals of various classification schemes can differ widely. While the classification of pressure fields on a purely statistical basis might reveal specific features of atmospheric dynamics, it might not provide the best basis for the explanation of the behavior of surface variables such as wind, temperature or precipitation. Under certain circumstances relatively small differences in the atmospheric conditions can lead to very different behavior of the surface variables. If one is interested in explaining the relationship between surface variables and atmospheric conditions then the purpose is to obtain classes of CPs with distinct conditional probabilities or distributions of the selected variables.

The first classifications were developed for regions in Europe on a subjective basis (Lamb, 1972 for Great Britain and Hess and Brezowsky, 1952 for Germany). Automated classifications were developed for different regions in Europe, North America, and China. In this paper fuzzy rule based classifications are developed for precipitation and waves in South Africa.

2. Methodology

The basic methodology of fuzzy rule-based classification was described for explaining precipitation behavior in Bárdossy et al. (1995). The main ideas are summarized here.

The classification is performed on anomalies of daily air pressure based variables: sea level pressures or geopotential heights g. These data can be obtained from reanalysis products on a regular grid. The anomalies are calculated under consideration of the annual cycle of both the mean and the standard deviation of the observed pressure. The anomaly at gridpoint x and time t is calculated as:

$$d(x, t) = \frac{g(x, t) - \bar{g}(x, \mathsf{J}(t))}{s_g(x, \mathsf{J}(t))} \tag{1}$$

where $\mathsf{J}(t)$ is the Julian date corresponding to day t (which is a value between 1 and 366), $\bar{g}(x, \mathsf{J}(t))$ is the mean and $s_g(x, \mathsf{J}(t))$ is the standard deviation of g at location x and Julian day $J(t)$. These anomalies d have zero mean and unit standard deviation for each grid location.

The classification is based on the location of certain anomalies. For each gridpoint x of the pressure grid G five different possibilities of anomalies are considered to define a classification class. A triangular fuzzy number is assigned to each of these possible anomalies:

1. positive anomaly $(0, 3, +\infty)_T$
2. negative anomaly $(-\infty, -3, 0)_T$
3. non-positive anomaly $(-4, -0.85, 0.25)_T$
4. non-negative anomaly $(0.25, 0.85, 4)_T$
5. non-representative anomaly $(-\infty, 0, +\infty)_T$

where the subscript T denotes a triangular fuzzy number with the membership function:

$$\mu_{(a,b,c)_T}(d) = \begin{cases} \frac{d-a}{b-a} & \text{if } a \leq d \leq b \\ \frac{d-c}{b-c} & \text{if } b < d \leq c \\ 0 & \text{else} \end{cases} \tag{2}$$

This means that for the classification of each gridpoint one of the above possible classes is assigned. Thus, a class k can be defined as a vector $j_k(x)x \in G$ where each $j_k(x)$ is an integer such that $1 \leq j_k(x) \leq 5$.

For a given day t and a given set of rules $j_k(x)$ $x \in G$ and $k = 1, \ldots, K$ the classification is performed as follows:

1. For each rule k and each location x the membership value of $d(x, t)$ in the fuzzy set corresponding to $j_k(x)$ is calculated. These values are $\mu_{j_k(x)}(d(x, t))$
2. These individual membership values are combined to an overall degree of fulfillment of the rule k by calculating:

$$\text{DOF}(k, t) = \prod_{m=1}^{4} \left[\frac{1}{\#\{x\, j_k(x) = m\}} \sum_{x|j_k(x)=m} \mu_{j_k(x)}(d(x, t))^{q_m} \right]^{\frac{1}{q_m}} \tag{3}$$

3. The k_0 index corresponding to the maximal DOF(k, t) is selected as class for day t

For further details the readers are referred to Bárdossy et al. (1995).

The fuzzy rule based classification is performed to explain the behavior of one or more selected variables. These are denoted with the variable V. Two types of objective functions are considered. The first one relates the CPs to the exceedance of certain thresholds of V. The objective is to define classes with frequencies of exceedances which differ from the unconditional frequency of occurrences. The first is O_1:

$$O_1(\theta) = \left(\sum_{t=1}^{T} \left(h_{CP(t)}(V > \theta | CP(t)) - h(V > \theta) \right)^2 \right)^{\frac{1}{2}} \quad (4)$$

where h stands for the frequency of an event, V is the variable under interest and θ is a prescribed threshold. This objective expresses that a classification should help to decide if a threshold is exceeded or not.

The second objective type is related to the mean magnitude of the variable V with respect to the CPs. It is formulated as:

$$O_2 = \frac{1}{T} \sum_{t=1}^{T} \left| \frac{(V | \bar{CP}(t))}{\bar{V}} - 1 \right| \quad (5)$$

The second objective function evaluates the ability of the algorithm to derive classes with average values of V that are different from the unclassified average. In other words this objective function measures the separability of the classes from the mean.

These objective functions can be used in combination—for example for different thresholds θ and even for different variables. A weighted combination of them is used as the classification objective function.

The value of the objective functions depends on the classification, which itself depends on the selected rules $\{j_k(x)x \in G \; k = 1, \ldots, K\}$, where K is the number of rules. Once objective functions for the classification are defined, different classifications can be compared with respect to their ability to explain the variability of the surface variable investigated. The higher the objective function values the better the classification is. Thus, one can use an optimization procedure to find rules $j_k(x)$ which maximize the objective functions. The number of possible rule systems for a given number of patterns is given by the combinatorial:

$$N_K = \begin{pmatrix} 5^{|G|} \\ K \end{pmatrix}$$

This is usually an extremely large number (for example for a small pressure grid 10×10 with $|G| = 100$ nodes and $K = 10$ rules the number of possible rule systems is $> 10^{340}$) thus the best rules cannot be found by trying all possibilities. Instead an optimization method has to be applied. Simulated annealing provides a reasonable alternative as described in Bárdossy et al. (2002).

2.1. Classification Quality

The quality of the classification can be measured by the above defined objective functions. Besides that other measures can be defined, which can be used for comparison, for example to find the optimal number of classes. For this one can use thresholds for the variable V. The entropy of the conditional distributions can be used to measure the binary quality of a classification:

$$H(K) = \sum_{k=1}^{K} h_k \left(p_k \log_2 p_k + (1 - p_k) \log_2(1 - p_k) \right) \quad (6)$$

where p_k is the probability of the exceedance of the threshold on a day with the k-th CP, and h_k is the frequency of the k-th CP. The quantity $H(0)$ is the entropy in the case no classification was performed:

$$H(0) = p_0 \log_2 p_0 + (1 - p_0) \log_2(1 - p_0) \quad (7)$$

A classification provides information for the variable V if $H(K) < H(0)$. In general a classification using K classes is better than another with L classes if:

$$H(K) < H(L)$$

2.2. Non-Uniqueness Issues

Different CP classifications can be obtained for the same region. In Philipp et al. (2014) the authors investigated 27 automatic CP classification approaches and found that different classification methods lead to very different classifications. The Fuzzy Rule Based classification method can lead to different classifications as the stochastic optimization obtained using simulated annealing does not necessarily lead to the same classification if another sequence of random numbers is selected. A different choice of stations or a different choice of thresholds or weights for the objective functions can lead to different classifications too. Different classifications can be compared from the viewpoint of their performance or from the viewpoint of the similarity of their classes. While the calculation of the objective functions is straightforward, the similarity of the classifications requires further measures.

Two statistics can be calculated based on the contingency tables of the pairs of classifications. For two different classifications n_{ij} is the number of days in class i for the first and in class j in the second classification. The χ^2 statistics to compare the classifications is calculated as:

$$\chi^2 = \sum_{i=1}^{r} \sum_{j=1}^{s} \frac{(n_{ij}n - n_i.n_{.j})^2}{n_i.n_{.j}n} \quad (8)$$

where r is the number of classes in the first classification, s is the number of classes in the second classification, $n_i.$ is the number of days in class i for the first classification, $n_{.j}$ is the number of days in class j for the second classification and n is the total number of days. If the classifications are independent then the χ^2 value is small, the bigger it is the more the classifications resemble each

other. Based on the χ^2 values two measures of dependence were calculated, the modified Pearson coefficient C:

$$C = \sqrt{\frac{\min(r, s)}{\min(r, s) - 1}} \sqrt{\frac{\chi^2}{\chi^2 + n}} \qquad (9)$$

and the Cramer coefficient (Hartung et al., 2005) V:

$$V = \sqrt{\frac{\chi^2}{n(\min(r, s) - 1)}} \qquad (10)$$

Both coefficients are bounded by 1, and the higher they are the stronger the association is. The associations of CP classifications for the same geographical regions using different objective functions or different stochastic optimization settings are usually strong, which is a consequence of the fact that the same variables (geopotential heights) are classified.

2.3. Data Used

The classifications were performed using ECMWF ERA reanalysis data sets. The classification is based on daily normalized anomalies, derived from the 700 hPa geopotential height with a grid resolution of 2.5^o (10°—50° S; 0°—50° W). Geopotential heights were obtained from the ERA-Interim data set of Dee et al. (2011) for the period 1979–2009 (http://apps.ecmwf.int/datasets/).

3. Classification for Precipitation

3.1. Objective Functions

Precipitation has a highly skewed distribution with above 80% probability of a dry day in many parts of South Africa. Individual very high values of precipitation can lead to "random" optima which are not robust. Instead a new variable related to the average wetness of a selected number of stations was considered:

$$W(t) = \frac{\#\{x_i; Z(x_i, t) > 0\}}{\#\{x_i; Z(x_i, t) \geq 0\}} \qquad (11)$$

by definition $0 \leq W(t) \leq 1$. This variable is taken as V for the objective functions in Equations (4, 5).

The 24 Climate Regions defined by Kruger (2004), slightly modified by concatenating some of the very small regions (mostly in dry areas) with larger ones, were used for the classification. The map with the locations of the regions is shown in **Figure 1**. A set of representative stations was selected for each region and the CPs were classified using the above defined objective function. The classification obtained using this objective function works well for precipitation in all selected regions both for the calibration and the validation time periods. For variety, we will show some CPs and resulting rainfall in **Figure 2** and specific CPs selected for region 6 in **Figure 3**.

3.2. Spatial Extent of Classification and Non-Uniqueness of CP Set Selection

We explore three sets of classifications driven by precipitation wetness. The first CP set is conditioned on wetness in region 5 and we compare the differences in rainfall distributions from
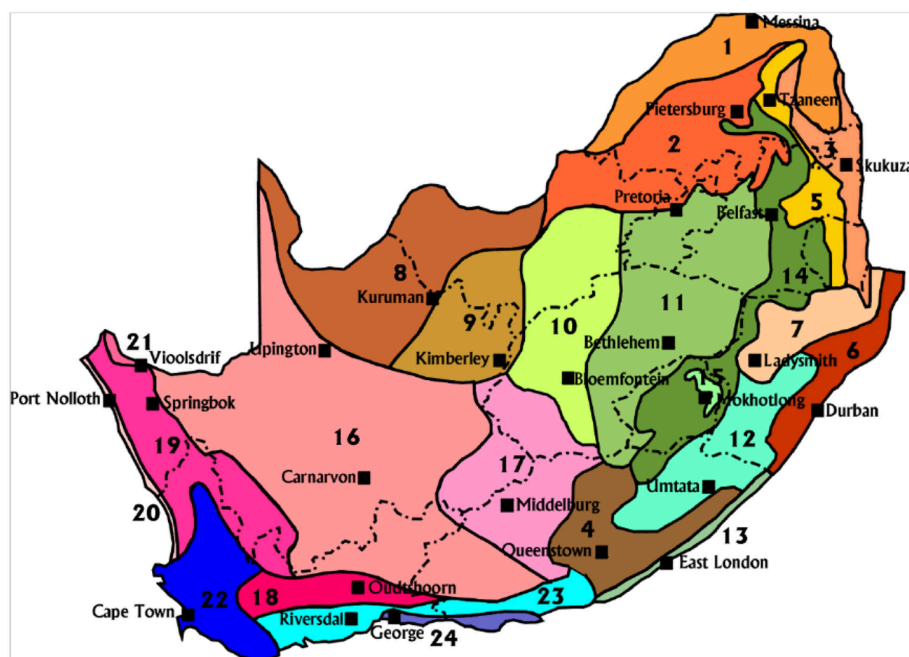
FIGURE 1 | The Kruger climate regions of South Africa after (Kruger, 2004).
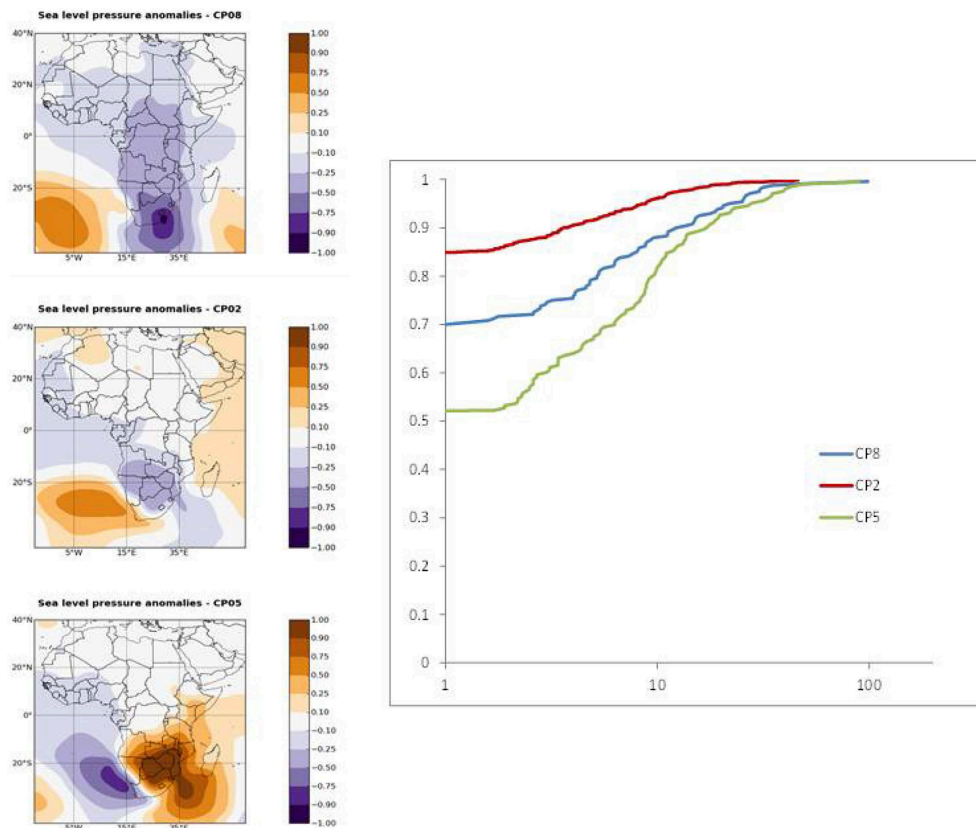
FIGURE 2 | Three different CPs and the related distributions of daily precipitation in Mpumalanga in Region 5 of Figure 1. The maps on the left are CPs 8, 2, and 5, appearing as blue (middle), red (dry), and green (wet) lines in the figure of frequency distributions.

three distinct sets of CPs. The second set involves determining the robustness of the method when different sets of gauges in a region are used for CP classification. For this purpose we use data from region 6 and randomly sample 2 sets for comparison. The third experiment treats CPs defined over three regions in **Figure 1**. These are region 6 which experiences subtropical summer rainfall and the occasional hurricane, 10 which is typically savannah, experiencing summer rainfall dominated by convective systems, and 22 which has a Mediterranean climate and experiences mostly frontal system winter rainfall.

Due to the stochastic optimization no unique best classification can be achieved. It is of interest to see how

- the selection of the stations for the objective function
- the randomness due to stochastic optimizations

influences the results. For this purpose the performance measures were calculated for different classification results.

To introduce the first experiment, which is to demonstrate the link between rainfall regimes and CPs, we offer **Figure 2**, which shows the correspondence between (i) three CPs chosen from a set of 8 in Mpumalanga and (ii) the rainfall distribution at a particular rain-gauge in the region. **Figure 2** shows the 700 hPa anomalies for three selected CPs and the corresponding distributions of daily precipitation. CP2 is the driest with the

highest probability of a dry day. CP5 is the wettest with a much lower probability of a dry day. CP8 is medium wet with statistics between CP5 and CP2. The distributions are significantly different from each other indicating that classification provides useful information on precipitation behavior.

To illustrate the methodology applied in the second experiment, we selected region 6, then we selected some gauges within the region, in different configurations, to classify the Circulation Pattern anomalies [CPs] which are the cause of different types of rainfall over this region.

We find we get similar CPs, enough similarity of shape to pick a set, [note that the labeling within each set is random, so we match by correlation of shape, not label]. **Figure 3** shows the 700 hPa anomalies for two different classifications.

This similarity allows us to settle on one set of CPs per region (and season) because we have a robust method. In the next section we turn to the Infilling/repair problem an extension of which we will use later in spatial interpolation between gauges.

The third experiment was to make comparisons between CP sets within and between 3 regions. This started by selecting 5 random subsets of 12 gauges from the historical datasets in each of the regions. CPs were conditioned on each of the 5 subsets in each region independently. We then set out to determine whether the similarity of the sets within each region was materially greater

FIGURE 3 | Two pairs of CPs: top two similar to each other and the bottom two likewise, selected from the CPs chosen on 2 sets of gauges in Region 6.
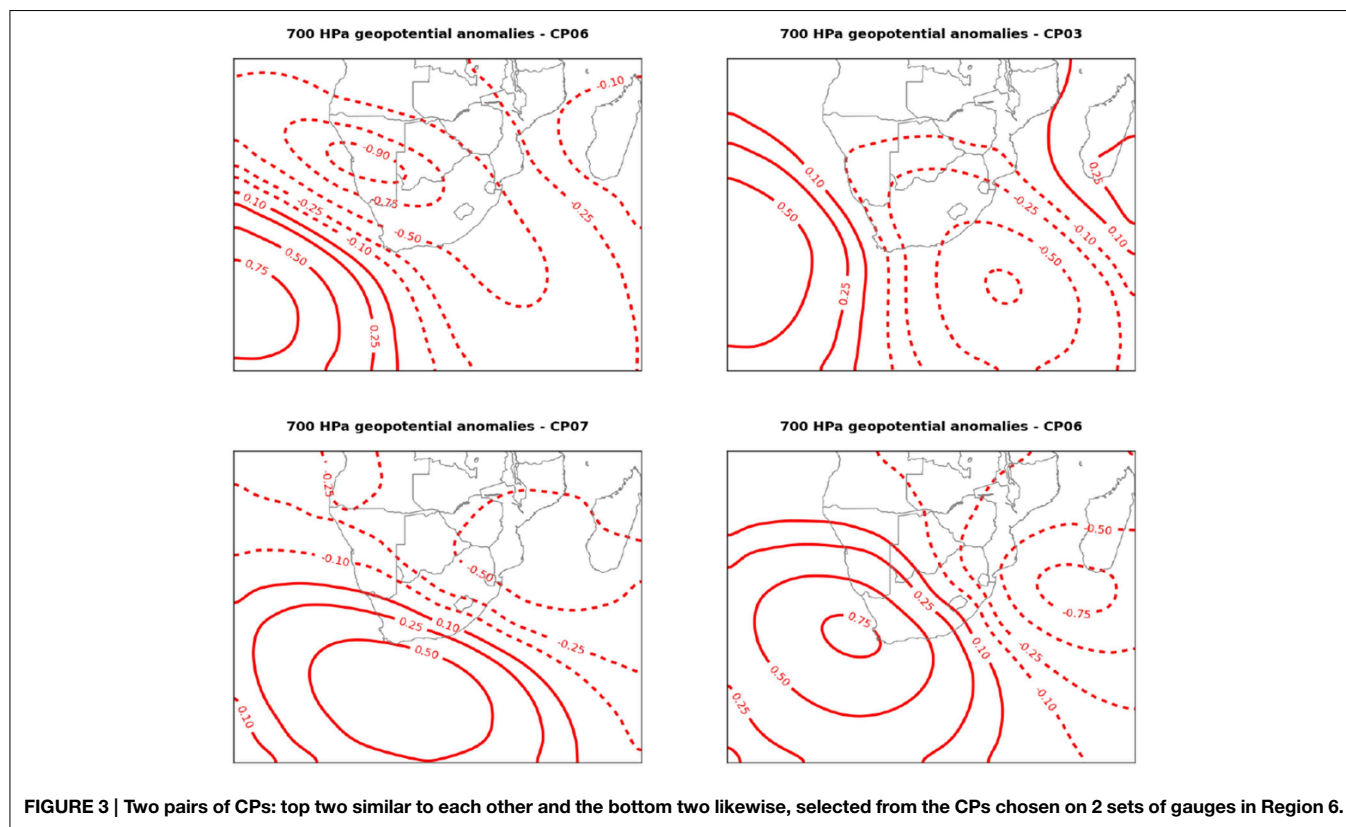
than between regions. Because these are categorical data it does not make sense to compute correlation coefficients between sets, so Pearson and Cramer coefficients (Equations 9, 10) based on the χ^2 were the statistics used.

We chose three climate regions within South Africa to compare sets of CPs. The regions chosen and shown in **Figure 1** are: region 6 (KwaZulu-Natal), region 10 (Free State), and region 22 (Western Cape). We used 5 different random groupings of gauges for classifications in each region, thus for each region we derived 5 independent sets of CPs, making 15 in all.

The purpose of this calculation was to determine if the CPs derived for a given region had a higher inter-association than between regions. These coefficients were calculated for all pairs of classifications for the same regions. Then the averages of the association measures were calculated for classifications corresponding to the same (excluding the comparison of a classification with itself), and corresponding to different regions leading to 2 sets of 3 by 3 matrices.

The average of the 20 within-region statistics are compared with the averages of the 25 between-region statistics and appear in **Tables 1**, **2** (the difference in the numbers in each group is because we omitted the diagonal elements of comparing a set with itself). The result is that there is a significant difference between the within against the between coefficients, supporting our exploitation of this CP selection procedure based on daily wetness.

All classifications show significant dependence, which of course is reasonable as the atmospheric conditions on the

TABLE 1 | CP similarities for different classifications using the Pearson coefficient in the regions numbered 6, 10, and 22 in Figure 1.

Region	6	10	22
6	0.699	0.617	0.640
10	0.617	0.674	0.592
22	0.640	0.592	0.698

TABLE 2 | CP similarities for different classifications using the Cramer coefficient in the regions numbered 6, 10, and 22 in Figure 1.

Region	6	10	22
6	0.263	0.213	0.226
10	0.213	0.247	0.201
22	0.226	0.201	0.262

same region are classified in all cases. On the other hand the within block average statistics are larger than the between block counterpart, inferring that there is a stronger within relationship than between blocks. The conclusion is that the choosing of CPs dependent on regions is valuable and worth the effort.

4. Classification for Waves

Atmospheric circulations drive regional wave climates through atmosphere-ocean interactions. In particular they control the

generation of the extreme wave events that cause severe coastal erosion. They are therefore also fundamental drivers of coastal vulnerability. The link between the wave climates and atmospheric circulation is complex. However, statistical models that link synoptic scale atmospheric circulation to regional wave characteristics have recently been shown to give significant insights (Pringle et al., 2014). We propose that the classification of atmospheric drivers can improve coastal vulnerability assessments and the prediction of climate change effects. For example it provides a natural way to identify and isolate the effects of independent storm events, which is required for extremum analysis. For example (Corbella and Stretch, 2012a) identified independent events based on the autocorrelation or by using a 6-h inter-arrival window. The transition of CPs between classes is a physically more meaningful method for defining independent events. Atmospheric CPs also contain important information regarding the distribution of wave height, direction and period, because when a particular CP type occurs the associated wave height, direction, and period can be (statistically) predicted. Linking wave events to CPs can also be used to extend current data sets and to infill missing data (Hewitson and Crane, 2002). Finally the prediction and evaluation of climate change impacts on coastal vulnerability would be more robust if linked to changes in the atmospheric CPs that are the basic drivers of wave climates and extreme wave events.

4.1. Case Study Description

The KwaZulu-Natal (KZN) coastline (**Figure 4**) is associated with a high energy wave climate. A number of weather types have been cited as the drivers of this wave climate. For example tropical cyclones, mid-latitude (extra-tropical) cyclones and cut off lows (Rossouw et al., 1982; Corbella and Stretch, 2012c; Mather and Stretch, 2012). The location and persistence of tropical cyclones (TC's) are believed to drive large wave events that cause severe beach erosion in KZN (Corbella and Stretch, 2012c; Mather and Stretch, 2012). Cut-off lows are deep low pressure systems that

FIGURE 4 | Locations of the wave observation buoys at Durban and Richards Bay, along the KwaZulu Natal coastline.

are displaced from the normal path of west-east moving mid-latitude cyclones (Preston-Whyte and Tyson, 1988). They are caused by instabilities within the westerly zonal flow due to the high wind shear. Vortices can become cut-off and move equator-ward (Preston-Whyte and Tyson, 1988). These features lead to seasonality in the wave climate and the occurrence of storms in particular. On average autumn and winter (April to September) are associated with the largest wave energy, while summer (January to March) has the smallest (Corbella and Stretch, 2012c). The significant wave height (Hs) is the key variable of interest for coastal vulnerability applications. Our algorithm considers both the daily average significant wave height and the daily maximum significant wave height. Wave data for the period 1992–2009 were obtained from wave buoys located near Durban and Richards Bay on the KZN coastline (**Figure 4**).

In this application the goal of the classification is to obtain a set of CP classes which explain extreme wave events. Wave heights larger than 3.5 m have been shown to cause significant erosion along the KZN coastline (Corbella and Stretch, 2013). The objective functions (Equations 4, 5) were used as performance measures.

The wave height threshold θ can be exploited to incorporate various scenarios. Two different thresholds were used. The first relates to the occurrence of extreme events ($\theta_1 = 3.5$ m), while the second relates to midrange wave heights ($\theta_2 = 2.5$ m). The second objective function type is also used to provide a more detailed classification.

To account for the persistence of CPs during extreme events (Equation 4) was modified to include storm durations, defined as the duration of wave height excursions above 3.5 m.

4.2. Dominant CP Classes

Figure 5 shows the average anomaly patterns for all the CP classes. CP99 refers to an unclassified class. Useful statistical parameters for each CP class are their frequency of occurrence, their contribution to extreme events, and the average and maximum significant wave heights (H_s) associated with them. These parameters are shown in **Table 3**.

The results reflect a number of trends in CP-wave generation. However, only the two most significant trends are discussed herein. Firstly CP01 and CP02 (**Figure 5A**) occur most frequently (about 17% of the time). Both CP classes resemble a mid-latitude cyclone in its different stages of development. The CP01 resembles the central low pressure region of a mid-latitude cyclone as it moves from west to east south of the country, while CP02 resembles the high-pressure region that follows. Secondly, **Table 4** shows a class (CP03) that comprises 60% of all extreme wave events. The CP03 is shown to contribute significantly to extreme events all year round with highest contribution in winter (65%). However, CP03 (**Figure 5C**) occurs infrequently (9% of the time). Its occurrence is associated with large average and maximum significant wave heights ranging from 2.4 to 3.0 m and 5.0 to 8.5 m, respectively. CP05 and CP06 (**Figures 5E,F**) contribute approximately to 30% of extreme events in spring and summer, respectively. The CP06 resembles a pattern similar to TC's south of Madagascar. TC's located within this region have been
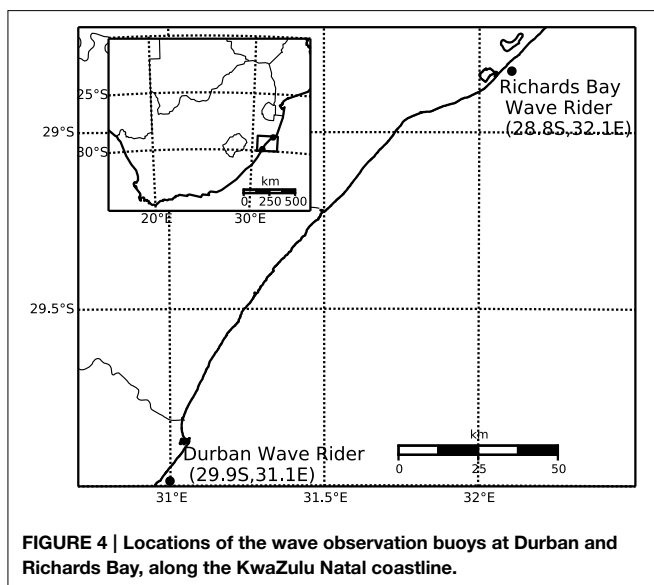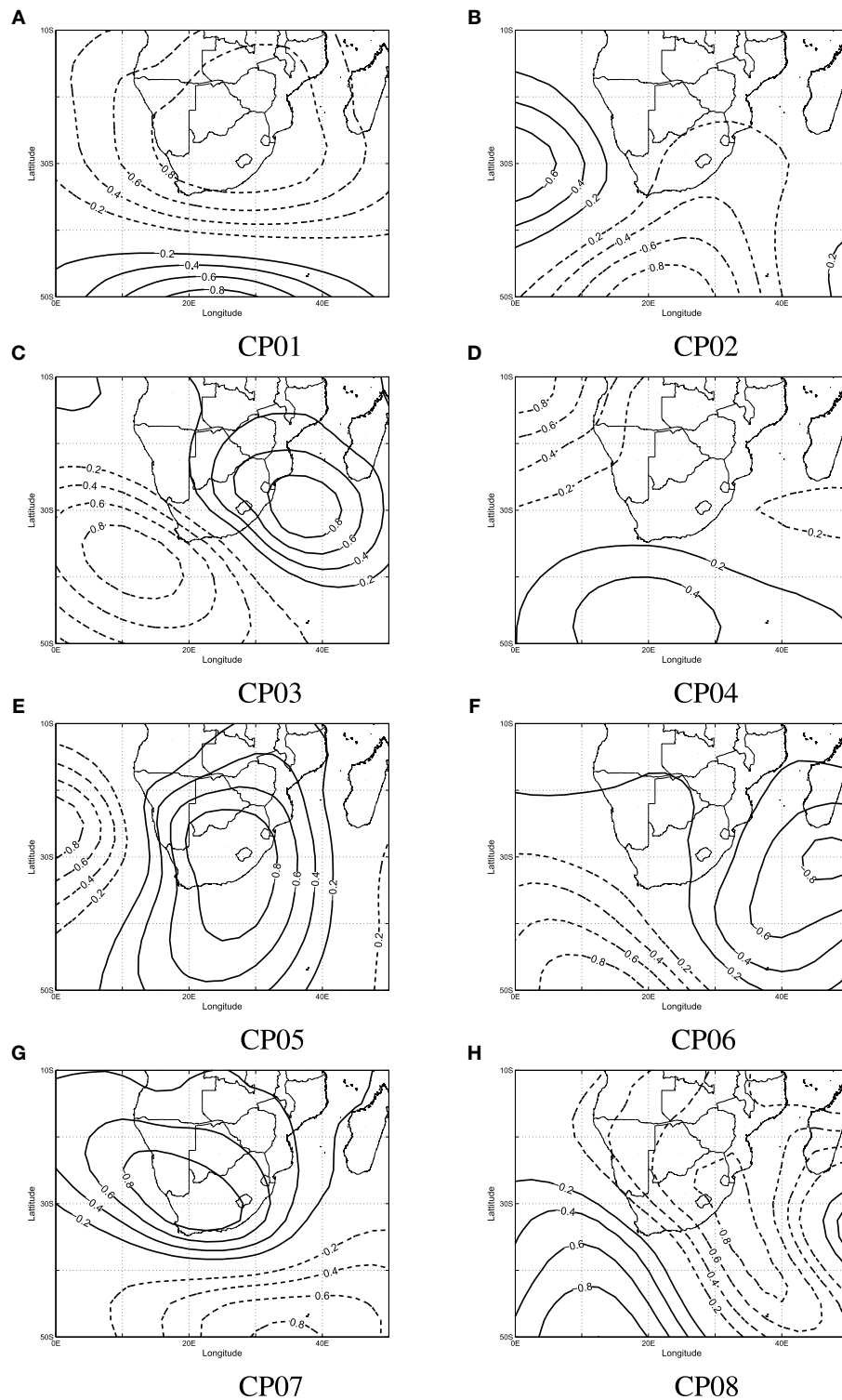
FIGURE 5 | Average anomaly patterns for 8 CP classes derived from the regional wave climate data. Negative (low) pressure anomaly contours are shown as solid lines while positive pressure contours are dashed.

cited to drive large swells toward the KZN Coast (Mather and Stretch, 2012). The CP05 resembles low-pressure systems over the interior.

The algorithm only considered CPs associated with extreme events at the time the event was recorded. In other words no time lags were considered when deriving the CP classes. Therefore, the

TABLE 3 | CP Occurrence frequencies and wave height statistics associated with each CP class.

Statistics	CP01	CP02	CP03	CP04	CP05	CP06	CP07	CP08	CP99[a]
OCCURRENCE FREQUENCY ($p(CP)$%)									
Summer	18	18	8.0	13	7.5	8.1	5.6	15	8.3
Autumn	18	19	8.0	11	10	7.2	5.1	13	8.8
Winter	16	17	8.1	12	11	8.4	4.5	14	8.9
Spring	17	16	9.1	12	9.4	7.7	5.0	15	9.2
All Seasons	17	17	8.3	12	9.6	7.8	5.1	14	8.8
THRESHOLD EXCEEDANCE FOR A GIVEN CP ($p(H_s \geq \theta \mid CP)$%)									
Summer	–	0.4	8.0	0.3	–	3.5	2.6	0.7	–
Autumn	1.2	1.5	12	1.6	2.1	2.0	5.6	0.6	5.0
Winter	0.9	0.8	14	–	0.9	0.4	2.3	0.8	0.4
Spring	0.3	–	4.6	0.6	2.2	–	0.7	–	–
All Seasons	0.6	0.7	9.6	0.6	1.4	1.5	2.8	0.5	1.4
EXCEEDANCE CONTRIBUTION ($p(CP \mid H_s \geq \theta)$%)									
Summer	–	5.6	50	2.8	–	22	11	8.3	–
Autumn	7.7	10	33	6.4	7.7	5.1	10	2.6	17
Winter	7.5	7.5	64	–	5.7	1.9	5.7	5.7	1.9
Spring	4.5	–	55	9.1	27	–	4.5	–	–
All Seasons	5.8	7.4	48	4.2	7.9	6.9	8.5	4.2	7.4
AVERAGE H_s (m) FOR EACH CP									
Summer	1.8	1.9	2.5	1.8	1.8	2.2	2.2	1.9	1.9
Autumn	1.8	1.9	2.7	1.9	2.0	2.0	2.1	1.9	2.1
Winter	2.0	2.0	2.9	1.9	2.1	2.0	2.2	2.0	1.9
Spring	2.0	1.9	2.4	1.9	2.2	2.0	2.2	2.0	2.0
All Seasons	1.9	1.9	2.6	1.9	2.1	2.1	2.2	2.0	2.0
STANDARD DEVIATION of H_s (m) FOR EACH CP									
Summer	0.48	0.49	1.1	0.49	0.53	0.76	0.74	0.61	0.49
Autumn	0.58	0.66	1.0	0.70	0.76	0.66	0.90	0.55	1.0
Winter	0.58	0.61	0.94	0.55	0.66	0.58	0.66	0.55	0.67
Spring	0.51	0.49	0.84	0.52	0.71	0.50	0.61	0.50	0.49
All Seasons	0.54	0.57	1.0	0.56	0.69	0.63	0.74	0.56	0.70
MAX H_s (m) FOR EACH CP									
Summer	3.4	4.0	8.5	3.7	3.4	5.0	5.2	5.6	3.3
Autumn	4.0	5.5	5.7	5.5	6.3	4.3	5.1	4.0	5.4
Winter	4.2	3.8	5.6	3.4	3.8	3.5	4.3	4.8	3.6
Spring	3.9	3.3	5.3	4.5	5.4	3.4	3.7	3.5	3.3
All Seasons	4.2	5.5	8.5	5.5	6.3	5.0	5.2	5.6	5.4

[a] CP99 is the unclassified class. Blank entries imply zero occurrences in the data set.

algorithm assumes that extreme events are driven by relatively stationary CPs.

4.3. CP Variability

The degree of fit (DOF) describes the membership of a CP for given day to a particular class. The larger the DOF the stronger the belief that the CP belongs to a particular class. **Figure 6** shows the average anomaly pattern for CP03 and the CPs associated with both the strongest and weakest membership for that class. CP03 is associated with a strong low pressure region east/south-east of South Africa. The pattern also shows a strong high-pressure region to the southwest. The coupling between the strong low and high pressure drive strong winds and subsequently large waves toward the coastline. The CP with the weakest membership to CP03 is shown to be a weak anomaly pattern (refer to **Figure 6C**).

4.4. Variability within Classes

It is expected that in regions of high pressure pattern variation should be low. This is attributed to the stability of high pressures in their positions. In contrast pattern variation in regions of low pressure should be higher primarily due to the movement of low pressure systems. This is reflected in **Figure 6D**, which shows significantly larger variation (standard deviation of 1)

in the vicinity of the low-pressure region. The magnitude of the variation also indicates that CPs driving extreme events are associated with strong low pressures.

4.5. CP Rules and Extreme Events

Daily CP realizations associated with extreme wave events ($H_s \geq$ 3.5 m) were compared to the average class pattern to which they belong. **Figure 7** shows the average pattern for CP03 together with selected extreme events corresponding to CP03. The locations of the peak negative anomalies are shown in the plot. Significant pattern variability within the class is apparent. **Figure 8** and **Table 4** show the CPs associated with six of the

largest significant wave height events. The majority of the six events have been classified as belonging to CP03. **Figure 8F** from visual inspection shows a pattern similar to CP04 and CP08. Both classes are associated with low-pressure regions southeast of Madagascar. However, the CP has been classified as belonging to class CP08 and not CP04. From a visual account it appears to better resemble class CP04. **Figures 8A,C** are the CPs associated with the March 2007 storm which caused severe coastal erosion along the KZN coastline (Corbella and Stretch, 2012b; Mather and Stretch, 2012) with significant wave heights reaching 8.5 m.

5. Discussion and conclusions

In this paper different problems related to the fuzzy rule based classification of CPs were discussed. It was shown that reasonable classifications can be developed for precipitation and waves in South Africa. We did this by selecting long sequences of CPs in the region surrounding Southern Africa and conditioning the selection of the CPs on selected variables germane to the task; daily wetness for rainfall and wave height frequencies of ocean waves. The classifications yield classes with significantly different behavior depending on the classification goal. It was shown in the

TABLE 4 | Six of the most extreme wave events on record and their associated CPs for the period 1992–2009.

Fig	Date	CP	H_S (m)
(a)	19/03/2007	CP03	8.50
(b)	05/05/2001	CP05	6.30
(c)	18/03/2001	CP03	5.92
(d)	03/04/2001	CP03	5.66
(e)	23/09/1993	CP03	5.64
(f)	19/03/2001	CP08	5.63
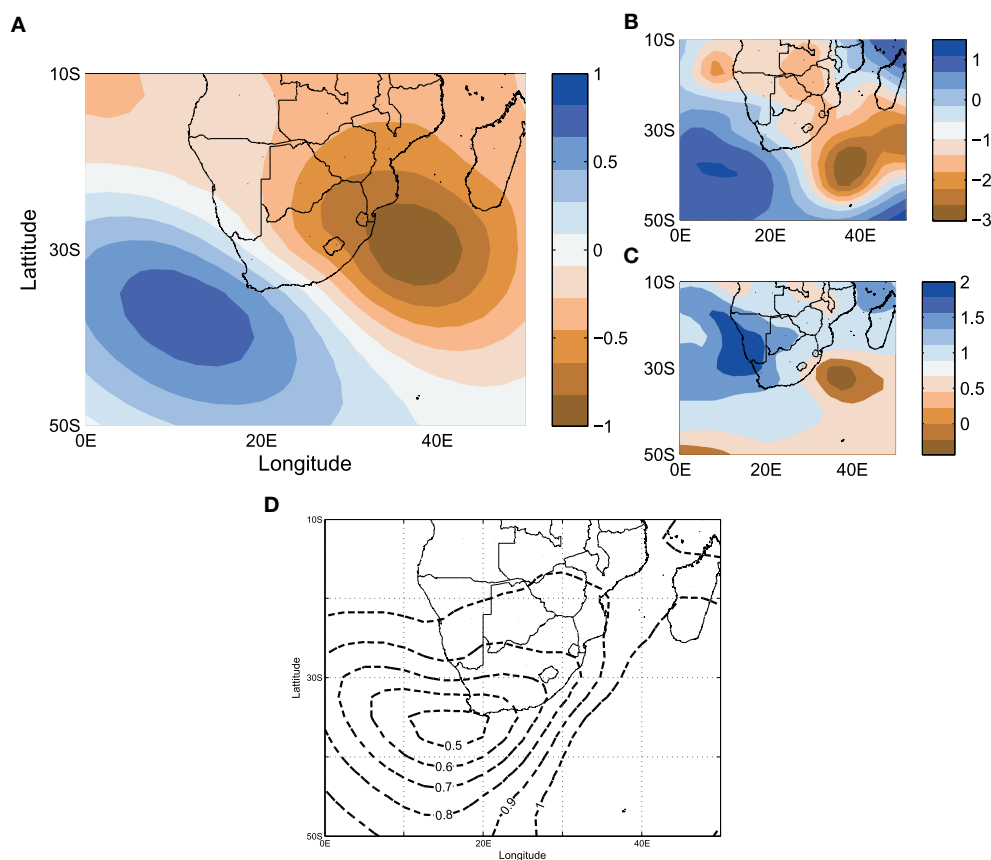
FIGURE 6 | Average anomaly pattern for CP03 (A) showing (B) the anomaly with highest DOF, (C) the anomaly with lowest DOF value, and (D) the standard deviation for all CP03 anomalies.
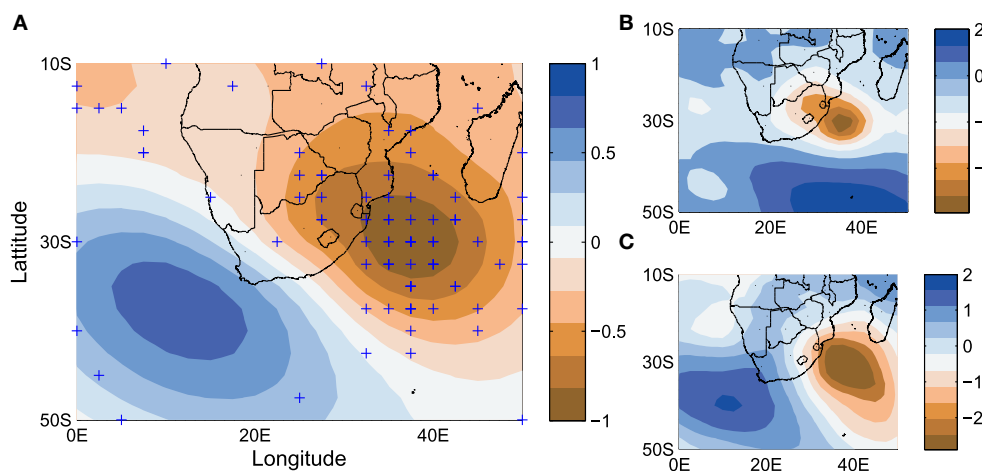
FIGURE 7 | (A) Average anomaly pattern CP03 with (+) symbols indicating the centers of all negative anomalies (low pressures) contributing to the class. **(B,C)** show actual CP's for the dates 19/03/2007 and 30/08/2006, respectively, both of which were classified as members of the CP03 class.
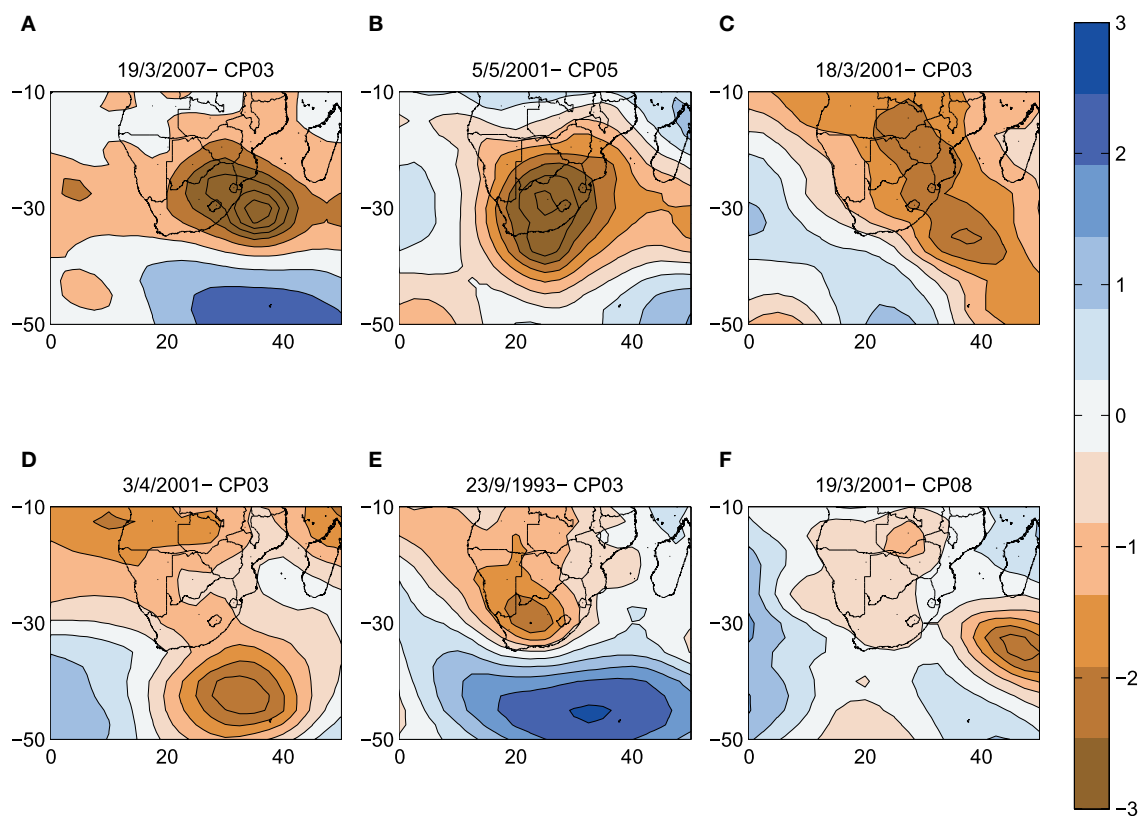
FIGURE 8 | CP's associated with the six largest significant wave heights for the dates (A) 19/3/2007, (B) 5/5/2001, (C) 18/3/2001, (D) 3/4/2001, (E) 23/9/1993, and (F) 19/3/2001.

precipitation part of the study, that using different stations of a climatic region for the classification objective leads to different classifications, but the performance of these classifications is nevertheless very similar. Different classifications for the same region are more similar than classifications corresponding to different regions. This justifies the use of different classifications for the different regions and variables, because they add discriminatory power to the modeling procedure.

In the case of the wave study, the emphasis was on the statistical link between atmospheric CPs and extreme wave events. The results show that the classification algorithm is able to identify CPs that drive extreme wave events along the KZN coastline. The most frequent CPs associated with wave generation are revealed as low and high pressure anomalies south of the country. These reflect easterly traversing mid-latitude cyclones and their associated high pressures anomalies. The CP class that drives the majority of extreme wave events (labeled CP03) is associated with strong low pressure anomalies east of the country. A high/low pressure coupling drives strong winds toward the coastline and generates large waves. It is not clear what weather regimes are associated with these events since both mid-latitude cyclones and cut-off lows may belong to the CP03 class depending on their location. The classification algorithm does not currently identify CP anomalies as part of an overall structure developing in space and time: each class could be a snapshot in the temporal evolution of (perhaps distinct) CPs. Therefore, a particular weather system may be associated with a number of classes during its development, which makes for added complexity and requires further research.

There are similarities in the CP classes driven by the two surface variables because in some instances they are linked to similar synoptic weather systems. However, there are also significant differences in the details of the pressure fields. These differences are expected because large ocean waves are typically generated over fetches of the order of thousands of kilometers far off shore, whereas some rainfall is generated by local atmospheric variables including temperature, humidity, wind speed, and radiation over the area of concern.

Acknowledgments

References

Bárdossy, A., Duckstein, L., and I, I. B. (1995). Fuzzy rule - based classification of atmospheric circulation patterns. *Int. J. Clim.* 15, 1087–1097.

Bárdossy, A., Stehlik, J., and Caspary, H.-J. (2002). Automated objective classification of daily circulation patterns for precipitation and temperature downscaling based on optimized fuzzy rules. *Clim. Res.* 23, 11–22. doi: 10.3354/cr023011

Corbella, S., and Stretch, D. (2012a). Predicting coastal erosion trends using non-stationary statistics and process-based models. *Coast. Eng.* 70, 40–49. doi: 10.1016/j.coastaleng.2012.06.004

Corbella, S., and Stretch, D. (2012b). Shoreline recovery from storms on the east coast of South Africa. *Nat. Hazards Earth Syst. Sci.* 12, 11–22. doi: 10.5194/nhess-12-11-2012

Corbella, S., and Stretch, D. D. (2012c). The wave climate on the the KwaZulu Natal coast. *J. S. Afr. Inst. Civ. Eng.* 54, 45–54.

Corbella, S., and Stretch, D. D. (2013). Simulating a multivariate sea storm using Archimedean copulas. *Coast. Eng.* 76, 68–78. doi: 10.1016/j.coastaleng.2013.01.011

Dee, D., Uppala, S., Simmons, A., Berrisford, P., Poli, P., Kobayashi, S., et al. (2011). The era-interim reanalysis: configuration and performance of the data assimilation system. *Q. J. R. Meteorol. Soc.* 137, 553–597. doi: 10.1002/qj.828

Hartung, J., Bärbel, E., and Klösener, K. (2005). *Statistik*. München: Oldenburg Verlag.

Hess, P., and Brezowsky, H. (1952). *Katalog der Großwetterlagen Europas*. Bad Kissingen: Ber. DT. Wetterd. in der US-Zone 33.

Hewitson, B., and Crane, R. (2002). Self-organizing maps: applications to synoptic climatology. *Clim. Res.* 22, 13–26. doi: 10.3354/cr022013

Jacobeit, J. (2010). Classifications in climate research. *Phys. Chem. Earth A/B/C* 35, 411–421. doi: 10.1016/j.pce.2009.11.010

Kruger, A. C. (2004). *Climate of South Africa: Climate Regions*. Technical Report WS45, South African Weather Service, Pretoria.

Lamb, H. H. (1972). *British Isles Weather Types and a Register of the Daily Sequence of Circulation Patterns, 1861–1971*. London: HMSO; Meteorological Office. Geophysical Memoir No. 116.

Mather, A., and Stretch, D. (2012). A perspective on sea level rise and coastal storm surge from southern and eastern africa: a case study near Durban, South Africa. *Water* 4, 237–259. doi: 10.3390/w4010237

Philipp, A., Beck, C., Huth, R., and Jacobeit, J. (2014). Development and comparison of circulation type classifications using the cost 733 dataset and software. *Int. J. Climatol.* doi: 10.1002/joc.3920. [Epub ahead of print].

Preston-Whyte, R. A., and Tyson, P. D. (1988). *The Atmosphere and Weather of Southern Africa*. Cape Town: Oxford University Press.

Pringle, J., Stretch, D., and Bardossy, A. (2014). Automated classification of the atmospheric circulation patterns that drive regional wave climates. *Nat. Hazards Earth Syst. Sci.* 14, 2145–2155. doi: 10.5194/nhess-14-2145-2014

Rossouw, J., Coetzee, L. W., and Visser, C. J. (1982). "A South African wave climate study," in *IPCC*. 18, 87–107. doi: 10.9753/icce.v18.%25p

Weather types across the Maritime Continent: from the diurnal cycle to interannual variations

Vincent Moron[1,2]*, Andrew W. Robertson[2], Jian-Hua Qian[3] and Michael Ghil[4,5]

[1] CEREGE, UM 34 CNRS, Department of Geography, Aix-Marseille University, Aix en Provence, France
[2] International Research Institute for Climate and Society, The Earth Institute, Columbia University, Palisades, NY, USA
[3] Department of Environmental, Earth and Atmospheric Sciences, University of Massachusetts, Lowell, MA , USA
[4] Department of Geosciences, Ecole Normale Supérieure, Paris, France
[5] Department of Atmospheric and Oceanic Sciences, University of California, Los Angeles, Los Angeles, CA, USA

Six weather types (WTs) are computed across the Maritime Continent during austral summer (September–April) using cluster analysis of unfiltered, daily, low-level winds at 850 hPa, by a *k*-means algorithm. This approach is shown to provide a unified view of the interactions across scales, from island-scale diurnal circulations to large-scale interannual ones. The WTs are interpreted either as snapshots of the intraseasonal Madden-Julian Oscillation (MJO); or as seasonal features, such as the transition between boreal- and austral-summer monsoons; or as slow variations associated with the El Niño–Southern Oscillation (ENSO). Scale interactions are analyzed in terms of the different phenomena that modulate regional-scale wind speed and direction, or the diurnal-cycle strength of rainfall. Decomposing atmospheric anomalies, relative to the mean annual cycle, into interannual and sub-seasonal components yields similar WT structures on both of these time scales for most of the WTs (4 out of 6). This result suggests that slow (viz. ENSO) and fast (viz. MJO) oscillatory variations superimposed on the mean annual cycle modulate the occurrence rate of WTs, without modifying radically their mean patterns. The latter pattern invariance holds especially true for MJO-type, propagating variations, while the quasi-stationary, planetary-scale ENSO variations have more impact on WT structure. These findings are interpreted with the help of dynamical systems theory. Interannual modulation of WT frequency is strongest for the "transitional" WTs between the boreal- and austral-summer monsoons, as well as for the "quiescent" WT, for which low-level winds are reduced over the whole of monsoonal Indonesia. The WT that characterizes NW monsoon surges, and peaks during the austral-summer monsoon in January-February, does not appear to be strongly modulated at the interannual time scale. The diurnal cycle is shown to play an important role in determining the rainfall over islands, particularly in the case of the quiescent WT that is more frequent during El Niño and the suppressed phase of the MJO; both of these lead to more rainfall over southern Java, western Sumatra, and western Borneo.

Keywords: ENSO, frequency modulation, *k*-means clustering, MJO, pattern modulation, scale interaction

1. INTRODUCTION AND MOTIVATION

The atmospheric circulation exhibits a broad spectrum of motions. Multiple-flow regimes have been used to help understand large-scale, persistent and recurrent atmospheric patterns in mid-latitudes (Mo and Ghil, 1988; Vautard and Legras, 1988; Kimoto, 1989; Vautard, 1990; Michelangeli et al., 1995; Ghil and Robertson, 2002). Weather types (WT) have been employed extensively to diagnose and describe such regimes. This approach, however, has been used less often in the tropics (Pohl et al., 2005; Moron et al., 2008; Lefèvre et al., 2010), where space-time filtering has typically been used in order to focus on specific temporal scales—such as the intraseasonal one of 20–60 days associated with the Madden-Julian Oscillation (MJO) (Madden and Julian, 1971)—and removing the annual cycle is standard practice. The

latter approach may be misleading when the annual cycle is modulated in phase or amplitude, since these modulations may be aliased into both shorter and longer time scales (Moron et al., 2012). Such aliasing might be particularly problematic in the tropics, where seasonal migrations of the intertropical convergence zone (ITCZ) and monsoon circulations represent a large fraction of the total variability.

We present, therefore, results of weather typing across the Maritime Continent (MC), and show that WTs computed using dynamical cluster analysis of unfiltered, daily, low-level winds do provide a unified and flexible view of the scale interactions. The MC provides a good example where multiscale interactions amongst various phenomena produce a particularly rich spectrum of atmospheric variations (Hendon, 2003; Chang et al.,

2005a; Juneng and Tangang, 2005; Moron et al., 2010; Qian et al., 2010, 2013; Rauniyar and Walsh, 2011; Robertson et al., 2011). The asymmetrical annual cycle of the Asian-Australian monsoon (Chang et al., 2005a) provides a planetary-scale picture of the NW–SE movement of the ITCZ from Southeast Asia, in May–September, to Northern Australia in January-February. The huge amount of heat within the deep surface mixed layer of the Western Pacific Warm Pool, just east and north of Papua New Guinea, as well as the complex topography—with mountainous and flat islands of varying sizes dispersed across waters usually warmer than 28°C—lead to deep convection on small-to-regional scales, in association with the diurnal cycle (Qian, 2008; Rauniyar and Walsh, 2011; Teo, 2011) and with mountain and sea breezes (Qian et al., 2010, 2013). The MC and the Western Pacific are also located at the longitudes where the MJO reaches its highest amplitude in austral summer (Hendon and Liebmann, 1990; Wheeler and Hendon, 2004; Matthews and Li, 2005), a region that is also the western pole of the Pacific's Walker circulation and the Southern Oscillation (Bjerknes, 1969; Klein et al., 1999; Hendon, 2003).

At the interannual time scale, the MC thus plays a central role in the El Niño–Southern Oscillation (ENSO), with warm events usually associated with large-scale subsidence and low-level easterly anomalies (Klein et al., 1999; Hendon, 2003; McBride et al., 2003). Previous analyses showed that MC rainfall anomalies associated with ENSO are strongly modulated spatially across the annual cycle (Hendon, 2003; Juneng and Tangang, 2005) and that the onset of the austral-summer monsoon, between September and November (Haylock and McBride, 2001; Moron et al., 2009), is a key stage in this modulation, due to the difference in the way that anomalies and basic state are superimposed on either side of this stage. MC rainfall thus modifies the local air-sea coupling (Hendon, 2003), as well as the amplitude of the diurnal cycle and of the sea and mountain breezes (Qian et al., 2010, 2013). Our previous work (Moron et al., 2010; Qian et al., 2010, 2013) demonstrated that a quiescent-flow WT is key to understanding why ENSO causes wet anomalies over the central mountains of Java but dry anomalies over the plains during the monsoon season (Rauniyar and Walsh, 2011); this WT is more frequent during El Niño years and leads to an enhancement of the diurnal cycle of precipitation and of land-sea breeze circulation.

The goal of this paper is two-fold: (i) to build a unified picture of the impacts of ENSO and MJO on daily rainfall and circulation variability over the MC by using daily circulation regimes as the dynamical cross-scale interaction mechanism; and then (ii) to rely on the concepts of dynamical systems theory to interpret the multi-WT picture of the multi-scale interactions so obtained. We consider ENSO, MJO and the seasonal cycle as external forcings on regional atmospheric dynamics over the MC, and wish to determine to what extent these forcings change the nature of the regional dynamical attractor, rather than just causing certain parts of it to be visited more or less often (Ghil and Childress, 1987; Palmer, 1998; Ghil and Robertson, 2002). This determination has implications for sub-seasonal to seasonal predictability to the extent that these two distinct ways of affecting the regional dynamics imply different contributions

to its predictability, as well as to its representation in numerical models.

We investigate this fundamental question in terms of WTs, and use observational datasets and reanalyses to quantify the extent to which ENSO, the MJO and the seasonal cycle are associated with changes in WT frequency vs. changes in the WT patterns. By identifying each WT with distinctly different diurnal-cycle behavior, we seek to span the range of scales from diurnal to interannual.

2. MATERIALS AND METHODS

2.1. DATA

Our weather typing approach is based on daily winds at 850 hPa from the second version of the NCEP reanalyses (Kanamitsu et al., 2002), for the years 1979–2013, during the 1 September to 30 April season, and within the window (15°S–15°N, 90°E–160°E). The 850 hPa wind field was shown in our previous work (Moron et al., 2010) to provide a good description of monsoonal WTs over the MC, and we extend the dataset here to cover the whole MC archipelago, and the complete austral-summer monsoon season.

In order to analyze WT relationships with convection, we employ interpolated daily outgoing longwave radiation (OLR) from the NOAA (Liebmann and Smith, 1996) dataset for the same space and time windows. We also use 3-hourly and daily estimated rainfall from TRMM 3b42 (Huffman et al., 2007; Chen et al., 2013, version 7) available on a $0.25° \times 0.25°$ grid from January 1st, 1998, until the end of 2013. Units are converted from mm/hr to 1/10 mm/day and rainfall values are cube rooted to decrease skewness. Daily rainfall is available for only 15 complete seasons, from 1998/1999 on. All other atmospheric datasets have 242-day seasons, from 1 September to 30 April, over 34 years, with leap days removed, that is 242 days/year $\times$ 34 years $=$ 8228 days.

2.2. STATISTICAL METHODS

Before going into technical details, we present a broad picture of the overall methodology. We first extracted daily WTs from unfiltered low-level daily winds using dynamical clustering, also known as the k-means method (Michelangeli et al., 1995; Ghil and Robertson, 2002). The goal is to provide a coarse-grained view of the regional-scale atmosphere's phase space, by considering in principle all time scales from daily to decadal. The smallest spatial scales are nevertheless filtered out by considering only the leading Empirical Orthogonal Functions (EOFs) and their corresponding Principal Components (PCs).

The k-means clusters localize high concentrations of points in the phase subspace spanned by these EOFs. Their centroids are given by time averaging the low-level winds over all the days that belong to a given cluster and they define each distinct WT. Similar composites of OLR and rainfall over the days assigned to each cluster are then built to investigate the relationships between each low-level circulation type and large-scale convection or local-scale daily (and sub-daily) rainfall. Following the many previous studies cited in the previous section, we refer to the resulting patterns as "weather types" since they allow an interpretation of local rainfall variability in terms of regional-scale circulation and convection patterns.

Next, we investigate the impact of three key drivers of MC climate variability on the occurrence frequency and flow patterns of

these WTs, namely the seasonal cycle, the MJO and ENSO. Their impacts are quantified using conditional probability, composites of raw and anomalous low-level winds and OLR, and multinomial logistic regression, with respect to the time series of these drivers. The goal is to separate the impact of these drivers on the recurrence or persistence of the WTs from their impacts on the spatial patterns thereof. Lastly, we analyze the diurnal cycle of local-scale (0.25°) rainfall to look at scale interactions and assess the ability of the WTs to capture any systematic impact on a shorter time scale, which is not explicitly resolved by the dynamical clustering of daily fields.

The daily gridded wind data are first standardized using the long-term mean and standard deviation. The initial dimension of the dataset is then reduced by applying an EOF analysis that retains 75% of the total variance in the 26 leading PCs. The k-means method partitions iteratively the ensemble of 8228 days into k clusters in such a way as to minimize the sum of variances within clusters (Diday and Simon, 1976). The first step of dynamical clustering is the random selection of k days from the 8228 days in the 26-dimensional subspace.

These initial seeds are taken as the cluster centers, and each daily circulation map is then assigned to the nearest center, according to Euclidean distance. The centroid of each of the k clusters is then taken as the cluster center in the second step, and the same procedure is repeated until the sum of intra-cluster variance stops decreasing, within a given tolerance.

The optimal number of clusters is determined—without removing the mean seasonal cycle—by using a red-noise test defined in Michelangeli et al. (1995). The 8228 days in the 26-dimensional subspace are classified 1000 times, each time starting from a different random seed. The partition having the highest mean similarity with the 999 other ones is kept. A classifiability index CI, shown in **Figure 1** as a blue line with open circles, measures the average similarity within the 1000 sets of clusters and equals exactly 1 only if all 1000 partitions are identical, i.e., if the initial choice of random seeds has no impact on the final partition. The statistical significance of CI is tested by generating 100 classifications in exactly the same way as for the observed daily winds, projected onto the 26 leading PCs, except that one classifies red-noise processes having the same autocorrelation at a 1-day lag as the leading 26 PCs. The red-noise CIs are sorted in ascending order and the 90th value gives the one-sided 90th level of significance, shown as the red line in **Figure 1**.

The impact of the seasonal cycle, ENSO, and MJO on the WTs' frequency and pattern is analyzed by computing composite counts and maps for different phases of the respective cycle. The significance of the anomalies is tested using a battery of non-parametric and Monte Carlo tests.

For the ENSO-phase composite maps associated with a particular WT, we use a Kolgomorov-Smirnov (KS) test to quantify the distance between the empirical cumulative distribution function of the subset of days making up the WT–ENSO composite, and the cumulative distribution function of the whole sample of 8228 days. The KS test is non-parametric and is hence preferable to the use of a Student's t-test. We compute independently for each grid point the KS test and complement it by a global (or field) significance test (Livezey and Chen, 1983) to estimate the significance of
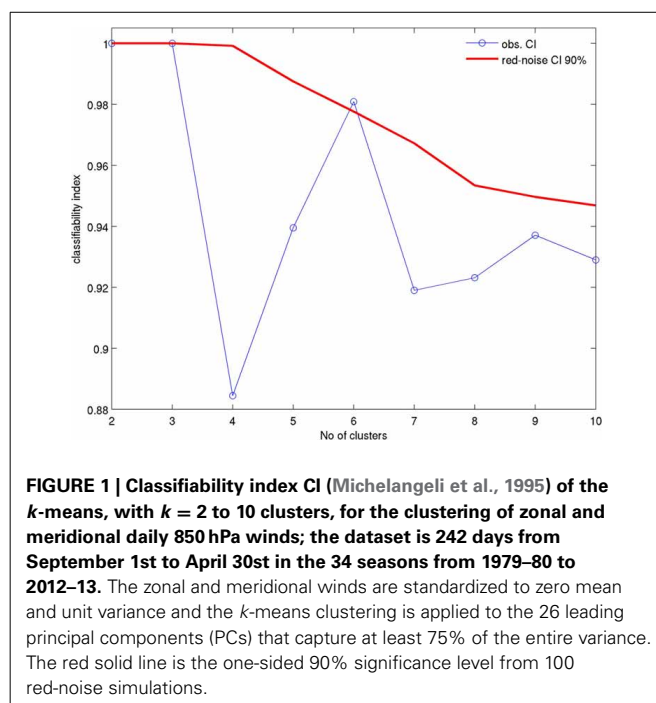
FIGURE 1 | Classifiability index CI (Michelangeli et al., 1995) of the k-means, with $k = 2$ to 10 clusters, for the clustering of zonal and meridional daily 850 hPa winds; the dataset is 242 days from September 1st to April 30st in the 34 seasons from 1979–80 to 2012–13. The zonal and meridional winds are standardized to zero mean and unit variance and the k-means clustering is applied to the 26 leading principal components (PCs) that capture at least 75% of the entire variance. The red solid line is the one-sided 90% significance level from 100 red-noise simulations.

the difference between, for example, cold and warm ENSO events. The null hypothesis of such a global test is that the WT pattern associated with cold events is identical to that of the warm ones. This procedure is carried out for warm and cold ENSO phases, as well as for the eight MJO phases.

In order to test the impact of the ENSO and MJO on WT frequency, we used a permutation bootstrap by sampling a random set of years, in case of warm and cold ENSO events, or reshuffling yearly WT sequences as well as blocks of WT sequences. The impact of the seasonal cycle, ENSO, and MJO on the WTs' frequency is also estimated using multinomial logistic regression (cf. Gloneck and McCullagh, 1995; Guanche et al., 2014).

In this exercise, cross-validated regression models are built to "predict" WT frequency, using one, two or all of our three predictors. Consider the daily sequence $\{z_i : i = 1, \ldots, N\}$ of WTs over the $N = 8228$ days that can potentially take one of K nominal (i.e., unordered) categories and a time series $\{x_i : i = 1, \ldots, N\}$ of a predictor; here there are $K = 6$ categories and the possible predictors are the seasonal cycle, ENSO and MJO variations. The nominal values of z_i are converted into an $N \times K$ matrix Y of zeroes, except for the observed WTs, which are categorized as ones, that is, for each day, $y_i = 1$ for the observed WT and $y_i = 0$ for the 5 remaining unobserved WTs.

In the following, π_{ik} is the probability of the kth WT, given a set of predictors x_i,

$$\pi_{ik} = \Pr(y_i = k | x_i), \qquad (1)$$

i.e., x_i could be a time series of scalars or of vectors, $\vec{x}_i = (x_i^j; j = 1, \ldots, J)$, for $J = 1, 2$ or 3, given the total number of our external forcings. This probability could be related to the set of x_i's through a set of $K - 1$ baseline WT logits. Taking k^* as the baseline category, the model is

$$\log \frac{\pi_{ik}}{\pi_{ik*}} = \alpha + \sum_{j=1}^{j=J} \beta_j x_i^j, \text{ with } k \neq k^*; \quad (2)$$

here α is a constant and the β_j's are the coefficients of each predictor variable.

Each coefficient β_j can be interpreted as the increase of log-odds of falling into k^{th} WT vs. the $(k^*)^{\text{th}}$ one that would result from a one-unit increase in the jth predictor, while holding the other predictors constant. The accuracy of the model fit is independent of the WT chosen as the baseline.

The maximum likelihood estimator $\hat{\beta}$ of β is calculated using the MATLAB function *mnrfit*. To estimate the model-based WT probability $\hat{\pi}_i$ from $\hat{\beta}$, the back transformation from Equation (2) is given by

$$\hat{\pi}_{ik} = \frac{e^{(\alpha + x_i \hat{\beta}_k)}}{1 + \sum_{j \neq k^*} e^{(\alpha + x_i \hat{\beta}_j)}} \text{ for } k \neq k^*, \text{ and} \quad (3)$$

$$\hat{\pi}_{ik*} = \frac{1}{1 + \sum_{j \neq k^*} e^{(\alpha + x_i \hat{\beta}_j)}} \text{ for } k = k^*. \quad (4)$$

The fit is estimated vs. a saturated model in which π was estimated independently for $i = 1, \ldots, N$. The deviance G^2 for comparing any model to a saturated one is given by

$$G^2 = 2 \sum_{i=1}^{N} \sum_{k=1}^{K} y_{ik} \log \frac{y_{ik}}{\hat{\pi}_{ik}}. \quad (5)$$

We test various combinations of predictors—amongst the seasonal cycle, ENSO and MJO—in Section 3.2. The change Δ_{G^2} in the deviance of Equation (5) serves to estimate the significance of the inclusion of added predictors relative to a "null" model that uses only an independent term β_0 as predictor or to a "parent" model that includes one or more predictors, up to $J - 1$, less than its "child"; for example, a "parent" model could include ENSO alone as a predictor, while a "child" could include both ENSO and MJO as predictors, i.e., in this case $J = 2$.

The statistic Δ_{G^2} follows a chi-square distribution with $\delta_p \times (k - 1)$ degrees of freedom, where δ_p is the difference in the number of predictors. The accuracy of the fit is also computed by cross-validation, i.e., the $\hat{\beta}$'s are learned using 33 years of data, while $\hat{\pi}$ is computed for each day of the remaining season using Equations (3, 4). We cannot expect to simulate properly the exact temporal sequence at the daily time scale, since only the annual (i.e., the seasonal cycle), interannual (i.e., ENSO) and sub-seasonal, 20–60-day (i.e., MJO) variations are explicitly considered.

We thus filtered out the shortest time scales in observed and hindcast WT sequences, by considering a running window of 11 days centered on the target day to get the 11-day mean of each $\hat{\pi}$ and y and then the highest mean as yielding the predicted and observed WT's for the target day so that a contingency table between observed and predicted WTs could be set up. We tested various window sizes (from 7 to 21 days) to compute the mean and it yields similar results (not shown). The side effect of this

choice is that some WTs are never predicted to occur, due to a systematic under-estimate of the standard variation of $\hat{\pi}$, i.e., each daily value tends to its long-term mean, i.e., close to 1/6, and is thus never sufficiently high to be the maximum of the six $\hat{\pi}$'s.

3. RESULTS

## 3.1. WEATHER TYPES: MEAN SEASONAL CYCLE AND MEAN ATMOSPHERIC PATTERN

Figure 2 illustrates the rich multiscale atmospheric variations across the MC during 1982–1984; the OLR index, defined as the spatial average of the OLR on (96.25°E–121.25°E, 6.25°S–6.25°N), is in the upper panel and the wind index, defined as the spatial average of the 850-hPa zonal wind on (96.25°E–121.25°E, 11.25°S–1.25°S) is in the lower one. The lowest OLR values in **Figure 2A** occur at the end of the calendar year. A large inter-annual variation occurs between the strong warm ENSO event in 1982–83, with suppressed deep convection over the MC, and the weak cold event in 1983–84, with enhanced deep convection there. Fast variations are superimposed on this seasonal and interannual variability, with a broad bandwidth mostly under 10 days.

The wind index in **Figure 2B** shows an asymmetric alternation between westerlies (i.e., WNW monsoon) that coincide with the austral summer monsoon, from early December to early April, and easterlies (i.e., trade-winds) during the rest of the year. As for the OLR index, the austral summer monsoon winds are clearly weaker in 1982–83 than in 1983–84, while there are pronounced intraseasonal fluctuations associated with the MJO (Madden and Julian, 1971; Wheeler and Hendon, 2004; Rauniyar and Walsh, 2011). These intraseasonal variations in zonal winds are at times as large as those associated with the mean annual cycle, for instance during November–December 1983 (**Figure 2B**).

We proceed with the WT classification in order to better understand the way that these large variations on different time scales occur. A significant peak at the one-sided 90% level appears for $k = 6$ in **Figure 1**. This number of WTs is one greater than in (Moron et al., 2010) but we consider here a larger spatial window and extend the analysis until the end of April, vs. February in (Moron et al., 2010), to include the decaying phase of the austral summer monsoon. Note also that considering 60 leading PCs (not shown), rather than 26 only, captures at least 90% of the total variance, rather than 75%, and still leads to the same results as those shown here, namely the days are clustered into the same WTs in 98% of cases.

The mean seasonal cycle of the frequency of occurrence of the six WTs (**Figure 3**) suggests that they can be interpreted first of all as snapshots of the mean annual cycle, consisting of an asymmetric alternation (Chang et al., 2005a) between the austral and boreal summer monsoons. The austral summer monsoon is exemplified by WT 4 with WTs 3 and 5 occurring during this season as well. WT 1 occurs almost exclusively before the austral summer monsoon, until early November, while WT 2 and 6 occur either in its early or late stages.

The predominance of the annual cycle is also visible in the total-field composites of low-level winds and OLR in **Figure 4**. WT 1 in panel (a) is associated with the end of boreal summer, with ESE winds and high OLR south of the equator. The low
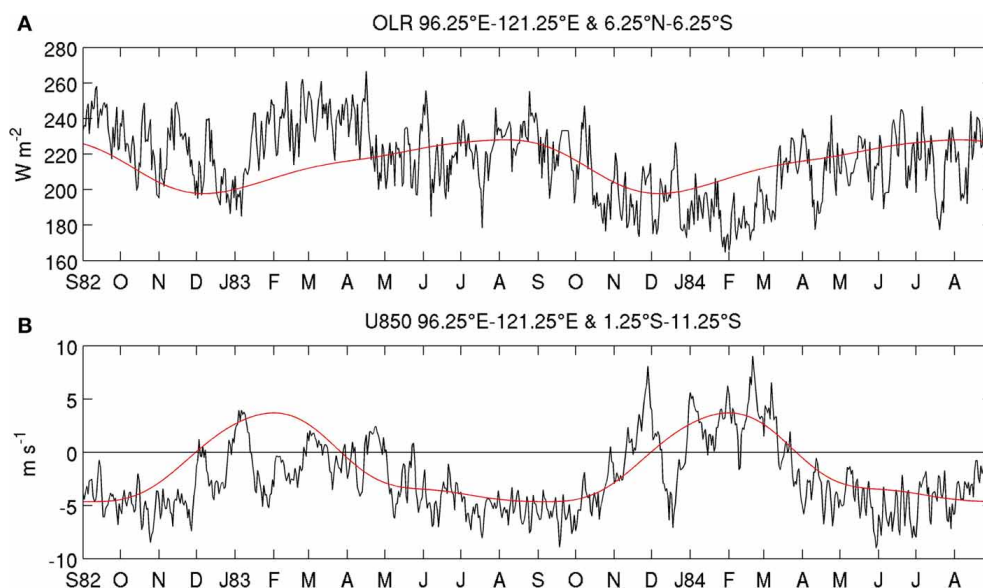
FIGURE 2 | Time evolution of the outgoing longwave radiation (OLR) and zonal winds. Plotted are the spatial average of **(A)** daily OLR on (96.25°E–121.25°E, 6.25°S–6.25°N) in Wm^{-2}; and **(B)** daily zonal wind on (96.25°E–121.25°E, 11.25°S–1.25°S) in ms^{-1} (black lines) over two seasonal cycles, from 1 September 1982 to 31 August 1984. The long-term daily mean, low-pass filtered with a recursive Butterworth filter (cut-off = 90 days) is added as a red line. The ticks on the abcissa refer to the first day of each month.
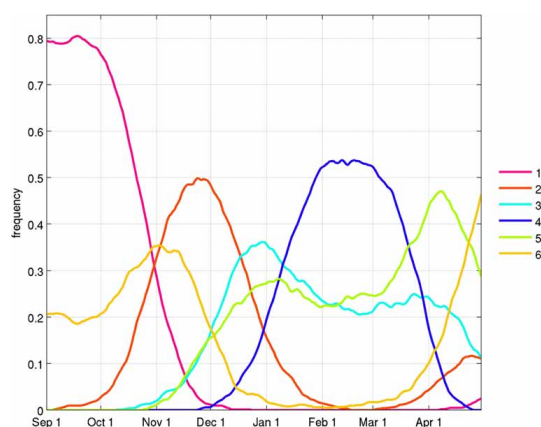
FIGURE 3 | Mean seasonal cycle of the frequency of occurrence of the weather types (WTs). The daily frequency is low-pass filtered with a 31-day running mean.

OLR values associated with deep convection tend to progressively shift southeastward in WTs 2–4 (**Figures 4B–D**) and the low-level winds tends to veer to the WNW over almost the whole MC south of the Equator in WTs 3–4. WT 4 in panel (d) is most prevalent from early January to mid-March and its ITCZ reaches the southernmost location, touching Australia, with strong WNW winds that extend to Cape York, Queensland. WT 5 in **Figure 4E** still exhibits NE winds north of the Equator but the winds are now weaker over the MC and large-scale deep convection weakens relative to WTs 3–4 with poles over west-central Indonesia and New Guinea. Following (Moron et al., 2010), we refer to this WT as the "quiescent" one. WT 6 in panel (f) shows increased ESE winds

south of the Equator all across the MC, while the ITCZ begins its northward migration.

3.2. WEATHER TYPES: INTERANNUAL AND SUB-SEASONAL VARIABILITY

The temporal sequences of WT occurrences (not shown) confirm the strong seasonal component seen in **Figures 3–4**; their statistics are given in **Table 1**. Before the start of the austral summer monsoon, WT 1, which is the most persistent WT, tends to alternate with WT 6 and, to a lesser extent, with WT 2. During the austral summer season, WTs 3–5 alternate almost equiprobably, even though WT 4 leads to the longest spells. WT 3 and 5 are the most intermittent ones on the interannual time scale and also the least persistent at the intraseasonal ones. For example, WT 3 can be almost absent during a whole season, as in 1986/87, 1989–1992 and 2001/02 or occur frequently, as in 1998/99. Likewise, WT 5 does not occur at all in 1998/99, yet it is present on 102 days during the preceding 1997/98 season.

3.2.1. Interannual variability

An obvious candidate to explain interannual variations in WT occurrences and related atmospheric anomalies is ENSO. We analyze ENSO effects on the modulation of WT occurrences first and then on WT spatial patterns. The temporal evolution of WTs is studied for the 10 warmest—1982/83, 1986/87, 1987/88, 1991/92, 1994/95, 1997/98, 2002/03, 2004/05, 2006/07, 2009/10—and the 13 coldest—1984/85, 1985/86, 1988/89, 1995/96, 1998/99, 1999/2000, 2000/01, 2005/06, 2007/08, 2008/09, 2010/11, 2011/12, 2012/13—ENSO events, based on December–February mean sea surface temperature (SST) anomalies in the Niño 3.4 box (190°E–240°E, 5°S–5°N) being above 0.5°C and below −0.5°C, respectively. The remaining

**FIGURE 4 | Mean raw OLR (shadings in Wm⁻²) and 850 hPa winds (vectors) for (A) WT 1, (B) WT 2, (C) WT 3, (D) WT 4, (E) WT 5, (F) WT 6 defined using _k_-means clustering of the standardized anomalies of 850** **hPa winds projected onto the leading 26 EOFs for 1 September 1979 to 30 April 2013, while using the extended austral-summer (September to April) seasons only.**
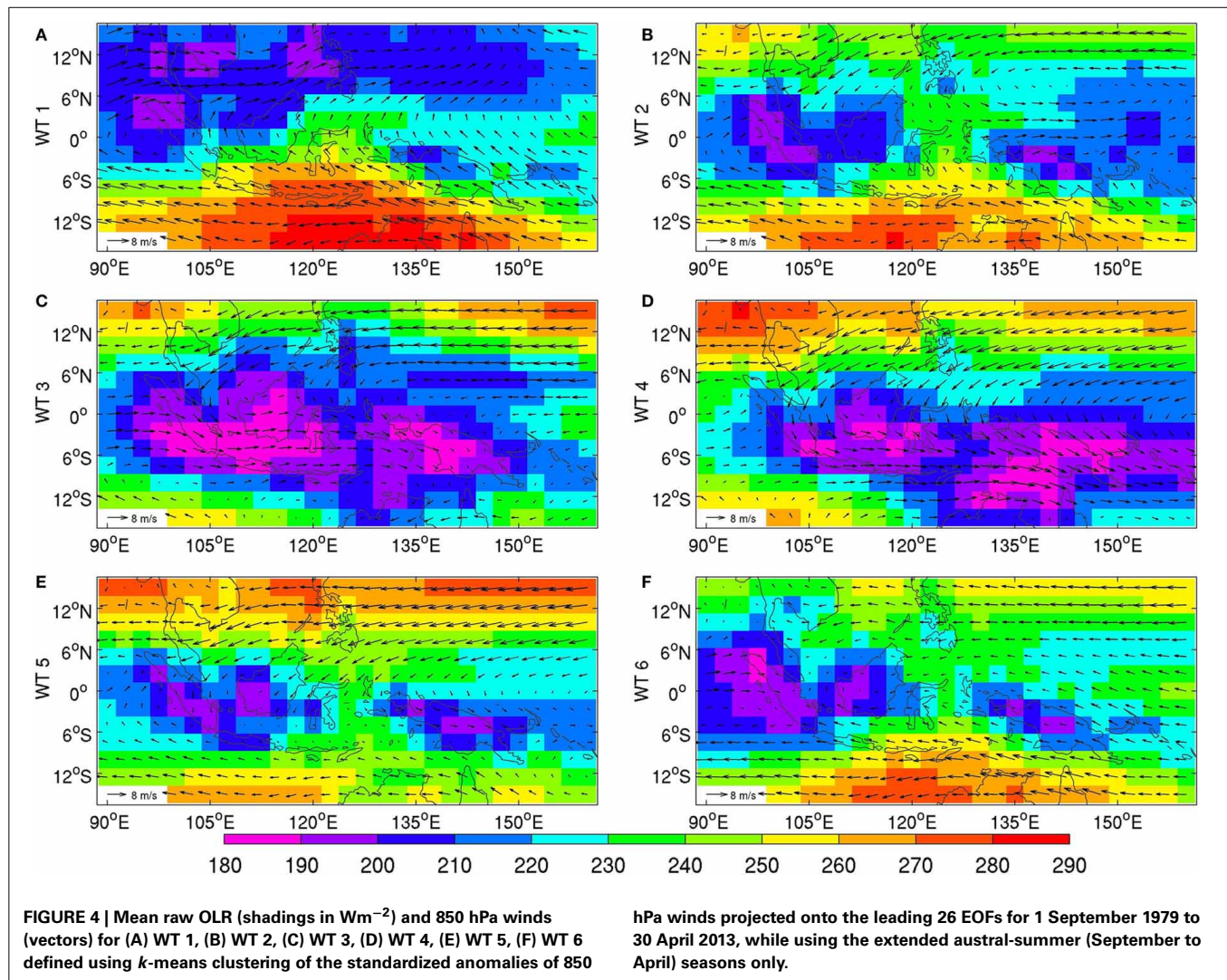
Table 1 | Mean statistics of the length and transitions between the six WTs.

	Mean frequency	Std	Mean length	WT 1	WT 2	WT 3	WT 4	WT 5	WT 6
WT 1	34	7.7	9.2	**0.63**	0.08	0.01	0	0.01	**0.21**
WT 2	35	19	4.9	0.09	**0.36**	0.12	0.03	0.13	**0.20**
WT 3	41	32.1	5.1	0	0.17	**0.26**	**0.24**	**0.23**	0.08
WT 4	42	10.6	7.8	0	0.03	**0.25**	**0.47**	**0.20**	0.02
WT 5	49	22.5	5.0	0	0.13	**0.29**	**0.25**	**0.30**	0.16
WT 6	41	14.9	4.6	**0.27**	**0.23**	0.07	0.01	0.13	**0.32**

The second and third columns show the mean seasonal frequency and interannual standard deviation (in days), while the fourth column contains the mean length of spells (in days). The following six columns show the probability transition from a given WT (in row) to another (in column). The probabilities are estimated as a percentage of the WT on day + 1. The probability transitions in bold occur more frequently than chance at the one-sided 95% level according to a Monte Carlo test (i.e., random permutation of the WT sequence 1000 times Vautard et al., 1990).

11 years are referred to hereafter as "neutral." The composite variations of WT frequency are computed within running 31-day windows and we use a permutation test that samples randomly 1000 times 10, 11, and 13 seasons in the 34 years to assess their significance (**Figure 5**).

Warm ENSO events (**Figure 5A**) are dominated by WT 1, followed by a large frequency increase of WT 2 until mid December. The core of the austral summer monsoon is almost equally dominated by WT 4 and the largely quiescent WT 5, which is significantly more frequent than usual.
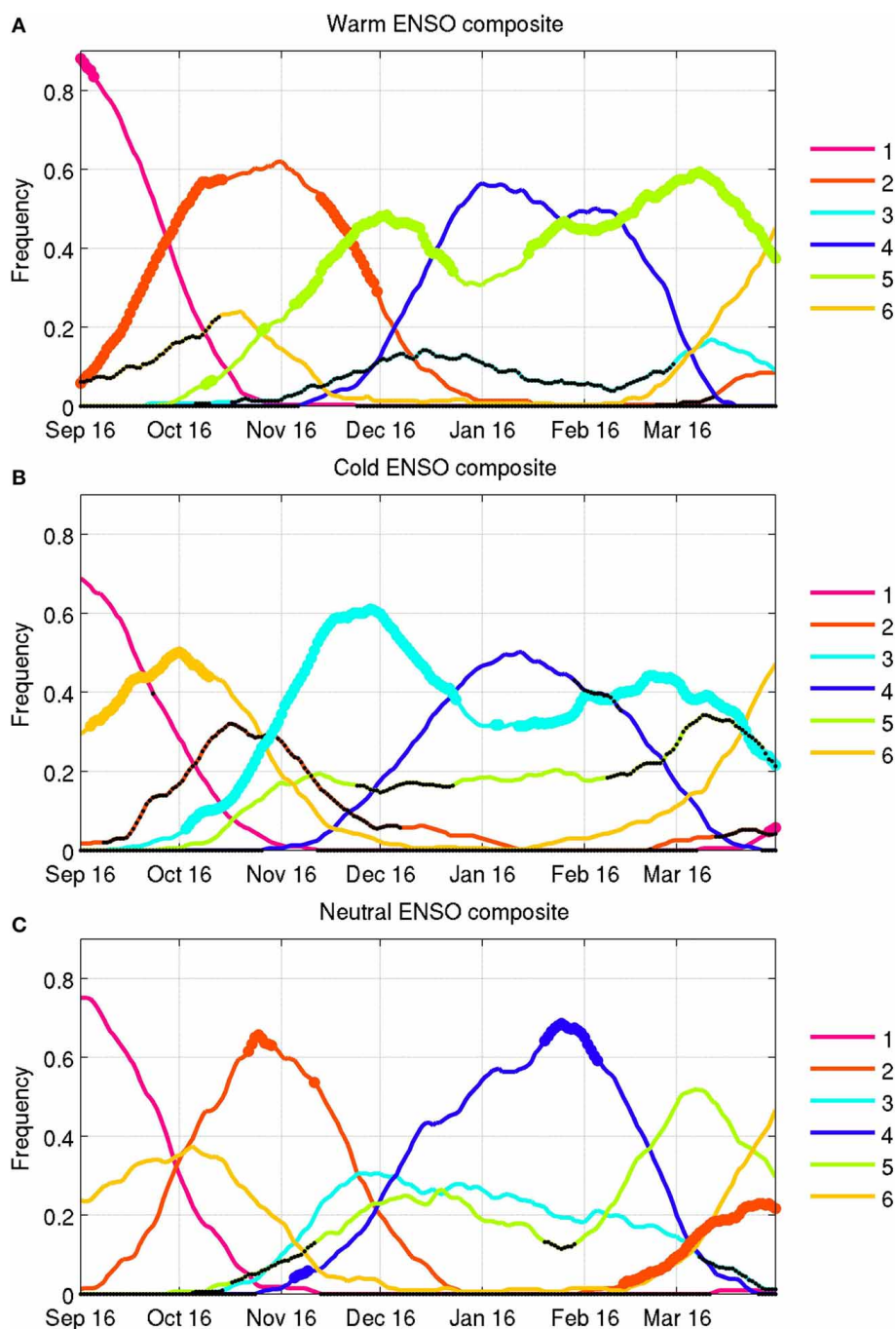
FIGURE 5 | WT composites in running 31-day windows, classified by (A) warm, (B) cold and (C) neutral ENSO events. These are defined as the mean December–February SST anomalies in the Niño 3.4 box lying above +0.5°C (warm), below −0.5°C (cold), and between −0.5°C and +0.5°C (neutral) relative to the 1979/80-2012/13 mean. The dots—large and colored for positive and small and black for negative frequency deviations—indicate statistical significance at the two-sided 95% level as tested by 1000 random permutations of the observed yearly sequence of WTs.

WT 3 occurs significantly less frequently than expected during the austral summer monsoon, with always < 15% of days. The cold ENSO events (**Figure 5B**) are mostly related to an increased frequency of WT 3, especially around November-December and also in February-April. WT 2, and secondarily WT 5, occur less frequently than usual. The correlation between the September-April averaged Niño 3.4 SST index and seasonal WT frequency equals 0.34, with p-value = 0.06 according to a random-phase test (Janicot et al., 1996), 0.54 (p-value < 0.01), −0.76 (p-value < 0.01), 0.16 (p-value = 0.17), 0.81 (p-value < 0.01) and −0.57 (p-value < 0.01) for WTs 1–6, respectively.
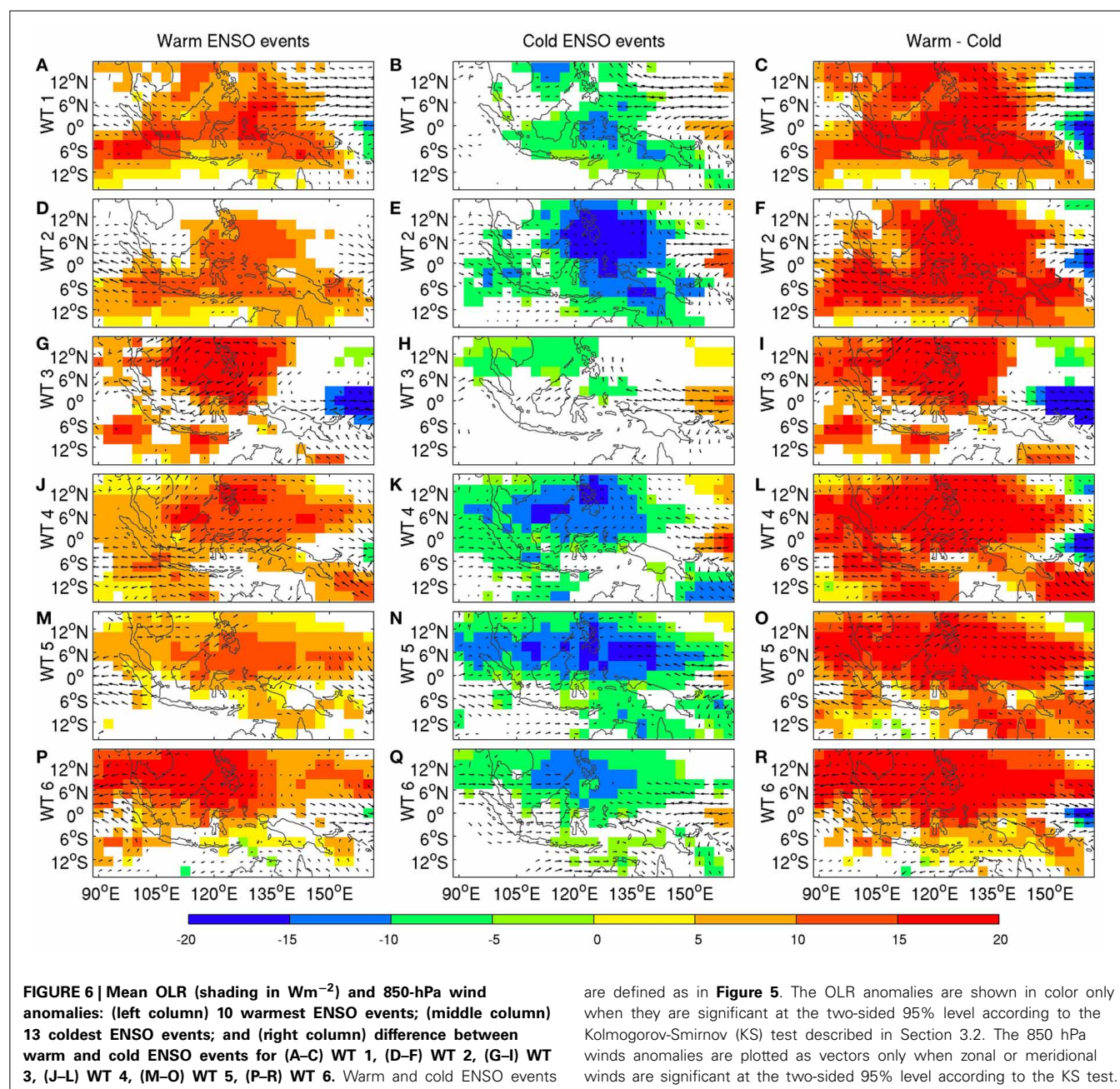
These results suggest that ENSO strongly modulates both the persistence and the recurrence of WTs. Moreover, the neutral years (**Figure 5C**) do not show large anomalies and the seasonal evolution is then close to the long-term mean—except for, usually short, spells of excess of WT 2 around mid-November and in March-April and WT 4 after mid-November and around mid-February.

We next investigate whether there are significant changes in WT pattern during the different ENSO phases. **Figure 6** shows composite WT anomalies for the warm (left column) and cold (middle column) ENSO events identified in the previous paragraphs, while the difference in WT pattern between warm and cold ENSO events is shown in the right column. The 850 hPa

winds (vectors) and OLR anomalies (shading) are expressed as anomalies relative to the total-field composites of each WT shown in **Figure 4**. These anomaly maps thus express the ENSO effect on changes in WT pattern and they are plotted in color only when they are significant at the two-sided 95% level, according to our KS test.

Large areas of significant ENSO impacts on WT pattern are visible, with El Niño tending to decrease convection and La Niña to increase it, broadly across all six WTs. To test globally the hypothesis whether the WTs patterns are significantly modulated by ENSO phase, the field significance of these composites is evaluated as follows: in place of the warm and cold years, respectively, 10 and 13 years are randomly chosen 1000 times and the

FIGURE 6 | Mean OLR (shading in Wm⁻²) and 850-hPa wind anomalies: (left column) 10 warmest ENSO events; (middle column) 13 coldest ENSO events; and (right column) difference between warm and cold ENSO events for (A–C) WT 1, (D–F) WT 2, (G–I) WT 3, (J–L) WT 4, (M–O) WT 5, (P–R) WT 6. Warm and cold ENSO events

are defined as in **Figure 5**. The OLR anomalies are shown in color only when they are significant at the two-sided 95% level according to the Kolmogorov-Smirnov (KS) test described in Section 3.2. The 850 hPa winds anomalies are plotted as vectors only when zonal or meridional winds are significant at the two-sided 95% level according to the KS test.

KS-significant areas are computed for each of the three columns of **Figure 6**.

For the composite wind fields, the significant area is never reached by more than 10% of the random samples, except for the wind of WT 3 (=33% for the zonal and meridional components) in cold ENSO events, and for the wind of WT 5 (=14% for the zonal and =11% for the meridional component), in warm ENSO events. For OLR, the significant area observed in warm and cold ENSO events is never reached by more than 8% of the random noise samples.

Our global KS tests thus confirm that the difference between WT patterns observed during cold vs. warm ENSO events cannot be attributed to sampling uncertainty, and that ENSO significantly modulates the WT patterns, in addition to WT frequency. This systematic modulation (right column of **Figure 6**) is nearly constant across the WTs, with an anomalous regional-scale divergence (convergence) at 850 hPa centered between Mindanao, Java and NW Australia, combined with anomalous subsidence (ascendance) over most of the MC, while a small area of enhanced (reduced) convection appears over the equatorial Pacific east of New Guinea, during warm (cold) ENSO events.

3.2.2. Sub-seasonal variability

At sub-seasonal scales, **Figure 7** quantifies the impact on WT frequency of phase locking with the eight MJO phases—as defined by Wheeler and Hendon (2004) and used for predictive purposes by Kondrashov et al. (2013). In the upper panel, it is clear that the occurrence of the active-monsoon WTs 3 and 4 is favored during MJO phases 5–7, during which convection is enhanced from Indonesia to the western Tropical Pacific, while WTs 5 and 6— which represent weak, or break, monsoon episodes—occur more frequently during MJO phases 1–3, associated with enhanced convection mostly over the Indian Ocean (Wheeler and Hendon, 2004).

The anomalous WT frequencies were also computed for the 10 warm ENSO and 13 cold ENSO seasons in the middle and lower panels of **Figure 7**. The association between WT frequency and MJO phases is also seen, separately, in El Niño and La Niña years. However, the active-monsoon WTs 3 and 4 are more strongly suppressed in MJO phases 1–3 and more strongly favored in MJO phases 4–7 during El Niño episodes (middle panel). Thus, MJO forecasts may be of particular value during El Niño years for early warning of drought and flood episodes.

A KS test of significant changes in WT pattern was also performed for the 8 MJO phases, analogous to the one described for the ENSO phases in **Figure 6**. However, in the case of MJO, the result of the global field significance test was negative—the observed significant area is usually beaten by more than 10% of the random samples except for respectively 3 and 1 cases out of 48 (=6 WTs × 8 MJO phases) tests in zonal and meridional winds—i.e., there is usually no significant perturbation of the WT patterns by MJO phase.

The above analyses suggest that (1) the annual cycle exerts a strong control on WT occurrence; (2) ENSO events impact the frequency of WTs (mostly WT 2, 3, 5, and 6) as well as their patterns, through spatially homogeneous, sustained atmospheric anomalies across the MC—i.e., suppressed regional-scale

convection during warm ENSO events—rather than changing the overall pattern of each WT; while (3) MJO impacts only the frequency of WTs. The relative impact of each of the three quasi-periodic forcings on WT frequency, and of their combinations, is estimated next, using a multinomial logistic regression.

3.2.3. Predictive models of WT frequency based on seasonal cycle, ENSO and MJO

Our goal here is to retrospectively forecast WT occurrence frequency, given perfect knowledge of these three regional climate drivers. We first construct two filtered daily time series to represent the seasonal cycle and Niño 3.4 SSTs, since the 8 MJO phases are already available from Wheeler and Hendon (2004). The seasonal cycle is estimated with the first PC of standardized anomalies of the zonal and meridional components of the 850-hPa wind, while keeping the seasonal cycle and analyzing the full year. The first PC is low-pass filtered with a recursive Butterworth filter of order 9 and with a cut-off = 1/90 cycle-per-day. The variability includes a quasi-regular seasonal cycle combined with a minor modulation at the interannual time scale related with ENSO variability: the correlation between the September–April average of PC 1 and the Niño 3.4 index is 0.63.

We remove the ENSO-related variance by linear regression as follows: A daily time series is created from the monthly SST anomaly of the Niño 3.4 index (NINO hereafter) by first sampling monthly values at a daily time scale and then filtering this time series with the same Butterworth filter as PC1 above. The Niño 3.4 effect is then removed from PC1 through linear regression and the extraction of the residual. The annual index so obtained is referred to hereafter as AN.

Table 2 shows the seven possible multinomial logistic regression models when using the three distinct predictors AN, NINO and MJO of daily WT occurrence. The "null" model (first row of the table) takes into account only an independent term and its deviance is analogous to the sum of squared errors in linear regression, providing a baseline for model comparison. All the changes in the model deviances Δ_{G^2} between a nested model, i.e., adding one or more predictors, and a parent one, are statistically significant at the one-sided 99.9% level, according to a chi-squared test with 5 degrees of freedom (Guanche et al., 2014), where 5 equals the number of added predictors (=1 in our cases), by the number of WTs (= k) minus 1. Hence the addition of the predictors significantly improves the model fit.

AN provides clearly the largest decrease of deviance, while MJO and NINO contribute roughly equally to this decrease. Considering the three predictors together improves the fit relative to the best model using two predictors, i.e., AN and NINO (fifth row of the table). In other words, the joint impact of AN, NINO and MJO provides the best fit of the observed sequences of daily WTs.

The cross-validated hit rates (rightmost 7 columns of the table) confirm the differential impact of the three predictors on the occurrence of each WT. NINO (third row in the table) is a major driver of the occurrence of WT 3 and WT 5 during the wet season, while WT 4 frequency is mostly affected by AN (row 2; cf. **Figure 3**). The marginal impact of MJO (row 4) is largest for WTs 4 and 5.
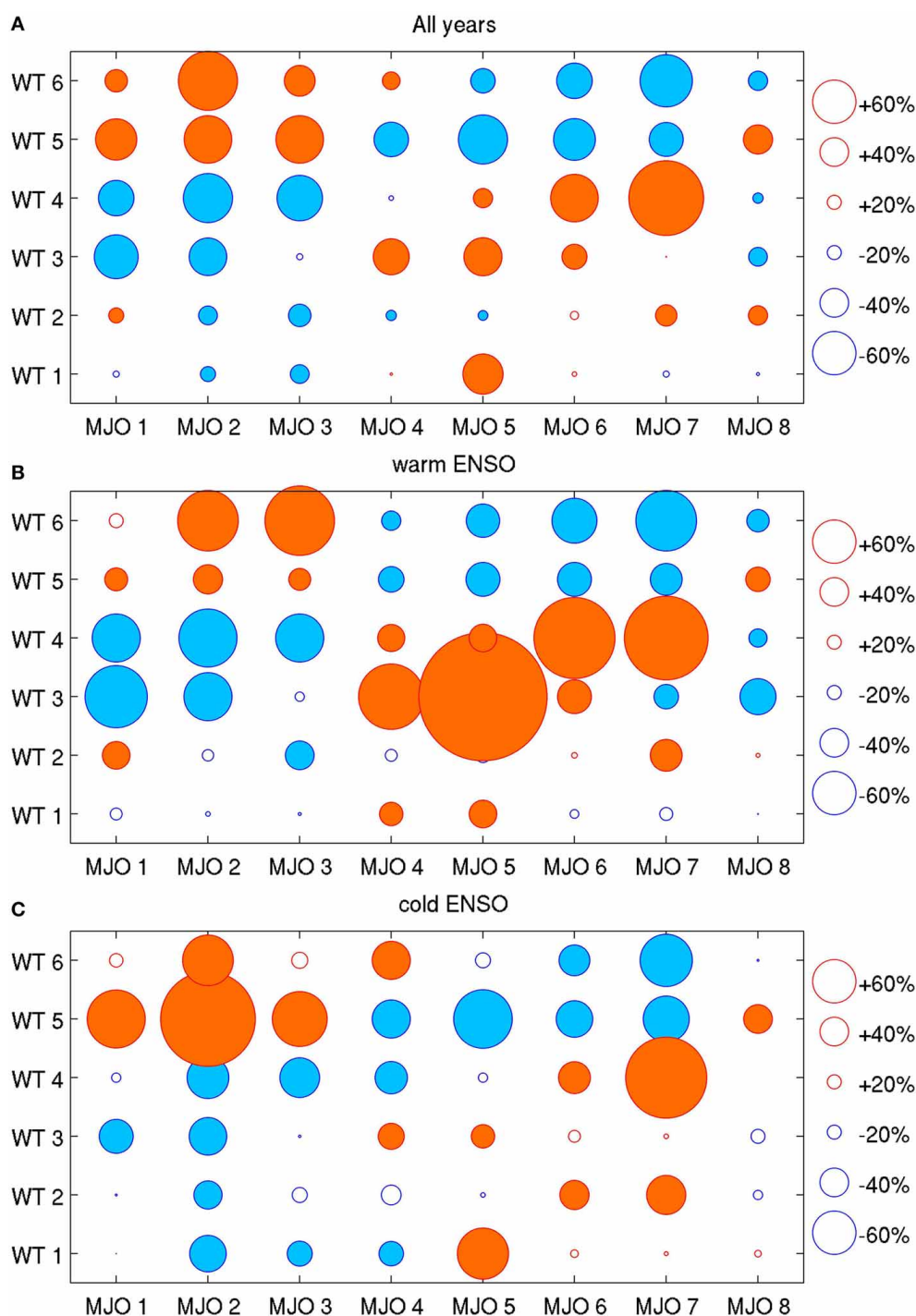
**FIGURE 7 | Phase locking of the WTs to the 8 phases of the MJO
(Wheeler and Hendon, 2004; Kondrashov et al., 2013) expressed as
anomalous conditional probability of WT occurrence during MJO
phases.** The filled orange and blue dots indicate significant positive and
negative anomalies, respectively, at the two-sided 95% level, as tested by
1000 random permutations of the observed daily sequences of the WTs. **(A)**
anomalies computed for all 34 seasons; and **(B,C)** anomalies discretized for
the warm and cold ENSO events, respectively, defined as in **Figure 5**.

The joint impact of AN and MJO is rather similar to that of
AN and NINO, except for WT 3, even though the marginal effects
of NINO and MJO (rows 3 and 4) strongly differ, AN being the
dominant one. The interannual variability of the WT probability

is well-specified by the model including all three AN, NINO and
MJO, with correlations between hindcast and observed seasonal
frequency equal to 0.73 (WT 1), 0.50 (WT 2), 0.78 (WT 3), 0.66
(WT 4), 0.83 (WT 5) and 0.58 (WT 6), all values being significant

Table 2 | Fitting diagnostic and cross-validated hit rates for different multinomial logistic models (Gloneck and McCullagh, 1995), including the three distinct predictors indicated in the first column (see text); the first model ("null") includes only the intercept and is not cross-validated.

Model	G^2	Δ_{G^2}	WT 1 (1180 days)	WT 2 (1245 days)	WT 3 (1393 days)	WT 4 (1463 days)	WT 5 (1628 days)	WT 6 (1319 days)	All WTs (8228 days)
1: Null	2.9362×10^4								
2: AN	1.8951×10^4	(vs. 1) 1.0411×10^4	978	260	0	**1189**	853	725	4005
3: NINO	2.8523×10^4	(vs. 1) 839	0	0	**950**	7	**1136**	190	2286
4: MJO	2.8789×10^4	(vs. 1) 573	0	0	0	915	1134	3	2052
5: AN + NINO	1.8005×10^4	(vs. 2) 945	973	364	720	1024	770	729	4580
6: AN + MJO	1.8265×10^4	(vs. 2) 686	1004	386	347	1171	873	695	4476
7: NINO + MJO	2.785×10^4	(vs. 3) 673	0	42	716	492	849	424	2953
8: All 3	1.7273×10^4	(vs. 5) 731	**1013**	**412**	751	1042	796	**751**	**4765**

The other models are cross-validated with parameters iteratively learned on 33 years and WT probability computed on the remaining year. The change of deviance Δ_{G^2} between a model (indicated in parenthesis) and a nested one using additional predictors is always significant at the one-sided 99.9% level, i.e., increasing the number of predictors is always justified at this level. The last 7 columns show the accuracy of the models, computed as the hit rate of each WT in cross-validation. The observed and hindcast WT are estimated as the maximum probability amongst the 6 WTs for running 11-day windows centered on each target day. The bold values show the highest hit rate for each WT.

at the one-sided 95% level according to a random-phase test (Janicot et al., 1996).

3.2.4. Filtering of WT patterns

Finally, we compare the interannual and sub-seasonal anomalies for each WT, with respect to the mean annual cycle calculated on a daily basis. The goal here is to separate the phenomena associated with each WT by filtering the contributions to the composite WT maps in **Figure 4** from the interannual and sub-seasonal frequency bands. For example, if they were solely a reflection of ENSO impacts, then applying a high-pass sub-seasonal filter would yield near-zero anomalies for each WT. This analysis complements the previous ones, since we do not assume a priori the special role of ENSO or MJO, while the dominant driver of WT occurrence, i.e., the mean seasonal cycle, is filtered out.

The anomalies are computed as deviations between raw values (shown in **Figure 4**) and the mean seasonal cycle; they are then decomposed into two additive components, on either side of a period of 242 days—i.e., the length of the extended austral summer, September 1–April 30—by using a 9th-order recursive Butterworth filter with a cut-off frequency of (1/242) cycle/day. The composites for each of the two frequency bands are then plotted for each WT in **Figure 8**. Note that this analysis makes no distinction between the impacts of the respective oscillation on WT frequency vs. WT amplitude: it merely assesses the relative roles of ENSO and MJO in giving rise to these WTs.

The pattern correlations between the interannually and sub-seasonally filtered WTs in **Table 3** indicate substantial similarity in both OLR and wind anomalies, especially for WTs 2, 3, and 5. These three WTs are also the most variable in their frequency of occurrence at the interannual time scale (cf. **Table 1**).

Figure 8 shows that the anomalies are generally stronger in the sub-seasonal than in the interannual band. WT 3 is associated with anomalous low-level convergence and enhanced deep convection over Central Indonesia, while anomalous subsidence and

therewith positive OLR anomalies, as well as increased low-level easterlies are observed over the Western Tropical Pacific. WT 5 shows an almost reversed pattern, with anomalous low-level divergence centered over New Guinea, accompanied by easterly anomalies and increased subsidence over most of Indonesia. WT 2 has some similarities with WT 5, except that anomalous low-level divergence, i.e., higher OLR, occurs between the South China Sea and Northern Australia.

The similarity between sub-seasonal and interannual components is less obvious for WTs 1, 4, and 6, which also tend to show rather weak interannual components (**Table 3**); this weakness suggests that these WTs do tend to be less excited by interannual forcing, and indeed the interannual variability of their frequency of occurrence tend to be small, cf. **Tables 1**, **3**.

3.3. WEATHER TYPES: ASSOCIATED LOCAL-SCALE RAINFALL ANOMALIES

The analyses so far have focused on regional-scale anomalies. Downscaling to local-scale anomalies is now considered, using the $0.25° \times 0.25°$ TRMM dataset (Huffman et al., 2007). We need to be cautious about these analyses since they refer to the second half of the period only and there are known biases in the TRMM remote-sensing data relative to *in situ* rain gages (Dinku et al., 2007).

As before, we decompose the rainfall anomalies according to time scale. This provides a measure of how interannual and sub-seasonal rainfall variability is described by changes in frequency and amplitude of daily WTs. We first computed interannual and sub-seasonal anomalies in rainfall as in **Figure 8**, after taking the cubic root of daily rainfall values to reduce skewness.

As for OLR and 850-hPa winds, there is a significant pattern correlation between interannual and sub-seasonal anomalies (**Table 3**). For each WT there is an expected broad-scale inverse relationship between OLR (**Figure 8**) and rainfall anomalies (**Figure 9**). However, this association does not hold everywhere, in particular not over islands. The quiescent WT 5, for example,
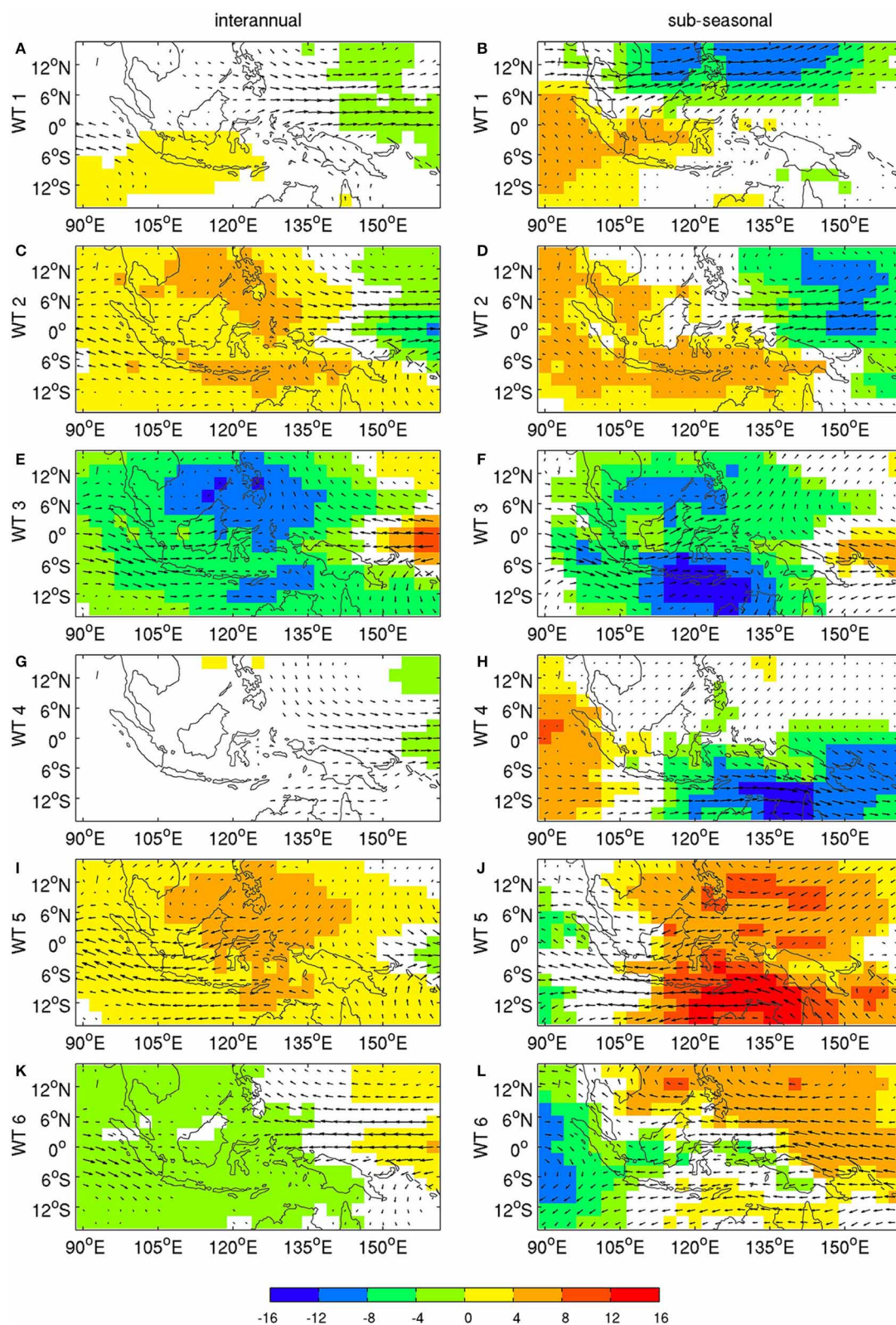
FIGURE 8 | OLR (shadings in Wm^{-2}) and 850 hPa winds: (left column) interannual and (right column) sub-seasonal anomalies associated with (A,B) WT 1, (C,D) WT 2, (E,F) WT 3, (G,H) WT 4, (I,J) WT 5 and (K,L) WT 6. The significance is computed by using 1000 random permutations of non-overlapping blocks of 22 days of daily WT sequences amongst the 34 years to account for the mean seasonal cycle, i.e., taken at the same stage of the cycle, and shown as color (OLR) and vectors (850-hPa wind) only when OLR, zonal or meridional components of the wind are above the two-sided 95% level of significance according to random permutations.

Table 3 | Pattern correlation between the interannual and sub-seasonal anomalies associated with each WT shown in Figure 6.

	U 850 hPa	V 850 hPa	OLR	TRMM rainfall
WT 1	0.32	0.03	0.46**	0.34**
WT 2	0.82**	0.55**	0.73**	0.63**
WT 3	0.82**	0.75**	0.76**	0.62**
WT 4	0.26	0.43*	0.22	0.23
WT 5	0.83**	0.81**	0.49**	0.38**
WT 6	0.60**	0.57**	0.54**	0.39**

One and two asterisks indicate significant values at the one-sided 95% and 99% level, respectively, according to a random permutation of non-overlapping blocks of 22 days of daily sequences amongst the 34 years (15 years for rainfall) to account for the mean seasonal cycle.

is associated at sub-seasonal scales (**Figure 8**) with positive OLR anomalies—almost everywhere, except over the eastern Indian Ocean—but positive rainfall anomalies are observed over Sumatra, western Borneo, Java, and Sulawesi, especially at sub-seasonal scales (**Figure 9**). Note also that dipolar precipitation anomalies appear over Borneo and New Guinea, especially for WTs 3, 5, and 6. The positive rainfall anomalies tend to be located in the lee of the mountains, in particular along the northwest coast of Borneo and in central New Guinea. This "island wake" effect (Qian et al., 2013) may be associated with land-sea breeze enhancement on the mountains' lee side.

The relationship between OLR and small-scale rainfall anomalies is further investigated in **Figure 10**. OLR is first interpolated onto the much finer TRMM grid over the same time interval, from 1998/99 on, as daily rainfall. The anomalies relative to the mean seasonal cycle of daily means are then standardized to zero mean and unit variance and spatially averaged for the core region of the MC (94°E–125°E, 10°S–6°N).

At this regional scale (**Figure 10A**), there is a broad anti-symmetry between OLR and rainfall anomalies, even though rainfall anomalies are closer to zero. Considering only the island points (**Figure 10B**) tends to weaken this anti-symmetry for WTs 2 and 3, where median rainfall anomalies tend to zero, and especially so for WT 5; in WT 5, OLR and rainfall anomalies are both positive, thus associating suppressed regional-scale deep convection with positive local-scale rainfall anomalies that could not be accurately captured by the OLR field's spatial resolution in our data. Such specifically asymmetric behavior of WT 5 appears also at even smaller scales, as seen over Java in **Figure 10C**.

3.4. WEATHER TYPES: VARIATIONS IN THE DIURNAL CYCLE
Diurnal-cycle variations are systematically analyzed for our six WTs by considering the 3-hourly mean rainfall at each grid point that corresponds to the climatological peak phase of the diurnal cycle; this peak occurs in the late afternoon to early night over islands and late night to early morning around islands, with no clear peak observed over open seas. The rainfall for the diurnal peak is standardized with respect to the mean seasonal cycle and averaged for each of our six WTs; the results are plotted in **Figure 11**.

The local-scale significance is estimated using the same permutation method as the one employed for **Figure 9**. The peak phase of the diurnal cycle is enhanced with respect to climatology over Java in WT 5, as expected, but also over most of Sumatra, southwest Borneo, Sulawesi, and most of the Sunda islands (**Figure 11E**), while peak daily rainfall is significantly below climatology over most of the open seas, except off the western coasts of Sumatra and Borneo.

The positive rainfall anomalies over islands east of 105°E in WT 5 are not related to enhanced large-scale convection, but rather to the increased strength of the diurnal cycle at small spatial scales, when eastward anomalies are superimposed on the normal westerlies associated with the austral summer monsoon (Moron et al., 2010; Qian et al., 2010, 2013), as well as to local-scale SSTs (Hendon, 2003; Qian et al., 2013). This special phenomenon for the "quiescent" WT 5 may be explained by the inverse relationship between the monsoonal wind speed and the intensity of diurnal cycle, increasing sea-breeze and valley-breeze convergence toward the mountains during weak monsoon, thus brings forth more rainfall over the mountains than over the adjacent plains and seas (Moron et al., 2010; Qian et al., 2010).

4. CONCLUDING REMARKS
4.1. SUMMARY
In this paper we have analyzed the characteristics of atmospheric variations over the Maritime Continent (MC) using the pattern recognition framework of weather typing. This framework has been extensively used for the extratropics (Mo and Ghil, 1988; Vautard and Legras, 1988; Kimoto, 1989; Vautard, 1990; Michelangeli et al., 1995; Ghil and Robertson, 2002) but less so in the tropics.

The MC shows a rich spectrum of temporal variations (**Figure 2**), including a strong seasonal cycle associated with the migration of the planetary-scale ITCZ. Our study focused on the austral summer monsoon, 1 September–30 April, for 34 seasons from 1979/80 to 2012/13. Six weather types (WTs) were obtained using *k*-means cluster analysis of unfiltered daily low-level wind fields (**Figures 3, 4**).

We interpreted these six WTs firstly as stages of the seasonal progression of the planetary-scale monsoon circulation (**Figure 3**) from the pre-monsoonal WT 1 through the core monsoonal WTs 3–5 and on to the post-monsoonal WT 6. The pre-monsoonal WT 1 and transitional WTs 2 are thus characterized by the low-level easterlies south of the equator that are common to both pre- and post-monsoonal stages.

Values of OLR below 210 Wm^{-2} are restricted to the north of the equator in WT 1 and shifted toward two near-equatorial minima, between Sumatra and Borneo, on the one hand, and between New Guinea and the Western Tropical Pacific, on the other, in WTs 2 and 6 (**Figure 4**). Marked seasonal changes take place in November–March, with a progression toward the monsoonal WTs 3–5 accompanied by westerlies that are strongest in WT 4, but quiescent in WT 5, and the strongest deep convection occurring south of the equator. WT 4 corresponds to the peak of the austral summer monsoon with strong westerlies reaching Northern Australia and a clear equatorial westerly flow from Sumatra to the Western Pacific (**Figure 4**).
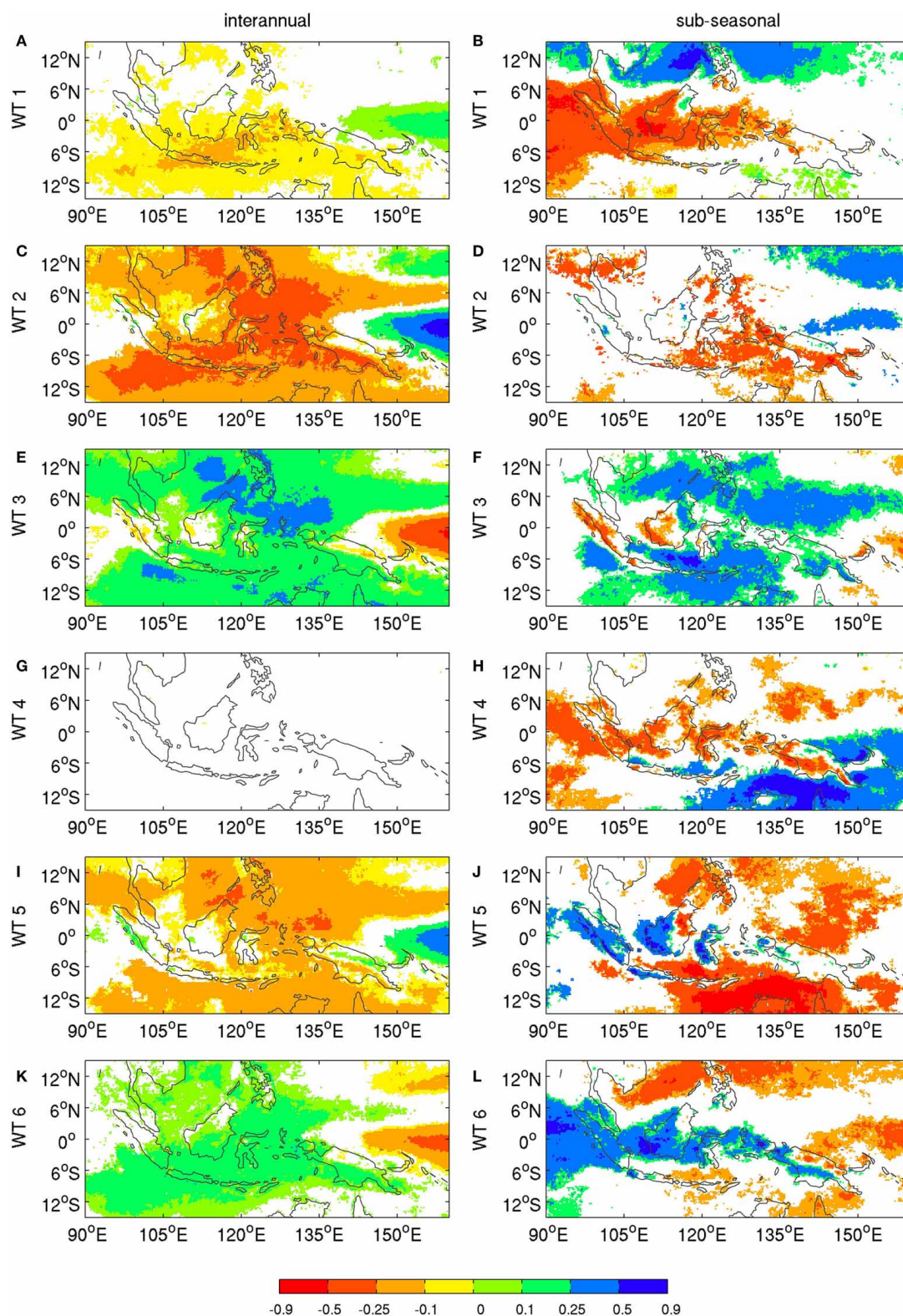
FIGURE 9 | Same as Figure 8, except for daily rainfall from the TRMM 3b42 (version 7) dataset (Huffman et al., 2007). Rainfall data are available from 1998/1999 on only. Daily rainfall (in 1/10 mm/day) are cube rooted before the computation of climatological mean and anomalies. The significance is computed as in **Figure 8**, except that only 15 years are available for the randomizing of the sequences.
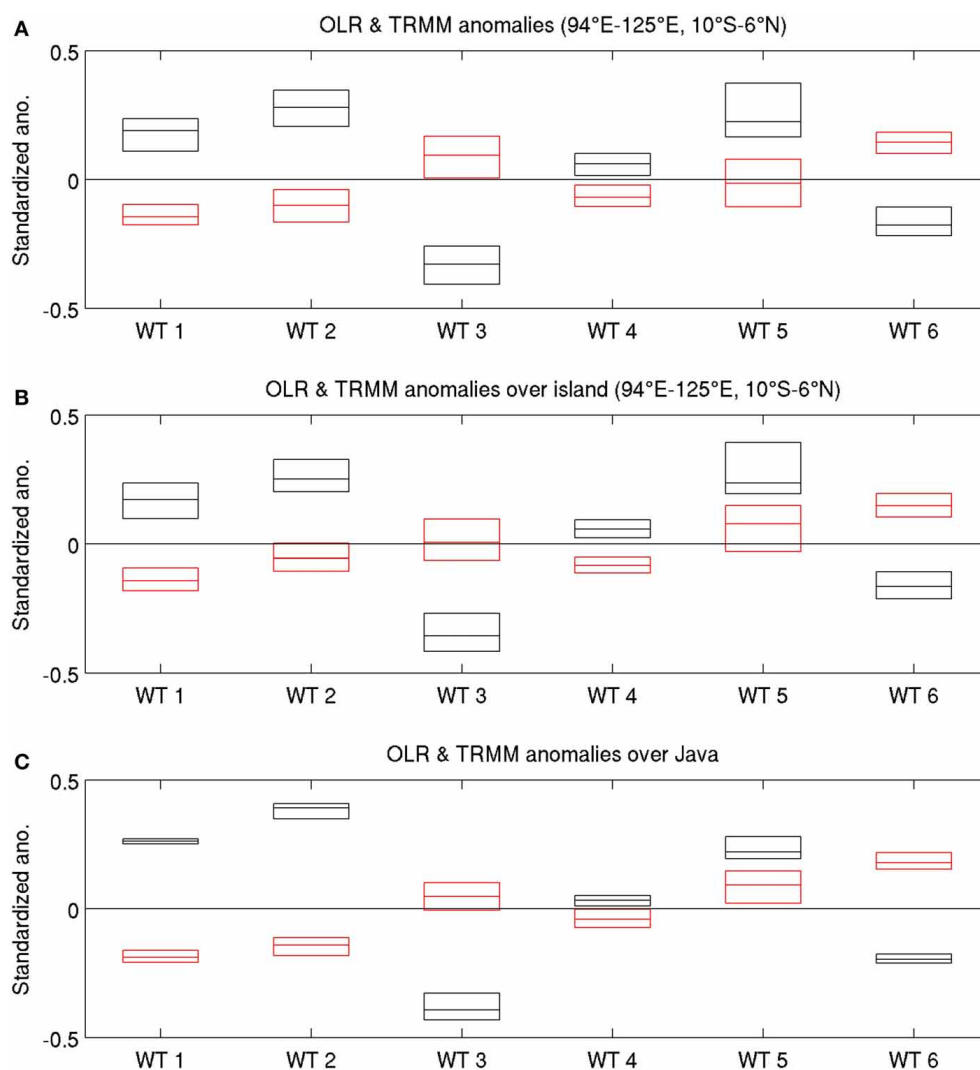
FIGURE 10 | OLR (black) and TRMM rainfall (red) standardized anomalies relative to the mean seasonal cycle for each WT, from 1998/1999 on only. Daily rainfall values (in 1/10 mm/day) are cube-rooted before the computation of c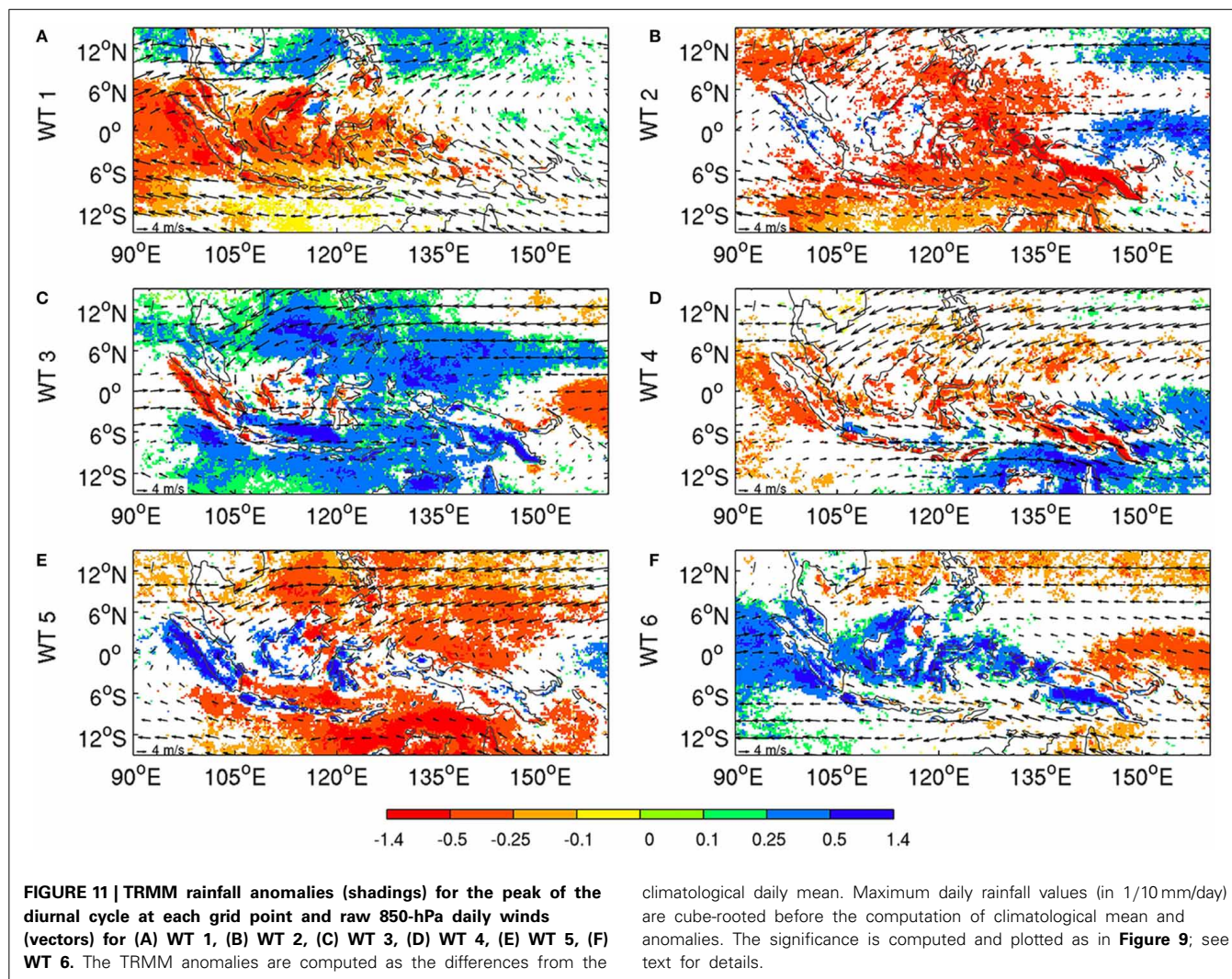limatological mean and anomalies; median—central horizontal line, upper and lower quartiles—upper and lower limits of the box. **(A)** Whole MC core area; **(B)** islands only; and **(C)** Java only. The plot for the sea only (not shown) is practically indistindinguishable from panel **(A)**. See text for details.

Using the WT framework, interannual and sub-seasonal variations lend themselves to interpretation in terms of changes in WT frequency of occurrence and their associated atmospheric anomalies at these scales (**Figures 5–8**). On the interannual time scale, the strongest anomalies are observed for WT 3, on the one hand, and WT 2 and 5, on the other: WT 3 (respectively WT 2 and 5) exhibits low-level anomalous convergence (respectively divergence) over eastern and/or central MC, along with enhanced (respectively suppressed) regional-scale deep convection (**Figure 8**). The interannual signal is weaker for the pre- and post-monsoon WTs 1 and 6, as well as for the peak WT 4 of the austral summer monsoon.

This behavior is consistent with the anomalies in WT frequency observed during ENSO events. Warm ENSO events are mostly associated with an increased occurrence of WT 1, followed by WT 2—which delays the regional-scale onset of the austral summer monsoon—and then by an increased frequency of the quiescent WT 5 during the rainy season; the latter corresponds to a superimposition of low-level easterly anomalies (**Figure 6**) upon the climatological westerlies associated with the austral summer monsoon (**Figure 4**). WTs 2 and 5 are associated with an enhanced diurnal cycle in the northern and southern MC, respectively, where synoptic winds are weak; weak winds lead to positive rainfall anomalies over some islands, or parts of islands, while large-scale subsidence promotes negative rainfall over most of the MC's inner seas (**Figure 11**). These results are consistent with our previous work (Moron et al., 2009, 2010; Qian et al., 2010, 2013), as well as with (Jourdain et al., 2013), who found that the anti-correlation between MC precipitation and the Niño 3.4 index in DJFM is

FIGURE 11 | TRMM rainfall anomalies (shadings) for the peak of the diurnal cycle at each grid point and raw 850-hPa daily winds (vectors) for (A) WT 1, (B) WT 2, (C) WT 3, (D) WT 4, (E) WT 5, (F) WT 6. The TRMM anomalies are computed as the differences from the climatological daily mean. Maximum daily rainfall values (in 1/10 mm/day) are cube-rooted before the computation of climatological mean and anomalies. The significance is computed and plotted as in **Figure 9**; see text for details.

more marked over ocean than over land in CMIP3 and CMIP5 model runs.

Cold ENSO events are not exactly symmetric, with more WT 6 episodes occurring just before the austral summer monsoon and especially more WT 3 than usual during the core of the rainy season. ENSO events do also modify the spatial pattern of WTs through the superposition of persistent anomalies associated with regional-scale anomalous subsidence (ascendance) during warm (cold) ENSO events (**Figure 6**).

On sub-seasonal time scales, the variation of WT frequencies is partly attributable to the MJO, with WTs 3–6 significantly locked with MJO phases. The sub-seasonal circulation anomalies are more pronounced amongst the WTs (**Figure 8**) but are similar to those on interannual time scales in their patterns, especially for WTs 2, 3, and 5. However, contrary to the effect of ENSO events, MJO does not appear to impact the WT patterns themselves significantly.

4.2. DISCUSSION

Our results show that the WT framework can provide flexible tools to diagnose atmospheric anomalies across time scales,

analyze potential predictability, and provide an easy way to spatially downscale any variable related to WT occurrence. Weather typing applied to unfiltered daily values covers in theory all time scales—from daily to interannual and interdecadal—i.e., up to the total number of years included in the analysis, equal here to 34 years. Of course, using EOF pre-filtering prior to the k-means clustering filters out the smallest and fastest variations. The reduction to a small set of WTs, equal here to six for 8228 days, also acts as a filter, while other clustering techniques (e.g., self-organizing maps) usually consider a larger set of situations, often more than 16, e.g., (Verdon-Kidd and Klem, 2009; Brown et al., 2010).

In any clustering, there is a trade-off between robustness and resolution. Transient mesoscale and synoptic-scale features, like the Borneo vortex (e.g., Chang et al., 2003, 2005b; Tangang et al., 2008) or individual tropical depressions or even cyclones (Chang et al., 2003) are obviously not captured by a small number of WTs, but this does not mean that WTs do not provide information on fast and small scales. As soon as one WT is associated with systematic and reproducible variations at any scale, this information is retrievable in the WT framework. It is the case here with the systematic modulation of the diurnal cycle over several islands

or parts thereof—including Sumatra, western Borneo, Java, and Sulawesi—mostly in WT 5 and, at least, in sectors where a combination of sub-seasonal to seasonal variations and the annual cycle weakens the regional-scale winds and thus increases the diurnal-cycle amplitude (Moron et al., 2010; Qian et al., 2013).

In their recent study, Peatman et al. (2013) concluded that 80% of the MJO precipitation signal over the MC is accounted for by changes in the amplitude of the diurnal cycle, which responds over islands about 6 days in advance of the arrival of the main MJO convective envelope. They argue that frictional and topographic moisture convergence and relatively clear skies then combine with the low thermal inertia of the islands, to allow a rapid response in the diurnal cycle. According to our results, the "quiescent" WT 5 is responsible for the strong diurnal signal over islands, and it is most prevalent in MJO phases 1–3, when the MJO convective envelope is over the Indian Ocean (**Figure 7**). We argue that the quiescent large-scale winds of WT 5 allow the diurnal cycle to amplify, as described in Qian et al. (2010, 2013).

Although the MJO modulation of WT 5 is most marked during La Niña events (**Figure 7C**), this is tempered by the much less frequent occurrence of WT 5 during the cold phase of ENSO (**Figure 5B**), so that this MJO modulation of diurnal precipitation is less likely to be observed at that time.

An early dynamical interpretation of extratropical WTs, or planetary flow regimes (Legras and Ghil, 1985; Ghil and Childress, 1987), was in terms of fixed points of the governing flow equations. In the tropics, moist processes play a larger role than in mid-latitudes, and one can thus expect the need for more complex interpretations. Moreover, boundary forcing by SSTs in the tropics is much more important than in mid-latitudes. In particular, we found here that WTs can capture transient modes or systematic variations, such as the seasonal cycle. We have shown, in fact, that WTs can be interpreted, to first order, as fixed snapshots of the annual cycle, since this time scale was retained in our analysis and not filtered out at the outset, as is typically done.

Furthermore, it was possible to separate the atmospheric anomalies associated with each WT according to large-scale climate phenomena on both the interannual and sub-seasonal scale, namely as being affected by either ENSO or the MJO, respectively. For example, the broad-scale easterly anomalies observed in WTs 2 and 5 refer clearly to warm ENSO events, acting through large-scale subsidence over eastern Indonesia. Likewise we found that WT 5 is more phase-locked to MJO than WT 2 is. Such a data-adaptive, WT-mediated decomposition of time scales is complementary to the usual a priori selection that is provided by removing the mean annual cycle or by bandpass filtering. Our WT framework helps one also to interpret the phase shifts associated with the seasonal cycle as the delayed onset of the austral summer monsoon during warm ENSO events, an aspect that may be blurred when the seasonal cycle is filtered out a priori.

Returning to the conceptual framework of dynamical systems theory introduced in Section 1, we may conclude that the importance of "external" forcings—i.e., of ENSO, the MJO and the seasonal cycle—in the Tropics in general and in the regional dynamics of the MC in particular—requires the application of the broader and more flexible concepts of open, non-autonomous, and possibly random dynamical systems (cf. Ghil et al., 2008;

Chekroun et al., 2011; Ghil, 2014) and references therein, while the more standard theory of closed, autonomous systems was largely sufficient for planetary-scale, extratropical phenomena (Ghil and Childress, 1987, Ch. 5). Thus, the seasonal cycle introduces a strong periodic modulation of the atmosphere's dynamical attractor over the MC, for which the six discrete WTs that occur in overlapping fashion at different stages of the monsoonal progression provide a robust "skeleton." For the sake of brevity, we will not enter into the technical aspects of the time-dependent pullback attractors that are required to describe the behavior of non-autonomous systems, and only use the concepts loosely in order to interpret the present findings.

The occurrence frequency of certain WTs is significantly impacted from year to year by ENSO and sub-seasonally by the MJO, modulating in time the size and shape of the corresponding attractor basins. Sub-seasonal to seasonal predictability of circulation over the MC may be partially framed in terms of the strength of these frequency modulations. In addition, ENSO was shown to exert an influence on the spatial structure of circulation patterns for certain WTs, thereby modulating, on interannual time scales, the position that the pullback attractor's successive "snapshots" occupy in the system's phase space. This effect is not found for the MJO, whose impact appears to be purely on the WTs' frequency of occurrence.

The atmospheric Southern Oscillation limb of ENSO modulates the strength of the planetary-scale Walker Circulation, whose ascending branch is located over the MC. Thus, it is very plausible that ENSO would modulate the structure of the MC's pullback attractor on shorter spatial scales. While the MJO also has a large wavenumber-one component zonally, it is transient on the time scale of WT transitions and propagates through the MC; it is therefore to be expected that its impact on the WTs would be largely by modulating their frequency, with less impact on the overall attractor structure.

Besides the theoretical considerations above, the connection between daily weather conditions and large-scale climate drivers afforded by the WT framework is very useful from the applied climate perspective. For example, farmers in Western Java plant their first rice crop after monsoon onset in October–December, followed by a second crop, which they plant in May-June. The first is vulnerable to flooding in January-February, and the second to drought, especially if the monsoon onset is delayed by El Niño (Boer and Subbiah, 2005; Moron et al., 2009). The work presented here could help identify the atmospheric drivers of flood and drought events at local scale within specific WT daily sequences, which in turn may help develop sub-seasonal to seasonal forecasts that are more accurate and better tailored to the needs of farmers.

REFERENCES

Bjerknes, J. (1969). Atmospheric teleconnections from the equatorial Pacific. *Mon. Wea. Rev.* 97, 163–172. doi: 10.1175/1520-0493(1969)097<0163:ATFTEP>2.3.CO;2

Boer, R., and Subbiah, A. R. (2005). "Agricultural droughts in Indonesia," in *Monitoring and Predicting Agricultural Drought: A Global Study*, eds V. S. Boken, A. P. Cracknell, and R. L. Heathcote (New York, NY: Oxford University Press), 330–344.

Brown, J. R., Jakob, C., and Haynes, J. M. (2010). An evaluation of rainfall frequency and intensity over the Australian region in a global climate model. *J. Clim.* 23, 6504–6525. doi: 10.1175/2010JCLI3571.1

Chang, C.-P., Liu, C.-H., and Kuo, H.-C. (2003). Typhoon Vamei: an equatorial tropical cyclone formation. *Geophys. Res. Lett.* 30. doi: 10.1029/2002GL016365

Chang, C.-P., Harr, P. A., and Chen, H.-J. (2005b). Synoptic disturbances over the equatorial Souttime Continent during boreal winter. *Mon. Wea. Rev.* 133, 489–503. doi: 10.1175/MWR-2868.1

Chang, C.-P., Wang, Z., McBride, J., and Liu, C.-H. (2005a). Annual cycle of Southeast Asia Maritime Continent rainfall and the asymmetric monsoon transition. *J. Clim.* 18, 287–301. doi: 10.1175/JCLI-3257.1

Chekroun, M. D., Simonnet, E., and Ghil, M. (2011). Stochastic climate dynamics: random attractors and time-dependent invariant measures. *Physica D* 240, 1685–1700. doi:10.1016/j.physd.2011.06.005.

Chen, Y., Ebert, E. E., Walsh, K. J. E., and Davidson, N. E. (2013). Evaluation of TRMM 3B42 precipitation estimates of tropical cyclone rainfall using PACRAIN data. *J. Geophys. Res.* 118, 1–13. doi: 10.1002/jgrd.50250

Diday, E., and Simon, J. C. (1976). "Clustering analysis," in *Digital Pattern Recognition*, Communication and Cybernetics, Vol. 10, ed K.S. Fu (Springer-Verlag), 47–94.

Dinku, T., Ceccato, P., Grover-Kopec, E., Lemina, M., Connor, S. J., and Ropelewski, C. F. (2007). Validation of satellite rainfall products over East Africa's complex topography. *Int. J. Remote Sensing* 28, 1503–1526. doi: 10.1080/01431160600954688

Ghil, M. (2014). "A mathematical theory of climate sensitivity or, How to deal with both anthropogenic forcing and natural variability?," in *Climate Change: Multidecadal and Beyond*, eds C. P. Chang, M. Ghil, M. Latif, and J. M. Wallace (London: World Scientific Publishing Co.; Imperial College Press).

Ghil, M., and Childress, S. (1987). *Topics in Geophysical Fluid Dynamics: Atmospheric Dynamics, Dynamo Theory and Climate Dynamics*. New York; Berlin; Tokyo: Springer-Verlag. doi: 10.1007/978-1-4612-1052-8

Ghil, M., and Robertson, A. W. (2002). "Waves" vs. "particles" in the atmosphere's phase space : a pathway to long-range forecasting? *Proc. Natl. Acad. Sci. U.S.A.* 99, 2493–2500. doi: 10.1073/pnas.012580899

Ghil, M., Chekroun, M. D., and Simonnet, E. (2008). Climate dynamics and fluid mechanics: natural variability and related uncertainties. *Physica D* 237, 2111–2126. doi: 10.1016/j.physd.2008.03.036

Gloneck, G. F. V., and McCullagh, P. (1995). Multivariate logistic models. *J. R. Stat. Soc. Ser. B* 57, 533–546.

Guanche, Y., Minguez, R., and Méndez, F. J. (2014). Autoregressive logistic regression applied to atmospheric circulation patterns. *Clim. Dyn.* 42, 537–552. doi: 10.1007/s003 82-013-1690-3

Haylock, M., and McBride, J. L. (2001). Spatial coherence and predictability of Indonesian wet season rainfall. *J. Clim.* 14, 3882–3887. doi: 10.1175/1520-0442(2001)014<3882:SCAPOI>2.0.CO;2

Hendon, H. H. (2003) Indonesian rainfall variability: impacts of ENSO and local air-sea interaction. *J. Clim.* 16, 1775–1790. doi: 10.1175/1520-0442(2003)016<1775:IRVIOE>2.0.CO;2

Hendon, H. H., and Liebmann, B. (1990). The intraseasonal (30–50 day) oscillation of the Australian summer monsoon. *J. Atmos. Sci.* 47, 2909–2923. doi: 10.1175/1520-0469(1990)047<2909:TIDOOT>2.0.CO;2

Huffman, G. J., Adler, R. F., Bolvin, D. T., Gu, G., Nelkin, E. J., Bowman, K. P., et al. (2007). The TRMM multi-satellite precipitation analysis: Quasi-global, multi-year, combined-sensor precipitation estimates at fine scale. *J. Hydrometeor.* 8, 38–55. doi: 10.1175/JHM560.1

Janicot, S., Moron, V., and Fontaine, B. (1996). Sahel drought and ENSO dynamics. *Geophys. Res. Lett.* 23, 515–518.

Jourdain, N. C., Sen Gupta, A, Taschetto, A. S., Ummenhofer, C. C., Moise, A. F., and Ashok, K. (2013). The Indo-Australia monsoon and its relationship to ENSO and IOD in reanalysis data and the CMIP3/CMIP5 simulations. *Clim. Dyn.* 41, 3073–3102. doi: 10.1007/s00382-013-1676-1

Juneng, L., and Tangang, F. (2005). Evolution of ENSO-related rainfall anomalies in SouthEast Asia region and its relationship with atmosphere-ocean variations in the Indo-Pacific sector. *Clim. Dyn.* 25, 337–350. doi: 10.1007/s00382-005-0031-6

Kanamitsu, M., Ebisuzaki, W., Woollen, J., Yang, S.-K., Hnilo, J. J., Fiorino, M., et al. (2002). NCEP-DOE AMIP-II Reanalysis (R-2). *Bull. Amer. Meteor. Soc.* 79, 1631-1643. doi: 10.1175/BAMS-83-11-1631

Kimoto, M. (1989). *Multiple Flow Regimes in the Northern Hemisphere Winter*. Ph.D. thesis, University of California, Los Angeles.

Klein, S. A., Soden, B. J., and Lau, N.-C. (1999). Remote sea surface temperature variations during ENSO: evidence for a tropical atmospheric bridge. *J. Clim.* 12, 917–932. doi: 10.1175/1520-0442(1999)012<0917:RSSTVD>2.0.CO;2

Kondrashov, D., Chekroun, M. D., Robertson, A. W. and Ghil, M. (2013). Low-order stochastic model and "past-noise forecasting" of the Madden-Julian oscillation. *Geophys. Res. Lett.* 40, 5305–5310. doi: 10.1002/grl.50991

Lefèvre, J., Marchesiello, P., Jourdain, N. C., Menkes, C., and Leroy, A. (2010). Weather regimes and orographic circulation. *Marine Poll. Bull.* 61, 413–431. doi: 10.1016/j.marpolbul.2010.06.012

Legras, B., and Ghil, M. (1985). Persistent anomalies, blocking and variations in atmospheric predictability. *J. Atmos. Sci.* 42, 433–471.

Liebmann, B., and Smith, C. A. (1996). Description of a complete (interpolated) outgoing longwave radiation dataset. *Bull. Amer. Meteor. Soc.* 77, 1275–1277.

Livezey, R. E., and Chen, W. Y. (1983). Statistical field significance and its determination by Monte Carlo techniques. *Mon. Wea. Rev.* 111, 46–59.

Madden, R. A., and Julian, P. R. (1971). Detection of a 40-50 day oscillation in the zonal wind in the Tropical Pacific. *J. Atmos. Sci.* 28, 702–708. doi: 10.1175/1520-0469(1971)028<0702:DOADOI>2.0.CO;2

Matthews, A. J., and Li, H.-Y.-Y. (2005). Modulation of station rainfall over the Western Pacific by the Madden-Julian oscillation. *Geophys. Res. Lett.* 32, L14827. doi: 10.1029/2005GL023595

McBride, J. L., Haylock, M. R., and Nicholls, N. (2003). Relationships between the Maritime Continent heat source and the El Niño Southern Oscillation phenomenon. *J. Clim.* 16, 2905–2914. doi: 10.1175/1520-0442(2003)016<2905:RBTMCH>2.0.CO;2

Michelangeli, R. A., Vautard, R., and Legras, B. (1995). Weather regimes: recurrence and quasi-stationarity. *J. Atmos. Sci.* 52, 1237–1256. doi: 10.1175/1520-0469(1995)052<1237:WRRAQS>2.0.CO;2

Mo, K., and Ghil, M. (1988). Cluster analysis of multiple planetary flow regimes. *J. Geophys. Res.* 93, 927–952. doi: 10.1029/JD093iD09p10927

Moron, V., Robertson, A. W., and Qian, J.-H. (2010). Local versus regional-scale characteristics of monsoon onset and post-onset rainfall over Indonesia. *Clim. Dyn.* 34, 281–299. doi: 10.1007/s00382-009-0547-2

Moron, V., Robertson, A. W., and Boer, R. (2009). Spatial coherence and seasonal predictability of monsoon onset over Indonesia. *J. Clim.* 22, 840–850. doi: 10.1175/2008JCLI2435.1

Moron, V., Robertson, A. W., and Ghil, M. (2012). Impact of the modulated annual cycle and intraseasonal oscillation on daily-to-interannual rainfall variability across monsoonal India. *Clim. Dyn.* 38, 2409–2435. doi: 10.1007/s00382-011-1253-4

Moron, V., Robertson, A. W., Ward, M. N., and Ndiaye, O. (2008). Weather types and rainfall over Senegal. Part I: observational analysis. *J. Clim.* 21, 266–287. doi: 10.1175/2007JCLI1601.1

Palmer, T. N. (1998). Nonlinear dynamics and climate change: Rossbys legacy. *Bull. Amer. Meteor. Soc.* 79, 1411–1423. doi: 10.1175/1520-0477(1998)079<1411:NDACCR>2.0.CO;2

Peatman, S. C., Matthews, A. J., and Stevens, D. P. (2013). Propagation of the Madden–Julian Oscillation through the Maritime Continent and scale interaction with the diurnal cycle of precipitation. *Quart. J. R. Meteorol. Soc.* 140, 814–825. doi: 10.1002/qj.2161

Pohl, B., Camberlin, P., and Roucou, P. (2005). Typology of pentad circulation anomalies over the Eastern Africa – Western Indian ocean region, and their relationship with rainfall. *Clim. Res.* 29, 111–127. doi: 10.3354/cr029111

Qian, J.-H. (2008). Why precipitation is mostly concentrated over islands in the Maritime Continent. *J. Atmos. Sci.* 65, 1428–1441. doi: 10.1175/2007JAS2422.1

Qian, J.-H., Robertson, A. W., and Moron, V. (2010). Multi-scale interaction between ENSO, monsoon and diurnal cycle over Java, Indonesia. *J. Atmos. Sci.* 67, 3509–3523. doi: 10.1175/2010JAS3348.1

Qian, J.-H., Robertson, A. W., and Moron, V. (2013). Diurnal cycle in weather regimes and rainfall variability over Borneo associated with ENSO. *J. Clim.* 26, 1772–1790. doi: 10.1175/JCLI-D-12-00178.1

Rauniyar, S. P., and Walsh, K. J. E. (2011). Scale interaction of the diurnal cycle of rainfall over the Maritime Continent and Australia: influence of the MJO. *J. Clim.* 24, 325–348. doi: 10.1175/2010JCLI3673.1

Robertson, A. W., Moron, V., Qian, J.-H., Chang, C.-P., Tangang, F., Aldrian, E., et al. (2011). "The maritime continent monsoon," in *The Global Monsoon System: Research and Forecast, 2nd Edn.*, eds C.-P. Chang, Y. Ding, G. N.-C. Lau, R. H. Johnson, B. Wang, and T. Yasunari (New Jersey: World Scientific Publishing Co.), 85–97. doi: 10.1142/9789814343411_0006

Tangang, F., Juneng, L., Salimun, E., Vinayachandran, P. N., Seng, Y. K., Reason, C. J. C., et al. (2008). On the roles of the northeast cold surge, the Borneo vortex, the Madden-Julian oscillation and the Indian ocean dipole during the extreme 2006/2007 flood in southern Peninsular Malaysia. *Geophys. Res. Lett.* 35. doi: 10.1029/2008GL033429

Teo, C.-K., Koh, T. Y., Lo, J. C.-F., and Bhatt, B. C. (2011). Principal component analysis of observed and modeled diurnal rainfall in the Maritime Continent. *J. Clim.* 24, 4662–4675. doi: 10.1175/2011JCLI4047.1

Vautard, R., and Legras, B. (1988). On the source of midlatitude low-frequency variability. Part II: nonlinear equilibration of weather regimes. *J. Atmos. Sci.* 45, 2845–2867. doi: 10.1175/1520-0469(1988)045<2845:OTSOML>2.0.CO;2

Vautard, R., Mo, K. C., and Ghil, M. (1990). Statistical significance test for transition matrices of atmospheric Markov chains. *J. Atmos. Sci.* 47, 1926–1931.

Vautard, R. (1990). Multiple weather regimes over the North Atlantic: analysis of precursors and successors. *Mon. Wea. Rev.* 118, 2056–2081. doi: 10.1175/1520-0493(1990)118<2056:MWROTN>2.0.CO;2

Verdon-Kidd, D. C., and Klem, A. S. (2009). On the relationship between large-scale climate modes and regional synoptic patterns that drive Victorian rainfall. *Hydrol. Earth Syst. Sci.* 13, 467–479. doi: 10.5194/hess-13-467-2009

Wheeler, M. C., and Hendon, H. H. (2004). An all-season real-time multivariate MJO index: development of an index for monitoring and prediction. *Mon. Wea. Rev.* 132, 1917–1932. doi: 10.1175/1520-0493(2004)132<1917:AARMMI>2.0.CO;2

A synoptic climatology of heavy rain events in the Lake Eyre and Lake Frome catchments

Michael J. Pook[1]*, James S. Risbey[1], Caroline C. Ummenhofer[2], Peter R. Briggs[3] and Timothy J. Cohen[4]

[1] Commonwealth Scientific and Industrial Research Organisation Oceans and Atmosphere, Hobart, TAS, Australia
[2] Department of Physical Oceanography, Woods Hole Oceanographic Institution, Woods Hole, MA, USA
[3] Commonwealth Scientific and Industrial Research Organisation Oceans and Atmosphere, Canberra, ACT, Australia
[4] GeoQuest Research Centre, School of Earth and Environmental Sciences, University of Wollongong, Wollongong, NSW, Australia

The rare occasions when Lake Eyre in central, southern Australia fills with water excite great interest and produce major ecological responses. The filling of other smaller lakes such as Lake Frome have less impact but can contribute important information about the current and past climates of these arid regions. Here, the dominant synoptic systems responsible for heavy rainfall over the catchments of Lake Eyre and Lake Frome since 1950 are identified and compared. Heavy rain events are defined as those where the mean catchment rainfall for 24 h reaches a prescribed threshold. There were 25 such daily events at Lake Eyre and 28 in the Lake Frome catchment. The combination of a monsoon trough at mean sea level and a geopotential trough in the mid-troposphere was found to be the synoptic system responsible for the majority of the heavy rain events affecting Lake Eyre and one in five of the events at Lake Frome. Complex fronts where subtropical interactions occurred with Southern Ocean fronts also contributed over 20% of the heavy rainfall events in the Frome catchment. Surface troughs without upper air support were found to be associated with 10% or fewer of events in each catchment, indicating that mean sea level pressure analyses alone do not adequately capture the complexity of the heavy rainfall events. At least 80% of the heavy rain events across both catchments occurred when the Southern Oscillation Index (SOI) was in its positive phase, and for Lake Frome, the SOI exceeded +10 on 60% of occasions, suggesting that the background atmospheric state in the Pacific Ocean was tilted toward La Niña. Hydrological modeling of the catchments suggests that the 12-month running mean of the soil moisture in a sub-surface layer provides a low frequency filter of the precipitation and matches measured lake levels relatively well.

Keywords: synoptic, front, monsoon trough, upper trough, cutoff low, Australia, Lake Eyre

INTRODUCTION

The lakes of Australia's arid interior are ephemerally filled and are for most of the time salt-crusted playa surfaces. The filling of such large playa lakes (including Australia's largest—Lake Eyre) is therefore an important climatological phenomenon triggering large-scale ecological responses (e.g., Kingsford and Porter, 1995; Poulter et al., 2014) and also being of great socio-economic and general cultural interest. Indeed, the "inland sea" of Australia was what many early explorers were searching for Cathcart (2009). The reality however is that such filling events occur rarely and under specific conditions only. Many of Australia's playa lakes lack significant catchment areas (relative to lake area) and are predominantly groundwater-fed, making them highly susceptible to evaporative processes. Others have large contributing catchment areas in the arid-zone (e.g., Lake Torrens or Lake Frome) or from the tropical northern latitudes (e.g., Lake Eyre). Most have contributing rivers which experience high transmission losses of discharge en route to the terminal lakes (Knighton and Nanson, 1994).

A number of attempts have been made to document the historical filling of Lake Eyre but little other work exists which documents when and how other large playa lakes (e.g., Torrens or Frome) have filled. Earlier work by the Lake Eyre Committee (1955) and Bonython and Fraser (1989) provide a useful review to some of the earlier lake fillings of Australia's largest lake, whilst Kotwicki (1986) provides a comprehensive assessment of the Lake Eyre Basin hydrological characteristics. Subsequent work by Kotwicki and Isdale (1991) has attempted to correlate historical Lake Eyre filling to proxy climate records and large-scale climatic influences, of which the El Niño-Southern Oscillation (ENSO) phenomenon is the dominant driver. The larger arid-zone lake systems also record a long history of fluctuating climate with the work of Magee et al. (2004) and Cohen et al. (2011, 2012a) all demonstrating that these inland catchments were much wetter about 100,000–50,000 years ago than at present with the presence of large "megalakes" and associated Pleistocene megafauna (Webb, 2010). Even more recently in the geological past (e.g., the medieval climatic anomaly, ~1000 years ago) it has been shown

that the Lake Frome-Callabonna system experienced exceptionally wet events that produced aggradational evidence of past lake filling (Cohen et al., 2012b; Gliganic et al., 2014).

It is not known what synoptic and climatic conditions were responsible for ancient lake fillings. However, there are reliable synoptic data available for the period since about 1950 and analysis of this data set provides the opportunity to examine the modern circulation types associated with large rainfall events in these arid zone catchments. The results of this analysis may then offer some insights into the characteristics of the enhanced rainfall periods in the geological record. Hence, in this paper we investigate the types of synoptic systems responsible for a selection of recent historical heavy rainfall events over the catchments of Lake Eyre and Lake Frome using accepted methods of synoptic climatology (e.g., Pook et al., 2006, 2012, 2014). We compare and contrast the dominant systems affecting the Lake Eyre catchment with those contributing to major events in the Lake Frome catchment. Both lakes are located in southern central Australia (**Figure 1**) and the lakes themselves fall within relatively uniform rainfall distribution zones. However, the headwaters of Lake Eyre lie within the summer-dominated rainfall zone of the tropical north and the headwaters of the Frome-Callabonna system are largely confined within the winter-dominated rainfall zone.

Lake-filling occurrences are not the result of isolated heavy precipitation events in the arid interior of Australia but rather follow extended periods of widespread rainfall over the catchments. While it is important to categorize the synoptic systems responsible for individual heavy rain events, it is also essential to place these synoptic events within the background atmospheric state. The intensity of the Australian monsoon has been shown to have a strong association with the filling of Lake Eyre (Allan, 1985) and historical evidence indicates that most episodes of enhanced

FIGURE 1 | Location of the Eyre (mid-gray) and Frome (dark-gray) drainage basins at 0.05 × 0.05° resolution. White areas within the basins are included in the analysis of the Australian Bureau of Meteorology daily rainfall (Jones et al., 2009) but excluded from the CSIRO Australian Water Availability Project monthly model outputs due to missing soil information (Raupach et al., 2009).

precipitation in subtropical and tropical Australia occur during the La Niña phase of ENSO (e.g., Allan et al., 1996, and references therein). Risbey et al. (2009) have shown that, among the various indices of ENSO in current use, the Southern Oscillation Index (SOI) has the highest simultaneous correlation with Australian rainfall. The correlation is positive. Sustained positive values of the SOI above a specified threshold tend to be associated with La Niña. Consequently, the mean monthly value of the SOI has been recorded for each of the heavy rain events examined in the synoptic analysis.
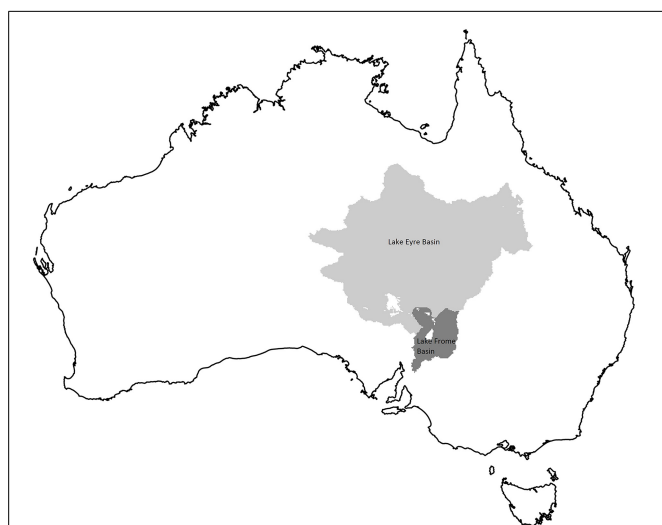
DATA AND METHOD
DATA
Daily rainfall data for each catchment for the period January 1, 1900 to February 28, 2014 were obtained by spatial averaging of the Australian Bureau of Meteorology's high-quality gridded rainfall surfaces at 0.05 × 0.05° resolution, prepared for the Australian Water Availability Project (AWAP) (Jones et al., 2009; Australian Bureau of Meteorology, 2014). Areas of missing daily data due to sparse network interpolation failure were filled with disaggregated monthly data interpolated using a larger length scale. Commonwealth Scientific and Industrial Research Organisation (CSIRO) AWAP model outputs of water fluxes and soil moisture in a near-surface (approximately 0 to 0.2 m) and a sub-surface layer (approximately 0.2 to 2 m) at monthly resolution (Raupach et al., 2009, 2014) were generated using the AWAP WaterDyn model (version 26M) driven by the same daily rainfall data and corresponding daily temperature and solar radiation data. The relative soil moisture in the AWAP product is defined as a fraction of the saturated water-holding capacity of the soil and is dimensionless. Spatial averages of AWAP model outputs exclude areas not modeled due to missing soil parameter information, shown as white areas within the two catchments (see **Figure 1**). These areas are unrelated to the areas filled with monthly rainfall data, but may overlap them.

The synoptic analysis was primarily based on the National Centers for Environmental Prediction (NCEP)—National Center for Atmospheric Research (NCAR) climate reanalysis data set (Reanalysis 1) (Kalnay et al., 1996; Kistler et al., 2001). The NCEP data consist of 4 analyses per day (at 6-hourly intervals from 0000 UTC) at a resolution of 2.5° latitude by 2.5° longitude for the standard atmospheric levels from the surface to the lower stratosphere. The reanalysis data are available from January 1948 although the Australian data have been used with caution prior to 1956 as the upper air data network was quite sparse prior to that time (Pook et al., 2012). The key fields sampled in the analysis were mean sea level pressure (MSLP), the 500 hPa geopotential height, the (computed) 1000-500 hPa atmospheric thickness and the 250 hPa wind. Additionally, the 1000-500 hPa thickness anomaly relative to the long-term climatology for a particular month was calculated and displayed for each analysis.

The Reanalysis data set was supplemented by daily weather maps at 0000 UTC published in the Australian Bureau of Meteorology's "Monthly Weather Review" series (Simmonds and Richter, 2000). These charts include frontal analysis which has been performed manually by expert analysts employing interpretation of satellite imagery in addition to standard analysis of

synoptic data (Guymer, 1978) and evaluation of output from a suite of numerical weather prediction models. Crucially, these charts provide the most reliable method of determining the occurrence of cold fronts, important rain-producing systems in southern Australia.

Monthly means of the SOI were obtained from the Australian Bureau of Meteorology (http://www.bom.gov.au/climate/current/soihtm1.shtml) in order to determine the phase of the ENSO at the time of each of the heavy rain events. The calculation of the SOI has evolved over time (Allan et al., 1996). In this paper the SOI is expressed as the monthly mean of the normalized pressure difference between Tahiti and Darwin.

METHOD

For each day on which the mean rainfall across the particular catchment network was greater than or equal to a threshold value, a particular synoptic system was identified as being responsible for the precipitation event. For the vast Lake Eyre catchment (see **Figure 1**), a threshold of 20 mm per day was selected for the heavy rainfall events in order to include isolated events large enough to produce runoff and therefore have the potential to contribute to lake filling episodes. For the much smaller Lake Frome catchment the threshold for the daily mean catchment rainfall of a heavy rainfall event was set at 25 mm per day. This approach produced comparable numbers of events in each catchment.

The primary classification of synoptic systems followed Pook et al. (2006, 2012, 2014) who specified three main categories: cold frontal systems associated with Southern Ocean depressions; cold-cored lows that have become separated from the westerly flow (cutoff lows); and a broad category labeled "other synoptic systems" that included, inter alia, troughs in the surface easterlies (easterly troughs) and cold troughs in the middle troposphere where a closed circulation was not present at 500 hPa. In this study the upper trough was required to contain a region of negative anomaly of 1000-500 hPa thickness of at least 20 geopotential meters. Within the cold frontal category, Pook et al. (2006) identified three main types of front; simple, complex and waves. The complex front is identified by the presence of a well-defined prefrontal trough which extends southwards from the subtropics and may interact with an existing subtropical cloud band. Expert judgment from forecasting and analysis experience was applied in order to make a realistic estimate of the typical displacement of synoptic systems in order to ensure that the system was located over the catchment during the 24 h period in which the rainfall was recorded.

As this analysis extends over the austral summer, an extra category of "monsoon trough" has been added. The monsoon trough was identified by the analyst in cases where the shear line between the low-level westerlies in the north and the southeast trades in the south as inferred from the isobaric pattern was located over northern Australia (McBride, 1998), and in close proximity to or over the Lake Eyre Basin (see **Figure 1**). The Australian monsoon is intermittent in intensity and southward extent (Sturman and Tapper, 1996) tends to develop well into the austral summer and is characterized by periods of days or weeks of relative inactivity known as "breaks." However, semi-permanent heat lows remain anchored over northwestern Australia and northeastern Australia

throughout the summer half of the year (Sturman and Tapper, 1996) but are rarely associated with widespread rain.

For each event, the MSLP, 500 hPa, and the 1000-500 hPa thickness analyses were carefully evaluated. Hence, synoptic types have been specified according to a combination of MSLP and upper air criteria. As an example, **Figure 2** shows typical MSLP and 500 hPa analyses for the synoptic classification referred to as "monsoon trough/upper trough."
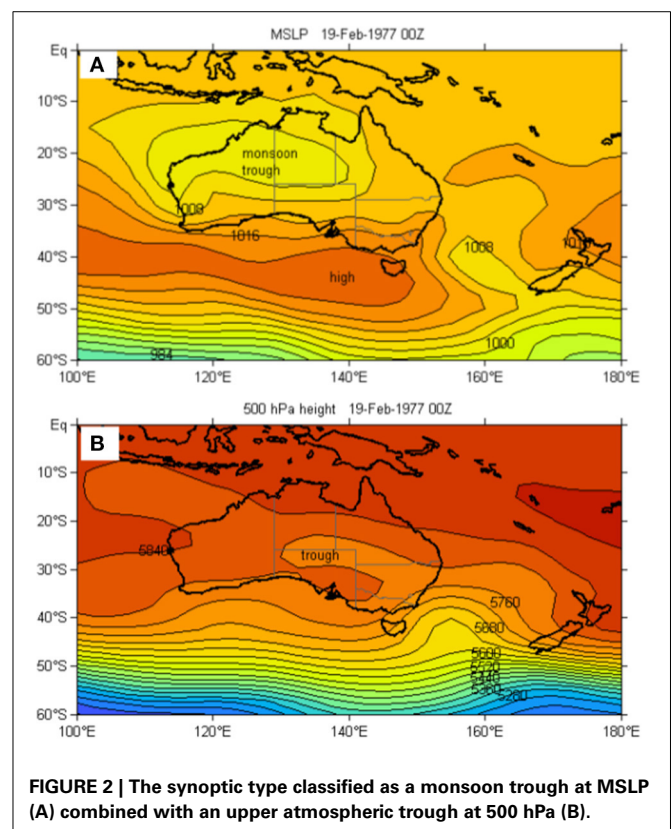
RESULTS

LAKE EYRE CATCHMENT

Over the period from January 1950 to February 2014 there were 25 individual events for which the mean daily rainfall for the Lake Eyre catchment (see **Figure 1**) was 20 mm or more. However, there were consecutive days of heavy rainfall in a number of these cases and this consideration reduces the number of independent episodes of heavy rain over the catchment to 15 in that 64-year period. **Table 1** records the results of the synoptic analysis of the heavy rain events in the Lake Eyre catchment.

The dominant system found to be responsible for the heavy rain events was the combination of a monsoon trough of low pressure on the MSLP surface and an upper trough as determined by the 500 hPa geopotential and 1000-500 hPa thickness analyses. An example of this synoptic type is shown in **Figure 2**. There were 15 events of this type.

Troughs in the easterlies which were not assessed as satisfying the requirements of the monsoon trough but were associated with an upper trough on the 500 hPa surface were analyzed as the
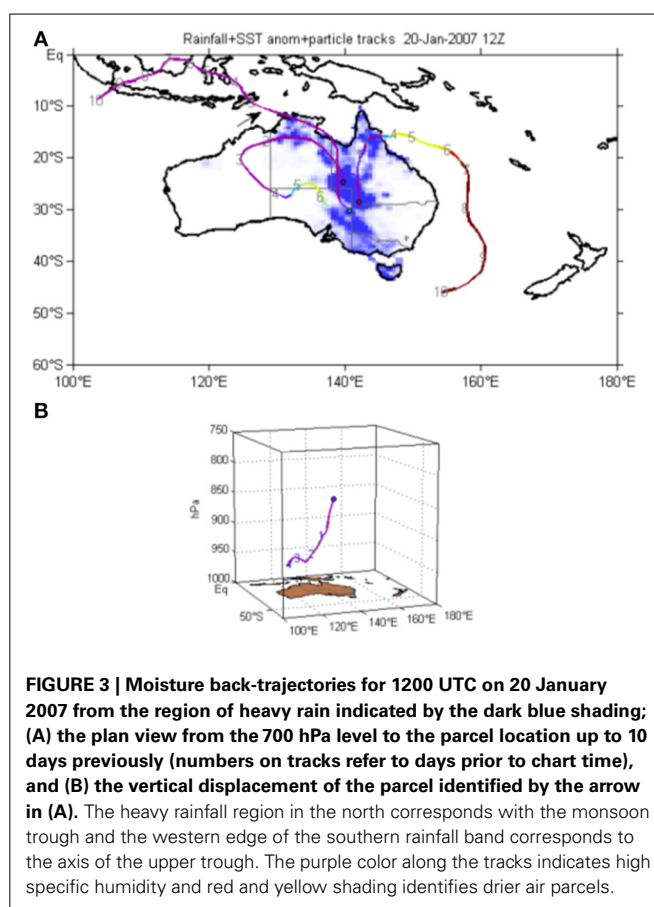

FIGURE 2 | The synoptic type classified as a monsoon trough at MSLP (A) combined with an upper atmospheric trough at 500 hPa (B).

Table 1 | Heavy daily rainfall events in the Lake Eyre catchment and the accompanying synoptic type as determined by the synoptic analysis.

Date	Mean catchment rain (mm/day)	Synoptic analysis
24-May-1955	23	E/ly Tr/upper Tr
25-May-1955	23	E/ly Tr/upper Tr
29-April-1968	21	cutoff low
05-March-1972	22	monsoon Tr/upper Tr
06-March-1972	21	monsoon Tr/upper Tr
07-February-1976	22	monsoon Tr/upper Tr
08-February-1976	24	monsoon Tr/upper Tr
09-February-1976	24	monsoon Tr/upper Tr
18-February-1977	21	monsoon Tr/upper Tr
19-February-1977	26	monsoon Tr/upper Tr
20-February-1977	23	monsoon Tr/upper Tr
10-July-1978	21	E'ly Tr/upper Tr
21-May-1981	21	E'ly Tr/upper Tr
12-January-1984	24	monsoon Tr/cutoff low
13-January-1984	30	monsoon Tr/cutoff low
31-March-1988	25	E'ly Tr/upper Tr
21-May-1990	22	E'ly Tr/cutoff low
22-May-1990	24	cutoff low
06-February-1991	22	monsoon Tr
28-February-1992	21	monsoon Tr/upper Tr
18-January-1995	29	monsoon Tr/upper Tr
19-January-1995	26	cutoff low
21-January-2007	22	monsoon Tr/upper Tr
28-February-2010	25	monsoon Tr/upper Tr
01-March-2010	26	monsoon Tr/upper Tr

The abbreviation "Tr" has been used for "trough."

FIGURE 3 | Moisture back-trajectories for 1200 UTC on 20 January 2007 from the region of heavy rain indicated by the dark blue shading; (A) the plan view from the 700 hPa level to the parcel location up to 10 days previously (numbers on tracks refer to days prior to chart time), and (B) the vertical displacement of the parcel identified by the arrow in (A). The heavy rainfall region in the north corresponds with the monsoon trough and the western edge of the southern rainfall band corresponds to the axis of the upper trough. The purple color along the tracks indicates high specific humidity and red and yellow shading identifies drier air parcels.

progenitors of a further 5 heavy rainfall events. One surface easterly trough was accompanied by a cutoff low at 500 hPa and 3 heavy rain events were associated with cutoff lows identifiable in both the upper air and at MSLP. Two of these events occurred in the austral autumn. Only one event was found to be caused by a surface trough without an accompanying trough in the middle and upper atmosphere. Additionally, only one heavy rain event occurred in the austral winter (10 July, 1978) and none in the austral spring, thus confirming the strong bias toward major rain events in the Lake Eyre catchment during summer and autumn.

For one event (21 January, 2007), an active monsoon trough was located over northern Australia while a cutoff low was centered just to the southwest of Adelaide and extended a cold trough at 500 hPa northwards over the Lake Eyre Basin. Although this location of the cutoff low would normally not be associated of itself with heavy rainfall over the majority of the Lake Eyre catchment, **Figure 3A** indicates that the warm conveyor belt on the eastern side of the cutoff system at 1200 UTC on (20 January, 2007) channeled moisture further southwards than would otherwise have occurred. The enhanced vertical motion leading to heavy rain is displayed in **Figure 3B** for the track indicated with the arrow in **Figure 3A**. This back trajectory shows air of high specific humidity originating in the boundary layer over the ocean to

the northwest of Australia and passing over northern Australia 2 days prior to chart time and rapidly ascending as it moved southwards. In this example, the axis of the monsoon trough at MSLP is closely aligned with the heavy rainfall region depicted in the north by the dark blue shading. The axis of the upper trough lies near the western edge of the southern rain band.

LAKE FROME CATCHMENT

For the analysis period, there were 28 heavy rainfall events resulting in an average daily rainfall of 25 mm or more over the Lake Frome catchment (**Table 2**). On four occasions, two or more days of heavy rain occurred consecutively. Clearly, the higher latitude of Lake Frome largely excludes its catchment from the meteorological activity so typical of the tropics in the monsoon season. Nevertheless, there were 5 days in the analysis when heavy rainfall events were recorded in both catchments concurrently. These 5 days were confined to three separate occurrences of heavy rain, in May 1955, February 1976 and January 1984. The mean catchment rainfall and the synoptic classification for the heavy rainfall events identified in the Lake Frome catchment are recorded in **Table 2**.

Monsoon troughs at MSLP combined with an upper trough were found to be responsible for about 20% of the 28 heavy rain events in the Lake Frome catchment. However, complex fronts were equally dominant causes of heavy rainfall events. These systems were characterized by strong interaction with a prefrontal trough and tropical moisture and often, a pre-existing subtropical

Table 2 | Heavy daily rainfall events in the Lake Frome catchment and the accompanying synoptic type as determined by the analysis.

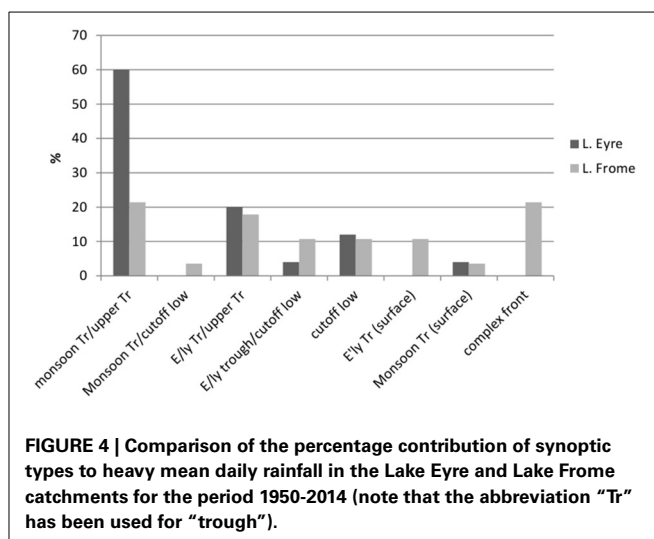| Date	Mean catchment rain (mm/day)	Synoptic analysis
02-February-1950	25	E'ly Tr
17-March-1950	47	E'ly Tr/upper Tr
24-May-1955	27	E'ly Tr/cutoff low
25-May-1955	36	cutoff low
17-January-1962	30	complex front
16-January-1968	25	cutoff low
29-December-1973	31	monsoon Tr
30-December-1973	26	complex front
29-January-1974	30	monsoon Tr/upper Tr
19-February-1974	27	E'ly Tr/upper Tr
23-October-1975	25	cutoff low
13-December-1975	32	E'ly Tr/upper Tr
08-February-1976	30	monsoon Tr/upper Tr
09-February-1976	49	monsoon Tr/upper Tr
10-February-1976	26	monsoon Tr/upper Tr
17-January-1979	25	monsoon Tr/upper Tr
22-February-1979	26	E'ly Tr/cutoff low
14-January-1984	44	monsoon Tr/cutoff low
26-January-1984	30	complex front
14-March-1989	49	monsoonTr/upper Tr
10-January-1990	26	E'ly Tr/cutoff low
16-March-1996	27	complex front
07-February-1997	31	E'ly Tr
12-February-2000	25	complex front
06-February-2011	40	complex front
29-February-2012	36	E'ly Tr/upper Tr
1-March-2012	29	E'ly Tr/upper Tr
15-February-2014	26	E'ly Tr

The abbreviation "Tr" has been used for "trough."

cloud band, and are similar to the "interacting frontal types" of Wright (1989, 1997). All of these complex front cases occurred in the austral summer and autumn when tropical moisture would be most likely to be available.

The next most important category of synoptic systems is a trough in the easterly flow at MSLP accompanied by an upper trough. There were also three cases where cutoff lows were the dominant synoptic system associated with daily rain events and four events where cutoff lows were associated with a trough on the MSLP surface. Additionally, four events were associated with troughs at the surface that were not also accompanied by troughs in the middle and upper atmosphere.

CATCHMENT COMPARISON

Figure 4 shows the comparison between the percentage contributions of synoptic systems to heavy daily rainfall events in the Lake Eyre and Lake Frome catchments. At Lake Eyre, more than 80% of cases involved an upper trough (including cutoff lows) associated with a trough at MSLP. Upper atmospheric systems were also important contributors to rainfall in the Lake Frome catchment where, in combination, they accounted for approximately 50%

FIGURE 4 | Comparison of the percentage contribution of synoptic types to heavy mean daily rainfall in the Lake Eyre and Lake Frome catchments for the period 1950-2014 (note that the abbreviation "Tr" has been used for "trough").
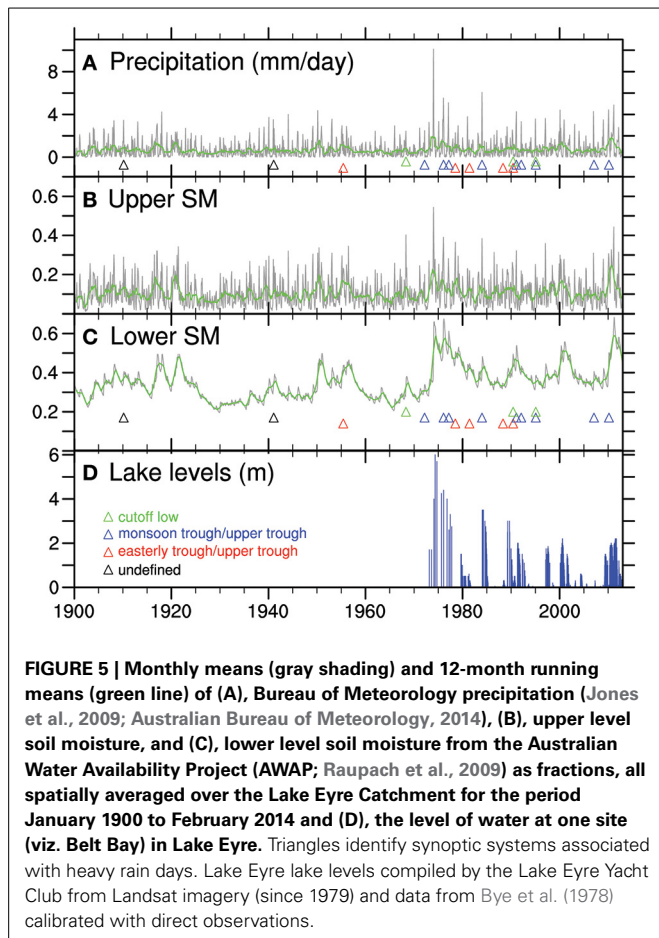
of events. Complex frontal systems were an equally important source of the Lake Frome heavy rain events (21%) to monsoon troughs accompanied by an upper trough. In these cases interactions occurred between a frontal system associated with a Southern Ocean depression and a prefrontal trough over subtropical Australia. In each catchment, individual cutoff lows extending from the mid-troposphere into the lower atmosphere resulted in approximately 12% of heavy rain days.

LAKE FILLING AND PRECIPITATION

Water levels in Lake Eyre have been recorded or estimated over many decades by the Lake Eyre Yacht Club (Bye et al., 1978). Prior to 1979, the lake levels were measured manually at Level Post Bay. Since 1979, satellite imagery in a range of visible and near-infrared wavelengths has become available for the Australian region from the LANDSAT series of polar-orbiting satellites. Interpretation of these data has been used to compile semi-quantitative lake levels with the addition of surface observations from 1973 to 1979. The site chosen here for comparing lake levels to catchment precipitation is known as Belt Bay which is located in the southern end of Lake Eyre North.

In order to better match the relatively slow lake-filling events with hydrological data, monthly precipitation data from AWAP are presented in **Figure 5A** for the Lake Eyre catchment. These data have been used as input for the AWAP hydrological model which provides estimates of runoff, water drainage and soil moisture in the catchment. Additionally, **Figure 5** shows upper soil moisture as a fraction of the total (B), lower soil moisture as a fraction of the total (C), and the estimated water level in Lake Eyre (D). The synoptic systems identified in the synoptic analysis as the dominant contributors to the individual heavy rain days are marked by colored triangles in **Figures 5A,C**. Prior to 1950, a synoptic type has not been assigned to each heavy rain event owing to the unavailability of reanalysis data.

In **Figure 5**, there is considerable noise in the monthly mean precipitation (A) and monthly mean of the upper soil moisture (B) (gray shading). The green line in each of the upper panels represents the 12-month running mean and provides a low

FIGURE 5 | Monthly means (gray shading) and 12-month running means (green line) of (A), Bureau of Meteorology precipitation (Jones et al., 2009; Australian Bureau of Meteorology, 2014), (B), upper level soil moisture, and (C), lower level soil moisture from the Australian Water Availability Project (AWAP; Raupach et al., 2009) as fractions, all spatially averaged over the Lake Eyre Catchment for the period January 1900 to February 2014 and (D), the level of water at one site (viz. Belt Bay) in Lake Eyre. Triangles identify synoptic systems associated with heavy rain days. Lake Eyre lake levels compiled by the Lake Eyre Yacht Club from Landsat imagery (since 1979) and data from Bye et al. (1978) calibrated with direct observations.

FIGURE 6 | Monthly means (gray shading) and 12-month running means (green line) of (A), Bureau of Meteorology precipitation (Jones et al., 2009; Australian Bureau of Meteorology, 2014), (B), upper level soil moisture, and (C), lower level soil moisture from the Australian Water Availability Project (AWAP; Raupach et al., 2009) as fractions, all spatially averaged over the Lake Frome Catchment for the period January 1900 to February 2014 and (D), the level of water at one site in Lake Frome. Triangles identify synoptic systems associated with heavy rain days. (Lake Frome lake levels compiled from Landsat imagery compiled by the Lake Eyre Yacht Club).
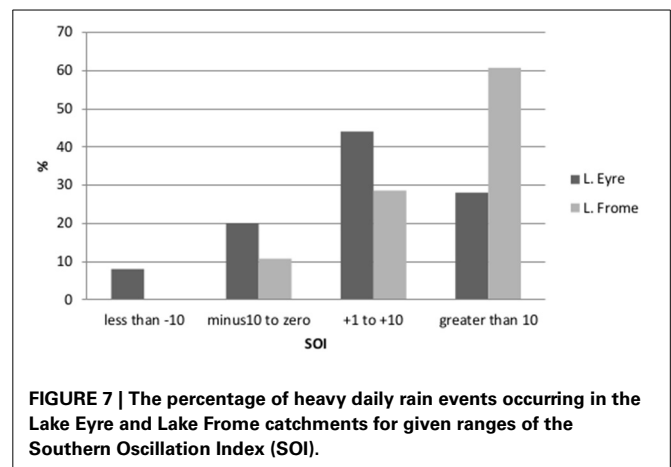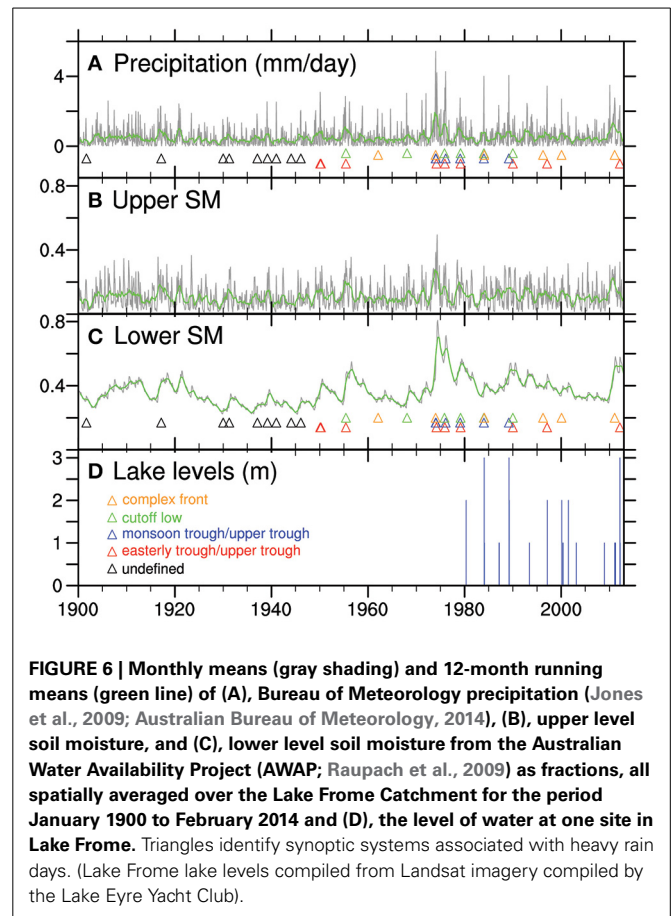
frequency filter. However, the lower soil moisture 12-month running mean is in close agreement with the monthly data and appears to match the lake level (D) quite well. This suggests that the behavior of this sub-surface layer acts as a low frequency filter on the precipitation.

The Lake Frome record displays some similar characteristics to the much larger Lake Eyre catchment but the lake level peaks are considerably lower than those recorded for Lake Eyre. **Figure 6** shows the precipitation, lower and upper soil moisture and lake levels for Lake Frome with the synoptic systems associated with heavy rain events marked by colored triangles in panels A and C. As in the Lake Eyre case, the lower level soil moisture 12-month running mean (C) matches the lake level data relatively well and appears to provide a measure of the low frequency response of Lake Frome and its catchment to precipitation.

LAKE FILLING AND ENSO

The strong tendency for the heavy rain events considered here to occur in the austral summer and autumn suggests that the intensity and persistence of the Australasian summer monsoon is a key factor in lake-filling episodes. In turn, the summer monsoon is closely influenced by the phase and intensity of the ENSO cycle. In order to investigate the association of ENSO with heavy rainfall in the lake catchments, the daily heavy rain events have been

FIGURE 7 | The percentage of heavy daily rain events occurring in the Lake Eyre and Lake Frome catchments for given ranges of the Southern Oscillation Index (SOI).

partitioned according to the mean value of the SOI for the month in which the event occurred.

Figure 7 indicates that about 90% of the heavy daily rain events in the Lake Frome catchment (25 events) occurred when the SOI was in its positive phase and over 70% in the case of Lake Eyre. Furthermore, at Lake Frome, the SOI exceeded +10 on 61% of occasions (17 events) and in the Lake Eyre analysis the SOI was greater than +10 in 28% of the cases (7). The Australian Bureau

of Meteorology applies a threshold figure to the SOI of +8 over a "sustained" period in order to define La Niña episodes.

DISCUSSION AND CONCLUDING REMARKS

A climatological analysis has been completed of the synoptic systems associated with heavy precipitation events in the Lake Eyre and Lake Frome catchments of central, southern Australia since 1950. The analysis reveals that tropical influences during the austral summer and autumn dominate significant daily precipitation occurrences in the Lake Eyre catchment. On the MSLP surface, these occurrences were characterized by convergence in a monsoon trough over northern Australia or, at the very least, a well-defined trough of low pressure in the easterly flow. However, the striking feature of the majority of these events was the presence of an accompanying trough or cutoff low in the middle troposphere (500 hPa) and a negative anomaly in 1000-500 hPa thickness relative to the long-term climatology. Further south, at Lake Frome, approximately one half of the events also had these characteristics but over 20% of events affecting that catchment were associated with Southern Ocean cold fronts which interacted with a prefrontal trough extending from the sub-tropics (complex fronts). Individual cutoff lows accounted for between 10 and 15% of heavy rain events in each catchment. Heavy rain events associated with surface troughs without upper air support were identified on only about 10% of occasions at Lake Eyre and 7% of occasions at Lake Frome. These findings indicate that synoptic analyses confined to mean sea level are inadequate for providing a complete understanding of these heavy rain events.

Although the climatology was based on heavy daily precipitation events, it is evident that one heavy fall of rain over a 24-h period is not capable of producing a lake-filling episode. These rare occurrences are associated with a persistence of rain events, usually in association with a well-developed Australasian summer monsoon which in turn, is closely influenced by the phase and intensity of the ENSO cycle. At least 80% of the heavy rain events examined in this study across both catchments occurred when the Southern Oscillation as measured by the SOI was in its positive phase. Strikingly, in the Lake Frome case, the SOI exceeded +10 on 60% of occasions, suggesting that the background atmospheric state in the Pacific Ocean and Australasia was tilted toward La Niña. At Lake Frome, all the events occurred outside winter, suggesting tropical interaction was a key component of the synoptic processes. Overall, it was a key finding of this study that the Lake Frome catchment derives significant rainfall from both tropical and subtropical synoptic types, and from connections between the higher latitudes and the tropics.

Hydrological modeling of the two catchments using high quality rainfall data as an input reveals that a 12-month running mean of the moisture content in the sub-surface soil layer coincides quite well with the historical lake levels. The degree of saturation of this sub-surface layer appears to act as a low pass filter on the catchment precipitation in a similar way to the finding of Ummenhofer et al. (2011). This property could possibly be employed in future attempts to predict lake levels following periods of heavy rain.

REFERENCES

Allan, R. J. (1985). *The Australasian Summer Monsoon, Teleconnections, and Flooding in the Lake Eyre Basin.* South Australian Geographical Papers No. 2. Royal Geographical Society of Australasia, Adelaide, SA.

Allan, R., Lindesay, J., and Parker, D. (1996). *El Niño Southern Oscillation and Climatic Variability.* Melbourne, VIC: CSIRO Publishing.

Australian Bureau of Meteorology. (2014). *Australian Water Availability Project Online Gridded Meteorological Surfaces.* Available online at: http://www.bom.gov.au/jsp/awap/ (Accessed June 2009–March 2014).

Bonython, C. W., and Fraser, A. S. (eds.). (1989). The great filling of Lake Eyre in 1974. *R. Geogr. Soc.* 119.

Bye, J. A. T., Dillon, P. J., Vandenberg, J. C., and Will, G. D. (1978). Bathymetry of Lake Eyre. *Trans. R. Soc. S. Aust.* 102, 85–89.

Cathcart, M. (2009). *The Water Dreamers (The Remarkable History of our Dry Continent).* Melbourne: Text Publishing.

Cohen, T. J., Nanson, G. C., Jansen, J. D., Gliganic, L. A., May, J.-H., Larsen, J., et al. (2012b). A pluvial episode identified in arid Australia during the Medieval Climatic Anomaly. *Q. Sci. Rev.* 56, 167–171. doi: 10.1016/j.quascirev.2012.09.021

Cohen, T. J., Nanson, G. C., Jansen, J. D., Jones, B. G., Jacobs, Z., Larsen, J. R., et al. (2012a). Late Quaternary mega-lakes fed by the northern and southern river systems of central Australia: varying moisture sources and increased continental aridity. *Palaeogeogr. Palaeoclimatol. Palaeoecol.* 356, 357, 89–108. doi: 10.1016/j.palaeo.2011.06.023

Cohen, T. J., Nanson, G. C., Jansen, J. D., Jones, B. G., Jacobs, Z., Treble, P., et al. (2011). Continental aridification and the vanishing of Australia's megalakes. *Geology* 39, 67–170. doi: 10.1130/G31518.1

Gliganic, L. A., Cohen, T. J., May, J.-H., Jansen, J. D., Nanson, G. C., Dosseto, A., et al. (2014). Late Holocene climatic variability indicated by three natural archives in arid Australia. *Holocene* 24, 104–117. doi: 10.1177/0959683613515732

Guymer, L. B. (1978). *Operational Application of Satellite Imagery to Synoptic Analysis in the Southern Hemisphere.* Technical Report, 29, Bureau of Meteorology, Melbourne, VIC.

Jones, D. A., Wang, W., and Fawcett, R. (2009). High-quality spatial climate datasets for Australia. *Aust. Meteorol. Ocean. J.* 58, 233–248.

Kalnay, E., Kanamitsu, M., Kistler, R., Collins, W., Deaven, D., Gandin, L., et al. (1996). The NCEP/NCAR 40-year reanalysis project. *Bull. Am. Meteorol. Soc.* 77, 437–471.

Kingsford, R. T., and Porter, J. L. (1995). Waterbirds of Lake Eyre, Australia. *Biol. Conserv.* 65, 141–151. doi: 10.1016/0006-3207(93)90443-5

Kistler, R., Kalnay, E., Collins, W., Saha, S., White, G., Woollen, J., et al. (2001). The NCEP/NCAR 50-year reanalysis project. *Bull. Amer. Meteor. Soc.* 82, 247–267. doi: 10.1175/1520-0477(2001)082<0247:TNNYRM>2.3.CO;2

Knighton, A. D., and Nanson, G. C. (1994). Flow transmission along an arid zone anastomosing river, Cooper Creek, Australia. Hydrol. *Process* 8, 137–154. doi: 10.1002/hyp.3360080205

Kotwicki, V. (1986). *Floods of Lake Eyre.* Adelaide, SA: South Australia Engineering and Water Supply Department.

Kotwicki, V., and Isdale, P. (1991). Hydrology of Lake Eyre, Australia El Niño link. *Palaeogeogr. Palaeoclimatol. Palaeoecol.* 84, 87–98. doi: 10.1016/0031-0182(91)90037-R

Lake Eyre Committee. (1955). Lake Eyre, South Australia:the great flooding of 1949–1950. *R. Geogr. Soc.* 75.

Magee, J. W., Miller, G. H., Spooner, N. A., and Questiaux, D. (2004). Continuous 150 k.y. monsoon record from Lake Eyre, Australia: Insolation-forcing implications and unexpected Holocene failure. *Geology* 32, 885–888. doi: 10.1130/G20672.1

McBride, J. L. (1998). "Indonesia, Papua New Guinea and tropical Australia: the Southern Hemisphere monsoon," in *Meteorology of the Southern Hemisphere*, Vol. 27, Meteorological Monograph, eds D. J. Karoly and D. G. Vincent (Boston, MA: American Meteorology Society), 89–99.

Pook, M. J., McIntosh, P. C., and Meyers, G. A. (2006). The synoptic decomposition of cool-season rainfall in the Southeastern Australian Cropping region. *J. Appl. Meteorol. Clim*. 45, 1156–1170. doi: 10.1175/JAM2394.1

Pook, M. J., Risbey, J. S., and McIntosh, P. C. (2012). The synoptic climatology of cool-season rainfall in the Central Wheatbelt of Western Australia. *Mon. Weather Rev*. 140, 28–43. doi: 10.1175/MWR-D-11-00048.1

Pook, M. J., Risbey, J. S., and McIntosh, P. C. (2014). A comparative synoptic climatology of cool-season rainfall in major grain-growing regions of southern Australia. *Theor. Appl. Climatol*. 117, 521–533. doi: 10.1007/s00704-013-1021-y

Poulter, B., Frank, D., Ciais, P., Myneni, R. B., Andela, N., Bi, J., et al. (2014). Contribution of semi-arid ecosystems to interannual variability of the global carbon cycle. *Nature* 509, 600–603. doi: 10.1038/nature13376

Raupach, M. R., Briggs, P. R., Haverd, V., King, E. A., Paget, M., and Trudinger, C. M. (2009). *Australian Water Availability Project (AWAP): CSIRO Marine and Atmospheric Research Component: Final Report for Phase 3*. Canberra, ACT: CAWCR Technical Report No. 013.

Raupach, M. R., Briggs, P. R., Haverd, V., King, E. A., Paget, M., and Trudinger, C. M. (2014). *CSIRO Australian Water Availability Project Model Data Release 26j. CSIRO Marine and Atmospheric Research, Canberra, Australia.* Available online at: http://www.csiro.au/awap (Accessed April 10, 2014).

Risbey, J. M., Pook, P., McIntosh, M., Wheeler, M. C., and Hendon, H. (2009). On the remote drivers of rainfall variability in Australia. *Mon. Wea. Rev*. 137, 3233–3253. doi: 10.1175/2009MWR2861.1

Simmonds, I., and Richter, T. (2000). Synoptic comparison of cold events in summer and winter in Melbourne and Perth. *Theor. Appl. Climatol*. 67, 19–32. doi: 10.1007/s007040070013

Sturman, A., and Tapper, N. (1996). *The Weather and Climate of Australia and New Zealand*. Melbourne, VIC: Oxford University Press.

Ummenhofer, C. C., Sen Gupta, A., Briggs, P. R., England, M. H., McIntosh, P. C., Meyers, G. A., et al. (2011). Indian and Pacific Ocean influences on Southeast Australian drought and soil moisture. *J. Clim*. 24, 1313–1336. doi: 10.1175/2010JCLI3475.1

Webb, S. (2010). Palaeotrophic reconstruction and climatic forcing of mega-Lake Eyre in late Quaternary Central Australia: a review. *Boreas* 39, 312–324. doi: 10.1111/j.1502-3885.2009.00120.x

Wright, W. J. (1989). A synoptic climatological classification of winter precipitation in Victoria. *Aust. Meteorol. Mag*. 37, 217–229.

Wright, W. J. (1997). Tropical-extratropical cloudbands and Australian rainfall: 1. Climatology. *Int. J. Climatol*. 17, 807–829.

ADVANTAGES OF PUBLISHING IN FRONTIERS

FAST PUBLICATION

Average 90 days
from submission
to publication

**COLLABORATIVE
PEER-REVIEW**

Designed to be rigorous –
yet also collaborative, fair and
constructive

RESEARCH NETWORK

Our network
increases readership
for your article

OPEN ACCESS

Articles are free to read,
for greatest visibility

TRANSPARENT

Editors and reviewers
acknowledged by name
on published articles

GLOBAL SPREAD

Six million monthly
page views worldwide

COPYRIGHT TO AUTHORS

No limit to
article distribution
and re-use

IMPACT METRICS

Advanced metrics
track your
article's impact

SUPPORT

By our Swiss-based
editorial team